DOE/ER-0313/26

Fusion Materials

Semiannual Progress Report
for Period Ending
June 30, 1999

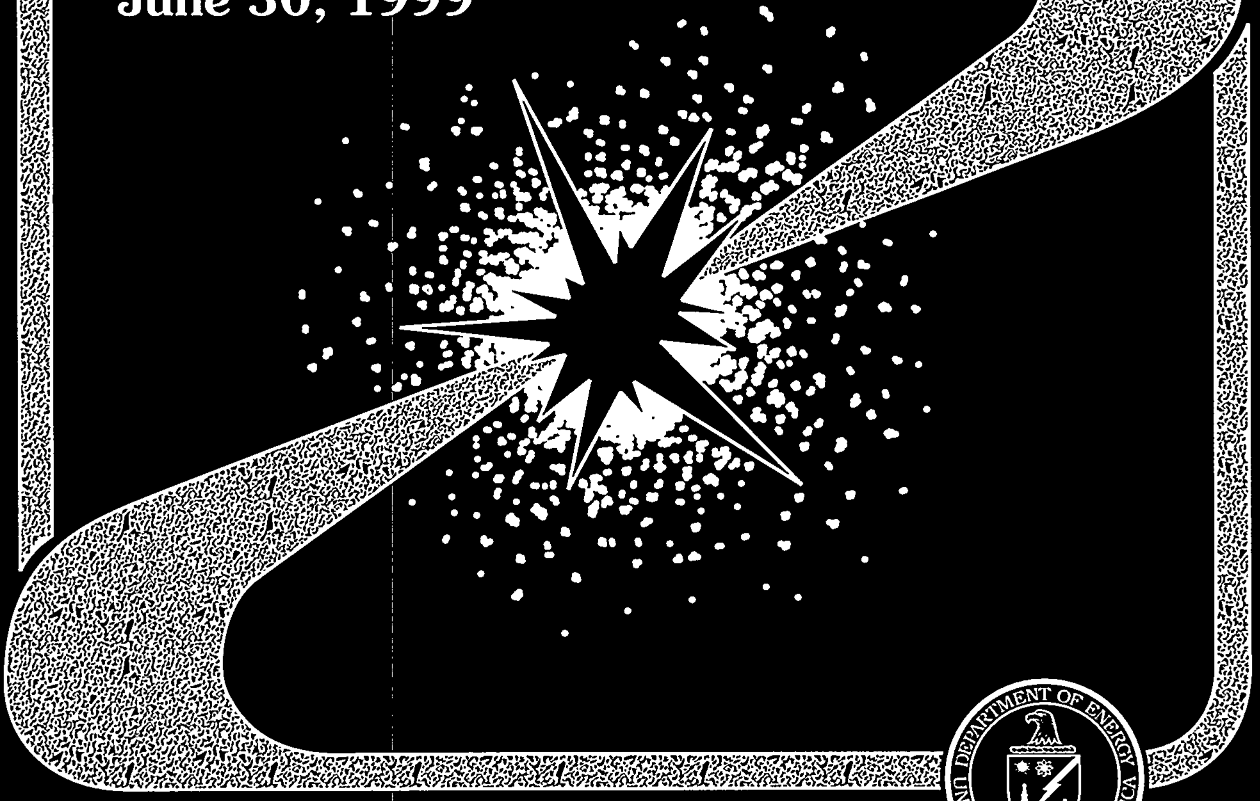

U. S. Department of Energy
Office of Fusion Energy Sciences

ORNL 99/08051/lld

DISCLAIMER

DOE/ER-0313/26
Distribution
Categories
UC-423, -424

FUSION MATERIALS SEMIANNUAL PROGRESS REPORT FOR THE PERIOD ENDING June 30, 1999

Prepared for
DOE Office of Fusion Energy Sciences
(AT 60 20 00 0)

DATE PUBLISHED: SEPTEMBER 1999

Prepared for
OAK RIDGE NATIONAL LABORATORY
Oak Ridge, Tennessee 37831
Managed by
Lockheed Martin Energy Research Corp.
for the
U.S. DEPARTMENT OF ENERGY
under Contract DE-AC05-96OR22464

FOREWORD

This is the tweny-sixth in a series of semiannual technical progress reports on fusion materials. This report combines the full spectrum of research and development activities on both metallic and non-metallic materials with primary emphasis on the effects of the neutronic and chemical environment on the properties and performance of materials for in-vessel components. This effort forms one element of the materials program being conducted in support of the Fusion Energy Sciences Program of the U.S. Department of Energy. The other major element of the program is concerned with the interactions between reactor materials and the plasma and is reported separately.

The Fusion Materials Program is a national effort involving several national laboratories, universities, and industries. A large fraction of this work, particularly in relation to fission reactor experiments, is carried out collaboratively with our partners in Japan, Russia, and the European Union. The purpose of this series of reports is to provide a working technical record for the use of the program participants, and to provide a means of communicating the efforts of materials scientists to the rest of the fusion community, both nationally and worldwide.

This report has been compiled and edited under the guidance of A. F. Rowcliffe by Gabrielle Burn, Oak Ridge National Laboratory. Their efforts, and the efforts of the many persons who made technical contributions, are gratefully acknowledged.

F. W. Wiffen
International and Technology Division

Reports previously listed in this series are as follows:

DOE/ER-0313/1	Period ending September 30, 1986
DOE/ER-0313/2	Period ending March 31, 1987
DOE/ER-0313/3	Period ending September 30, 1987
DOE/ER-0313/4	Period ending March 31, 1988
DOE/ER-0313/5	Period ending September 30, 1988
DOE/ER-0313/6	Period ending March 31, 1989
DOE/ER-0313/7	Period ending September 30, 1989
DOE/ER-0313/8	Period ending March 31, 1990
DOE/ER-0313/9	Period ending September 30, 1990
DOE/ER-0313/10	Period ending March 31, 1991
DOE/ER-0313/11	Period ending September 30, 1991
DOE/ER-0313/12	Period ending March 31, 1992
DOE/ER-0313/13	Period ending September 30, 1992
DOE/ER-0313/14	Period ending March 31, 1993
DOE/ER-0313/15	Period ending September 30, 1993
DOE/ER-0313/16	Period ending March 31, 1994
DOE/ER-0313/17	Period ending September 30, 1994
DOE/ER-0313/18	Period ending March 31, 1995
DOE/ER-0313/19	Period ending December 31, 1995
DOE/ER-0313/20	Period ending June 30, 1996
DOE/ER-0313/21	Period ending December 31, 1996
DOE/ER-0313/22	Period ending June 30, 1997
DOE/ER-0313/23	Period ending December 31, 1997
DOE/ER-0313/24	Period ending June 30, 1998
DOE/ER-0313/25	Period ending December 31, 1998
DOE/ER-0313/100	Technical Evaluation of the Technology of Vanadium Alloys for Use as Blanket Structural Materials in Fusion Power Systems

CONTENTS

1.0 VANADIUM ALLOYS 1

1.1 BIAXIAL THERMAL CREEP OF V-4Cr-4Ti AT 700°C AND 800°C — R. J. Kurtz and M. L. Hamilton (Pacific Northwest National Laboratory) 3

A study of the thermal creep properties of V-4Cr-4Ti is being performed using pressurized tube specimens. In a previous report relevant data on thermal creep of vanadium alloys was reviewed to guide the selection of an initial test matrix. Experimental details and results for exposure times of 1523 h at 700°C and 1784 h at 800°C were also covered. This report provides additional results for exposure times up to approximately 4000°C.

1.2 MICROSTRUCTURAL EXAMINATION OF V-4Cr-4Ti PRESSURIZED TUBES — D. S. Gelles, M. L. Hamilton, and R. J. Kurtz (Pacific Northwest National Laboratory) 11

Failed thermal creep pressurized tubes of V-4Cr-4Ti tested at 700 and 800°C have been examined using optical microscopy, scanning electron microscopy, and transmission electron microscopy in order to understand failure and creep mechanisms. Results show extensive thinning was controlled by dislocation c limb. Dislocation cell structure was not well developed, TiO_2 particles developed complex dislocation tangles and evidence for development of fine precipitation during creep was found.

1.3 UNIAXIAL CREEP BEHAVIOR OF V-Cr-Ti ALLOYS — K. Natesan, W. K. Soppet, and D. L. Rink (Argonne National Laboratory) 20

A systematic study has been initiated at Argonne National Laboratory to evaluate the uniaxial creep behavior of V-Cr-Ti alloys as a function of temperature in the range of 650-800°C and at applied stress levels in the range of 75-380 MPa. At present, the principal effort has focused on the V-4Cr-4Ti alloy of heat identified as BL-71; however, another heat of similar alloy from general Atomics (GA) will also be used in the study.

1.4 HIGH TEMPERATURE TENSILE PROPERTIES AND DEFORMATION BEHAVIOR OF V-4Cr-4Ti — A. F. Rowcliffe, D. T. Hoelzer, and S. J. Zinkle (Oak Ridge National Laboratory 25

The tensile deformation behavior of V-4Cr-4Ti has been determined over the range 20 to 800°C for strain rates in the range 10^{-1}/s to 10^{-5}/s. Changes in the strain rate sensitivity of stress parameters are linked to the existence of three different regimes of deformation, namely, Lüders extension, dislocation glide/strain hardening, and dislocation creep.

1.5 EFFECT OF ORIENTATION ON EFFECTIVE TOUGHNESS-TEMPERATURE CURVES IN V-4Cr-4Ti — E. Donahue, G. R. Odette, and G. E. Lucas (University of California, Santa Barbara) 33

Fracture tests were performed on fatigue precracked, 20% sidegrooved 0.26T compact tension specimens in LT and TL orientations under static loading conditions over temperatures ranging from −196 to −110°C. The effective toughness-temperature $K_e(T)$ curves were similar for both LT and TL orientations. The corresponding 100 $\mathrm{MPa}\sqrt{\mathrm{m}}$ transition temperature was estimated to be about −155°C. Additional tests to evaluate effects of specimen size, orientation, and material fabrication history on the K-T curves are under way.

1.6 STUDY OF IRRADIATION CREEP OF VANADIUM ALLOYS — H. Tsai, R. V. Strain, M. C. Billone, T. S. Bray, and D. L. Smith (Argonne National Laboratory) 36

Thin-wall tubing produced from the 832665 (500 kg) heat of V-4 wt.% Cr-4 wt.% Ti material was formed into pressurized tube specimens and irradiated in the HFIR RB-12J experiment to study irradiation creep. Irradiation and the required cool-down following irradiation have been completed and disassembly of the vehicle is under way. Calculated dose for the specimens ranged from 5.5 to 6.0 dpa and the calculated irradiation temperatures were 400 to 500°C.

1.7 FRACTOGRAPHY RESULTS FOR V-ALLOY TENSILE SPECIMENS IRRADIATED IN THE BOR-60 ATR, AND FFTF REACTORS — T. S. Bray, H. Tsai, R. V. Strain, M. C. Billone, and D. L. Smith (Argonne National Laboratory) 38

Fractography studies were conducted on numerous V-alloy specimens. These specimens had been irradiated in the ATR, FFTF, and BOR-60 reactors at temperatures ranging from 273 to 600°C and damage doses from 41 to 51 dpa. The results of the fractography studies show the medium dose (17 to 19 dpa), low irradiation temperature materials irradiated in BOR-60 to have mostly ductile fractures but with low areal reduction. The low dose (~4 dpa) ATR samples display a wide range of areal reductions with mostly ductile fractures. The fractography results for the FFTF samples with irradiation temperatures from 520 to 600°C and damage doses from 41 to 51 dpa show a wide range of reductions in area and all ductile fractures. Side-view observations revealed evidence of slip bands that are typically associated with dislocation channeling.

1.8 IMPURITY STUDIES OF GAS TUNGSTEN ARC WELDING OF VANADIUM ALLOYS — M. L. Grossbeck and J. F. King (Oak Ridge National Laboratory) 44

An improved getter system has been installed on the welding glove box since progress was last reported. Gas tungsten arc (GTA) welds using both oxygen and hydrogen getters resulted in very low oxygen levels but very high hydrogen levels in V-4Cr-4Ti. Charpy impact testing, nonetheless, determined a DBTT lower than previously achieved. The first weld with a DBTT at room temperature was made. Erratic results following post-weld heat treatments or low-temperature outgassing treatments were previously attributed to hydrogen cracking. It is now believed that this behavior is not so erratic and might result from precipitation. Transmission electron microscope studies have been initiated to study the unusual behavior.

1.9 IMPROVEMENT OF LASER WELD QUALITY OF V-Cr-Ti ALLOYS — Z. Xu, C. B. Reed, K. Natesan, and D. L. Smith (Argonne National Laboratory) 49

During this report period, the use of a YAG laser to weld sheet materials of V-Cr-Ti alloys has focused on (a) development of optimal laser welding parameters to produce deep penetration and defect-free welds, (b) integration of a custom-designed environmental control box (ECB) into the laser system to control the oxygen uptake during the processing, (c) examination of the porosity on longitudinally sectioned welds, and (d) analysis for oxygen content of the welds. An innovative method has been developed to obtain deep penetration and oxygen contamination free welds.

1.10 DIFFUSION BONDING OF VANADIUM ALLOYS — Z. Xu, D. L. Smith, and C. B. Reed (Argonne National Laboratory) 54

Preliminary investigations are in progress to evaluate the potential of diffusion bonding processes for joining vanadium-base alloys. Diffusion bonds were prepared on 3.8 mm thick V-4Cr-4Ti alloy plate on a 50 KVA welder with a range of process parameters. Preliminary microstructural analyses conducted on the test samples indicated that bonding was achieved for a range of process parameters.

1.11 DEVELOPMENT OF ELECTRICALLY INSULATING CaO COATINGS — K. Natesan, M. Uz, and S. Wieder (Argonne National Laboratory) 57

A systematic vapor transport study has been in progress to develop electrically insulating CaO coatings that are compatible with use in a liquid Li environment. Several experiments were conducted to study how the deposition of Ca on V-4Cr-4Ti substrate alloys is affected by variations in process temperature and time, and specimen locations, surface preparation, and pretreatment. During this reporting period, several specimens were prepared with a coating of CaO by thermal/chemical deposition and measurements were made of the electrical resistance of several CaO-coated specimens before and after exposure to an Li environment.

2.0 SILICON CARBIDE COMPOSITE MATERIALS 63

2.1 METHODS FOR JOINING SILICON CARBIDE COMPOSITES FOR HIGH TEMPERATURE STRUCTURAL APPLICATIONS — C. A. Lewinsohn, R. H. Jones, (Pacific Northwest National Laboratory), M. Singh (NASA Lewis Research Center), T. Shibayama (Center for Advanced Research of Energy Technology, Hokkaido University), T. Hinoki, M. Ando, Y. Katoh, and A. Kohyama (Institute of Advanced Energy, Kyoto University) 65

Joining methods are required to allow affordable fabrication of large or complex SiC/SiC components for fusion energy systems. Previous analysis of the criteria for successful and functional joints indicates that reactor-formed and polymer-derived silicon carbide should be considered as candidate joint materials. This report summarizes preliminary mechanical properties of silicon carbide joints formed by a reaction-based approach. Both the test methods and materials are preliminary in design and require further optimization. The values of the room temperature strength of the joints, tested in flexure, are one-third to one-quarter the expected value. It is believed that the material evaluated was not fully reacted during fabrication. Further annealing, in vacuum, also decreased the strength of the joints.

3.0 **FERRITIC/MARTENSITIC STEELS** 73

3.1 IMPURITY CONTENT OF REDUCED-ACTIVATION FERRITIC STEELS AND THE EFFECT ON THE REDUCED-ACTIVATION CHARACTERISTICS — R. L. Klueh (Oak Ridge National Laboratory), E. T. Cheng (TSI Research, Inc.), M. L. Grossbeck and E. E. Bloom (ORNL) 75

Three heats of reduced-activation martensitic steel were analyzed by inductively coupled plasma mass spectrometry for low-level impurities that compromise the reduced-activation characteristics: a 5-ton heat of modified F82H for which an effort was made during production to reduce detrimental impurities, a 1-ton heat of JLF-1, and an 18-kg heat of ORNL 9Cr-2WVTa. Specimens from commercial heats of modified 9Cr-1Mo and Sandvik HT9 were also analyzed. The objective was to determine the difference in the impurity levels in the F82H and steels for which less effort was used to insure purity. Silver, molybdenum, and niobium were found to be the tramp impurities of most importance. The modified F82H had the lowest levels, but in some cases the levels were not much different from the other heats. The impurity levels in the F82H produced with present technology did not achieve the limits for low activation for either shallow land burial or recycling. The results indicate the progress that has been made and what still must be done before the reduced-activation criteria can be achieved.

3.2 CONSTITUTIVE AND FRACTURE TOUGHNESS PROPERTIES OF AN ADVANCED FERRITIC/MARTENSITIC STEEL — P. Spätig, G. R. Odette, G. E. Lucas, and M. Victoria (University of California, Santa Barbara); M. Victoria (Technologie de la Fusion-Centre de Recherches en Physique des Plasmas, Ecole Polytechnique Fédérale de Lausanne) 83

A detailed investigation of the strain-hardening rate of the International Energy Agency (IEA) program heat of 8 Cr unirradiated F82H ferritic-martensitic steel has been undertaken in the temperature range [80K-723K]. The overall tensile flow stress is decomposed into an athermal/thermal yield stress contribution plus a mildly temperature-dependent strain-hardening component. The latter is based on a phenomenological dislocation mechanics model. Compared to simple power law treatments, this formulation provides a more accurate and physically based representation of the flow stress as a function of the key variables of test temperature, strain, and strain rate. Fracture toughness measurements from small 0.18 CT specimens are also reported and analyzed using a constraint correction model to estimate a small scale yielding K_{IC} (T) toughness curve. Finally, the status of the MACE collaboration is briefly summarized. The first irradiation at 250°C to 0.5 dpa has been tentatively completed, and is awaiting confirmation of the preliminary dosimetry. Near term plans for higher doses and other temperatures are described.

3.3 MICROSTRUCTURE OF ISOTOPICALLY-TAILORED MARTENSITIC STEEL HT9 IRRADIATED AT 400°C — N. Hashimoto, J. P. Robertson (Oak Ridge National Laboratory), and K. Shiba (Japan Atomic Energy Research Institute) 96

The microstructures of reduced-activation martensitic steel, HT9-std. (12Cr-1MoVW) and HT9 doped with ^{58}Ni and ^{60}Ni, irradiated at 400°C to 7 dpa in the High Flux Isotope Reactor (HFIR), were investigated by transmission electron microscopy. No cavities were observed in any alloys. Irradiation-induced a_0<100> and $(a_0/2)$<111> type dislocation loops were observed in all alloys; the number density and the mean diameter of a_0<100> type loops were higher and larger than that of $(a_0/2)$<111> type loops. Also, there was a tendency for the number density of loops in the HT9 doped with ^{60}Ni to be lower than those in the other alloys. Irradiation-induced precipitates were observed in all alloys, which were identified as $M_6C(\eta)$ type carbide, α' phase and M_2X phase. The $M_6C(\eta)$ type carbides and α' phase were formed along dislocation loops, suggesting that dislocation loops are sites of Cr segregation during irradiation and that Cr segregation plays an important role in the precipitation behavior in martensitic steels.

3.4 TENSILE PROPERTIES OF LOW ACTIVATION FERRITIC STEELS FOLLOWING IRRADIATION IN ORR — M. L. Hamilton and D. S. Gelles (Pacific Northwest National Laboratory) 102

Post-irradiation tensile test results are reported for a series of low activation steels containing Mn following irradiation in the Oak Ridge Reactor at 60, 200, 330, and 400°C to 10 dpa. Alloy compositions included 2Cr, 9Cr, and 12Cr steels with V to 1.5% and W to 1.0%.

Strength increases were higher in all alloys for irradiation conditions below 400°C, with peak hardening occurring following irradiation at 200°C, corresponding to a minimum of 4% total elongation. The 9Cr alloy class exhibited the smallest increases in hardening. Test results are provided and compared with behavior following irradiation in FFTF.

3.5 EFFECT OF HEAT TREATMENT AND IRRADIATION TEMPERATURE ON IMPACT PROPERTIES OF Cr-W-V FERRITIC STEELS — R. L. Klueh (Oak Ridge National Laboratory) and D. J. Alexander (Los Alamos National Laboratory) 117

Extended Abstract.

4.0 COPPER ALLOYS AND HIGH HEAT FLUX MATERIALS 119

4.1 POST-IRRADIATION ANNEALING RESPONSE OF PURE COPPER IRRADIATED AT 100°C — D. J. Edwards (Pacific Northwest National Laboratory), B. N. Singh, P. Toft, and M. Eldrup (Risø National Laboratory) 121

Extended Abstract.

4.2 MICROSTRUCTURES OF Ti-Al INTERMETALLIC COMPOUNDS IRRADIATED AT 674 K IN HFIR — Y. Miwa, T. Sawai (Japan Atomic Energy Research Institute) D. T. Hoelzer (Oak Ridge National Laboratory), and A. Hishinuma (JAERI) 126

Four kinds of Ti-Al intermetallic compounds were irradiated at 673 K to the fluence of 5.16×10^{25} n/m2 (E>1MeV) in HFIR. One consists of α_2-Ti$_3$Al single phase, and others consist of α_2-Ti$_3$Al and γ-TiAl duplex phases. After irradiation, transmission electron microscopy was carried out. In both α_2-Ti$_3$Al and γ-TiAl phases of the specimens, loop-shaped and dot-like clusters were observed. However, the nucleation behavior of cavities in α_2-Ti$_3$Al and γ-TiAl phases has been influenced by chemical compositions and fabrication processes.

5.0 AUSTENITIC STAINLESS STEELS 149

No contributions.

6.0 INSULATING CERAMICS AND OPTICAL MATERIALS 151

No contributions

7.0 SOLID BREEDING MATERIALS 153

No contributions.

8.0 RADIATION EFFECTS, MECHANISTIC STUDIES, AND EXPERIMENTAL METHODS 155

8.1 AN INTEGRATED THEORY, MODELING, EXPERIMENTAL, AND DATABASE PROGRAM FOR THE DEVELOPMENT OF ADVANCED FUSION MATERIALS — R. E. Stoller (Oak Ridge National Laboratory), G. R. Odette (University of California-Santa Barbara), and H. L. Heinisch (Pacific Northwest National Laboratory) 157

A *White paper on an Integrated Theory, Modeling, Experimental, and Database Program* has been prepared as part of the overall AMP planning process. A review of the current program status has lead to the following primary recommendations: (a) an ambitious integrated modeling program should be initiated and closely linked to the entire AMP program, (b) program planning should consider the items identified by the workshop participants described in Appendix A and those listed in Table 4.1, (c) the program should encourage inter-institutional collaborations, i. e. between national laboratories and universities as well as between national laboratories, (d) regular program exchanges and reviews should be an integral part of the program, (e) both new and ongoing research should demonstrate relevance to the issues described in this document and the overall AMP White paper.

8.2 A KINETIC MONTE CARLO STUDY OF MIXED 1-D/3-D DEFECT MIGRATION — H. L. Heinisch (Pacific Northwest National Laboratory), B. N. Singh (Risø National Laboratory), S. I. Golubov (Institute of Physics and Power Engineering) 179

Extended Abstract.

9.0 DOSIMETRY, DAMAGE PARAMETERS, AND ACTIVATION CALCULATIONS 185

9.1 RADIATION DAMAGE CALCULATIONS FOR THE FUBR AND BEATRIX IRRADIATIONS OF LITHIUM COMPOUNDS IN EBR-II AND FFTF — L. R. Greenwood (Pacific Northwest National Laboratory) 187

The Fusion Breeder Reactor (FUBR) and Breeder Exchange Matrix (BEATRIX) experiments were cooperative efforts by members of the International Energy Agency to investigate the irradiation behavior of solid breeder reactor materials for tritium production to support future fusion reactors. Lithium ceramic materials including Li_2O, $LiAlO_2$, Li_4SiO_4, and Li_2ZrO_3 with varying ^6Li enrichments from 0 to 95% were irradiated in a series of experiments in the Experimental Breeder Reactor (EBR II) and in the Fast Flux Test Facility (FFTF) over a period of about 10 years from 1982 to 1992. These experiments were characterized in terms of the nominal fast neutron fluences and measured ^6Li burnup factors, as determined by either mass spectrometry or helium measurements. Displacement per atom (dpa) values have been calculated for each type of material and irradiation. Values up to 11% ^6Li-burnup and 130 dpa are predicted for the longest irradiations. Using these new calculations, previously measured radiation damage effects in these lithium compounds can be compared or correlated with other irradiation data on the basis of the dpa factor as well as ^6Li-burnup.

9.2 NEUTRON DOSIMETRY AND DAMAGE CALCULATIONS FOR THE TRIST ER-1 EXPERIMENT IN HFIR — L. R. Greenwood (Pacific Northwest National Laboratory) and C. A. Baldwin (Oak Ridge National Laboratory) 194

Neutron fluence measurements and radiation damage calculations are reported for the TRIST ER-1 experiment, which was conducted in the removable beryllium position in the High Flux Isotope Reactor (HFIR) at Oak Ridge National Laboratory (ORNL). The maximum neutron fluence at midplane varied from 1.38 to 1.57×10^{22} n/cm^2 resulting in about 2.4 to 2.8 dpa in Al_2O_3.

9.3 NEUTRON DOSIMETRY AND DAMAGE CALCULATIONS FOR THE HFIR-CTR-62 AND 63 IRRADIATIONS — L. R. Greenwood (Pacific Northwest National Laboratory) and C. A. Baldwin (Oak Ridge National Laboratory 199

Neutron fluence measurements and radiation damage calculations are reported for the CTR-62 and –63 experiments, which were conducted in the High Flux Isotope Reactor (HFIR) at Oak Ridge National Laboratory (ORNL). The maximum neutron fluence at midplane was 6.9E+22 n/cm^2 resulting in about 14 dpa in the 316 stainless steel.

10.0 MATERIALS ENGINEERING AND DESIGN REQUIREMENTS

No contributions.

11.0 IRRADIATION FACILITIES, TEST MATRICES, AND EXPERIMENTAL METHODS 205

11.1 CONCEPTUAL DEVELOPMENT OF FUSION-2 EXPERIMENT FOR IRRADIATION TESTING OF VANADIUM ALLOYS IN A LITHIUM ENVIRONMENT AT ≈500-750°C N THE BOR-60 REACTOR — V. Kazakov, V. Chakin, V. Efimov, V. Petukhov, A. Tuktabiev, P. Gabiev (Research Institute of Atomic Reactors), H. Tsai, T. S. Bray, D. L. Smith (Argonne National Laboratory), and A. F. Rowcliffe (Oak Ridge National Laboratory) 207

The requirements of this task are to complete the conceptual designs of irradiation capsules to be exposed to a neutron dose of ≈20 dpa in BOR-60. The specimen matrix will include sheet tensile specimens, compact tension specimens, bend bars, TEM disks, and pressurized creep tubes. To better utilize the test volume and provide additional temperature options, it was decided to modify the experiment from a two-capsule to a threeOcapsule design. All capsules will be liquid-metal-bonded for temperature uniformity. Goal temperatures for the three capsules will be 450, 600, and 700-750°C, with an emphasis on 600°C. A key objective of the experiment will be to generate irradiation creep data for vanadium-base alloys, especially at the emphasized temperature of 600°C, where thermal creep may not be dominant.

11.2 SCHEDULE AND STATUS OF IRRADIATION EXPERIMENTS — A. F. Rowcliffe (Oak Ridge National Laboratory) 210

The current status of reactor irradiation experiments is presented in tables summarizing the experimental objectives, conditions, and schedule.

1.0 VANADIUM ALLOYS

BIAXIAL THERMAL CREEP OF V-4Cr-4Ti AT 700°C AND 800°C – R. J. Kurtz and M. L. Hamilton (Pacific Northwest National Laboratory)*

OBJECTIVE

To determine the biaxial thermal creep characteristics of V-4Cr-4Ti over the temperature range 600 to 800°C at realistic stresses for comparison with uniaxial creep tests and irradiation creep experiments.

SUMMARY

A study of the thermal creep properties of V-4Cr-4Ti is being performed using pressurized tube specimens. In a previous report [1] relevant data on thermal creep of vanadium alloys was reviewed to guide the selection of an initial test matrix. Experimental details and results for exposure times of 1523 h at 700°C and 1784 h at 800°C were also covered [1]. This report provides additional results for exposure times up to approximately 4000 h.

PROGRESS AND STATUS

An initial test matrix was developed from an evaluation of existing thermal creep data for vanadium alloys and consideration of design basis service loads [1]. Three test temperatures were selected, 600, 700 and 800°C. Stress levels were chosen to be below the tensile yield strength at the test temperature of interest. Table 1 gives pertinent information for each specimen in the first series of tests. The complete test matrix is given in Reference 1. Specimen codes in italic type denote failed specimens. Two unpressurized tube samples were also included at each test temperature to enable periodic microstructural and chemical assays to be performed.

Table 1. Unpressurized creep tube dimensions, fill pressures and mid-wall hoop stress levels.

Test Temp., °C	Specimen Code	Specimen OD, mm	Specimen Wall, mm	Fill Press., MPa	Mid-Wall Hoop Stress, MPa
700	AR11	4.5674	0.2601	2.896	72.5
	AR12	4.5662	0.2532	3.909	99.9
	AR13	4.5672	0.2456	4.937	129.6
	AR14	4.5657	0.2499	5.930	151.9
	AR15	4.5659	0.2553	6.964	173.4
800	*AR16*	4.5684	0.2477	2.654	77.3
	AR17	4.5667	0.2507	3.571	101.2
	AR18	4.5664	0.2461	4.482	128.7
	AR19	4.5667	0.2543	5.419	149.4
	AR20	4.5659	0.2527	1.793	52.0
	AR21	4.5679	0.2454	0.910	28.9

---

*Pacific Northwest National Laboratory (PNNL) is operated for the U.S. Department of Energy by Battelle Memorial Institute under contract DE-AC06-76RLO-1830.

Results and Discussion

Specimens are heated to 700 and 800°C in an ultra-high vacuum furnace for specific time intervals and then periodically removed to measure the change in OD with a high precision laser profilometer. The OD measurements were converted to strain values as described previously [1]. Tables 2 and 3 give the effective mid-wall creep strain at 700°C and 800°C, respectively. Rupture strains are denoted by bold type in the tables. These data are plotted in Figures 1 and 2. An interesting feature of the curves is that they do not show evidence of primary or secondary creep. Their shape is suggestive of tertiary creep from a very early stage in the test. This behavior may be due to the presence of shallow longitudinal scratches or defects found on the tube ID. Results of microstructural examinations of several failed tubes and an as-received specimen indicate that these defects are common [2] and are probably caused by the tube fabrication technique. Further work is needed to fully assess the significance of these defects on the biaxial creep properties of V-4Cr-4Ti.

Table 2. Time dependence of effective mid-wall creep strain for 700°C tests.

Time, h	AR11	AR12	AR13	AR14	AR15
168	0.0072	0.0000	0.0072	0.0072	0.0217
242	0.0072	0.0000	0.0072	0.0145	0.0361
357	0.0072	0.0072	0.0072	0.0289	0.0795
598	0.0072	0.0217	0.0145	0.0578	0.2096
1375	0.0072	0.0145	0.0217	0.1229	0.9246
1523	0.0072	0.0000	0.0361	0.1373	1.2783
2157	0.0361	0.0289	0.0578	0.3468	4.5424
2780	0.0289	0.0217	0.0578	0.8596	10.247
2804	-	-	-	-	**12.956**
2881	0.0289	0.0361	0.0867	0.9896	-
3258	0.0289	0.0217	0.0867	1.5309	-
3365	0.0361	0.0289	0.0939	1.6896	-
3532	0.0289	0.0289	0.0939	2.1008	-
3699	0.0289	0.0361	0.1011	2.3676	-
3890	0.0217	0.0361	0.1445	2.7712	-
4057	0.0217	0.0361	0.1300	3.1820	-

Comparison of the creep behavior of V-4Cr-4Ti at 700°C with results generated on HT-9 tube specimens show that V-4Cr-4Ti has much better creep resistance. The stress required to cause 1% creep strain (a typical design limit) in 3000 h at 700°C is about 140 MPa for V-4Cr-4Ti. For HT-9, 1% creep strain is reached at a stress of 120 MPa and a temperature of only 605°C [3].

Figure 3 and 4 give plots of the dependence of the creep rate on applied stress. The creep rates shown in Figures 3 and 4 are instantaneous values determined from

$$\dot{\varepsilon} = \frac{\varepsilon_{i+1} - \varepsilon_i}{t_{i+1} - t_i} \qquad (1)$$

where ε is the effective mid-wall creep strain and t is time. The times given in Figures 3 and 4 are the mid-point of the interval. Rough estimates of the stress exponent were obtained by fitting the data to the following equation

$$\dot{\varepsilon} = A\sigma^n \tag{2}$$

where σ is the effective stress and A and n are material constants.

Table 3. Time dependence of effective mid-wall creep strain for 800°C tests.

Time, h	AR16	AR17	AR18	AR19	AR20	AR21
167	-	-	-	-	0.0000	0.0072
168	0.0289	0.0650	0.1445	3.5917	-	-
242	0.0361	0.1156	0.6212	**14.709**	-	-
358	-	-	-	-	0.0217	0.0217
412	0.1156	0.8089	5.7999	-	-	-
488	0.1806	1.5306	10.832	-	-	-
516	-	-	-	-	0.0434	0.0217
578	0.3466	2.9363	**24.141**	-	-	-
727	0.8375	6.4173	-	-	-	-
864	1.5156	**13.561**	-	-	-	-
1031	2.6327	-	-	-	-	-
1343	5.4454	-	-	-	-	-
1491	7.1108	-	-	-	-	-
1784	10.835	-	-	-	-	-
2125	16.000	-	-	-	-	-
2460	21.295	-	-	-	-	-
2812	26.827	-	-	-	-	-
2956	29.201	-	-	-	-	-
3239	33.912	-	-	-	-	-
3346	35.806	-	-	-	-	-
3513	38.907	-	-	-	-	-
3680	42.279	-	-	-	-	-
3871	46.557	-	-	-	-	-
4029	**51.885**	-	-	-	-	-

At 700°C the stress exponent, n, is 5.7 or greater for all time intervals and at 800°C n ranges from 7.2 to 10.6. High values of n suggest that dislocation creep is the predominant deformation mechanism [4]. Microstructural studies [2] of several failed creep specimens support this conclusion. It should be noted, however, that grain boundary sliding and accommodation processes must also contribute significantly to creep deformation since extensive wall thinning is observed [2] near the failure location, but grain boundary cavitation is not found.

A comparison of the creep-rupture behavior of specimens tested here to data gathered on V-4Cr-4Ti (Heat BL-47) by Chung et al. [5] is presented in Figure 5. The data sets are correlated using the Larsen-Miller Parameter, that is

$$P = \frac{T(\log t_r + 20)}{1000} \tag{3}$$

where T is the test temperature in K, and t_r is the time-to-rupture in hours. The trend line is reasonable, but the data are too sparse to firmly establish a Larsen-Miller Parameter correlation for creep-rupture of this alloy.

Chemical analyses for pick-up of oxygen and nitrogen were performed on one of the unpressurized 800°C tube specimens (Sample ID: 8-2). This specimen was in the vacuum furnace for 2812 h. The chemical analyses were performed at Siemens Power Corporation in Richland, Washington. The specimen was sectioned into three parts and each section was prepared by etching in 10% HNO_3 : 4.8% HF for 30 seconds to one minute, followed by deionized water and acetone rinses with air drying. A LECO TC436 Nitrogen Oxygen Determinator was used for the analyses. The method uses inert gas fusion of the sample in a graphite crucible with nickel as a flux. Nitrogen is measured by thermal conductivity, and oxygen is measured as carbon dioxide by an infrared detector. Four control standards were analyzed along with the three sections of tube 8-2. Data for the control samples and unknowns are presented in Table 4.

Table 4. Chemical analysis results for unpressurized tube specimen 8-2, tested for 2812 h at 800°C.

Sample ID	Certified Content, wppm	Measured Levels	
		N, wppm	O, wppm
NBS 73C	370 N	404	NA
LECO 501-551	148 O	NA	146
LECO 502-047	1340 O	NA	1376
8-2 A	NA	57.1	747
8-2 B	NA	57.3	731
8-2 C	NA	65.1	721

The average oxygen and nitrogen levels after 2812 h at 800°C are 733 wppm O and 60 wppm N. These levels may be compared with the as-received values of 560 wppm O and 95 wppm N [6]. The data indicate that a relatively modest 30% increase in oxygen level was experienced during the course of the 2812 h exposure at 800°C. Additional chemical analyses on as-received and exposed samples are planned to verify this trend.

ACKNOWLEDGEMENTS

We acknowledge the significant efforts of L. K. Fetrow and R. M. Ermi in performing the experiments described in this report.

REFERENCES

1. R. J. Kurtz and M. L. Hamilton, "Biaxial Thermal Creep of V-4Cr-4Ti at 700°C and 800°C," in Fusion Materials: Semiannual Progress Report for Period Ending December 31, 1998, DOE/ER-0313/24 (1999) 7.

2. D. S. Gelles, M. L. Hamilton and R. J. Kurtz, "Microstructural Examination of V-4Cr-4Ti Pressurized Tubes," in Fusion Materials: Semiannual Progress Report for Period Ending June 30, 1999, DOE/ER-0313/25 (1999).

3. Unpublished research.

4. G. E. Dieter, “Mechanical Metallurgy,” McGraw-Hill, New York, (1986) 447.

5. H. M. Chung, B. A. Loomis and D. L. Smith, "Thermal Creep of Vanadium-Base Alloys," in U.S. Contribution, 1994 Summary Report, Task T12: Compatibility and Irradiation Testing of Vanadium Alloys, ANL/FPP/TM-287, ITER/US/95/IV MAT 10 (1995) 87.

6. H. Tsai, H. Matsui, M. C. Billone, R. V. Strain and D. L. Smith, “Irradiation Creep of Vanadium-Base Alloys,” J. of Nuc. Matls. 258-263 (1998) 1472.

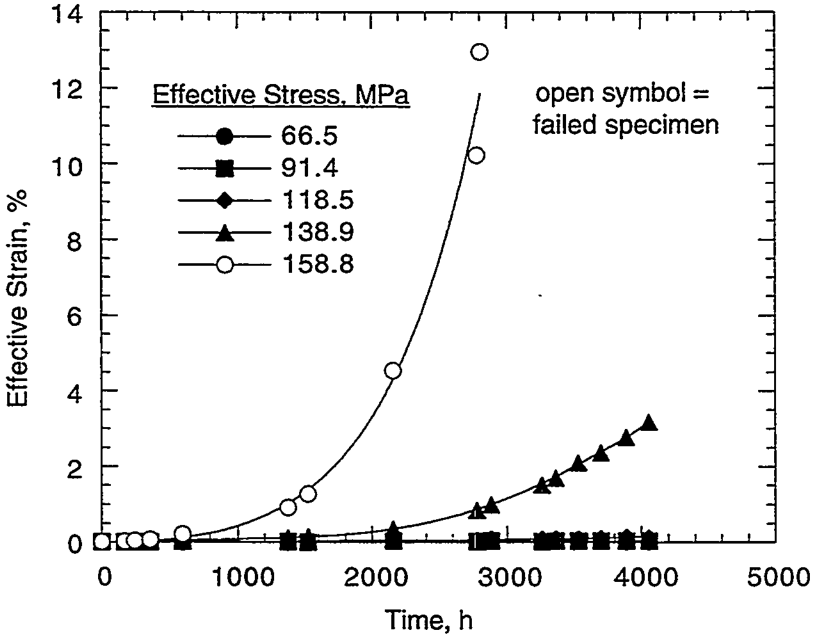

Figure 1. Time dependence of effective mid-wall creep strain at 700°C for unirradiated V-4Cr-4Ti.

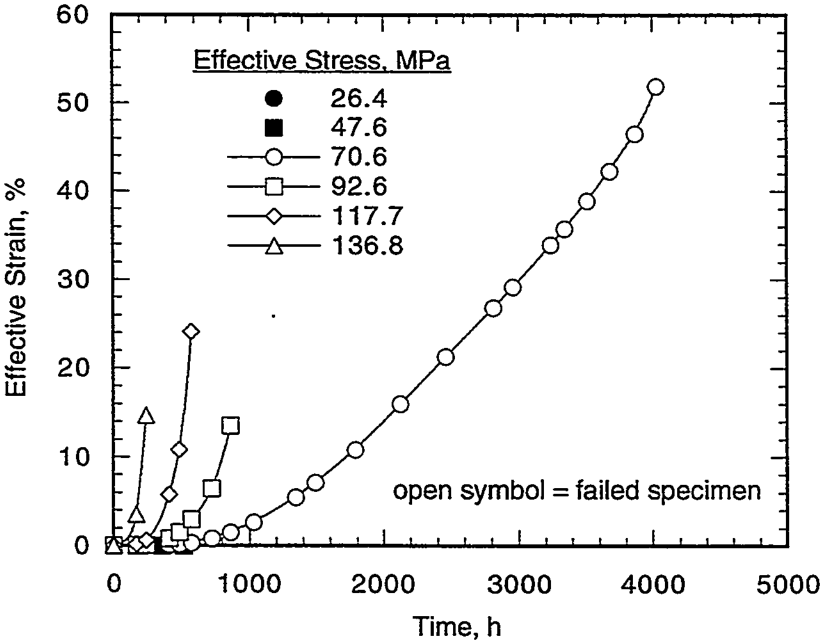

Figure 2. Time dependence of effective mid-wall creep strain at 800°C for unirradiated V-4Cr-4Ti.

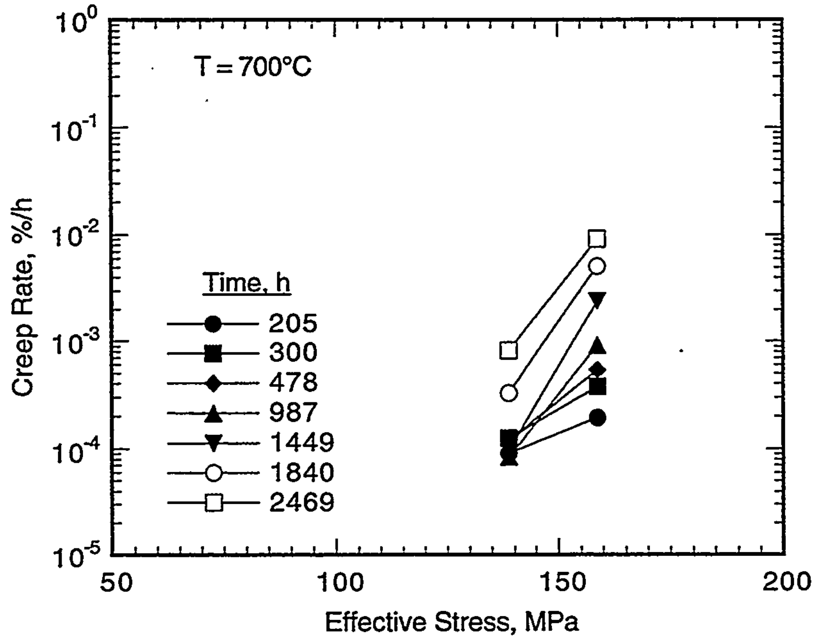

Figure 3. Stress dependence of the creep rate at 700°C for unirradiated V-4Cr-4Ti.

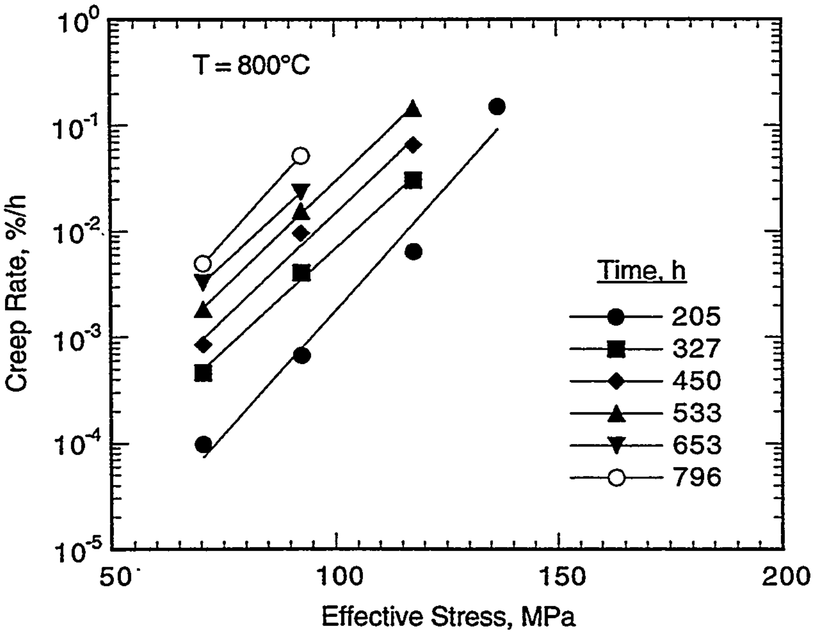

Figure 4. Stress dependence of the creep rate at 800°C for unirradiated V-4Cr-4Ti.

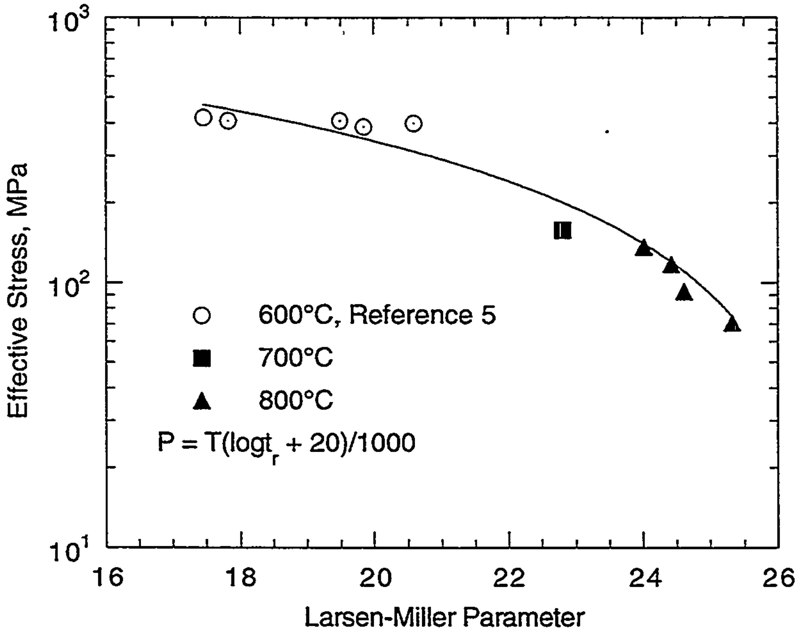

Figure 5. Larsen-Miller Parameter correlation for creep-rupture of unirradiated V-4Cr-4Ti. The 600°C data was taken from Reference 5.

MICROSTRUCTURAL EXAMINATION OF V-4Cr-4Ti PRESSURIZED TUBES

- D. S. Gelles, M. L. Hamilton, and R. J. Kurtz (Pacific Northwest National Laboratory)*

OBJECTIVE

The objective of this effort is to provide understanding of the processes controlling thermal creep in vanadium alloys in order to provide comparison with response under irradiation.

SUMMARY

Failed thermal creep pressurized tubes of V-4Cr-4Ti tested at 700 and 800°C have been examined using optical microscopy, scanning electron microscopy and transmission electron microscopy in order to understand failure and creep mechanisms. Results show extensive thinning was controlled by dislocation climb. Dislocation cell structure was not well developed, TiO_2 particles developed complex dislocation tangles and evidence for development of fine precipitation during creep was found.

PROGRESS AND STATUS

Introduction

Biaxial thermal creep response for V-4Cr-4Ti at 700 and 800°C was recently reported.[1] The present effort describes examination of specimens that failed using optical microscopy (OM), scanning electron microscopy (SEM) and transmission electron microscopy (TEM) techniques. The OM and SEM examinations were intended to locate the failure sites and to begin evaluating the failure mechanism. The work was extended to include microstructural examination by TEM in order to verify the controlling deformation mechanism. Creep tests at lower temperatures had shown high values for the stress dependence of secondary creep whereas grain boundary sliding could apply for the test conditions used.

Experimental Procedure

Specimens that failed during thermal creep testing of pressurized tubes are listed in Table 1.

Specimens AR15, AR17, AR18 and AR19 were examined by OM, and specimens AR18 and AR19 were examined by SEM using standard techniques. Pieces remaining after sectioning for OM and SEM were prepared for TEM by cutting 3 mm curved sections from tubes AR15, AR17 and AR19 using an ultrasonic drill, grinding the disks flat and then thinning the disks using standard electropolishing procedures in a Struers twin jet polisher. Microscopy was performed on a JEM 1200 EX using standard procedures.[3]

---

* Pacific Northwest National Laboratory (PNNL) is operated by the U.S. Department of Energy by Battelle Memorial Institute under contract DE-AC06-76RLO-1830.

Table 1. Test conditions for failed pressurized tube specimens of V-4Cr-4Ti (heat 832665[2]).

Specimen ID	Temp. (°C)	Effective Stress (MPa)	Time to failure (hrs)	Effective mid-wall strain (%)
AR15	700	159	2804	13.0
AR17	800	93	864	13.6
AR18	800	118	578	24.1
AR19	800	137	242	14.7

Results

Macroscopic features

Photographs of tubes AR18 and AR19 using OM are shown in Figures 1a, and b, and c, and d, respectively. The tubes have been oriented to show the likely failure sites in the center of the tube in a) and c) and at the top of the tube in b) and d). Tubes are 27.4 mm in length. In both cases failure appears to be due to formation of a longitudinal crack.

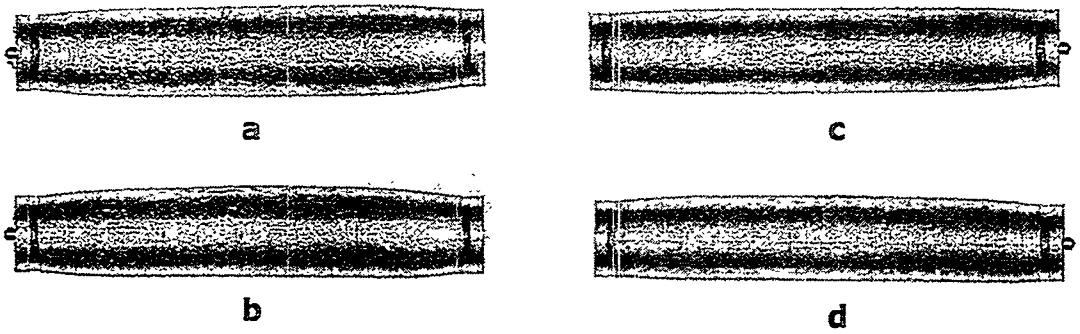

Figure 1. Failed pressurized tubes AR18 in a) and b) and AR19 in c) and d) shown with the likely failure site face-on at the top and rotated towards the top at the bottom.

The tubes were then sectioned in order to examine the failure sites from the inside of the tube. Photographs of the inner surfaces of the same specimens are provided in Figure 2, further illustrating the longitudinal failure.

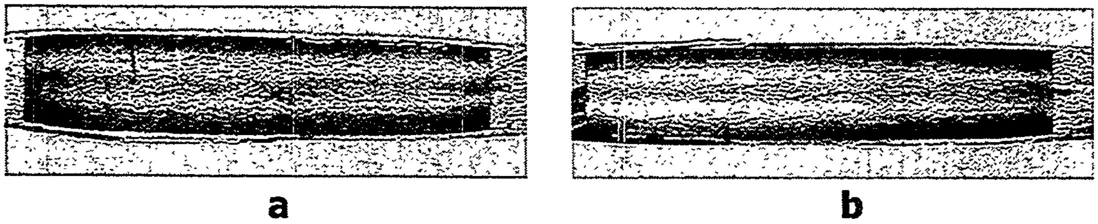

Figure 2. Failed pressurized tubes AR18 and AR19 showing the inner wall in the vicinity of the likely failure site for AR18 in a) and for AR19 in b).

SEM examination failed to conclusively identify the failure sites. The inner surfaces of specimens AR18 and AR19 were examined, and selected images are provided in Figures 3 and 4 that correspond to the photographs in Figure 2. From the low magnification examples in Figures 3 and 4, a number of fine longitudinal cracks can be identified. In each figure sequence, an area within the low magnification image has been enlarged in order to show surface features in greater detail. However, it cannot be demonstrated that these are through-thickness cracks.

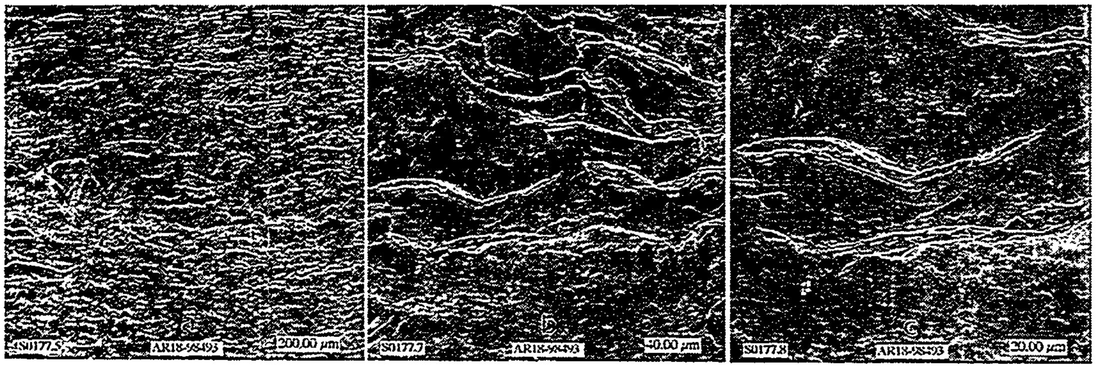

Figure 3. Surface features found on specimen AR18 at the failure location

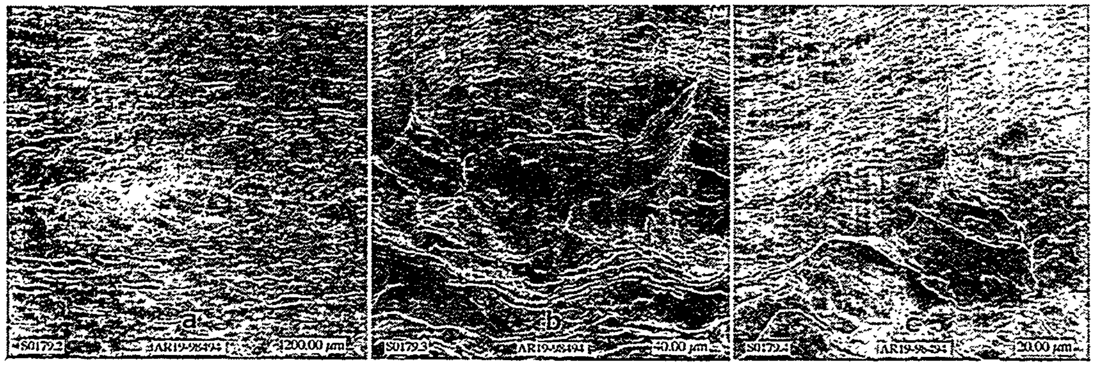

Figure 4. Surface features found on specimen AR19 at the failure location.

Metallographic sections were then prepared in order to locate through-thickness cracks, Examples are provided in Figure 5 showing regions in specimens AR15, AR17 and AR19 that contain areas that have been reduced in wall thickness between 60 and 75%. Figure 5 also includes transverse and longitudinal examples of unthinned sections of specimen AR17. From Figure 5, examples of grain elongation can be identified in each of the thinned sections, indicating that strain within grains reached high levels in comparison to grains in unthinned regions. Figure 5e) illustrates the bimodal distribution in grain size present in the tubing, i.e., the existence of a group of large grains interspersed with smaller grains.

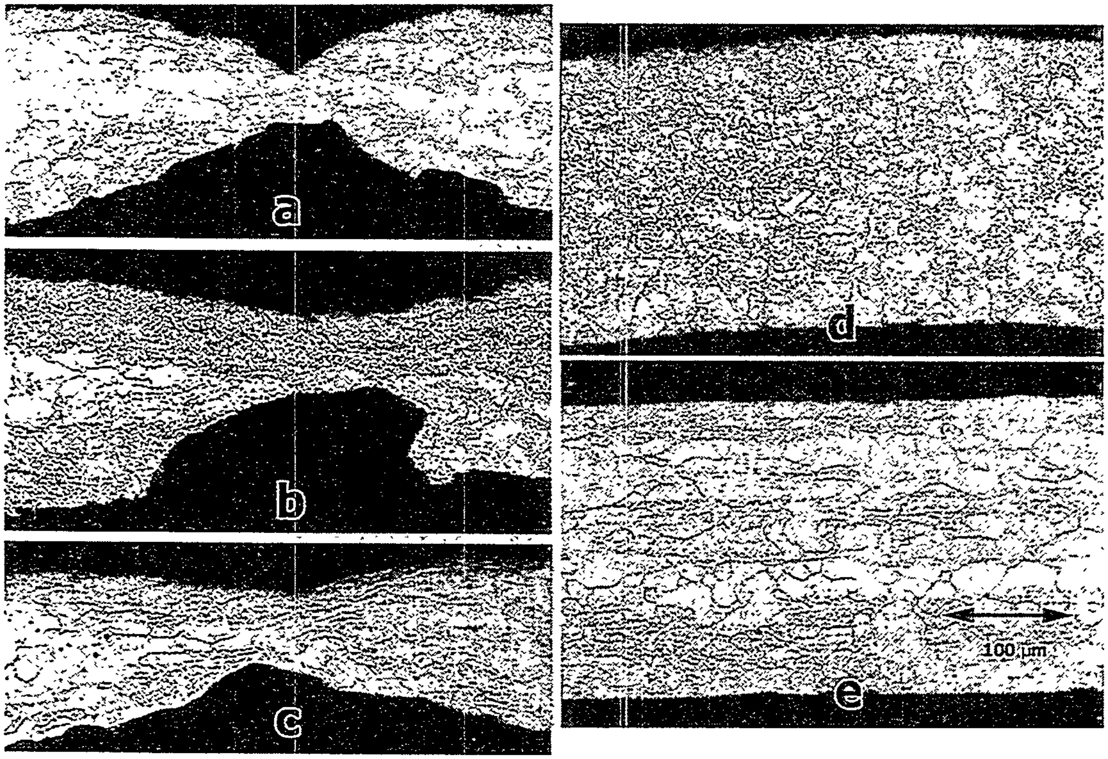

Figure 5. Optical metallographic examples of thinned sections of specimens AR15, AR17 and AR19 with unthinned transverse and longitudinal sections of specimen AR17 provided for comparison.

Microstructure

Specimens for TEM were successfully prepared from specimens AR15, AR17 and AR19 but thin area was limited. All microstructures were found to contain a moderate density of dislocations non-uniformly distributed. However, evidence for clearly defined cell walls and therefore a cell diameter characteristic of dislocation-controlled thermal creep behavior were not found. Instead the structure contained areas with higher or lower dislocation density, depending on location. However, in the vicinity of larger TiO_2 precipitate particles (~200 nm in diameter), the dislocation density was significantly higher, indicating that such particles were probably obstacles to dislocation evolution.

Examples of the microstructures found are given first for specimens tested at 800°C and then for the specimen tested at 700°C. Figure 6 shows low magnification examples of specimen AR17, tested at 800°C. Figures 6 a) and c) provide examples of grain boundary nodes indicating that most grain boundaries are straight and precipitate free, but some are heavily decorated with precipitation, presumably formed on cooling during heat treatment.[4] Figures 6 b) and c) indicate that the dislocation structure consists of a moderate dislocation density, but 200 nm diameter precipitate particles may be decorated at higher density. Also, figure 6 b) shows evidence of a poorly defined cell structure towards the center of the micrograph.

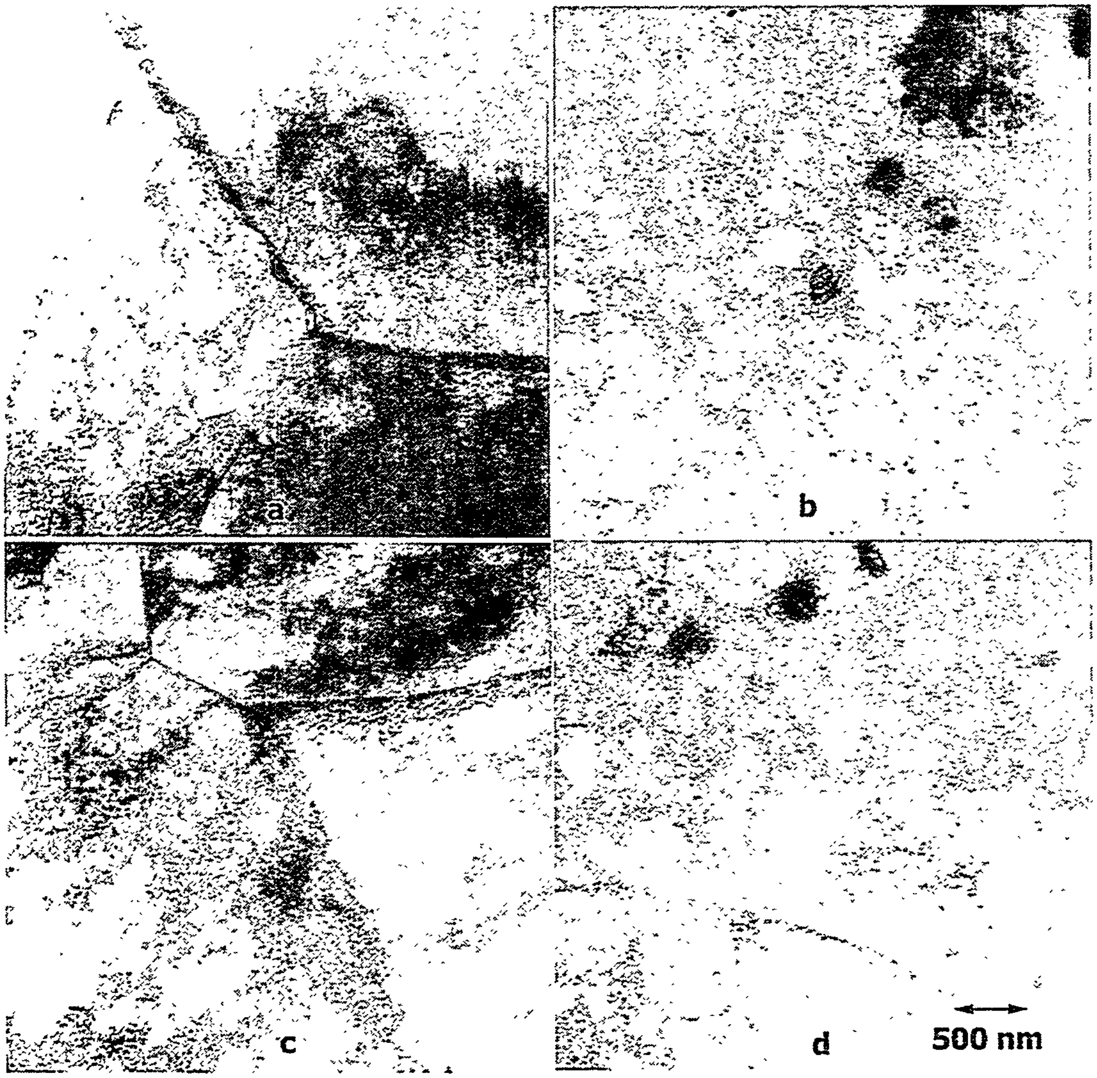

Figure 6. Low magnification examples of the microstructure of specimen AR17.

Figures 7 and 8 show the dislocation structure in greater detail for specimens AR17 and AR19, respectively. In each case, the structure is shown as a series of bright field stereo pairs, involving extensive tilting. Figures a) and b) give <110> images taken near (001), Figures e) and f) give and <01$\bar{1}$> in the latter do you mean bar 1? images taken near (011) and Figures c) and d) give <002>images taken between (001) and (011). Assuming that dislocations in vanadium alloys are of type a/2 <111>, then <002> images should show all dislocations present in equal contrast, whereas <110> and <01$\bar{1}$> images will only show two of the four sets, one of which will be seen in both sets of images. By process of elimination, it should therefore be possible to identify the Burgers vectors for all dislocations present.[3] From these figures, several observations can be made. The dislocation structure is non-uniformly distributed, with highest density near large TiO_2 particles, but with formation of poorly defined cell walls, and containing lowest densities between these cell walls. However, many small dark features can be identified, believed to be precipitation of Ti(O,C,N) type that formed during thermal creep exposure.

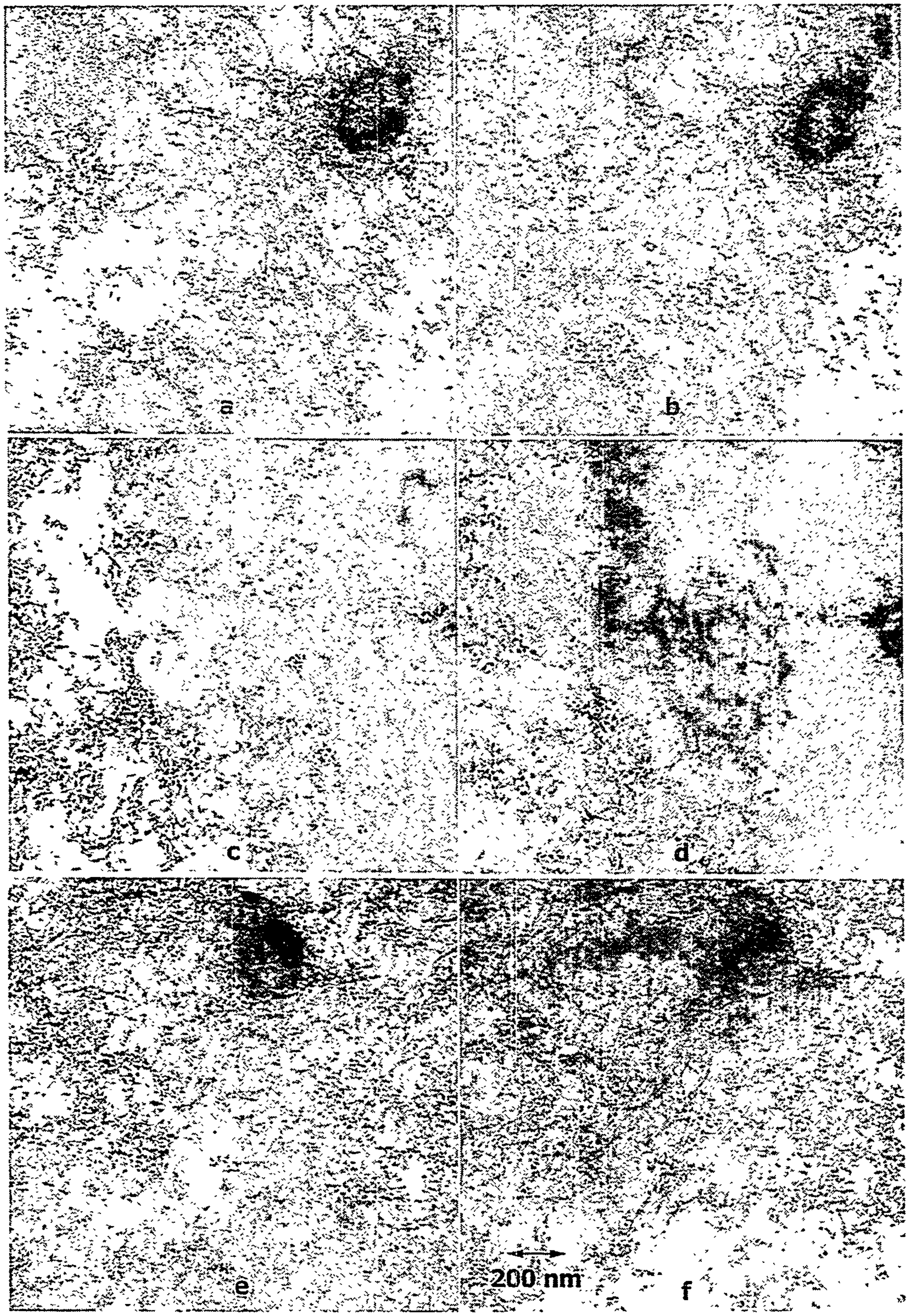

Figure 7. Stereo pair images of the dislocation structure found in specimen AR17 showing $g=\bar{1}01$, 002 and $01\bar{1}$ in a) and b), c) and d), and e) and f), respectively with g vertical in all cases.

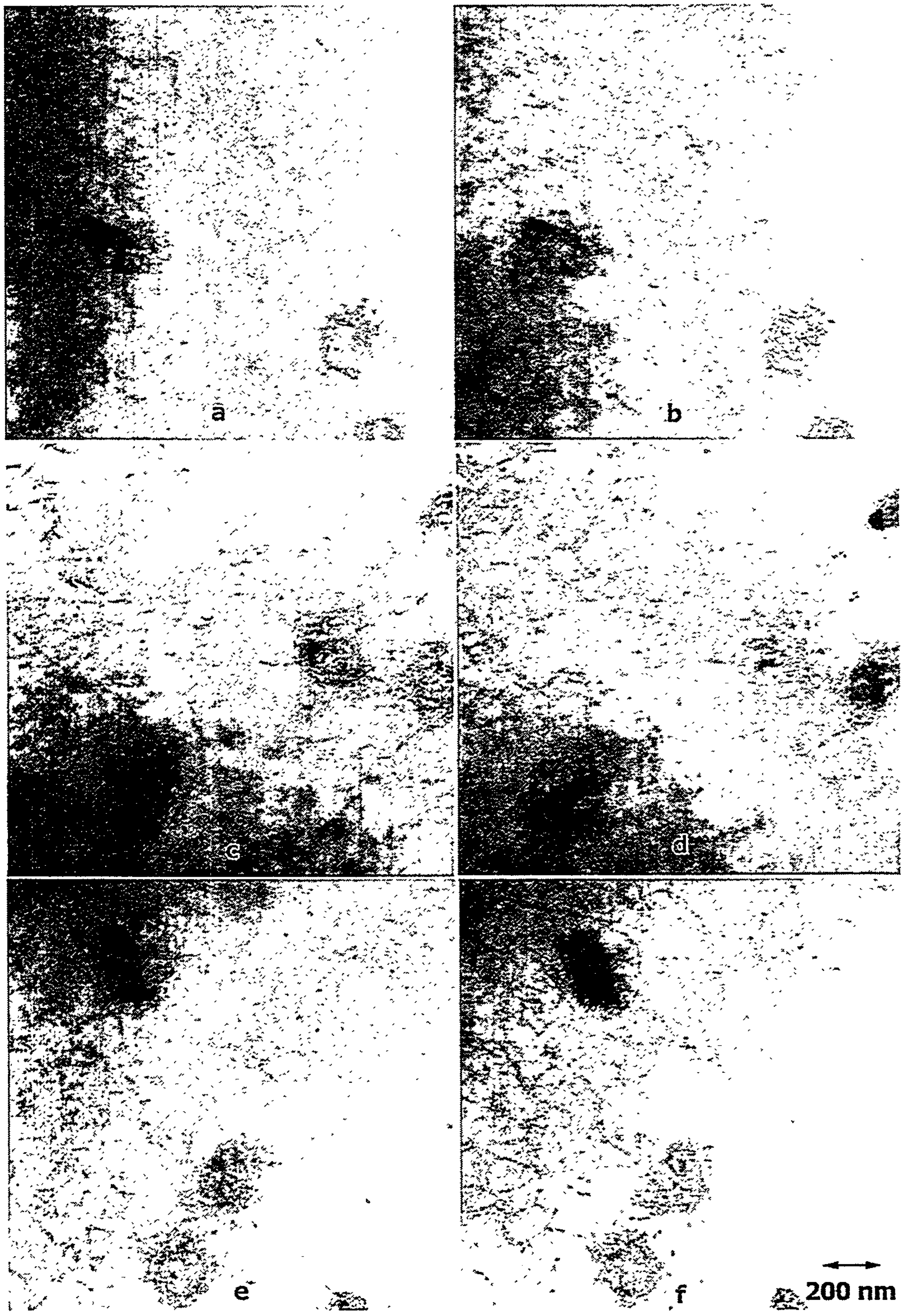

Figure 8. Stereo pair images of the dislocation structures found in specimen AR19 showing g=$\bar{1}01$, 002 and $01\bar{1}$ in a) and b), c) and d), and e) and f), respectively with g vertical in all cases.

Finally, Figure 9 is provided, showing examples of the dislocation structure found in specimen AR15, tested at 700°C. In each case, contrast is due to <011> but the region was not considered sufficiently uniform to provide a stereo sequence. Figure 9 demonstrates that dislocation evolution during thermal creep at 700°C is similar to that found at 800°C

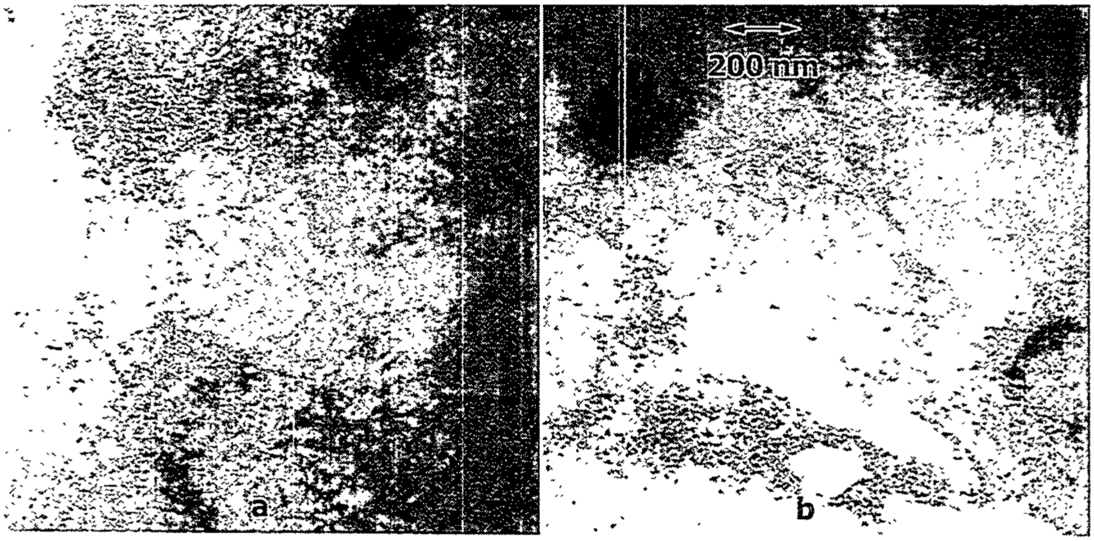

Figure 9. Examples of dislocation structures found in specimen AR15.

Discussion

Creep measurements using pressurized tube techniques are inevitably limited by the quality of the tubing used. Figures 3 and 4 reveal a number of small longitudinal defects and figure 5 indicates that where large strains have occurred, strain can be very non-uniform, showing that surface defects probably played a role in strain localization. SEM investigations also revealed larger inner surface defects such as radial scratches or gouges, but those examples are not included in this report because they apparently did not play a role in failure. It is therefore possible that failure to observe steady state creep response during biaxial thermal creep testing of V-4Cr-4Ti could be a consequence of internal surface defects. Also, rupture times can be expected to be underestimates for bulk material. Nonetheless, the quality of the tubing used is demonstrably adequate to provide good estimates for bulk thermal creep properties.

Figures 5 b) and e) can be interpreted to indicate that oxidation occurred on the outer surface of specimen AR17 during testing. Unfortunately, the dark banding on one side of the tube is believed due to staining, a metallographic artifact. This can be corroborated based on oxygen content measurements. An unpressurized control specimen in the 800°C furnace beside the pressurized tubes contained 59.8 wppm N and 733 wppm O. Therefore, the increase in the oxygen content was on the order of 30% over the levels after fabrication of 560 wppm.[2] Also, calculations indicated that oxygen penetration for the relevant time and temperature should be on the order of 2000 μm, approximately ten times the thickness of the stain.

The microstructures found following thermal creep indicate that strain is controlled by dislocation climb. This is confirmed by the elongated grain structure shown in figures 5 a), b) and c) and in agreement with the high stress exponent found for other tests.[1] However, it is also apparent that TiO_2 plays a role in controlling creep rates by acting as obstacles to dislocation climb. And the consequences of the small features expected to be Ti(O,C,N) precipitation are not yet understood. The lack of a well-defined dislocation cell structure, and therefore, a well-defined cell size, is possibly a consequence of the lack of steady state creep response.

A concern with the microstructural observations is that specimen preparation procedures may have affected the observed dislocation structures. TEM specimen preparation using ultrasonic drilling has not been used in the past, but was warranted because of the variation in tube diameter found following creep testing. As control specimens were not prepared, it cannot be shown conclusively that ultrasonic preparation has not influenced the results. Also, although most dislocation images appear to be typical of climbing dislocations, the stereo pair of figures 7e) and f) can be interpreted to contain a large number of slip dislocations oriented for optimum slip.

CONCLUSIONS

Failed V-4Cr-4Ti biaxial thermal creep specimens have been examined using OM, SEM and TEM in order to assess creep and failure mechanisms. It was found that deformation is probably due to dislocation climb, influenced by TiO_2 precipitation, and that lack of steady state creep response could be due to minor tube defects.

FUTURE WORK

This work will be continued within the confines of funding and specimen availability.

REFERENCES

1. R. J. Kurtz and M. L. Hamilton, DOE/ER-0313/25 (1999) 7.

2. H. Tsai, M. C. Billone, R. V. Strain, and D. L. Smith, DOE/ER-0313/23 (1998) 149.

3. D.S. Gelles, A. Kimura and R. J. Puigh, DOE/ER-0313/12 (1992) 123.

4. D. S. Gelles and H. Li, DOE/ER-0313/19 (1995) 22.

UNIAXIAL CREEP BEHAVIOR OF V-Cr-Ti Alloys*

K. Natesan, W. K. Soppet, and D. L. Rink (Argonne National Laboratory)

OBJECTIVE

The objectives of the creep test program are to (a) to establish time/temperature relationships for creep properties such as creep rupture strength, 1% creep in 10,000 hr, onset of third-stage creep, etc., all of which are key parameters in designing structural components for service at elevated temperatures; (b) provide a basis to establish the upper-use temperature associated with creep limits for application of V-base alloys; and (c) evaluate the influence of variations in substitutional and interstitial element concentrations on the creep properties of fusion-reactor-relevant V-base alloys.

SUMMARY

A systematic study has been initiated at Argonne National Laboratory to evaluate the uniaxial creep behavior of V-Cr-Ti alloys as a function of temperature in the range of 650-800°C and at applied stress levels in the range of 75-380 MPa. At present, the principal effort has focused on the V-4Cr-4Ti alloy of heat identified as BL-71; however, another heat of a similar alloy from General Atomics (GA) will also be used in the study.

INTRODUCTION

Refractory alloys based on V-Cr-Ti are being considered for use in first-wall structures in advanced blanket concepts that employ liquid Li as a coolant and breeding material. Further, advanced concepts that use He as a coolant also require structural alloys such as V-Cr-Ti alloys that can withstand the thermal loading at high temperature. For the advanced fusion system design concepts, it is important to establish the upper temperature limits for structural components based on various design criteria. At temperatures above 600°C, the time-dependent creep properties of V alloys must be considered when evaluating performance limits.

Limited data on the creep and stress-rupture properties of unirradiated V and V-base alloys have been reported by Chung et al.,[1] Schirra,[2,3] Bohm and Schirra,[4] Bajaj and Gold,[5] Kainuma et al.,[6] Van Thyne,[7] Carlander,[8] Bohm,[9] and Tesk and Burke.[10] Results from these studies showed that alloying of V with up to 3 wt.%Ti produces a significant increase in creep strength, but that additional Ti concentrations cause a substantial decrease in creep resistance. Addition of up to 15 wt.% Cr to V-(3-5)Ti alloy also produces significant strengthening in creep, while addition of 1 wt.% Si to V-3 wt.% Ti causes a significant decrease in the creep strength of this alloy. The data reported in these studies indicate that substitutional and interstitial element contents in V-base alloys have a significant effect on the creep properties. There are insufficient data available on the reference composition of V-4 wt.%Cr-4 wt.%Ti, especially at temperatures above 650°C.

The long-term creep properties of the V-base alloys will be influenced by the time-dependent nucleation and growth of precipitates that involve nonmetallic elements such as O, N, and C. Several of the microstructural studies of V-base alloys have identified precipitates such as face-centered-cubic Ti(O, N, C) with variable O, N, and C ratios. It is essential to establish the time-dependent evolution of type, number, and location of precipitates in V-base alloys to correlate the microstructual development with the creep properties. Further, development of several of these precipitates can be influenced by the exposure environment during creep testing. Over the long term, creep data are needed for environments with a wide range of chemistry and that encompass high vacuum to low

---

*This work has been supported by the U.S. Department of Energy, Office of Fusion Energy Research, under Contract W-31-109-Eng-38.

partial pressures of oxygen and hydrogen, and helium of various purities.

SCOPE OF WORK

The program in the near term will experimentally evaluate uniaxial creep properties of V-Cr-Ti materials in high-vacuum environments at temperatures of 650 to 800°C, with emphasis on baseline creep behavior of the alloys and correlations between microstructures and properties. Another aspect of the program will be to conduct creep tests on different heats of V-base alloys with a range of both substitutional and interstitial concentration variations, in order to provide an understanding of the effects of these variables on creep behavior.

EXPERIMENTAL PROGRAM

The effort will initially focus on the ANL-procured large heat of nominal composition V-4Cr-4Ti and on the GA heat of a similar composition. Four uniaxial creep-test machines have been allocated for this program. Two of the machines are equipped with high-vacuum systems and with furnaces capable of 900°C. The other two machines have vacuum capability and gas flow systems capable of conducting tests in low-partial-pressure environments and helium of various purities. We plan to use 1-mm-thick flat creep specimens (see Fig. 1 for details) of the alloy designed and fabricated according to ASTM Standard E8-69. A few specimens with cylindrical cross sections will be tested to validate the effects, if any, of specimen geometry on creep properties. Initial tests are conducted on specimens annealed at 1000°C for 1 hr in vacuum. During this period, a test was conducted at 725°C and 260 MPa. The specimen was wrapped in Ti foil to minimize contamination of the sample, especially by oxygen.

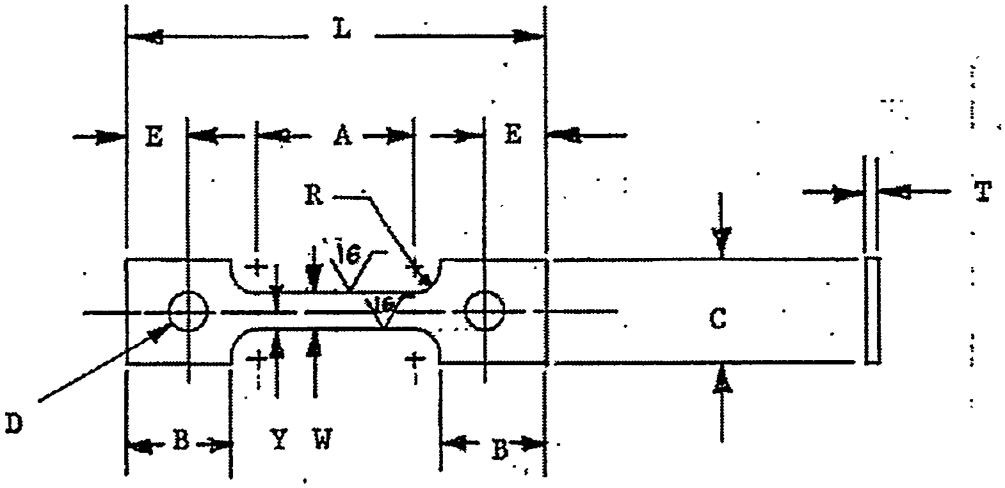

Dimensions in mm

A = 19 ± 0.50	Y = 2.2
B = 12.7	W = 4.5
C = 12.7	T = 1.0
D = 4.0	R = 3.175
E = 7.6	L = 50.8

Fig. 1. Schematic diagram of creep specimen designed according to ASTM Standard E8-69.

Creep strain in the specimen is measured by a linear-variable-differential transducer (LVDT), which is attached between the fixed and movable pull rods of the creep assembly. Displacements of 5×10^{-3} mm could be accurately determined with the LVDT. Before each test, the LVDT was calibrated by measuring its output for displacements that were set manually on a micrometer. The linear portion of the calibration curve is used to measure strain in a specimen during creep testing. The strain measurements are made at sufficiently frequent intervals during a test to define the creep strain/time curve.

A three-zone resistance-heated furnace is used in each testing machine to conduct creep tests at elevated temperatures. Chromel-Alumel thermocouples with small beads are used to measure specimen temperatures. Ceramic insulators are used on the thermocouples in the hot zone. In general, three thermocouples are fed through the specimen chamber, one spot-welded onto each end of the grips on the specimen near the shoulder region. The third thermocouple is held in the vacuum environment adjacent to the gauge-length portion of the specimen. Temperature is maintained within 2°C of the desired value for each test. The specimens are loaded at a constant rate to full load at the test temperature.

A detailed microstructural evaluation of the tested specimens is planned to characterize the morphologies as a function of exposure temperature and time and to establish the mechanisms of creep failure. The test program is aimed at obtaining the steady-state creep rate, onset of tertiary creep, rupture strain, and rupture life. At least four different stress levels are planned at each temperature to obtain sufficient data to develop Larson-Miller correlation between time, temperature, and applied stress. The information will be used to assess the upper-use temperature for the material, based on appropriate design criteria and as a basis for alloy improvement.

RESULTS

During this period, creep test facilities were set up with computerized data acquisition systems. Figure 2 shows the creep strain/time plot for a V-4Cr-4Ti alloy specimen tested in vacuum at 725°C and 260 MPa. Figure 3 is a scanning electron microscopy (SEM) photomicrograph of the specimen fracture surface. It is evident that the fracture morphology is indicative of ductile mode of failure. Figure 4 is an SEM photomicrograph of the polished cross section of the same specimen near the fracture surface, after creep testing at 725°C and 260 MPa. Grain size is in the range of 20-25 µm, and a significant number of minute cavities are seen at the grain boundaries.

To examine the extent of O contamination, if any, on the creep specimen, cross sections of the tested specimen were mounted and polished, after which Vickers hardness measurements were made at two locations along the thickness direction. Figure 5 shows the hardness profile for the tested specimen. Hardness values ranged from 150 to180, with most of the region in a range of 150-160, indicating that the contamination is minimal even at the test temperature of 725°C. Additional tests are in progress at 650, 725, and 800°C, and the results will be reported in the future as they become available.

REFERENCES

1. H. Chung et al., J. Nucl. Mater. 212-215 (1994) 772.
2. M. Schirra, Das Zeitstandfestigkeits- und Kriechverhalten von Vanadin-Basis-Legierungen, KfK Report 2440, Jan. 1989.
3. M. Schirra, Creep and Creep-Rupture of Vanadium Based Alloys, United States-Euratom Fast Reactor Exchange Program, EURFNR-1449 (1977).

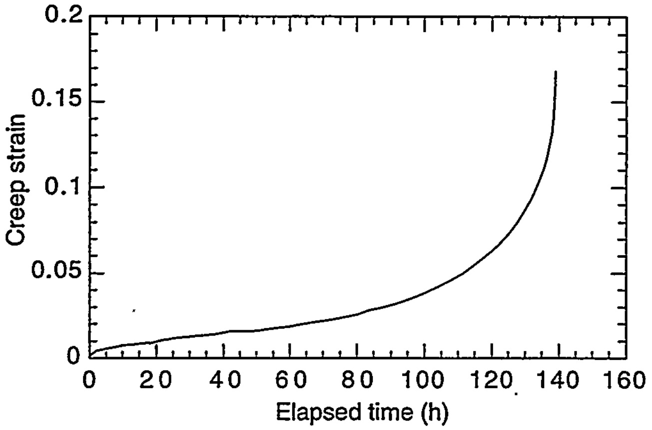

Fig. 2. Creep strain vs. time plot for V-4Cr-4Ti specimen creep tested at 725°C and 260 MPa in vacuum environment.

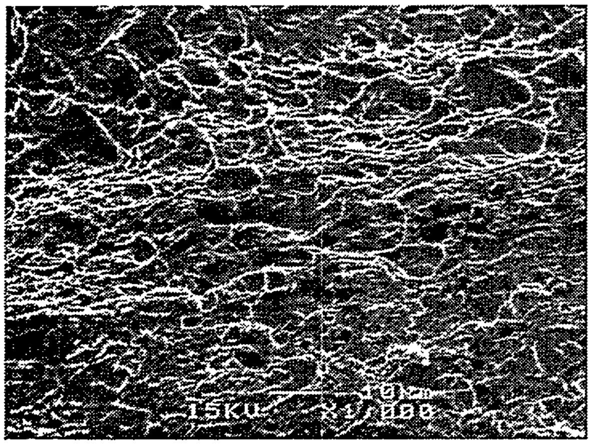

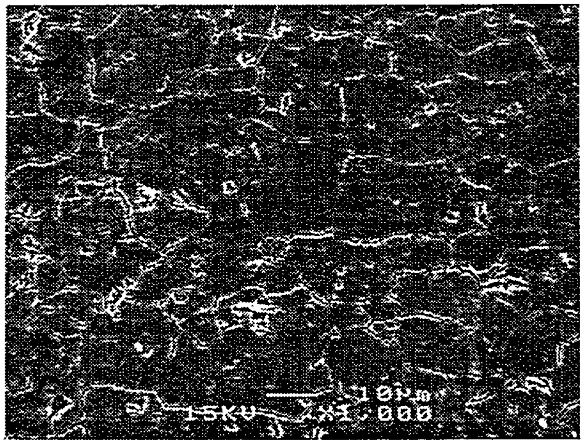

Fig. 3. SEM photomicrograph of cross section of fracture surface of V-4Cr-4Ti specimen, after creep testing at 725°C and 260 MPa.

Fig. 4. SEM photomicrograph of polished cross section of V-4Cr-4Ti specimen near fracture surface, after creep testing at 725°C and 260 MPa.

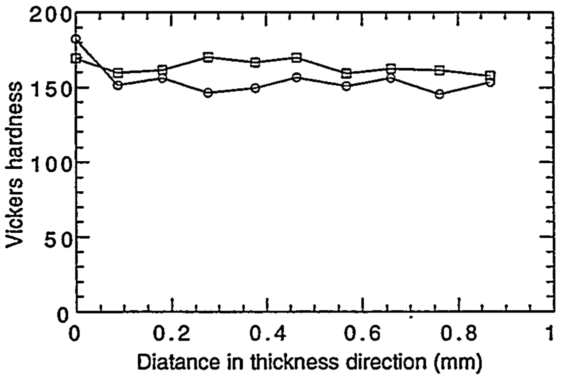

Fig. 5. Vickers hardness profile in thickness direction for V-4Cr-4Ti specimen, after creep testing at 725°C and 260 MPa.

4. H. Bohm and M. Schirra, J. Less-Comm. Met. 12 (1967) 280.

5. R. Bajaj and R. E. Gold, Alloy Development for Irradiation Performance, Semiann. Prog. Rep. DOE/ER-0045/10, Oak Ridge National Laboratory, Oak Ridge, TN (1983) 74.

6. T. Kainuma, N. Iwao, T. Suzuki, and R. Watanabe, J. Less-Comm. Met. 86 (1982) 263.

7. R. J. Van Thyne, in Reactive Metals, Vol. 2 (Buffalo, NY, 1958) 415.

8. R. Carlander, Quarterly Prog. Rep., Irradiation Effects on Structural Materials, BNWL-790 (1968) 3.7.

9. H. Bohm, Nucl. Metall. 18 (1973) 163.

10. J. A. Tesk and W. F. Burke, ANL Reactor Development Prog. Rep. ANL 7553 (1969) 85.

HIGH TEMPERATURE TENSILE PROPERTIES AND DEFORMATION BEHAVIOR OF V-4Cr-4Ti — A. F. Rowcliffe, D. T. Hoelzer, and S. J. Zinkle (Oak Ridge National Laboratory)

OBJECTIVE

The objective of this work is to determine the strain-rate sensitivity of the tensile properties of V-4Cr-4Ti as a function of temperature over the range RT to 800°C.

SUMMARY

The tensile deformation behavior of V-4Cr-4Ti has been determined over the range 20 to 800°C for strain rates in the range 10^{-1}/s to 10^{-5}/s. Changes in the strain rate sensitivity of stress parameters are linked to the existence of three different regimes of deformation, namely, Lüders extension, dislocation glide/strain hardening, and dislocation creep.

PROGRESS AND STATUS

Introduction

The work described here is a continuation of an investigation into the strain rate sensitivity of the deformation behavior of the 500 kg-heat of V-4Cr-4Ti (No. 832665). In an initial study [1], the hardening strain rate sensitivity, m, was determined at room temperature for the 500-kg heat and also for the 30-kg heat of V-3Cr-3Ti and V-6Cr-6Ti, where m is defined as

$$m=\frac{1}{\sigma}\frac{\partial\sigma}{\partial\ln\dot{\varepsilon}}\bigg|_{\varepsilon,T} \tag{1}$$

where σ is the stress and $\dot{\varepsilon}$ is the strain rate. It was found that for all three materials, m fell in the range 0.022 to 0.024, which agrees well with the value of 0.024 for pure vanadium (containing 265 wppm oxygen) reported by Bradford and Carlson [2]. Dynamic strain aging (DSA) was observed for all three alloys in the 400 to 700°C regime at a strain rate of 10^{-3}/s. Later work extended the range of strain rates from 10^{-1}/s to 10^{-5}/s and it was shown that a regime of negative strain-rate sensitivity associated with DSA extended down to 300°C in the V-4Cr-4Ti alloy [3]. Measurements of m for V-4Cr-4Ti irradiated in various reactors at temperatures ranging from 200 to 500°C were reported [4] and the radiation-induced changes in m were discussed in terms of a weakly positive component introduced by a high number density of defect clusters. Unirradiated tensile data generated in these studies were presented and combined with data obtained at other laboratories to derive equations describing the temperature dependence of strength and ductility properties at a strain rate of ~10^{-3}/s [5]. In this report, new experimental data and the strain rate sensitivities of several stress parameters are discussed in terms of related deformation mechanisms.

Experimental Procedure

Tensile measurements were performed on type SS-3 specimens (nominal gage dimensions 0.76 × 1.52 × 7.6 mm). The specimens used were from the RC/RD series that were prepared from heat no. 832665 using the fabrication steps shown in Table 1. As reported earlier [6], this procedure resulted in a uniform microstructure with an average grain size of ~23 μm and a hardness of 137 DPH after the final anneal at 1000°C for two hours. Testing was carried out under a vacuum of

Table 1. Temperature and Strain Rate Dependence of RD, RC Series Tensile Properties

Specimen ID	Test Temp. °C	Strain Rate S^{-1}	Initial Yield Stress σ_i MPa	Lower Yield Stress σ_y MPa	Ultimate Stress σ_u MPa	Stress for 8% Strain σ_r	Luders Strain ε_L %	Uniform Strain ε_u %	Total Strain ε_t %
Ann. 1000°C, 2h									
RD16	RT	10^{-3}	354	335	429	412	0.8	15.7	30.0
RD13	200	10^{-3}	259	259	350	338	1.2	14.8	23.8
RC03	300	10^{-1}	283	330	349	346	0.5	11.7	22.3
RC16	300	10^{-2}	—	271	332	330	—	13.5	22.3
RC02	300	10^{-3}	212	233	345	326	0.8	15.0	22.7
RC11	300	10^{-4}	175	228	346	327	0.7	15.4	22.5
RC12	300	10^{-5}	190	220	367	342	0.7	19.2	26.0
RD04	300	10^{-5}	175	217	365	350	0.4	11.9	18.0
RC08	400	10^{-1}	204	234	330	320	0.8	12.7	21.1
RC07	400	10^{-3}	179	214	353	330	0.5	16.3	23.0
RC04	400	10^{-3}	198	220	351	330	0.8	16.5	23.0
RC13	400	10^{-5}	196	224	375	356	0.6	16.3	21.9
RC09	500	10^{-1}	187	230	337	323	0.5	15.0	22.9
RC05	500	10^{-3}	225	225	365	342	0.9	17.7	24.0
RD01	500	10^{-3}	221	221	366	347	0.8	17.1	24.2
RD22*	500	10^{-3}	209	220	400	378	0.3	14.6	22.1
RD05	500	10^{-5}	189	231	400	377	0.5	15.2	19.2
RC14	500	10^{-5}	213	225	387	366	0.6	19.6	24.4
RC10	600	10^{-1}	207	222	351	336	0.4	13.3	20.0
RC06	600	10^{-3}	191	233	384	364	0.8	16.1	21.1
RC15	600	10^{-5}	275	275	455	404	—	15.0	21.2
RD25	700	10^{-1}	177	214	340	325	0.8	14.8	21.0
RD14	700	10^{-3}	—	222	388	364	0.7	12.3	18.8
RD15	700	10^{-5}	—	227	409	397	1.0	12.7	22.3
RD26	750	10^{-1}	200	215	338	326	0.7	12.0	19.0
RD02	750	10^{-3}	236	243	396	387	0.7	10.0	16.0
RD17	750	10^{-5}	200	225	353	353	0.8	10.8	25.5
RD27	800	10^{-1}	218	224	331	322	0.7	11.7	19.7
RD06	800	10^{-3}	242	234	337	334	0.9	11.0	19.0
RD18	800	10^{-5}	185	210	280	—	0.3	6.7	31.1

*Ann. 1150°C, 1h

~2 x 10^{-7} torr using a screw-driven machine. Specimens were held at test temperature for 20-30 minutes before starting the test. Data were acquired digitally at a rate of 20 points per second.

Results

Testing was carried out at 20, 300, 300, 400, 500, 600, 700, 750, and 800°C at five strain rates between 10^{-1} and 10^{-5}. These data are summarized in Table 1. The main features of the engineering stress-strain curves for V-4Cr-4Ti are shown in Fig. 1, which contains data for nine temperatures obtained at a strain rate of 10^{-3}/s.

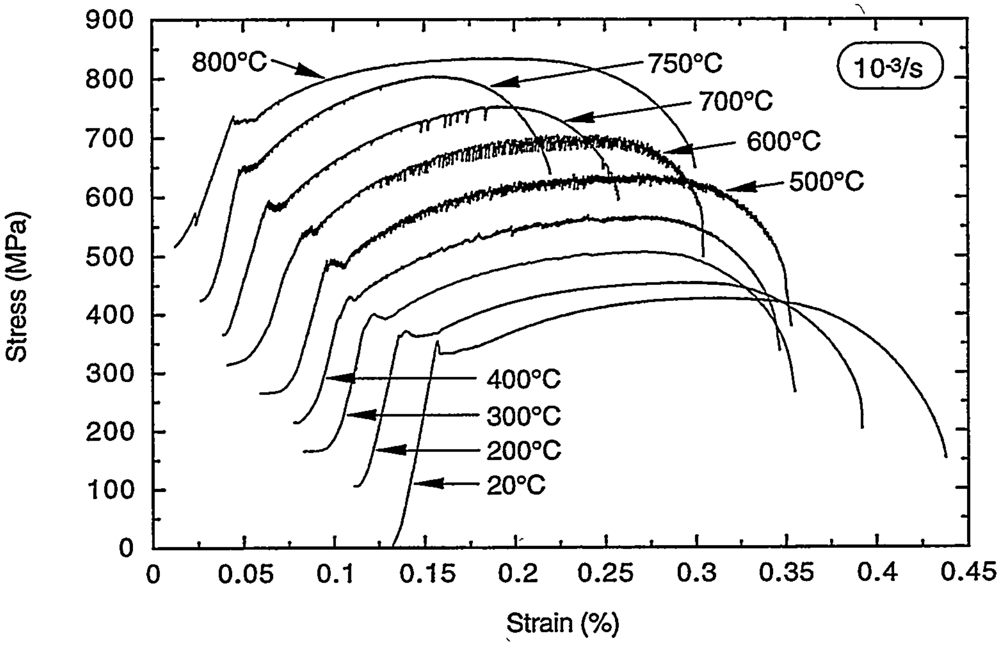

Fig. 1. The stress-strain curves for the V-4Cr-4Ti alloy tested at temperatures between 20 and 800°C.

In the majority of cases, the end of the elastic extension is marked by a small permanent plastic strain of the order of 0.1 to 0.2%. This is followed by a Lüders extension typically ranging from 0.5 to 1.0%. The lower yield stress, σ_y, is the stress required to propagate the Lüders extension. After the Lüders extension is complete, deformation occurs throughout the specimen on a rising stress-strain curve; eventually the work hardening rate decreases and the ultimate stress, σ_u, is achieved. For temperatures between 300 and 750°C, the flow curves exhibit jerky flow, which is related to the diffusion of solute atoms to dislocations during the test, i.e. the phenomenon of dynamic strain aging (DSA). As reported earlier [1], both the shape and magnitude of the serrations changes with temperature, strain, and with strain rate; further analysis of this behavior will be presented in future reports.

The strain-rate dependence was determined for the lower yield stress, σ_y, and for a parameter, σ_s, which is the stress required to produce a strain of 8% after the completion of the Lüders extension. The 8% strain is an arbitrary value selected to represent material in the strain-hardening regime. The strain-rate sensitivities of these parameters are presented in Figs. 2 and 3.

At 20°C, the lower yield stress exhibits a positive strain rate sensitivity (SRS). The SRS is also positive at 300°C for strain rates ≥10^{-3}/s, however, at lower strain rates, the SRS is markedly less positive (Fig. 2). For temperatures in the range 400 to 800°C, the lower yield point is virtually independent of strain rate over the entire range.

The stress for 8% strain, σ_s, shows very different behavior (Fig. 3). At 20°C, the SRS is positive over the range 10^{-1} to 10^{-4}/s. At 300°C, however, there is a transition from positive to negative behavior as the strain rate is decreased below ~10^{-3}/s. This temperature-dependent transition to a negative SRS coincides with the appearance of jerky flow in the stress-strain curve (Fig. 1).

At 400, 500, 600, and 700°C, the SRS is negative over the full range of strain rates examined with m values in the range (-0.012 to -0.022). All stress strain curves in this regime are characterized by jerky flow behavior with the exception of tests carried out at a rate of 10^{-1}/s. For these tests, it is possible that the data acquisition system was not sufficiently rapid to detect the load drops; it is planned to repeat these tests with an upgraded, high-speed system.

A different type of behavior was observed at test temperatures of 750 and 800°C. At both temperatures the strain rate sensitivity is negative over the range 10^{-1} to 10^{-3}/s. At lower strain rates, however, m becomes positive, indicating a transition into a different deformation regime.

The temperature-dependence of stress and strain parameters at a strain-rate of 10^{-3}/s is plotted in Fig. 4.

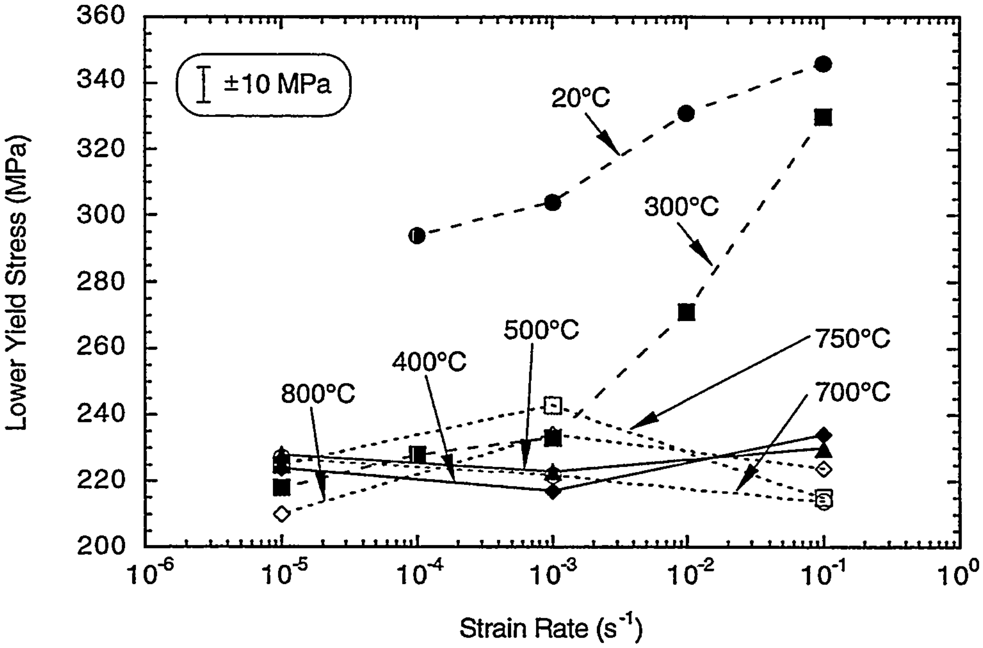

Fig. 2. Effect of strain rate on the lower yield strength of the V-4Cr-4Ti alloy tested at temperatures between 20 and 800°C.

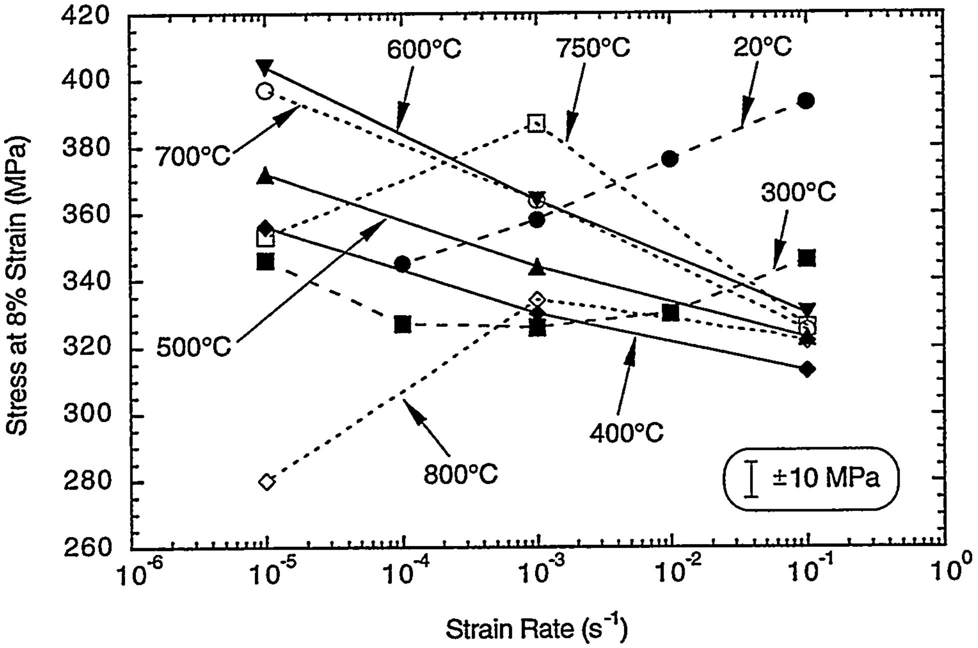

Fig. 3. Effect of strain rate on the tensile strength (measured at 8% strain in the strain-hardening regime) of the V-4Cr-4Ti alloy tested at temperatures between 20 and 800°C.

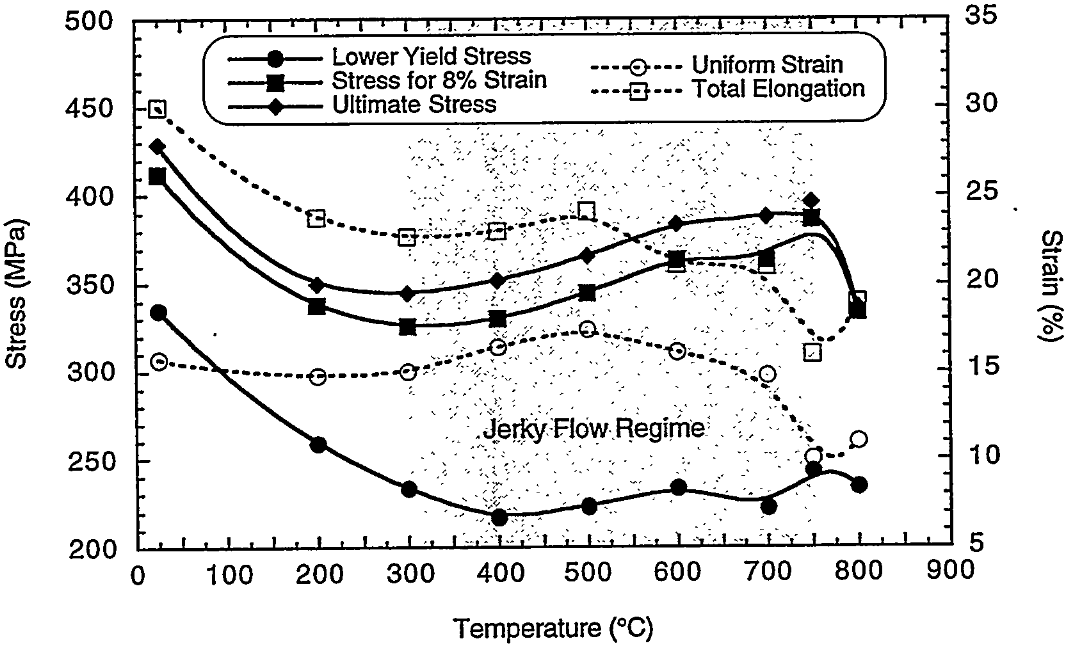

Fig. 4. The temperature-dependence of stress and strain parameters of the V-4Cr-4Ti alloy tested at a strain rate of 10^{-3}/s.

Discussion

The phenomenon of strain aging occurs in a wide range of FCC, BCC, and HCP alloys (for reviews see references [7, 8]). Strain aging is related to the segregation of mobile solute atoms to temporarily arrested dislocations, which partially impedes dislocation motion. Both substitutional and interstitial solutes can be involved. This pinning of dislocations by solute atmospheres gives rise to the yield point phenomenon that occurs over a broad temperature range. After reaching a peak, the flow stress drops to a lower value as a Lüders deformation front propagates along the specimen gage length at a constant stress. At temperatures where solutes are mobile, the phenomenon of dynamic strain aging (DSA) may occur in which diffusion of solutes to dislocation occurs during straining. The local solute concentration at arrested dislocations, C_s, is a function of the waiting time at obstacles t_w. When the strain rate is increased, a decrease in flow stress occurs due to a decrease in C_s resulting from the decrease in t_w. Thus, the regime of DSA, which is bounded by certain values of temperature and strain rate, is characterized by negative values of the strain rate sensitivity parameter defined by equation (1) above.

The DSA phenomenon gives rise to changes in the appearance of the flow curves. In BCC materials containing interstitial solutes, regular serrations occur in the region of the Lüders extension in the temperature range where interstitials are mobile; this "serrated yielding" occurs at a constant average stress. As the applied stress is increased and the material enters the work hardening regime, the flow curve is characterized by small serrations whose frequency and magnitude vary with strain, temperature and strain-rate. This is the regime of "jerky flow." The ability to detect the upper yield point, serrated yielding, and jerky flow depends upon the sensitivity of the test machine and upon specimen geometry. Detection of serrations is favored by: (a) the use of a "hard" machine, in which a small specimen extension produces a large drop in load, and (b) by a high speed digital data acquisition system. Detection of the upper yield and the observed magnitude of the load drop is sensitive to the specimen geometry, specimen alignment, and surface quality.

Early work by Bradford and Carlson [9] related strain-aging phenomena in pure vanadium at 150-170°C to the diffusion of oxygen and carbon. Subsequently, Thompson and Carlson [10], also working with pure vanadium, were able to relate strain-aging peak over the range 300 to 450°C to the diffusion of nitrogen. In the V-4Cr-4Ti alloy it is expected that a positive interaction between the substitutional titanium atom and the interstitial species [11], will shift the appearance of DSA phenomena to somewhat higher temperatures in the alloy.

The data for the lower yield stress, σ_y, and for the stress at 8% strain, σ_s, shown in Figs. 2 and 3 represent deformation in two quite different deformation regimes, and consequently, exhibit rather different strain rate sensitivities. During the Lüders extension, weakly pinned dislocations are activated and slip bands form on only a limited set of available slip planes. Once the Lüders front has propagated along the gage length, the stress must be increased to unlock further dislocations; the dislocation density increases rapidly as the material enters the strain-hardening regime. At room temperature, the SRS of σ_y is positive with $m \approx 0.025$. At 300°C, m is positive only for strain rates $\geq 10^{-3}$/s, and for these conditions, serrated yielding in the Lüders regime could not be detected. At lower strain rates, m becomes markedly less positive and serrations begin to appear in the Lüders extension. At all test temperatures above 300°C, although serrated yielding occurs within the Lüders extension for all strain rates, σ_y is essentially insensitive to strain rate.

The σ_s parameter is measured at a fixed value of the strain (8%), which is well into the strain-hardening regime. At room temperature, the SRS of σ_s is positive, with $m \approx 0.019$ (Fig. 3). At

300°C, the strain rate dependence of σ_s displays a classic U-shape, with a positive sensitivity at high strain rates undergoing a transition to a negative sensitivity for strain rates $\leq 10^{-3}$/s. Based upon the relative diffusivities of the interstitial species in vanadium, it seems likely that the appearance of jerky flow at low strain rates at 300°C is related to the mobility of carbon and oxygen [1]. At temperatures of 400, 500, 600, and 700°C, the SRS for σ_s is always negative, with m in the range (-0.012 to −0.022).

At these temperatures, nitrogen is sufficiently mobile to play a role in DSA. At some temperature, all of the interstitial solutes will be sufficiently mobile to migrate with dislocations moving at the highest strain rates used and will lose their effectiveness in pinning dislocations. It is possible that at sufficiently high temperatures, DSA effects could arise from the substitutional solutes Ti and Cr.

It can be seen from Fig. 1 that the appearance of serrated yielding in the Lüders extension coincides with the appearance of jerky flow in the strain hardening regime, suggesting that the load-drops have a common origin in the locking of dislocations by mobile interstitial species. This type of behavior has been observed in mild steel [12].

The strain rate insensitivity of σ_y in the 400 to 700°C range contrasts with the strong negative strain rate sensitivity of σ_s over the same range; this difference is not understood at present.

At 750 and 800°C, the negative SRS of σ_s for strain rates in the range 10^{-1} to 10^{-3}/s is similar to that for lower temperatures with m in the range (-0.037 to -0.008). At lower strain rates, however, m becomes positive. This reversal in SRS indicates a change in deformation mode and is probably related to a transition into a power law creep regime. Additional intermediate strain rate tests are in progress to allow determination of an activation energy for deformation in this regime. The stress-strain curves at 750°C are compared for two strain rates in Fig. 5. The two curves are very similar,

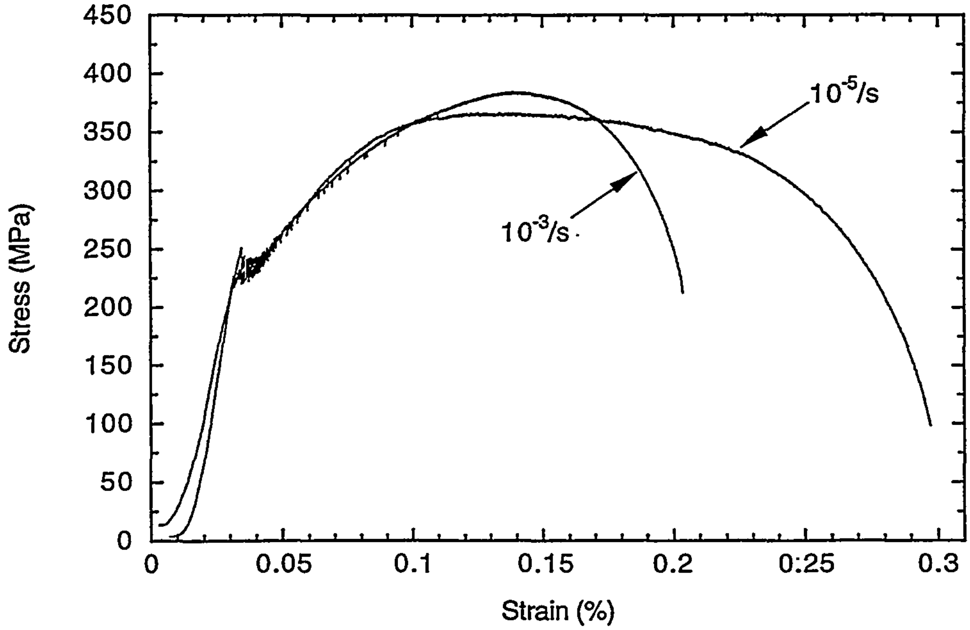

Fig. 5. The stress-strain curves for the V-4Cr-4Ti alloy tested at 750°C and strain rates of 10^{-3}/s and 10^{-5}/s.

initially. However, at a strain-rate of 10^{-5}/s, the strain-hardening rate decreases more rapidly due to climb-enhanced dislocation rearrangement.

Work is continuing to determine the strain rate sensitivity of V-4Cr-4Ti, pure V, and V-4Cr-4Ti weld metal and is also being carried out utilizing hardness and resistivity measurements. Together, these studies will provide the basic information needed to advance our understanding of the effects of test temperature, strain rate, and irradiation on the flow and fracture of V-Cr-Ti alloys.

REFERENCES

1. A. N. Gubbi, A. F. Rowcliffe, W. S. Eatherly, and L. T. Gibson, "Effects of Strain Rate, Test Temperature, and Environment on the Tensile Properties of Vanadium Alloys," Fusion Materials Semiannual Progress Report, DOE/ER-0313/20, June 1996, p. 38.

2. S. A. Bradford and O. N. Carlson, Trans. AIME **224** (1962), pp. 738-742.

3. S. J. Zinkle, L. L. Snead, J. P. Robertson, and A. F. Rowcliffe, "Strain Rate Dependence of the Tensile Properties of V-4Cr-4Ti Irradiated in EBR-II and HFBR," Fusion Materials Semiannual Progress Report, DOE/ER-0313/23, December 1997, p. 77.

4. S. J. Zinkle, L. L. Snead, A. F. Rowcliffe, D. J. Alexander, and L. T. Gibson, "Effects of Irradiation Temperature and Strain Rate on the Mechanical Properties of V-4Cr-4Ti Irradiated to Low Doses in Fission Reactors," Fusion Materials Semiannual Progress Report, DOE/ER-0313/24, June 1998, p. 33.

5. S. J. Zinkle, A. F. Rowcliffe, and C. O. Stevens, "High Temperature Tensile Properties of V-4Cr-4Ti," Fusion Materials Semiannual Progress Report, DOE/ER-0313/24, June 1998, p. 11.

6. A. F. Rowcliffe and D. T. Hoelzer, "Microstructural Inhomogeneities in V-4Cr-4Ti Mechanical Property Specimens Prepared for Irradiation Experiments in HFBR, BOR-60, and HFIR," Fusion Materials Semiannual Progress Report, DOE/ER-0313/25, December 1998, p. 42.

7. B. J. Brindley and P. J. Worthington, "Yield-Point Phenomena in Substitutional Alloys," Metallurgical Reviews 15, 101, 1970.

8. J. D. Baird, Metallurgical Reviews 5, 1-18, 1971.

9. S. A. Bradford and O. N. Carlson, "The Role of Oxygen in Strain-Aging of Vanadium," Trans AIME 224, Aug. 1962, p. 738

10. R. W. Thompson and O. N. Carlson, "Strain-Aging Effects of Nitrogen in Vanadium, J. Less Common Metals 7, 1964, p. 321.

11. T. Shikama, S. Ishino, and Y. Mishima, "The Interaction Between Interstitital Impurities and Substitutional Solutes in Vanadium," J. Nucl. Mats 68, 1977, p. 315.

12. Y. Bergström and W. Roberts, Acta Met. 19, 815-823, 1971.

EFFECT OF ORIENTATION ON EFFECTIVE TOUGHNESS-TEMPERATURE CURVES IN V-4Cr-4Ti — E. Donahue, G.R. Odette, and G. E. Lucas (University California, Santa Barbara)

OBJECTIVE

The results reported here are part of a larger effort to characterize effective fracture toughness - temperature $K_e(T)$ curves of the program heat of V-4Cr-4Ti alloy as a function of specimen size, geometry and orientation as well as for plates with somewhat different processing histories. The current report focuses on tests of specimens larger than previously studied and in two different orientations with respect to rolling direction.

SUMMARY

Fracture tests were performed on fatigue precracked, 20% sidegrooved 0.26T compact tension specimens in LT and TL orientations under static loading conditions over temperatures ranging from -196°C to -110°C. The effective toughness-temperature $K_e(T)$ curves were similar for both LT and TL orientations. The corresponding 100 MPa√m transition temperature was estimated to be about -155°C. Additional tests to evaluate effects of specimen size, orientation and material fabrication history on the K-T curves are underway.

MATERIALS AND PROCEDURES

Specimens were fabricated from a cold-rolled 6.6 mm thick plate fabricated from the large program heat of V-4Cr-4Ti (#832665) produced by Teledyne Wah Chang [1]. Compact tension specimens (0.26T) were machined in LT and TL orientations, annealed at 1000°C for 2 hours under vacuum, precracked to crack length (a) to specimen width (W) ratio a/W~0.5, and sidegrooved to depths of about 10% on each side. These specimens were tested over the temperature range from -196°C to -110°C under static loading conditions. Effective toughness values were calculated from load-displacement traces.

RESULTS

Figure 1 shows the toughness-temperature data for LT and TL orientations. The 100 MPa√m transition temperatures of about -155°C are similar for both orientations as are the lower knee toughness values at around 60 MPa√m. Notably, the $K_e(T)$ curves for these larger CT specimens were shifted up in temperature by about 20-30°C relative to that measured using smaller 3.3 x 3.3 x 25.4 mm precracked three point bend bar specimens [2]. Specimens tested at low temperatures exhibited classical cleavage fracture surfaces, while specimens tested at higher temperatures also exhibited large, transverse fissures.

Fracture Reconstruction (FR) methods have also been used on selected specimens to characterize the sequence of events which lead to fracture. Figure 2 shows the fracture area maps from the FR for a specimen in LT orientation tested at -140°C. It shows limited damage up to a crack tip opening displacement of about $\delta = 100$ µm and then a large pop-in at about $\delta = 130$ µm. This corresponds to a $K_\delta = 137$ MPa√m as calculated from $K_\delta = \sqrt{2E'\sigma_y\delta^*}$ [3,4]. This value is in excellent agreement with the standard $K_e = 130$ MPa√m measured from the load-

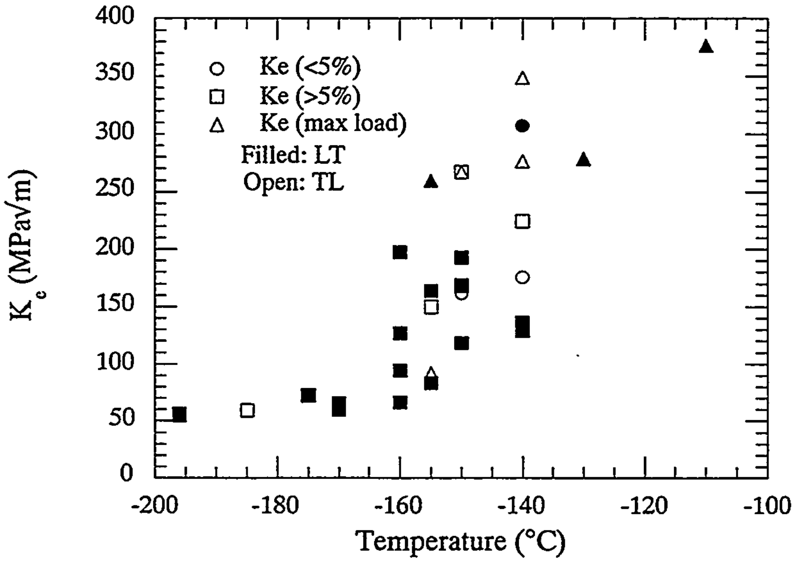

Figure 1. Toughness - temperature data for 0.26T CTs in LT and TL orientations. Toughness was evaluated at the first sign of crack advance if lower than 5% load shed, pop-ins of >5% load shed, and maximum loads in the load-displacement traces. Data shows no effect of specimen orientation on K-T curves.

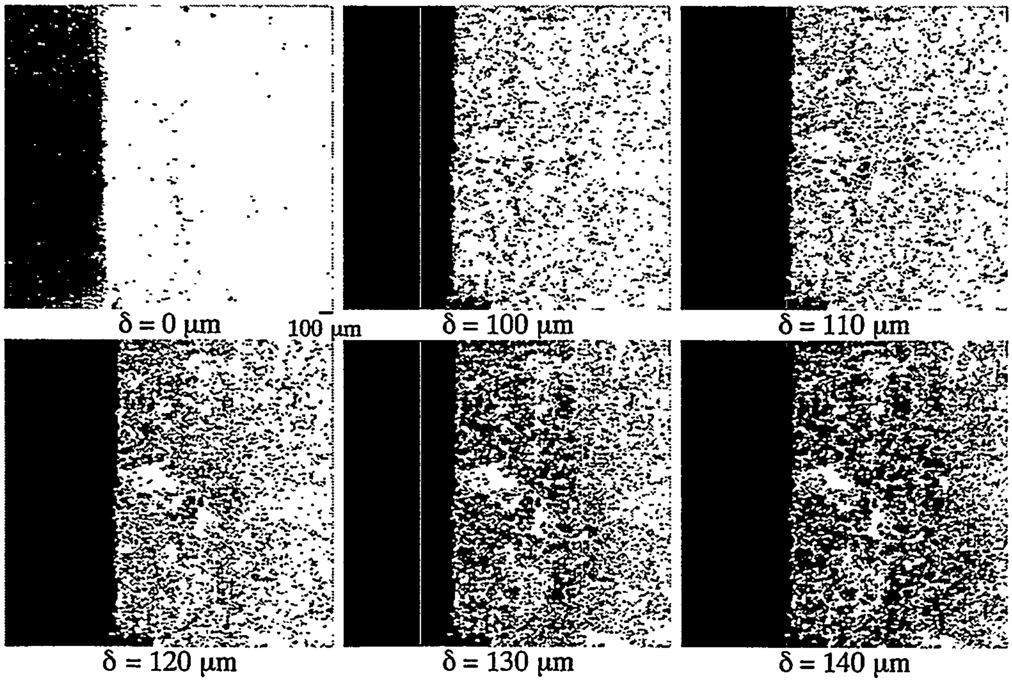

Figure 2. The Fracture Reconstruction for a specimen tested in LT orientation at -140°C. The critical crack opening is about δ = 130μm.

displacement record. The FR shows that damage in the form of isolated cleavage facets was widely distributed prior to reaching the critical displacement for macroscopic fracture.

FUTURE WORK

Future work will involve additional tests of specimens with different orientations, sizes and material fabrication histories. The overall data base, coupled with extensive fractographic and FR studies as well as constitutive models, will be used to develop self-consistent predictive models of cleavage initiation and ductile tearing toughness including the effects of irradiation, loading rate and specimen/flawed component geometry.

REFERENCES

1. Chung, H.M., Tsai, H.-C., Smith, D.L. Peterson, R., Curtis, C., Wojcik, R., Kinney, C., DOE/ER-0313/17, March 1994
2. Odette, G.R., Donahue, E., Lucas, G.E., Sheckherd, J.W., DOE/ER-0313/20, 1996.
3. K. Edsinger, Ph.D. Thesis, Department of Chemical Engineering, UCSB, 1996.
4. K. Edsinger, G.R. Odette, G.E. Lucas, Proceedings of Miniature Specimen Symposium, KFA Julich, 1995, p 150.

STUDY OF IRRADIATION CREEP OF VANADIUM ALLOYS,[1] H. Tsai, R. V. Strain, M. C. Billone, T. S. Bray, and D. L. Smith (Argonne National Laboratory); M. L. Grossbeck (Oak Ridge National Laboratory); K. Fukumoto, and H. Matsui (Tohoku University, Japan)

SUMMARY

Thin-wall tubing produced from the 832665 (500 kg) heat of V-4 wt.% Cr-4 wt.% Ti material was formed into pressurized tube specimens and irradiated in the HFIR RB-12J experiment to study irradiation creep. Irradiation and the required cool-down following irradiation have been completed and disassembly of the vehicle is underway. Calculated dose for the specimens ranged from 5.5 to 6.0 dpa and the calculated irradiation temperatures were 400 to 500°C.

OBJECTIVE

Vanadium alloys are candidate structural materials for fusion first walls and blankets because of their attractive high-temperature properties and low activation. While many alloy properties have been extensively studied, irradiation-induced creep has not. Data on irradiation creep are important because creep may be a principal contributor to deformation and is potentially performance-limiting. The objective of this task is to determine the creep rate at 500°C under a range of loading conditions.

CREEP SPECIMEN FABRICATION

The creep specimens used in the RB-12J experiment are 25.4 mm long x 4.57 mm OD x 0.25 mm wall tubes with welded end plugs, as shown in Fig. 1. The tubes were fabricated by drawing of bar stock,and the end plugs were produced by electric-discharge machining of plate stock[1]. Circumferential plug-to-tube welds were made with an electron-beam welder in vacuum. The specimens were vacuum-annealed at 1000°C for 1.0 h while wrapped in Ti foil, then pressurized, through a 0.25-mm-dia. meter hole in the top end plug, with high-purity helium in a pressure chamber. The final closure weld of the hole was made with a laser through the quartz window in the chamber. Six specimens, with at-temperature hoop stresses ranging from 0 to 200 Mpa, were irradiated in the RB-12J experiment. The specified pressure loading was determined with a code that accounted for thermal expansion of the creep tubing and compressibility of the helium gas. Following the leak check, the dimensions of the assembled creep specimens were measured with a precision laser profilometer at 5 axial (x/L = 0.1, 0.3, 0.5, 0.7, and 0.9) and 19 azimuthal locations to an accuracy of 10^{-4} mm.

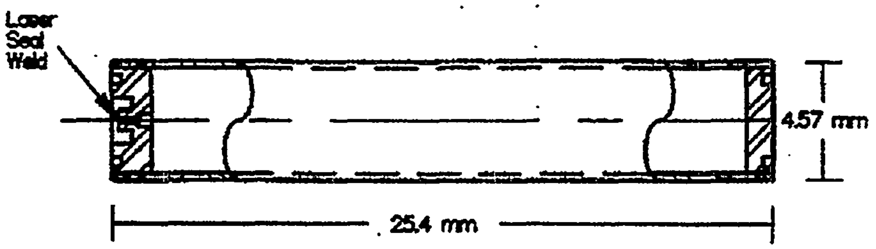

Fig. 1. Schematic Diagram of Creep Specimens

To mitigate gaseous impurity uptake, the six creep specimens were loaded in two sealed thin-wall

---

[1] This work has been supported by the U.S. Department of Energy, Office of Fusion Energy Research, under Contract W-31-109-Eng-38.

Zircalloy capsules, which acted as an impurity getter. A pinhole was drilled in the end plug of the Zircalloy capsule to prevent pressure buildup in case of an unexpected specimen failure. The inside dimensions of the Zircalloy tubing were 81.3 mm long x 5.05 mm ID and the wall thickness was 0.10 mm.

IRRADIATION SUMMARY

The irradiation of RB-12J was completed in 10 HFIR cycles, from Cycle 352 (Feb. 7, 1997) through Cycle 361 (Jan. 17, 1998). The irradiation location was RB-5B.

Calculated temperatures and neutron damage [2] for the six creep specimens are shown in Table 1. The range of temperatures reflected the impact of several factors: changes in HFIR power levels during operation, 180° capsule rotation at the end of each cycle, movement of the HFIR control plates, uncertainties in the relationship between specimen temperatures and thermocouple temperatures, and variation in individual thermocouples over the course of the 10 cycles.

In Cycle 353, an attempt to recover from a computer failure led to three separate high-temperature excursions; total duration was about 4 min. The peak temperatures during these times were estimated to be ≈40°C above those shown in Table 1 [2].

Table 1. Creep Specimens from HFIR-12J Experiment

Specimen No.	Calculated Temp.(°C)	Calculated Dpa	Nominal Hoop Stress (MPa)
B1	496±22	5.96	0
B12	399±21	5.96	50
B11	496±22	5.75	100
B3	476±22	5.45	150
B9	496±22	5.75	150
B5	476±22	5.45	200

STATUS OF EXPERIMENT

Following the postirradiation cool-down in the HFIR pool, the RB-12J vehicle was moved to the ORNL hot cell in January 1999 for disassembly. At the time of writing, the specimens have been retrieved from the irradiation vehicle but not from the Zircalloy getter tubes.

FUTURE ACTIVITIES

The specimens will be retrieved from the Zircalloy getter tubes and their diameters will be measured with a precision laser profilometer. Stress dependence of the creep strains will be evaluated, and stress-free swelling of the material from the 0-MPa specimens will also be evaluated. These results will be compared with the limited previously published in-reactor creep data on vanadium alloys.

REFERENCES:

1. H. Tsai, R. V. Strain, and D. L. Smith, "Study of Irradiation Creep of Vanadium Alloys," Fusion Materials Semiannual Progress Report, DOE/ER-0313/22, June 1997, pp. 57-60.
2. K. E. Lenox and M. L. Grossbeck, "Operating History of the HFIR MFE-RB-11J and –12J (P3-2 and P3-3) Experiments," Fusion Materials Semiannual Progress Report, DOE/ER-0313-25, December 1998, pp. 307-323.

FRACTOGRAPHY RESULTS FOR V-ALLOY TENSILE SPECIMENS IRRADIATED IN THE BOR-60, ATR, AND FFTF REACTORS. T. S. Bray, H. Tsai, R. V. Strain, M. C. Billone, and D. L. Smith (Argonne National Laboratory)

Summary

Fractography studies were conducted on numerous V-alloy tensile specimens. These specimens had been irradiated in the ATR, FFTF, and BOR-60 reactors at temperatures ranging from 273 to 600°C and damage doses from 41 to 51 dpa. The results of the fractography studies show the medium dose (17 to 19 dpa), low irradiation temperature materials irradiated in BOR-60 to have mostly ductile fractures but with low areal reduction. The low dose (~4 dpa) ATR samples display a wide range of areal reductions with mostly ductile fractures. The fractography results for the FFTF samples with irradiation temperatures from 520°C to 600°C and damage doses from 41 to 51 dpa show a wide range of reductions in area and all ductile fractures. Side-view observations revealed evidence of slip bands that are typically associated with dislocation channeling.

Objective

The objective of the task was to determine the failure mode and measure the reduction in area for tensile specimens irradiated in ATR, FFTF, and BOR-60.

Background

The tensile properties of these specimens were measured and results were reported [1-4]. The compositions of the materials are presented in Table 1. The summary of the tensile results are presented in Table 2. The results of the tensile testing for the BOR-60 irradiated specimens corroborate previous findings [3-8]; a significant loss of work hardening capability in the materials exists. Fractographic examinations of samples tested at room temperature (irradiation temperatures from 318 to 323°C) show a mixture of ductile tear and brittle cleavage. Consistent with the poor elongations, the reduction in area values were low (3-4%) [2].

Table 1. Nominal composition of the alloys investigated

Heat	Nom. Composition (wt.%)	Impurity content (wppm)			
		O	N	C	Si
832665	V-3.8Cr-3.9Ti	310	85	80	780
T87	V-5.0Cr-5.0Ti	380	90	110	550
VX8[a]	V-3.7Cr-3.9Ti	350	70	300	500
BL-42[b]	V-3.1Ti-0.5Si	580	190	140	n/a
BL-47	V-4.1Cr-4.3Ti	350	220	200	870

[a] From Russia. Contains (in wppm) 1120 Al, 280 Fe, 500 Co, 270 Mo, 1280 Nb, and 19 Zr.
[b] Contains 0.02 wt% Fe.

Table 2. Tensile data summary for specimens subject to fractography studies in this report [1,2,7,8].

Reactor Exp.	Specimen ID No.	Material/Heat	Irrad. Temp. (°C)	Tensile Test Temp. (°C)	dpa	0.2% YS (MPa)	UTS (MPa)	UE (%)	TE (%)
BOR-60 Fusion-1	71-2	V-4Cr-4Ti/832665	318	23	17	1115	1120	0.3	0.4
	71-2H-1	V-4Cr-4Ti/832665	318	318	17	892	926	0.4	2.2
	71-2H-2	V-4Cr-4Ti/832665	318	23	17	1100	1115	0.3	0.5
	71-A	V-4Cr-4Ti/832665	318	318	17	953	962	0.4	1.3
	71-B	V-4Cr-4Ti/832665	318	23	17	1120	1125	0.5	0.8
	69-1	V-4Cr-4Ti/VX8	323	323	19	909	936	0.5	2.3
	69-2	V-4Cr-4Ti/VX8	323	23	19	1135	1170	1.4	2.8
	72-1	V-5Cr-5Ti/T87	323	323	19	953	955	0.1	1.8
	72-2	V-5Cr-5Ti/T87	323	23	19	1145	1150	0.4	0.4
	71-LZ-1	832665/Laser	320	320	18	a	782	0.0	0.0
ATR ATR-A1	71-F	V-4Cr-4Ti/832665	273/280	290	4.3	945	983	0.7	2.1
	47-E	V-4Cr-4Ti/BL-47	288/302	290	4.6	844	866	0.5	4.9
	72-D	V-5Cr-5Ti/T87	284/300	290	4.1	880	941	1.1	4.1
	71-LZ-B	832665/Laser	288/302	290	4.6	a	607	0.0	0.0
FFTF MOTA 11	143	V-3.1Ti-0.5Si/BL42	520	520	41	525	624	4.2	8.1
	144	V-3.1Ti-0.5Si/BL42	520	520	46	453	559	7.7	16.4
	146	V-3.1Ti-0.5Si/BL42	600	600	47	373	541	11.0	15.9
	147	V-3.1Ti-0.5Si/BL42	600	600	51	368	566	10.4	14.4
	148	V-3.1Ti-0.5Si/BL42	600	600	51	380	539	11.7	17.2
	149	V-3.1Ti-0.5Si/BL42	600	22	51	424	615	11.7	15.0

[a] No measurable plastic deformation; offset yield strength could not be determined.

Results

Fractographic examinations were conducted with a scanning electron microscope (SEM). The objective of the examination was to determine the mode of fracture and the reduction of gauge cross-sectional area. All fractures except for 71-LZ-1 and 71-LZ-B (laser weld samples) were ductile fractures as shown in Figures 1 and 2. Sample 71-LZ-1, irradiated in BOR-60 at 320°C to a damage dose of 18 dpa, shows brittle cleavage except for a small corner that displays ductile tear (Figures 3 and 4). This ductile tear corner could be the result of the fracture not following the plane of the weld. Sample 71-LZ-B, irradiated in the ATR-A1 experiment at 288/302°C to a damage dose of 4.6 dpa, shows brittle cleavage.

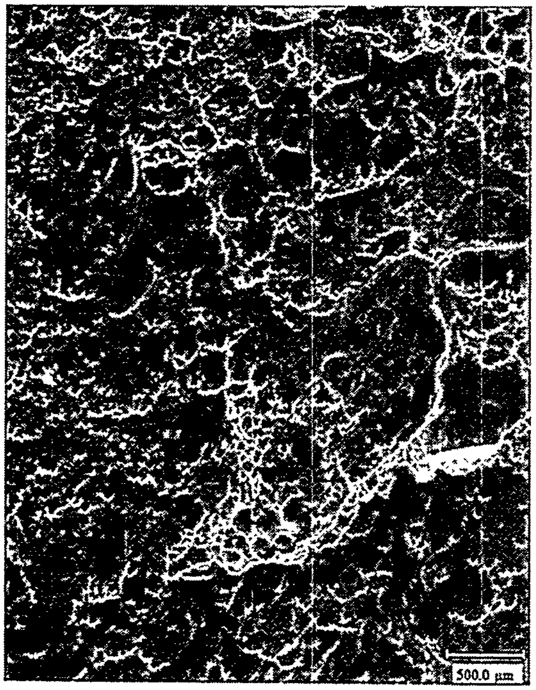

Figure 1: Sample 146 ductile fracture (ET 325643).

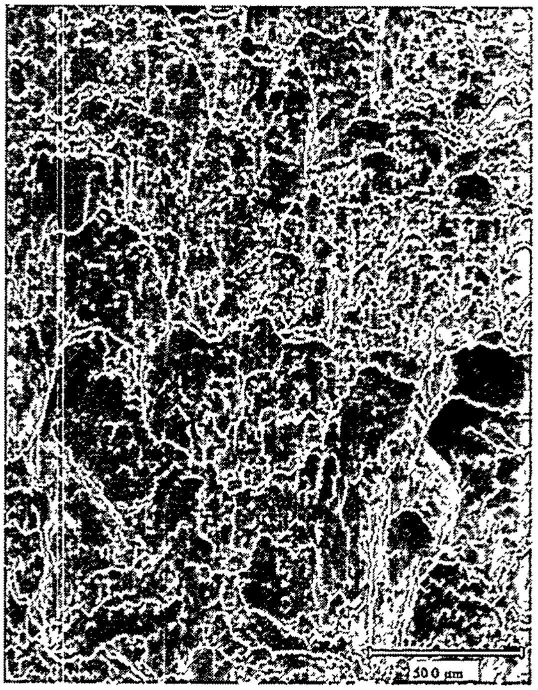

Figure 2: Sample 72-1 ductile fracture (ET 325623).

Figure 3: Sample 71-LZ-1 brittle fracture (ET 325627).

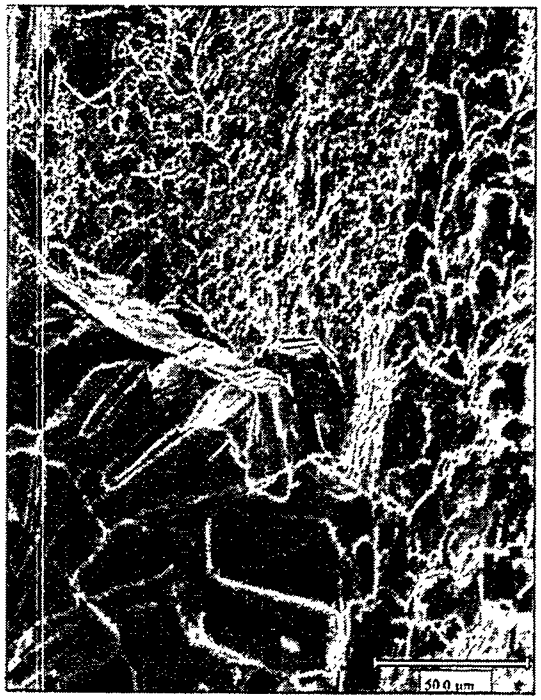

Figure 4: Sample 71-LZ-1 corner showing both ductile and brittle fracture (ET 325630).

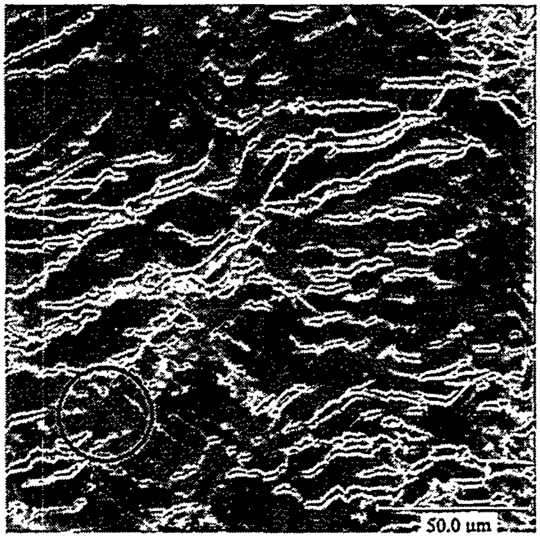

Figure 5: Example of surface steps from Sample 69-1 indicating dislocation channeling. (ET 325620)

Side surface examinations were conducted to determine if slip bands that are characteristic of dislocation channeling were formed during testing. Slip bands were apparent in most samples examined. A typical example of slip bands is shown in Figure 5. Side surface examinations also revealed short transverse cracks initiated at the surface. These transverse cracks, observed in necked regions, grew perpendicular to the direction of the applied tensile load.

Reduction-in-area measurements completed are reported in Table 3. The low reduction in area results (0 to 17%) for the BOR-60 specimens were consistent with previously reported reduction in area and elongation data. The laser weld sample (71-LZ-1) fracture was brittle, and as expected did not have a measurable reduction-in-area. This fractography data supports findings that the V-4Cr-4Ti alloys may be susceptible to significant low-temperature embrittlement [3,5,6,7].

The low damage dose samples irradiated in ATR displayed a higher reductions-in-area than the majority of the samples irradiated in BOR-60. These differing results are consistent with the tensile test data and can be explained by saturation effects. The laser weld sample (71-LZ-B) fracture was brittle, and as expected did not have a measurable reduction-in-area.

Reduction in area measurements for the BL-42 heat, irradiated at higher temperatures in FFTF, showed good reductions-in-area even at high damage doses of 41 to 51 dpa (13 to 41%). The only exception is sample 147. This sample displays a ductile fracture through SEM analysis, but did not have a measurable areal reduction. This result is currently under further investigation.

The variability in these results can be attributed to saturation effects and impurity content variations in the samples.

Table 3. Reduction in area measurement results.

Reactor	Specimen ID No.	Material/Heat	Irrad. Temp. (°C)	Tensile Test Temp. (°C)	dpa	%RA
BOR-60	71-2[a]	V-4Cr-4Ti/832665	318	23	17	1
	71-2H-1	V-4Cr-4Ti/832665	318	318	17	0
	71-2H-2[a]	V-4Cr-4Ti/832665	318	23	17	1
	71-A	V-4Cr-4Ti/832665	318	318	17	0
	71-B[a]	V-4Cr-4Ti/832665	318	23	17	1
	69-1	V-4Cr-4Ti/VX8	323	323	19	17
	69-2[a]	V-4Cr-4Ti/VX8	323	23	19	4
	72-1	V-5Cr-5Ti/T87	323	323	19	10
	72-2[a]	V-5Cr-5Ti/T87	323	23	19	1
	71-LZ-1	832665/Laser	320	320	18	0
ATR	71-F	V-4Cr-4Ti/832665	273/280	290	4.3	16
	47-E	V-4Cr-4Ti/BL-47	288/302	290	4.6	12
	72-D	V-5Cr-5Ti/T87	284/300	290	4.1	32
	71-LZ-B	V-4Cr-4Ti/Laser	288/302	290	4.6	0
FFTF	143	V-3.1Ti-0.5Si/BL42	520	520	41	35
	144	V-3.1Ti-0.5Si/BL42	520	520	46	41
	146	V-3.1Ti-0.5Si/BL42	600	600	47	34
	147	V-3.1Ti-0.5Si/BL42	600	600	51	0
	148	V-3.1Ti-0.5Si/BL42	600	600	51	13
	149	V-3.1Ti-0.5Si/BL42	600	22	51	17

[a] Results originally reported in Reference 3, included here for completeness.

References

1. H. Tsai, L. J. Nowicki, T. S. Bray, M. C. Billone, and D. L. Smith, “Tensile and Impact Properties of a V-3.1Ti-0.5Si Alloy After Irradiation in the Fast Flux Test Facility,” Fusion Materials Semiannual Progress Report for Period Ending December 31, 1998, DOE/ER-0313/25, pp. 25-31.

2. H. Tsai, J. Gazda, L. J. Nowicki, M. C. Billone, and D. L. Smith, “Tensile Properties of Vanadium-Base Alloys Irradiated in the Fusion-1 Low-Temperature Experiment in the BOR-60 Reactor,” Fusion Materials Semiannual Progress Report for Period Ending June 30, 1998, DOE/ER-0313/24, pp. 15-19.

3. J. Gazda et. al., “Room-Temperature Fracture in V-(4-5)Cr-(4-5)Ti Tensile Specimens Irradiated in Fusion-1 BOR-60 Experiment,” Fusion Materials Semiannual Progress Report for Period Ending June 30, 1998, DOE/ER-0313/24, pp. 20-27.

4. H. Tsai et al., "Tensile and Impact Properties of Vanadium-Base Alloys Irradiated at Low Temperatures in the ATR-A1 Experiment," Fusion Materials Semiannual Progress Report for Period Ending December 31, 1997, DOE/ER-0313/23, pp. 70-76.

5. H. Chung, H. Tsai, L. J. Nowicki, and D. L. Smith, "Tensile Properties of Vanadium Alloys Irradiated at 390°C in EBR-II," Fusion Material Semiannual Progress Report for Period Ending June 30, 1997, DOE/ER-0313/22, pp. 18-21.

6. S. J. Zinkle et al., "Effects of Fast Neutron Irradiation to 4 dpa at 400°C on the Properties of V-(4-5)Cr-(4-5)Ti Alloys," Fusion Materials Semiannual Progress Report for Period Ending December 31, 1996, DOE/ER-0313/21, pp. 73-78.

7. D. J. Alexander et al., "Effects of Irradiation at Low Temperature on V-4Cr-4Ti," Fusion Materials Semiannual Progress Report for Period Ending June 30, 1996, DOE/ER-0313/20, pp. 87-95.

8. H. Tsai et al., "Tensile and Impact Properties of Vanadium-Base Alloys Irradiated at Low Temperatures in the ATR-A1 Experiment," Fusion Materials Semiannual Progress Report for Period Ending December 31, 1997, DOE/ER-0313/23, pp. 70-76.

IMPURITY STUDIES OF GAS TUNGSTEN ARC WELDING OF VANADIUM ALLOYS –

M.L. Grossbeck and J.F. King (Oak Ridge National Laboratory)

OBJECTIVE

The goal of this research is to acquire a fundamental understanding of the metallurgical processes in welding vanadium alloys and to develop techniques for joining structural components made from vanadium alloys.

SUMMARY

An improved getter system has been installed on the welding glove box since progress was last reported. Gas tungsten arc (GTA) welds using both oxygen and hydrogen getters resulted in very low oxygen levels but very high hydrogen levels in V-4Cr-4Ti. Charpy impact testing, nonetheless, determined a DBTT lower than previously achieved. The first weld with a DBTT at room temperature was made. Erratic results following post-weld heat treatments or low-temperature outgassing treatments were previously attributed to hydrogen cracking. It is now believed that this behavior is not so erratic and might result from precipitation. Transmission electron microscope studies have been initiated to study the unusual behavior.

INTRODUCTION

The susceptibility of vanadium alloys to interstitial embrittlement is most pronounced in welding. In welding, it is usually not possible to achieve the ultra-high vacuum necessary for high temperature processing. In addition to the contamination from the welding environment, the rapid heating and cooling associated with welding quenches interstitials in the lattice. Thicker plates result in lower cooling rates so that techniques used for welding thin sheet might be useless for thicker plates required for building an actual structure. Electron beam (EB) welding, which can be used to successfully weld vanadium alloys is limited by the size of the vacuum chamber available. Although EB welding is likely to be used in joining small parts, it will never be practical for welding the large structures associated with fusion devices.

For the present study, 6.4 mm plate of V-4Cr-4Ti (Wah Chang heat 832665) has been selected as a reasonable thickness for which to study welding methods. When methods have been developed to weld 6.4 mm plate, thicker sections can be researched. However, since unacceptable embrittlement is observed after GTA welding of 6.4 mm plate, beneficial research can be conducted on this material.

EXPERIMENTAL RESULTS AND DISCUSSION

The welding methods for GTA vanadium alloy welding have been previously described.[1] The primary test method to evaluate brittleness of the welds remains the Charpy impact test. Static fracture toughness tests on pre-cracked Charpy specimens are expected to be done in the future. However, since a DBTT below room temperature has not yet been achieved, such tests will be deferred in order to avoid the necessity for pre-cracking at elevated temperatures. Previously, oxygen levels below 1 wt. ppm were achieved in the glove box atmosphere by the addition of a molecular sieve filter combined with a hot titanium getter.[1] In doing so the oxygen contamination level was lower than previously achieved, but the sample, GTA 16, was contaminated with hydrogen to a level of 3000 at. ppm.[1] To alleviate this problem, an additional getter was added to the system. Unlike the titanium getter which was part of a recirculating gas system, the hydrogen getter was placed in the glove box directly. It consisted of a Zr-Al alloy deposited on a constantan substrate.[1] The getter is heated to dissolve the oxide surface layer to expose a clean metal surface. The getter is then cooled to dissolve hydrogen.

Using the hydrogen getter system, the oxygen level in the glove box atmosphere was off scale using a zirconia detector. An additional weld on V-4Cr-4Ti, GTA 17, was made using these conditions. In this case, the hydrogen level in the fusion zone was measured by inert gas fusion analysis to be 5000 at. ppm. The impurity concentrations in the weld and the welding atmosphere are shown in Table 1 for this weld and the previous weld, GTA 16. This high level of hydrogen was attributed to an incorrect use of the hydrogen getter. Since there was no thermocouple on the hydrogen getter, its temperature could only be monitored by color. Because the substrate begins to melt above 800°C, the getter had to be heated conservatively, which was probably the cause of the poor performance of the getter in absorbing hydrogen.

Table 1. Impurity concentrations in welding atmosphere and in the weld fusion zones

		Welding Atmosphere		Fusion Zone Concentration			
Weld	PWHT	Oxygen Wt. ppm	Moisture Wt. ppm	Oxygen Wt. ppm	Nitrogen Wt. ppm	Hydrogen Wt. ppm	DBTT °C
GTA 16	AS WELDED	0.8	25	370	107	63	85
GTA 16	400°C/1h						38
GTA 17	AS WELDED	<<1	≤1	347	99	99	20
GTA 17	400°C/1h					1.9	

Charpy impact tests were performed on weld GTA 17 despite its high level of hydrogen contamination. A DBTT of 20°C was obtained, the lowest value for at GTA weld in 6.4 mm

---

[1] Manufactured by SAES Getters, Milan, Italy

vanadium alloy plate. Not only hydrogen interstitial hardening, but hydrogen embrittlement from stress induced hydride formation could have occurred at such a high level of hydrogen resulting in a reduced DBTT do to the hydrogen alone. To investigate this possibility, samples were outgassed at 400°C for one hour. Theresulting Charpy impact curves obtained before and after the outgassing treatment are shown in Fig. 1. As can been seen from the curve for the as welded samples, the data fit the curve reasonably well, giving a well defined DBTT. In the case of the outgassed samples, the data are badly scattered. Previously, this phenomenon has been attributed to pre-existing cracks resulting from hydrogen embrittlement. The proximity to the hydride solvus is also shown in Fig. 1. Application of a stress could shift the solvus to a higher temperature resulting in cracking significantly above the stress-free hydride solvus.[2] However, weld GTA 16, which had 3000 at. ppm hydrogen, was treated similarly. The Charpy impact curves for this weld appear in Fig. 2. As with GTA 17, the as welded curve is well behaved, in this case, giving a DBTT of 85°C. Following outgassing at 400°C for one hour, the data are again scattered. However, comparison of the curves for the two welds shows that it is not random scatter. There is a dip in the Charpy energy curve at 50 and 100°C for GTA 17 and GTA 16, respectively. Other welds have shown a similar phenomenon following higher temperature heat treatments. Weld GTA 10 exhibits dips in the Charpy energy curves between 100 and 150°C following post-weld heat treatments of 750, 850, and 950°C for two hours.[3] In all cases of unusual lower shelf behavior, the fracture surfaces exhibit entirely cleavage fracture. However, this would also be expected to result from hydrogen embrittlement. Nonetheless, this phenomenon of unexpected dips in the Charpy energy curves is now believed to be a real effect.

A precipitation phenomenon is a possible explanation for the effect. Transmission electron microscopy (TEM) is being use at the present time to investigate the microstructure. A brittle second phase could explain a high DBTT. However, it is difficult to explain a dip in the Charpy energy curve in terms of a brittle precipitate. As shown in Figs 1 and 2, the ductility returns at a lower temperature. This phenomenon is observed in the case of hydrogen embrittlement, but even the 400°C heat treatment in an vacuum has been shown to reduce the hydrogen concentration to below 2 wt. ppm.

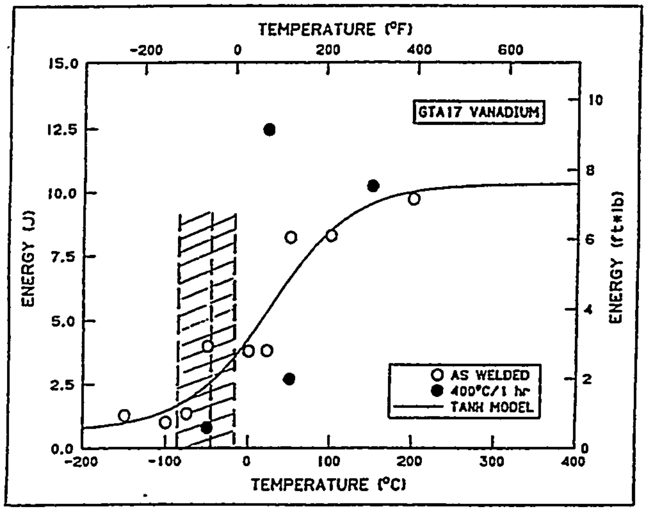

Figure 1. Charpy impact curves for weld GTA 17 before and after outgassing treatment to remove hydrogen. The cross hatched area is the zone of hydride formation under stress.

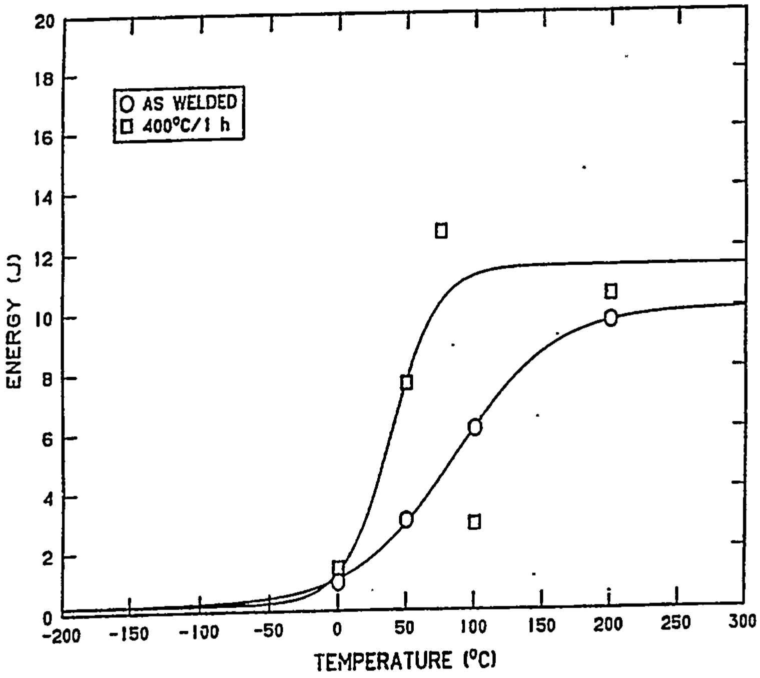

Figure 2. Charpy impact curves for weld GTA 16 before and after outgassing to remove hydrogen

FUTURE DIRECTIONS

Two improvements have been made to the welding glove box. A thermocouple has been installed on the hydrogen getter so that it may be properly activated at a sufficiently high temperature. In addition, a gas chromatograph has been installed to monitor the hydrogen concentration in the glove box atmosphere. A quadrapole mass spectrometer residual gas analyzer will also be added to the glove box system. In the future, a weld will not be made when the hydrogen concentration is high.

CONCLUSIONS

1. Reduction of oxygen concentration in the GTA welding atmosphere reduces the DBTT. A DBTT of room temperature has been achieved.

2. A strongly gettered system is necessary to reduce both oxygen and hydrogen to levels below 1 wt. ppm.

3. The unexpected dips in the Charpy energy curves, previously attributed to hydrogen embrittlement cracking, are believed to be related to precipitation during post-weld heat treatments or outgassing heat treatments.

REFERENCES

1. M.L. Grossbeck, J.F. King, D.J. Alexander, and G.M. Goodwin, "Recent Progress on Gas Tungsten Arc Welding of Vanadium Alloys," Fusion Materials Semiannual Progress Report for Period Ending June 30, 1997, DOE/ER-0313/22, U.S. Department of Energy (1997) p. 61.

2. M.L. Grossbeck, and H.K. Birnbaum, "Low Temperature Hydrogen Embrittlement of Niobium II – Microscopic Observations," Acta Met. 25 (1977) 135.

3. J.F. King, M.L. Grossbeck, G.M. Goodwin, and D.J. Alexander, "Recent Progress on Gas Tungsten Arc Welding of Vanadium Alloys," Fusion Materials Semiannual Progress Report for Period Ending December 31, 1996, DOE/ER-0313/21, U.S. Department of Energy (1996) p. 57.

IMPROVEMENT OF LASER WELD QUALITY OF V-Cr-Ti ALLOYS

Z. Xu, C. B. Reed, K. Natesan, and D. L. Smith (Argonne National Laboratory)

SUMMARY

During this report period, the use of a YAG laser to weld sheet materials of V-Cr-Ti alloys has focused on (a) development of optimal laser welding parameters to produce deep penetration and defect-free welds, (b) integration of a custom-designed environmental control box (ECB) into the laser system to control the oxygen uptake during the processing, (c) examination of the porosity on longitudinally sectioned welds, and (d) analysis for oxygen content of the welds. An innovative method has been developed to obtain deep penetration and oxygen contamination free welds.

EXPERIMENTAL PROGRAM

Vanadium alloy heat #832665, nominal composition V-4 wt% Cr-4 wt%Ti (designated as BL–71) was selected for the study. Bead-on-plate (BOP) welds were produced on 4 mm thick sheets of the alloy using a 1.6 kW pulsed YAG laser with optical fiber beam delivery. Welds made with the same laser parameters but different beam travel speeds were EDM wire cut longitudinally along the centerlines of the welds to comprehensively examine for porosity. A custom-designed environmental control box (ECB) capable of purging with high-purity argon (99.995%) has been integrated with the YAG laser to improve the quality of the welding atmosphere. Figure 1 schematically shows the set-up of the laser system with the ECB. The specimen was placed in the ECB with fixtures. The high-purity argon was purged into the box from both sides and the flow rate was well controlled such that a slow flow of argon out from the slit on the top of the box could be formed This provided a good welding atmosphere to minimize the oxygen uptake during the welding. A shielding disk just above the slit enhanced the shielding effect and also provided a guiding surface for the lens protection gas. The content of oxygen, nitrogen, and carbon of laser-welded samples produced with and without using the ECB were analyzed by Inert Gas Fusion (IGF) method.

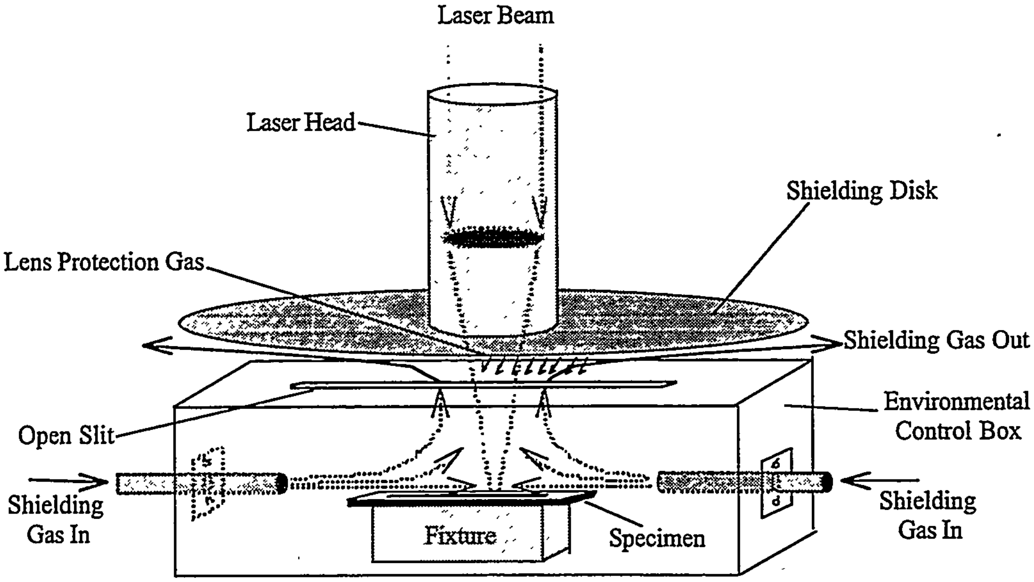

Figure 1 Set-up of the laser welding system

RESULTS AND DISCUSSION

Examination of Porosity on Longitudinally sectioned welds

Cross-sectioned samples of welds with and without root porosity were reported on in the previous report [1]. Cross-sectioned weld samples do not, however, reveal completely the existence of porosity, since the randomly chosen section could be located just between porosities. Table I lists the welding conditions and weld depths of four samples used to examine for porosity in longitudinal sections. The side view of the longitudinal section of the four welds is shown in Figure 2. Detailed views of individual sections are presented in Figures 3 to 6. As it is revealed by the figures, the number of porosities decreases as the beam travel speed decreases. Porosity-free welds were obtained when the weld depth reached full penetration. It appears that full penetration provided a path on the bottom side of the sample for the gas trapped in the welding keyhole to escape, thus eliminating porosity.

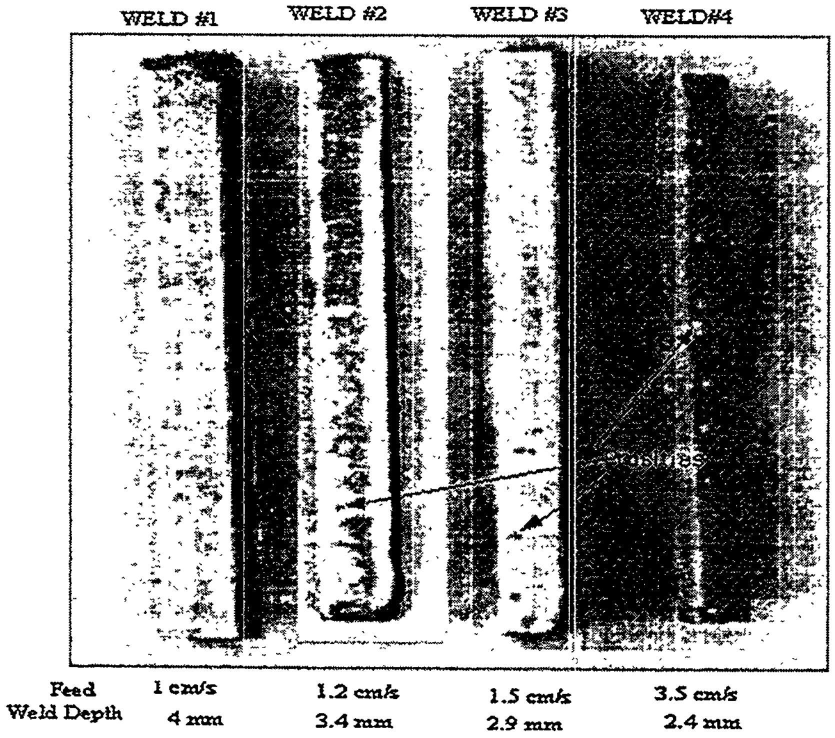

Figure 2. Longitudinal section views of laser-welded samples showing welds with porosity and a full penetration weld without porosity

Table 1. Welding Conditions and Weld Depths

Weld No.	Laser Energy (Joules/ms)	Pulse width (ms)	Repetition Rate (Hz)	Feed Rate (cm/s)	Weld Depth (mm)
1	4	3	132	1	4
2	4	3	132	1.2	3.4
3	4	3	132	1.5	2.9
4	4	3	132	3.5	2.4

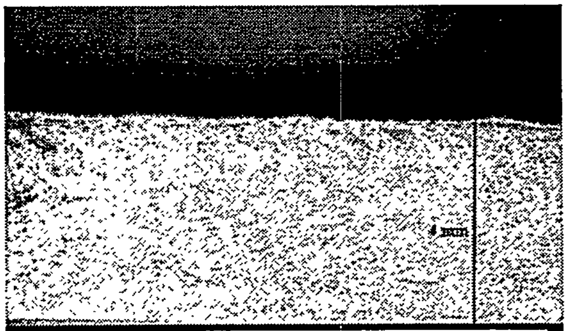

Figure 3. Closeup of longitudinal section view of weld No. 1 in Table I.

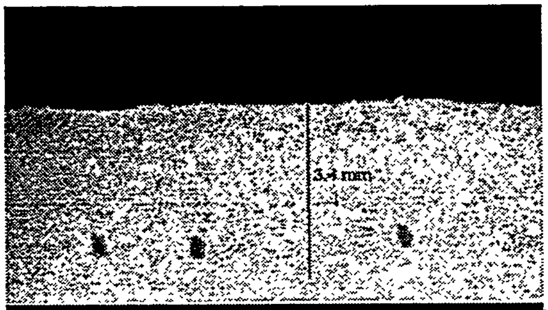

Figure 4. Closeup of longitudinal section view of weld No. 2 in Table I.

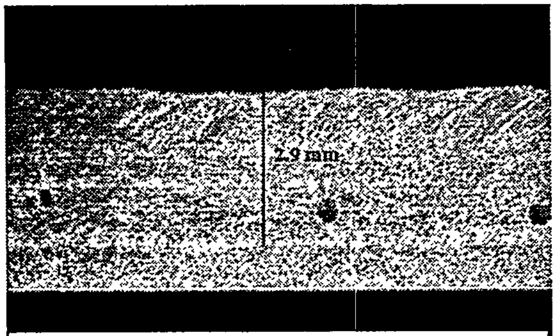

Figure 5. Closeup of longitudinal section view of weld No. 3 in Table I.

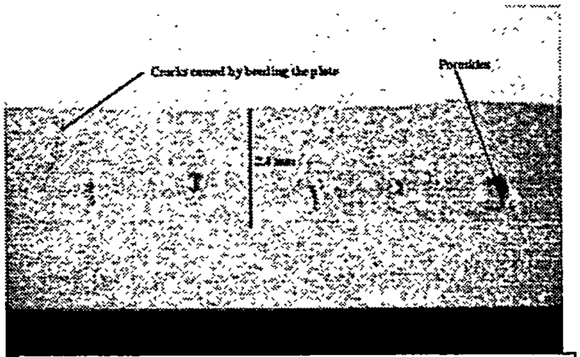

Figure 6. Closeup of longitudinal section view of weld No. 4 in Table I.

Chemical Analysis of Laser-Welded V-Cr-Ti Alloy

Uptake of oxygen leads to embrittlement of the alloy and therefore must be avoided. Table I shows the cleaning and welding conditions used to prepare samples for chemical analysis. The samples were wiped with acetone before and after welding except sample 990709B, which was cleaned in a pickling solution after welding. The chemical analysis results of the welds in Table II by IGF method are shown in Table III; values for the reference heat are also shown for information. The welds produced in the ECB with nearly optimal shielding gas (990712B and 990712C) have the lowest oxygen content. Welds using the ECB but with a less than optimal gas shielding arrangement have higher oxygen content compared to those with nearly optimal shielding. The welds obtained without using the ECB have the highest oxygen content. The O, N, and C contents of welds produced using the ECB with near-optimal shielding gas are essentially the same as the reported values for the reference heat. Oxygen analyses obtained from the chip samples apparently include additional contamination. Subsequent specimens were not milled into chips prior to chemical analysis, but rather submitted as small bars. This approach yielded O, C, and N measurements close to those of the reference analysis for the Heat.

TABLE II. Cleaning and Welding Conditions of Chemical Analysis Samples
(Same laser parameters were used for all the welds, laser energy: 4 joules/ms, pulse width: 3 ms, and pulse repetition rate: 133)

Samples	Beam travel speed (cm/s)	ECB used? Y/N	Clean conditions before & after welding	Sample supplied shape
990223A	Base material	Base material	Acetone wiped	Chips
990223B	1	N	Acetone wiped	Chips
990223C	1	N	Acetone wiped	Chips
990709A	0.6	Y, but non-optimal shielding gas	Acetone wiped	Bar
990709B	0.5	Y, but non-optimal shielding gas	Cleaned in pickling solution after welding	Bar
990712B	0.4	Y, near-optimal shielding gas	Acetone wiped	Bar
990712C 990712D	0.25	Y, near-optimal shielding gas	Acetone wiped	Bar

TABLE III. IGF Chemical Analysis Results of Laser-Welded V-Cr-Ti Alloy Samples

Sample	O (wppm)	C (wppm)	N (wppm)	Welded in Environmental control box?
Heat 832665	310	80	85	Reference Analysis
990223A	780	100	80	Base material
990223B	1460	60	1970	No
990223C	1690	80	2710	No
990709A	360	100	180	Yes, but non-optimal shielding gas flow
990709B	390	100	290	Yes, but non-optimal shielding gas flow
990712B	320	100	70	Yes
990712C	320	100	80	Yes

A microhardness profile across the width of weldment 990712D is presented in Figure 7. This profile shows only a slight increase in hardness in the weld metal, in comparison to the adjacent base metal.

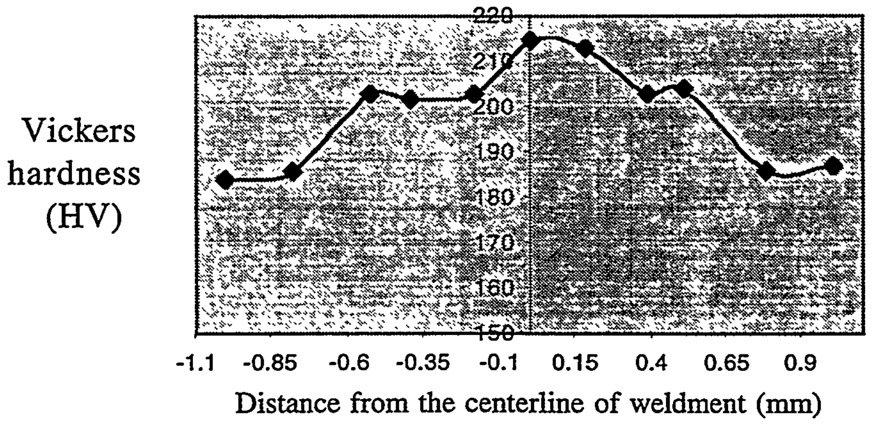

Figure 7. Microhardness profile for oxygen-uptake-free weldment (990712D) at half-width of weldment.

In the next report period, deep penetration, defect free and oxygen contamination free welds will be produced on the vanadium plates using the ECB, then Charpy impact test samples will be cut from the plates and tested. Further work on oxygen pickup and weldment microhardness will be performed in the next report period.

REFERENCES

1. K. Natesan, D. L. Smith, Z. Xu, and K. H. Leong, "Laser-Welded V-Cr-Ti Alloys: Microstructural and Mechanical Properties," Fusion Reactor Materials Progress Report for the Period Ending June 30, 1998, Argonne National Laboratory, DOE/ER-0313/24, p. 87, June 1998.

DIFFUSION BONDING OF VANADIUM ALLOYS

Z. Xu, D. L. Smith, and C.B. Reed (Argonne National Laboratory)

OBJECTIVE

The objective of this task is to investigate the potential of diffusion bonding for joining of vanadium-base alloys.

SUMMARY

Preliminary investigations are in progress to evaluate the potential of diffusion bonding processes for joining vanadium-base alloys. Diffusion bonds were prepared on 3.8 mm thick V-4Cr-4Ti alloy plate on a 50 KVA welder with a range of process parameters. Preliminary microstructural analyses conducted on the test samples indicated that bonding was achieved for a range of process parameters.

BACKGROUND

Continuous diffusion bond-type joining (roll bonds) potentially offers several advantages for fabrication of vanadium alloy for firstwall/blanket systems. Current blanket designs for vanadium/lithium systems provide for joining of ~4 mm thick sheet with long weld joints. This type of joining produces minimal effects on the alloy microstructure since melting is not required. Also, the extent of the heat-affected zone is more limited than in most types of welds. This approach may also reduce the stringent environmental control required to avoid excessive oxidation effects frequently observed in more conventional weld processes.

EXPERIMENTAL PROGRAM

Weld specimens were prepared from 3.8 mm thick V-4Cr-4Ti alloy (heat #832665) in the annealed condition. Specimens were surface polished and cleaned with acetone before joining. Lap-type diffusion bonds on these sheet specimens were produced on a 50 KVA welder at ANL. Process parameters that were set or varied included: transformer tap, tip geometry and size, tip force, preweld squeeze time, weld time, power setting, and post-weld hold time. Based on previous experience for other materials, several of these parameters were held constant for the first series of experiments. Primary variables included weld time and power setting.

Diffusion bonds of the specimens were metallurgically prepared and etched to reveal the microstructural features of the joints. A Nikon MSZ-B stereomicroscope, a Nikon optical microscope and a COHU high performance CCD camera were used for the microstructural evaluation.

RESULTS AND DISCUSSION

Table 1 presents a summary of the parameters and results of the diffusion bonds produced in the first series of experiments. The apparent bond strength of five of the bonds appeared to be quite good. The parameters used for test #1 produced a large heat affected zone and significant porosity in the joint (see Figure 1) indicating excessive power in this test. Tests 2, 3, 7, 10, 11, and 12 resulted in either no bonding or limited bonding, indicating insufficient power. Tests 4, 5, 6, and 8 appear to provide good bond strength with only modest restructuring. Test #6 appears to provide the best joint with apparent good bond strength with minimal restructuring. Results obtained thus far are quite encouraging since the bond strength appears to be good and only modest changes in microstructure of the bond region are observed for several machine parameters.

TABLE I. Diffusion bonding parameters and bond characteristics of V-Cr-Ti alloy

Test No.	Squeeze (Cycles)	Weld time (Cycles)	Heat (%)	Hold time (Cycles)	Bond characteristic	Porosity
1	50	50	95	30	Good bond, grain growth	Y
2	30	25	95	30	Minimal bond	N
3	30	20	95	30	No bonding	
4	30	99	75	30	Good bond, significant structure change	N
5	30	75	75	30	Good bond, some structure change	N
6	30	50	75	30	Good bond, minimal structure change	N
7	30	25	75	30	No bonding	
8	30	99	70	30	Good bond, some structure change	N
9	30	99	65	30	Minimal bond	N
10	30	75	65	30	Broke on cooling	
11	30	99	50	30	No bonding	
12	30	25	50	30	No bonding	

FUTURE WORK

More detailed analyses will be conducted on these test specimens to further characterize the bond microstructure, strength, and any contamination; and to develop a better understanding of the effects of the machine parameters on the bond characteristics. Additional test samples will be prepared with more optimal process parameters and mechanical test specimens will be prepared from samples with good bonds.

Figure 1 Cross section view of diffusion bond of V-Cr-Ti alloy (Test No. 1 in TABLE I) showing porosity and grain growth due to overheating.

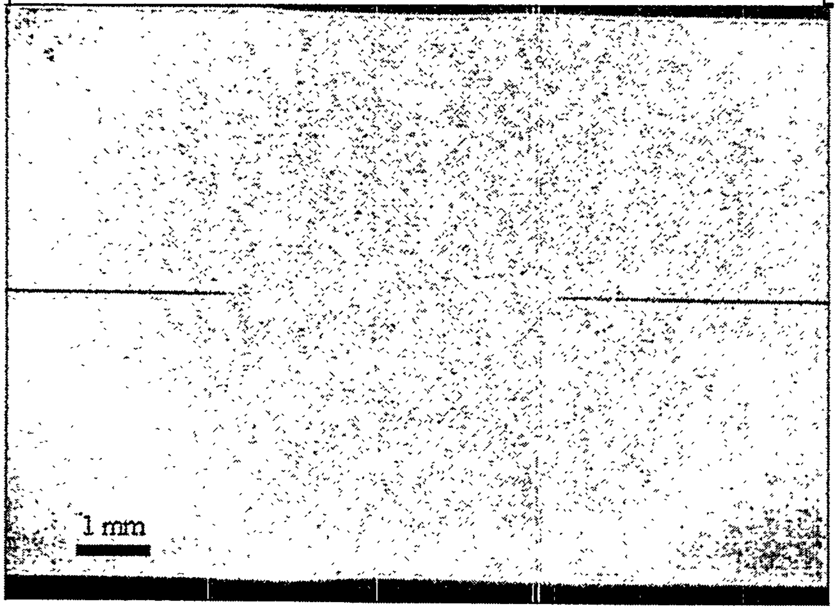

Figure 2 Cross section view of diffusion bond of V-Cr-Ti alloy (Test No. 6 in TABLE I) indicating good bond and minimal structure change of the bond.

DEVELOPMENT OF ELECTRICALLY INSULATING CaO COATINGS*

K. Natesan, M. Uz, and S. Wieder (Argonne National Laboratory)

OBJECTIVE

The objectives of this task are to (a) develop electrically insulating coatings, with emphasis on the basic understanding of the thermodynamic conditions and kinetics of coating development needed to achieve stable coatings of CaO that are compatible in an Li/Li-Ca environment; (b) perform detailed postexposure analysis of the surface layers by several electron/optical techniques to characterize the elemental and phase compositions, quantify stratification in the layers, and establish the role of compositional changes in the coating defects and microstructure; (c) measure the electrical resistance of the coatings, before and after exposure external to Li; and (d) establish optimal procedures from the standpoint of sample preparation procedures, exposure time and temperature, and sequence of operations in order to obtain reliable and reproducible coatings with adequate electrical resistance for use in an Li environment.

SUMMARY

A systematic vapor transport study has been in progress to develop electrically insulating CaO coatings that are compatible with use in a liquid Li environment. Several experiments were conducted to study how the deposition of Ca on V-4Cr-4Ti substrate alloys is affected by variations in process temperature and time, and specimen location, surface preparation, and pretreatment. During this reporting period, several specimens were prepared with a coating of CaO by thermal/chemical deposition and measurements were made of the electrical resistance of several CaO-coated specimens before and after exposure to an Li environment.

EXPERIMENTAL PROGRAM

Experiments were conducted to develop Ca-rich coatings by using the thermal/chemical deposition process. The experiments involved exposure of V alloy specimens to a pack of fine Ca pellets at 700-800°C. The specimens were either completely enclosed within the pack or hung above the pack material in a static Ar environment. Figure 1 shows the temperature dependence of the vapor pressure of Ca. Above 700°C, the vapor pressure of Ca is >0.1 torr and is sufficient to deposit a layer of Ca on the specimens. Several geometrical arrangements were examined to obtain a uniform coating of Ca on the specimens, which were typically coupons that measured 5 to 10 x 5 x 1 mm. Effort during this period concentrated on developing procedures to develop a thick adherent coating of CaO on a V-4Cr-4Ti alloy substrate and on measuring the electrical resistance of the coated specimens as a function of temperature up to ≈710°C.

RESULTS AND DISCUSSION

In previous reports, we discussed the procedure for the deposition of Ca and subsequent oxidation to convert the Ca into CaO.[1,2] The coated specimens exhibited insulating characteristics after this oxidation step. X-ray diffraction studies on these specimens showed good correlation between high resistance values at room temperature and a high concentration of Ca in oxide form. Calcium concentrations in the range of 60-80 wt.% were obtained in several specimens. However, coating thickness in a given specimen or among various specimens was not uniform; in some specimens, coating spallation was noted. The results also showed that Ca deposition via vapor phase transport is possible but that the coating thickness and the adhesive bonding of the coating to the substrate after a single deposition/oxidation procedure was not adequate to produce the desired insulating characteristics.

---

*This work has been supported by the U.S. Department of Energy, Office of Fusion Energy Research, under Contract W-31-109-Eng-38.

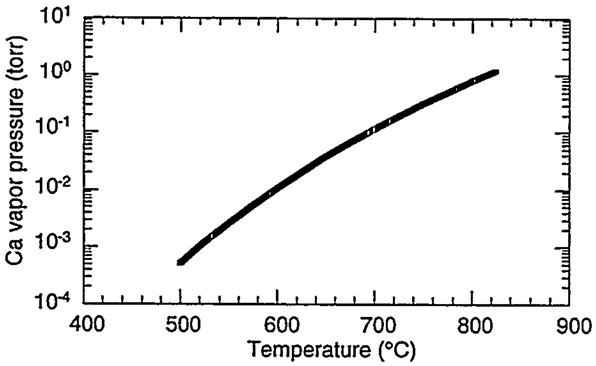

Fig. 1. Temperature dependence of Ca vapor pressure.

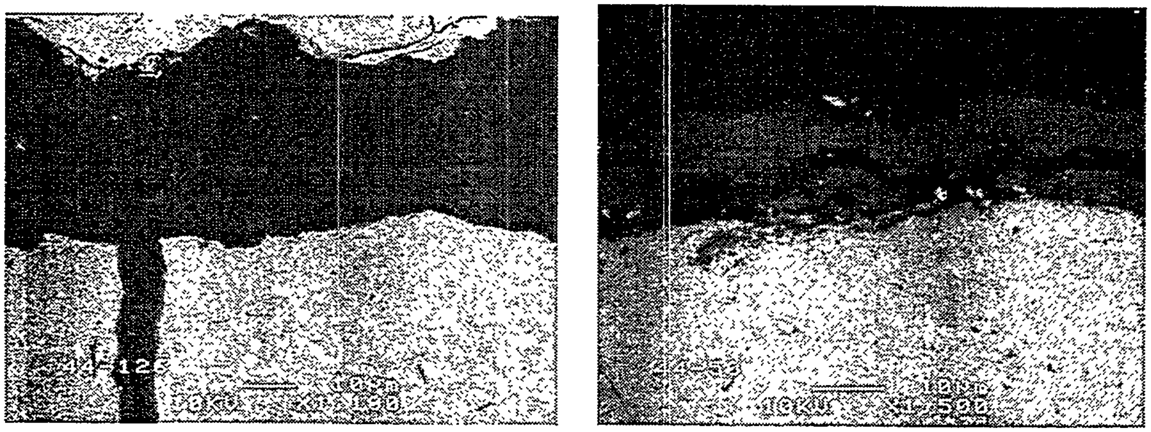

Fig. 2. SEM photomicrographs of cross sections of two V-4Cr-4Ti alloy specimens after double Ca deposition/oxidation treatment.

Additional experiments, with several procedural modifications, were conducted and, finally, a double deposition/oxidation treatment seemed to produce a thicker coating that was more adherent and exhibited adequate insulating characteristics at room temperature. Preliminary results on electrical resistance (measured by a two-probe method) of the coatings as a function of temperature up to ≈550°C were described in Ref.2.

During this period, several additional specimens were coated using the double Ca deposition/oxidation treatment, and the microstructural and compositional characteristics of the coatings were evaluated in detail. Figure 2 shows typical scanning electron microscopy (SEM) photomicrographs of cross sections of two V-4Cr-4Ti alloy specimens after a double Ca deposition/oxidation treatment. Coating thicknesses in these specimens were 15 to 30 μm. Energy-dispersive X-ray (EDX) analysis of the specimen surfaces showed the coatings to be CaO and also revealed the virtual absence of any elements from the substrate alloy. Figure 3 shows a typical EDX spectrum of the coating surface and indicates primarily Ca and O peaks. Cross sections of several specimens were analyzed as a function of depth for constituent elements of the coating and substrate. Depth profiles for two of the coated specimens are shown in Figs. 4a and 4b; the profiles in indicate coating thicknesses of 16 and 34 μm, respectively. The coating composition was predominantly CaO in both specimens, and negligible amounts of substrate elements were detected in the coating region. The difference in scale thickness between the two specimens in due to the proximity of different specimens in the Ca pack. Both specimens, after double Ca and oxidation treatment, were exposed to Li of normal purity at 500°C for 68 h.

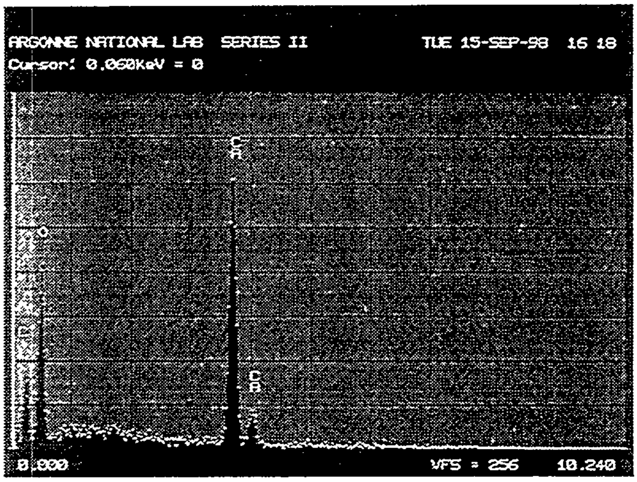

Fig. 3. EDX spectrum of surface of V-4Cr-4Ti alloy specimen after double Ca deposition/oxidation treatment.

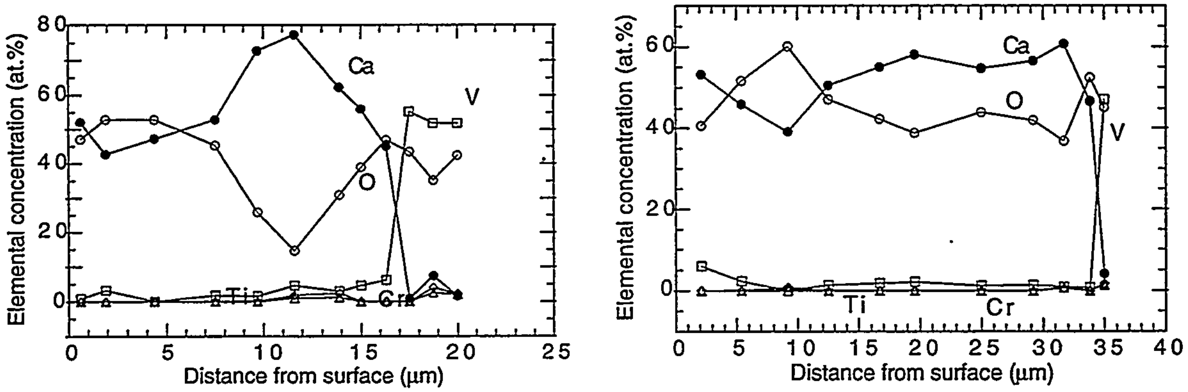

Fig. 4. Elemental concentrations as a function of coating thickness for V-4Cr-4Ti alloy specimens after double Ca deposition/oxidation treatment: (a) coating thickness = 16 μm;
(b) coating thickness = 34 μm.

To examine the stability of the coating and its electrical resistivity at elevated temperature, a two-probe method was used to measure resistance in some of the coated specimens at temperatures up to ≈700°C. The variation in the product of resistance times area (R x A) as a function of temperature obtained on specimens of V-4Cr-4Ti alloy with Ca deposition/oxidation and with Ca deposition/oxidation and redeposition of Ca was discussed in Ref.2. Those results showed that the as-coated specimen (with a double Ca and oxidation treatment) had resistance values of 10^4 to 10^5 Ω·cm^2. During this reporting period, resistance measurements were made on specimens that were double Ca/oxidation treated and subsequently exposed to liquid Li of normal purity at 500°C for 68 h. Figure 5 shows the variation in R x A as a function of temperature obtained on a CaO-coated and Li-exposed specimen of V-4Cr-4Ti alloy. The figure shows that R x A values are >10^7 Ω·cm^2 from room temperature to 200°C; the value gradually decreases to ≈5 x 10^6 Ω·cm^2 as temperature is increased from 200 to 540°C. The specimen was maintained isothermally at ≈540°C for ≈6h, after which it was further heated to ≈700°C. Even at 700°C, the specimen exhibited an R x A value of 10^4 Ω·cm^2, at least two orders of magnitude higher than that required in a fusion device using a Li blanket. Figure 6 shows variation in R x A as a function of exposure time obtained on a CaO-coated and Li-exposed specimen of V-4Cr-4Ti alloy. It is evident that the coating had R x A values of 10^5 and 10^4 Ω·cm^2 at 541 and 702°C, respectively.

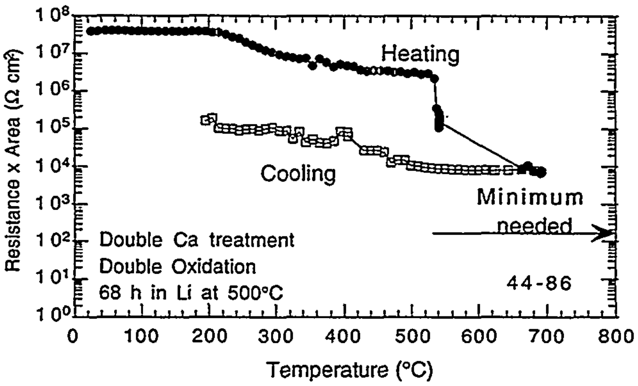

Fig. 5. Product of resistance times area as a function of temperature for V-4Cr-4Ti alloy with double Ca deposition/oxidation after 68-h exposure in Li environment at 500°C.

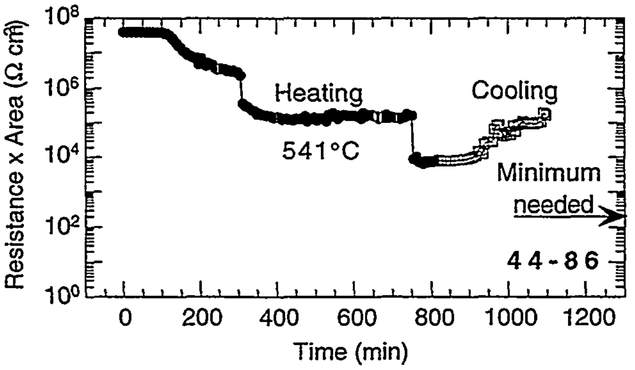

Fig. 6. Product of resistance times area as a function of time for V-4Cr-4Ti alloy with double Ca deposition/oxidation after 68-h exposure in Li environment at 500°C.

During this period, specimens of V-4Cr-4Ti alloy with a coating of CaO developed in-situ in an Li-Ca environment were examined to characterize the microstructure and coating resistance. Figure 7 shows an SEM photomicrograph of the surface of a "CaO"-coated V-4Cr-4Ti alloy specimen after exposure to an Li environment. The surface region consisted of Li_2O as the outer layer (characterized by a rough, light toned texture) and a Ca-enriched inner layer (a smooth gray texture). Figure 8 shows the variation in R x A as a function of temperature for this specimen. The value for R x A at temperatures up to ≈300°C is more than the minimum needed, but the value decreases substantially as temperature increases to 614°C. Maintaining the specimen at 614°C for extended time periods seems to improve the resistance of the coating; further increase in temperature to 713°C results in a slight reduction in resistance. In the cooling part of the cycle, the resistance values are at least two orders of magnitude higher than in the heating part of the cycle, with a probable inference of coating consolidation/densification and subtle change in chemistry of the coating during the heating part of the cycle. Figure 9 shows the variation in R x A value as a function of time for the same coated specimen. The results indicate that the resistance values for the coating in the cooling part of the cycle are substantially higher than in the heating part of the cycle, even though the coating is maintained nominally at the same temperature (e.g., 336/339 and 539/538°C) during both the heating and cooling portions of the cycle. Additional experiments are planned in which multiple heating/cooling cycles will be conducted on the same coated sample to evaluate whether the coating characteristics become stabilized and to see whether the coating resistance attains a stable value at each isothermal condition, irrespective of heating or cooling cycle.

Additional experiments are underway to evaluate the characteristics of coatings developed on several other specimens. Furthermore, the microstructures of several of these coated specimens will be characterized and compositional gradients will be determined. Also, planned is the in-situ measurement of the resistance of the coating in a Li environment.

REFERENCES

1. K. Natesan, C. B. Reed, M. Uz, and D. L. Rink, "Development of Electrically Insulating CaO Coatings," Fusion Reactor Materials Progress Report for the Period Ending June 30, 1998, Argonne National Laboratory, DOE/ER-0313/24, p. 82, Sept.1998.
2. K. Natesan, M. Uz, and S. Wieder, "Development of Electrically Insulating CaO Coatings," Fusion Reactor Materials Progress Report for the Period Ending December 31, 1998, Argonne National Laboratory, DOE/ER-0313/25, p. 69, April 1999.

Fig. 7. SEM photomicrograph of surface of V-4Cr-4Ti alloy specimen with "CaO" coating developed in-situ in Li-Ca mixture.

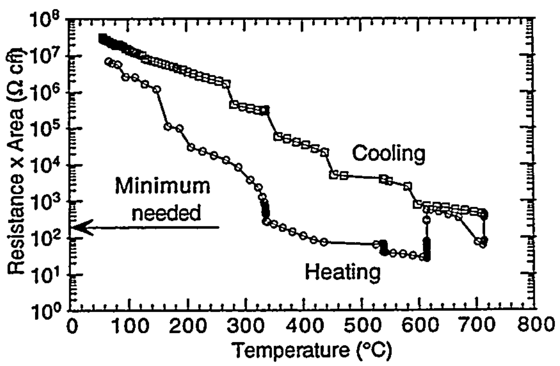

Fig. 8. Product of resistance times area as a function of temperature for V-4Cr-4Ti alloy with "CaO" coating developed in situ in Li-Ca environment

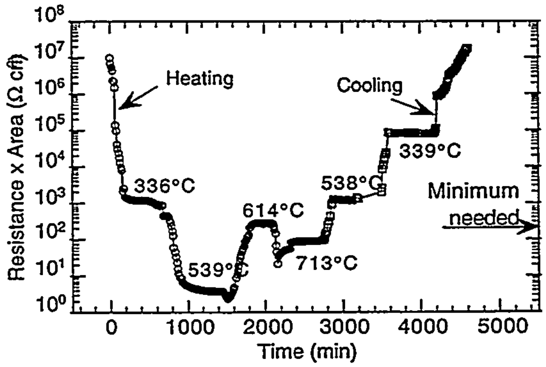

Fig. 9. Product of resistance times area as a function of time for V-4Cr-4Ti alloy with "CaO" coating developed in situ in Li-Ca environment

2.0 SILICON CARBIDE COMPOSITE MATERIALS

METHODS FOR JOINING SILICON CARBIDE COMPOSITES FOR HIGH TEMPERATURE STRUCTURAL APPLICATIONS - C. A. Lewinsohn, R. H. Jones (Pacific Northwest National Laboratory)*, M. Singh (NASA Lewis Research Center), T. Shibayama (Center for Advanced Research of Energy Technology, Hokkaido University), T. Hinoki, M. Ando, Y. Katoh, and A. Kohyama (Institute of Advanced Energy, Kyoto University)

OBJECTIVE

Reliable and practical joining techniques are required to enable the use of silicon carbide composites in fusion energy systems. Based on criteria relevant to fusion applications, silicon carbide has been selected as a promising joint material. The objective of this work is to evaluate the thermal stability and mechanical properties of silicon carbide joints fabricated via reaction-forming.

SUMMARY

Joining methods are required to allow affordable fabrication of large or complex SiC/SiC components for fusion energy systems. Previous analysis of the criteria for successful and functional joints indicates that reaction-formed and polymer-derived silicon carbide should be considered as candidate joint materials. This report summarizes preliminary mechanical properties of silicon carbide joints formed by a reaction-based approach. Both the test methods and materials are preliminary in design and require further optimization. The values of the room temperature strength of the joints, tested in flexure, are one-third to one-quarter the expected value. It is believed that the material evaluated was not fully reacted during fabrication. Further annealing, in vacuum, also decreased the strength of the joints.

PROGRESS AND STATUS

Introduction

Silicon carbide has many desirable properties for use as a "first-wall" in a fusion energy system [1-4]. Composites consisting of continuous silicon carbide fibers in a matrix of silicon carbide offer mechanical reliability that is not available in unreinforced silicon carbide. A limitation of these composite materials, however, is that they can only be produced in limited sizes and shapes. Therefore, to fabricate a complete fusion energy system a method of joining SiC/SiC components, without compromising the properties that are needed, is required. In fusion energy systems utilizing silicon carbide first-wall materials it would be undesirable to use a joining technique that introduces dissimilar materials at the inner face of the first wall. In addition, to avoid poisoning the plasma the first wall must be hermetic. Therefore, two attractive methods of joining silicon carbide with other forms of silicon carbide have been developed: reaction bonding [5-8], and preceramic polymer adhesives [9-15]. In this paper, preliminary results obtained from joints formed by reaction based forming will be presented. Although other investigators have demonstrated that joints with required values of strengths can be formed [5-8], the long term stability of the joint, and consequent affects on the mechanical properties of the joint, require further attention. In this study joints were

---

[*] Pacific Northwest National Laboratory (PNNL) is operated by the U.S. Department of Energy by Battelle Memorial Institute under contract DE-AC06-76RLO-1830.

annealed under long term static and cyclic, high temperature conditions and the resulting mechanical properties and microstructures were examined.

Experimental Technique

To evaluate the suitability of joints formed by the reaction-based forming approach, plates of monolithic silicon carbide (Hexoloy SA, Carborundum Co., Niagara, NY) were joined using the ARCjoinT technique [6-8]. Two plates of monolithic silicon carbide were cut into 25 mm-long by 4 mm-thick pieces. A carbonaceous mixture was applied to the ends of the plates that were to be joined and this was cured at 110-120°C for 10 to 20 minutes. Subsequently, a slurry of pure silicon powder was applied to the surface of the joint region and heated up to 1425°C for 5-10 minutes. Capillary forces drew the molten silicon into the joint region where it reacted with the carbon to form silicon carbide. The resulting joint material consisted of silicon carbide with controllable amounts of silicon and other phases as determined by the composition of the raw materials and infiltrant.

A limited number of joints between pieces of silicon carbide composite material were also fabricated. This composite was reinforced with Hi-Nicalon fibers (Nippon Carbon Co., Yokohama, Japan) that had been coated with a 1 µm-thick layer of carbon prior to matrix infiltration via chemical vapor infiltration. In addition, an approximately 2 µm-thick layer of silicon carbide was deposited on the outside of the composite to inhibit oxidation at high-temperatures.

The plates that were joined using the method described above were cut into bars that were 44 x 4 x 4 mm. The bars were cut so that the joint was at the middle of the bar and the plane of joining was aligned so that it was parallel to the applied load. Several of the bars were annealed in a resistively-heated, quartz-image, furnace under vacuum. A series of specimens was annealed at 1100°C for ten consecutive 10 h long cycles. The microstructure of untreated and annealed specimens was investigated via scanning electron microscopy (SEM), energy dispersive X-ray analysis (EDX), transmission electron microscopy (TEM), and high-resolution transmission electron microscopy (HRTEM).

Mechanical tests were performed by applying flexural loading to the bars described above. Two types of loading configurations were used. The first was standard 1/4, four-point bending (Figure 1a). This configuration subjects the specimens to a constant tensile stress in the region between the two inner load points. This test, therefore, is a measure of the tensile strength of the joint. The other test uses asymmetrical four-point loading (Figure 1b). This test, as described by Unal [16], subjects the specimens to a constant, through-thickness shear stress in the middle of the specimen. This test, therefore, is a measure of the shear properties of the joint material. Flexural loading was obtained by applying a compressive force on the fixtures using a rigid, mechanical test frame.

Results

As reported earlier [17], (Figure 2), joining pieces directly or between the outer coating of silicon carbide was equally successful and no evidence of a deleterious reaction between the joint material and the composite was observed, despite the high-temperature used to melt the pure silicon infiltrant. Apparently, these composite materials are not affected by exposure to the liquid silicon during the short infiltration time.

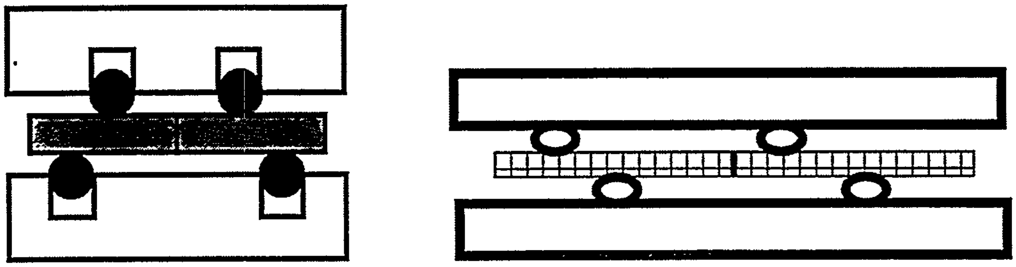

(a) (b)

Figure 1. Schematic drawings of mechanical test configurations: (a) 1/4, four-point bending, and (b) assymetric, four-point bending.

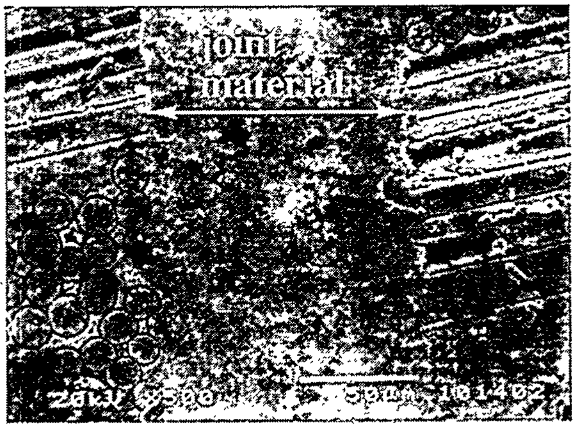

Figure 2. Micrograph of a cross section of two pieces of silicon carbide joined with reaction-bonded silicon carbide.

Experiments were conducted to investigate the long term stability of the reaction-formed joint material at elevated temperatures. Several specimens were annealed in a treatment that involved heating the specimens from 25°C to 1100°C in 55 min, holding the temperature at 1100°C for ten hours, rapidly cooling the specimens to 25°C (about 30 min), and repeating this cycle until the specimen had been subject to ten hold periods. Initial SEM microscopy and EDX results, Figure 3, indicate that after this treatment the silicon signal across a typical cross section of a joint is relatively constant. In addition, the appearance of the joint material near the interface with the monolithic silicon carbide is different from that in the middle of the joint. It is possible that further reactions between unreacted silicon and the extremely fine-grained carbon in the untreated joints occurred during annealing. Further microscopy will be conducted to investigate this hypothesis.

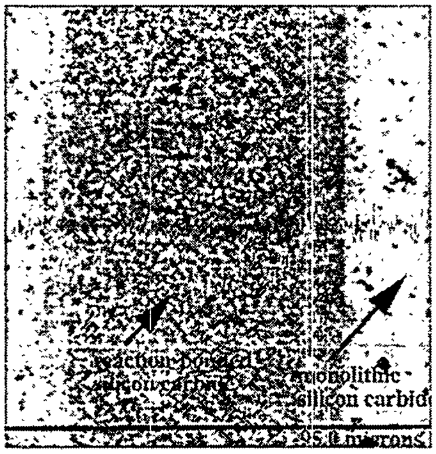

Figure 3. Scanning electron micrograph, with EDX spectra from silicon superimposed, of a cross section of two pieces of monolithic silicon carbide joined by reaction-bonded silicon carbide after annealing for ten cycles to 1100°C.

At room temperature, the maximum tensile stress obtained in flexural loading of joined composites and unreinforced SiC (monolithic) were similar (Figure 4). Unfortunately, the measured values of strength were lower than the first matrix-cracking stress, roughly 80-100 MPa [18], for the composites used. As mentioned earlier, the materials were not optimized for mechanical properties. The room temperature strength of reaction-formed silicon carbide joints has been reported as 255 ± 3.2 MPa [6]. The reasons for the lower than anticipated tensile stress values are not fully understood. The initial microstructural investigation [17], however, revealed that the untreated joints contained excess carbon and silicon that is indicative of an incomplete reaction. Therefore, it is likely that the joints were weaker than expected because the reaction to silicon carbide had not been completed.

The through-thickness shear properties of the joints were also tested. As described above, asymmetric, four-point bend tests were used to measure this property. As expected, the maximum through-thickness shear strength is lower than the maximum tensile stress in flexure (Figure 5). Despite the less than optimum strength properties of these joints, the through-thickness shear strengths were approximately one-third to one-quarter of a typical value for a reliable joint. Of course, the actual strength value required is highly dependent on the joint geometry and service stresses. After annealing in vacuum at 1000°C for either 100 h or ten 10 h cycles, the value of the through-thickness shear strength decreased significantly (Figure 6). Initial microscopy [17] revealed that these annealing conditions promoted the formation of additional SiC at the interface between the joint material and the substrate. Although the formation of additional silicon carbide at the interface between the joint and the substrate would seem to be desirable, diffusion of the required reactants from the joint material may have created porosity in the joint and made it weaker (Figure 3). This hypothesis must be examined further. These results emphasize the importance of carefully controlling the processing conditions during fabrication of the joints. Finally, the strength of composite material joined between approximately 2 μm-thick outer layers of unreinforced CVD SiC oxidation-protection coating were almost identical to the strength of those joined

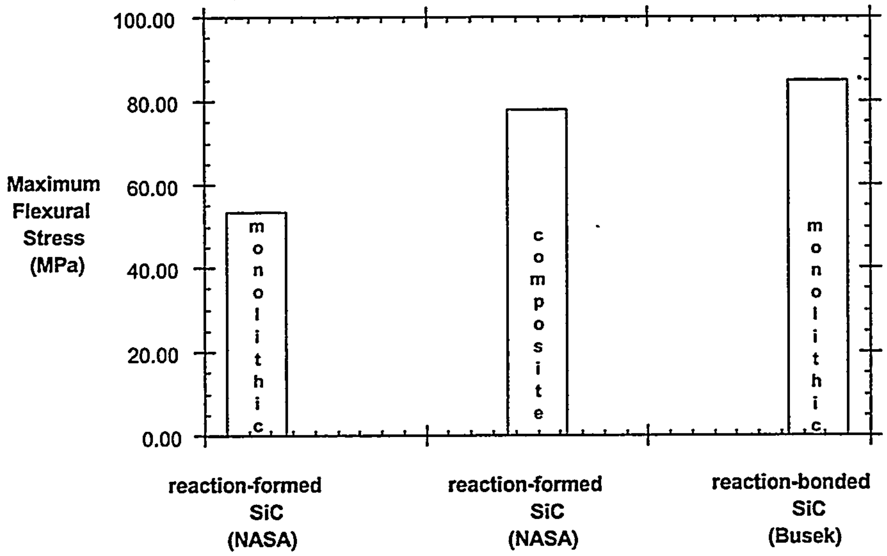

Figure 4. Comparison of room-temperature flexural strength.

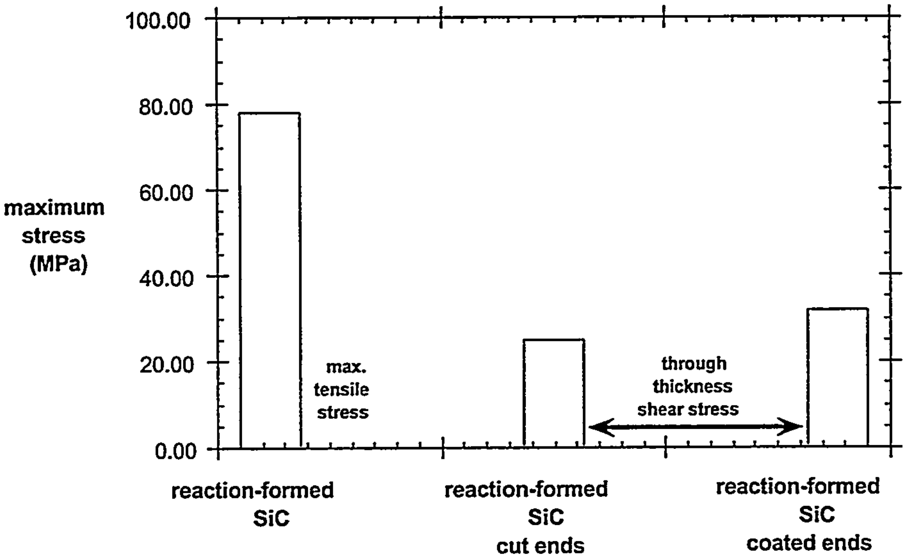

Figure 5. A comparison of the room temperature tensile stress and the through-thickness shear strength.

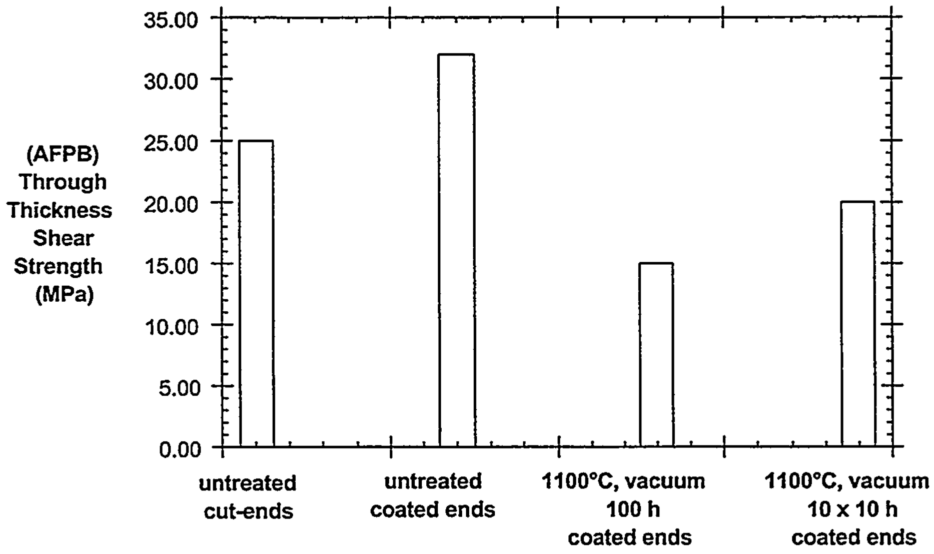

Figure 6. A comparison of the through-thickness shear strength after thermal annealing.

between cut surfaces. These results indicate that there need not be any special fabrication requirements prohibiting the cutting of materials with a protective layer supplied by a manufacturer.

CONCLUSIONS

Preliminary studies have shown that joints between silicon carbide and silicon carbide composites can be fabricated by a reliable, low-cost reaction-forming technique. Initial mechanical test data indicates that the joints have lower than anticipated strength values. In addition, annealing further decreases the measured values of strength. Additional work is required to characterize the microstructure and mechanical properties of untreated and annealed joints.

REFERENCES

1. R.H. Jones, C.H. Henager, and G.W. Hollenberg, J. Nuc. Mat., **191-194**, 75-83 (1992).

2. P. Fenici and H.W. Scholz, J. Nuc. Mat., **212-215** (1994).

3. P. Rocco, H.W. Scholz, M. Zucchetti, "Silicon Carbide and the New Low Activation Requirements for a Fusion Reactor First Wall," J. Nuc. Mat., **191-194**, 1474-1479 (1992).

4. P. Rocco, M. Zucchetti, "The Impact of Low-activation Criteria on the Development of Novel Materials for Fusion," J. Nuc. Mat., **212-215**, 649-654 (1994).

5. B.H. Rabin, and G.A. Moore, "Joining of SiC-Based Ceramics by Reaction Bonding Methods," J. Mat. Synth. & Proc., **1** [3], 195-201 (1993).

6. M. Singh, "A Reaction Forming Method for Joining of Silicon Carbide-Based Ceramics," Scripta Mater., **37** [8], 1151-1154 (1997).

7. M. Singh, S.C. Farmer, and J.D. Kiser, "Joining of Silicon Carbide-Based Ceramics by Reaction Forming Approach," Cer. Eng. Sci. Proc. 18 [3], 161-166 (1997).

8. M. Singh, "Joining of Sintered Silicon Carbide Ceramics For High Temperature Applications," J. Mat. Sci. Lett, in press.

9. S. Yajima, K. Okamura, T. Shishido, Y. Hasegawa, and T. Matsuzawa, "Joining of SiC to SiC Using Polyborosiloxane," Am. Ceram. Soc. Bull., **60**, 253, (1981).

10. A. Donato, P. Colombo, and M.O. Abadirashid, "Joining of SiC to SiC using a preceramic Polymer," pp. 431-436 in High-Temperature Ceramic -Matrix Composites I, A.G. Evans and R. Naslain (eds.), Ceram. Trans., **57**, The American Ceramic Society, Westerville, Ohio, USA, 1995.

11. W.J. Sherwood, C.K. Whitmarsh, J.M Jacobs, and L.V. Interrante, "Joining Ceramic Composites Using Active Metal/HCPS Preceramic Polymer Slurries," Cer. Eng. Sci. Proc., **18**, 177-184 (1997).

12. O. Unal, I.E. Anderson, M. Nostrati, S. Ijadi-Maghsoodi, T.J. Barton, and F.C. Laabs, "Mechanical Properties and Microstructure of a Novel SiC/SiC Joint," pp. 185-194 in Ceramic Joining, I.E. Reimanis, C.H. Henager, Jr., and A.P. Tomsia (Eds.), Ceramic Transactions, vol. 77, The American Ceramic Society, Westerville, Ohio, USA, 1997.

13. P. Colombo, "Joining Ceramics Using Preceramic Polymers," in Interfacial Science in Ceramic Joining, NATO Advanced Research Workshop, Bled, Slovenia, November 12-15, 1997.

14. P. Colombo, V. Sglavo, E. Pippel, and J. Woltersdorf, "Joining of Reaction-Bonded Silicon Carbide Using a Preceramic Polymer," J. Mat. Sci., **33**, 2409-2416 (1998).

15. E. Pippel, J. Woltersdorf, P. Colombo, and A. Donato, "Structure and Composition of Interlayers in Joints Between SiC Bodies," J. Eur. Ceram. Soc., **17**, 1259-1265 (1997).

16. O. Unal, I.E. Anderson, and S.I. Maghsoodi, "A Test Method to Measure Shear Strength of Ceramic Joints at High Temperatures," J. Am. Ceram. Soc., **80** [5], 1281-1284 (1997).

17. C.A. Lewinsohn, R.H. Jones, M. Singh, T. Shibayama, T. Hinoki, M. Ando, Y. Katoh, and A. Kohyama, "Methods for Joining Silicon Carbide Composites for High Temperature Structural Applications," Fusion Materials Semiannual Progress Report for the Period Ending December 31, 1998, DOE/ER.

18. C.A. Lewinsohn, C.H. Henager, Jr., unpublished work.

3.0 FERRITIC/MARTENSITIC STEELS

IMPURITY CONTENT OF REDUCED-ACTIVATION FERRITIC STEELS AND THE EFFECT ON THE REDUCED-ACTIVATION CHARACTERISTICS—R. L. Klueh (Oak Ridge National Laboratory), E. T. Cheng (TSI Research, Inc.), M. L. Grossbeck, and E. E. Bloom (Oak Ridge National Laboratory)

OBJECTIVE

This work was conducted to obtain concentrations of important impurity elements in reduced-activation ferritic steels, to estimate the lowest concentrations of the impurities that could be achieved with present technology, and concentrations that could be achieved in the future with innovative processing techniques.

SUMMARY

Three heats of reduced-activation martensitic steel were analyzed by inductively coupled plasma mass spectrometry for low-level impurities that compromise the reduced-activation characteristics: a 5-ton heat of modified F82H for which an effort was made during production to reduce detrimental impurities, a 1-ton heat of JLF-1, and an 18-kg heat of ORNL 9Cr-2WVTa. Specimens from commercial heats of modified 9Cr-1Mo and Sandvik HT9 were also analyzed. The objective was to determine the difference in the impurity levels in the F82H and steels for which less effort was used to insure purity. Silver, molybdenum, and niobium were found to be the tramp impurities of most importance. The modified F82H had the lowest levels, but in some cases the levels were not much different from the other heats. The impurity levels in the F82H produced with present technology did not achieve the limits for low activation for either shallow land burial or recycling. The results indicate the progress that has been made and what still must be done before the reduced-activation criteria can be achieved.

PROGRESS AND STATUS

Introduction

Development of low- or reduced-activation materials for fusion has focused on the issue of radioactive waste disposal [1] or recycling [2] of materials from fusion power plant components after they have reached the end of their service lifetime. The objective has been to eliminate or minimize those elements from an alloy that would produce long-lived radioactive isotopes during irradiation in a fusion neutron spectrum. Emphasis in the development process has generally centered on eliminating Nb, Cu, Ni, Mo, and N, widely used alloying elements, with niobium usually receiving the most attention, because of the very low levels (<1 wppm) that niobium cannot exceed if the steel is to meet low-activation criteria.

Besides the elements listed above, Butterworth and co-workers [2-4] have pointed out that there are various other elements that must be restricted to extremely low levels. Such elements could appear in the materials as tramp impurities and include Ag, Ho, Bi, Co, Sm, Lu, Dy, Gd, and Cd. Murphy and Butterworth [4] calculated the maximum amount of these elements allowed for recycling based on the assumption that "the concentrations of impurity elements were restricted to levels that would allow attainment of a surface γ dose rate not exceeding the "hands-on" dose rate limit of 25 μSvh^{-1} at a 100 y cooling time for material subjected to a first wall neutron fluence of 12 $MWym^{-2}$. This limit was suggested as a "target value" [4].

Since the Murphy and Butterworth work [4], an updated library of activation cross sections, FENDL/A-2.0, was developed as part of the Fusion Nuclear Data Library (FENDL) under the coordination of the International Atomic Energy Agency [5,6]. These new cross sections were used previously to calculate the concentration limits of natural elements in low-activation fusion materials [7], and they will be used in this paper to compare the values obtained by analysis of selected steels. It needs to be emphasized that these criteria have no "official" status relative to what might be required in the future (when fusion power plants are built or when they are decommissioned) for recycling or shallow land burial (should that be allowed at that time).

Activation calculations to determine the decay characteristics of radioactive products produced during irradiation of a material in a fusion environment have often ignored many of the tramp impurities listed above. In this paper, several of these elements have been determined in selected steels by analytical techniques to establish a base concentration for activation calculations and also to give an indication of what elements may need to be considered when processes are developed for maximizing reduced-activation characteristics for potential structural materials. A similar procedure was used previously to explore impurities in V-Cr-Ti alloys [8].

Murphy and Butterworth [4] chose to apply the criterion to each element individually and disregard additive effects. However, they pointed out that additive effects could be important for real materials. Under those conditions, the concentration of an individual element must be less than the limit for that element, and the amount allowed for the material to meet the guidelines for shallow land burial or recycle will depend on all the non-reduced-activation elements present. For n restricted elements, shallow land burial will be allowed if the waste disposal rating (WDR) is

$$WDR=\sum_{i=1}^{n}\frac{c_i}{c_{imax}}\leq 1 \qquad (1)$$

where c_i is the concentration of the *ith* element present in the alloy and c_{imax} is the maximum allowable concentration for that element as determined by the guideline for shallow land burial. A similar materials recycling rating (MRR) can be defined, where c_{imax} is the concentration of the *ith* element and c_{imax} is the maximum allowable concentration of that element according to guidelines for recycling.

Experimental Procedure

A sample from a heat of ferritic/martensitic reduced-activation steel was analyzed by inductively coupled plasma mass spectrometry (ICPMS). The steel specimen was taken from a 5-ton heat of modified F82H (IEA Mod F82H) , a nominal Fe-7.5Cr-2W-0.2V-0.02Ta-0.1C steel (all compositions are in weight percent) that was purchased by the Japan Atomic Energy Research Institute, Tokai, Japan, from NKK Corporation, Kawasaki, Japan, for use in a collaborative test program by investigators in the U.S., Japan, and the European Union coordinated by the International Energy Agency (IEA) to establish the feasibility of using ferritic steels for fusion. During the production of this heat, an effort was made to minimize niobium in the steel, but no special effort was made to reduce any of the other elements that are not specified (i.e., Ag, Cd, Co, etc).

To determine the variation in impurities in current fusion-program steels (reduced-activation and commercial steels), several other steels were analyzed by ICPMS. These included specimens taken from: (1) a 1-ton heat of JLF-1, a nominal Fe-9Cr-2W-0.2V-0.09Ta-0.02N-0.1C reduced-activation steel (also used in the IEA collaboration) produced in Japan by Nippon Steel Corporation; (2), an experimental 18-kg heat of the ORNL 9Cr-2WVTa, a nominal Fe-9Cr-2W-0.25V-0.07Ta-0.01C steel produced by Combustion Engineering, Chattanooga, TN, (3) a commercial heat of modified 9Cr-1Mo, a nominal 9Cr-1Mo-0.2V-0.07Nb-0.06N-0.1C steel; and (4) a commercial heat of Sandvik HT9, a nominal 12Cr-1Mo-0.3V-0.5W-0.5Ni-0.2C steel.

The metal samples for the ICPMS were dissolved in a mixture of HNO_3, HF, and H_2O_2. A reagent blank was prepared with the sample. A semiquantitative scan was conducted of the samples, and the spectra were examined for elements of interest and any other elements that were present. Before analyzing the sample, the instrument was checked for mass calibration and resolution. All elements reported were obtained by quantitative analysis using a blank, 10 ppb and 60 ppb standard for all the elements in a calibration curve. A calibration verification combined of an EPA QC standard and a multi-element SPEX standard was analyzed to validate the calibration standards. All elements in the verification standard were within 10% of the calibration standards. A ten-fold dilution was made on the dissolved sample that was analyzed, and the reagent blank was subtracted and calculated with an appropriate dilution factor applied. A portion of the diluted sample was spiked with 20 ppb of all elements reported. Spike recoveries were within 10%, which is the accuracy reported for the technique. Two readings were made and the precision for the elements for the first specimen are given in Table 1.

Table 1. Precision for elements analyzed by inductively coupled plasma mass spectrometry (wppb)

Element	Concentration	Element	Concentration	Element	Concentration
Li	0.01	Cd	0.23	Ta	0.3
Zr	0.67	Co	0.43	Er	1.5
Cr	0.11	Fe	0.65	Tb	0.2
Al	0.4	Ir	0.6	Ho	0.4
Ni	1.2	Nb	0.7	Y	2.0
Ag	0.4	Mo	1.2	Hf	0.14
B	1.8	Pd	0.04	W	0.5
Bi	0.03	Sn	0.5	Eu	0.14

Results

The following elemental impurities that must be limited for reduced-activation consideration were determined by ICPMS: Ag, Bi, Cd, Co, Dy, Er, Eu, Ho, Ir, Mo, Nb, Ni, Os Tb, and U. Results for two specimens of the IEA Mod F82H are given in Table 2. Also shown in the table are results for the JLF-1, ORNL 9Cr-2WVTa, Modified 9Cr-1Mo, and HT9 steels.

Discussion

Table 2 indicates that with the exception of two elements, cobalt and nickel, the concentrations of the individual impurity elements in the IEA F82H steel are lower or as low as in any of the other five steels. Nickel and cobalt are lowest in the JLF-1. These results provide an indication of what may be possible for reduced-activation steels. They can also serve as the starting point for determining how these steels can be processed to the purity levels required. That is, a detailed analysis of the materials processing techniques used for these heats could indicate reasons for the differences and how the impurities might be further reduced.

For the IEA Mod F82H heat produced by NKK Corporation, high purity iron ingots were produced using a converter, after which only ingots containing below 0.5 ppm Nb were selected for the heat [9]. Clean materials were also selected for the other alloying additions, and vacuum-induction melting (VIM) was used. This choice of materials resulted in this steel having the lowest silver and niobium content for the steels in Table 2. Despite the chosen process to reduce niobium content, the concentration for the IEA F82H was only slightly lower than for JLF-1 and 9Cr-2WVTa. The exact procedure used for choosing the melt stock for the JLF-1 is not known, but VIM was used for melting. The ORNL 9Cr-2WVTa was a small 18-kg experimental heat of steel made using off-the-shelf melt stock that was air melted and then electro-slag remelted. Molybdenum was slightly lower in the IEA Mod F82H and the JLF-1 steel than the 9Cr-2WVTa, but only by a factor of 3. The Sandvik HT9 and modified 9Cr-1Mo steels were large commercial heats, probably made with scrap. The niobium concentration was an order of magnitude higher in the HT9 than for the reduced-activation steels (niobium is part of the specified composition of modified 9Cr-1Mo steel).

Table 2. Chemical composition of deleterious impurity elements in reduced activation of ferritic steels determined by inductively coupled plasma mass spectrometry (wppm)

Element	IEA Mod F82H		JLF-1	ORNL 9Cr-2WVTa	Modified 9Cr-1Mo	HT9
Ag	<0.05	<0.1	0.21	0.16	0.23	1.3
Bi	<0.2	<0.05	<0.1	<0.05	<0.1	<0.1
Cd	<0.4	<0.05	<0.05	<0.05	3.3	5.1
Co	28	16	7.6	34	58	393
Ir	<0.02	<0.05	<0.05	<0.05	<0.05	<0.05
Mo	21	19	20	70	**	**
Nb	3.3	2.4	4.3	4	**	23
Ni		474	13	402	1251**	5692**
Os		<0.05	<0.05	<0.02	<0.02	<0.05
Pd		<0.05	<0.05	0.18	0.27	0.4
Dy		<0.05	<0.05	<0.05	<0.05	<0.05
Er		<0.05	<0.05	<0.05	<0.05	<0.05
Eu	<0.02	<0.05	<0.05	<0.05	<0.05	<0.05
Ho	<0.05	<0.05	<0.05	<0.05	<0.05	<0.05
Tb	<0.02		<0.05		<0.05	<0.05
U	<0.003	<0.05	<0.05	0.6	0.12	<0.05

** Element is part of the specified composition

Table 3. Limits of deleterious impurity elements for shallow land burial and recycle compared to the concentration of these elements in present and future reduced-activation steels (wppm)[a]

Element	Waste Disposal Limit[b]	Materials Recycle Limit[b]	IEA F82H	Present	Future
Ni	15-38%	87-470 (1.6-4.3%)[c]	474	13	0.1
Mo	31-37	3.6-20 (4.1-23)	20	5	1
Ag	1.2-2.7	0.012-0.026 (0.017-0.036)	<0.1	<0.05	<0.005
Bi	22-109	0.017-0.41 (0.48-3.2)	<0.2	<0.05	<0.01
Cd	0.14-1.7%	2.1-24 (2.9-29)	<0.4	<0.05	<0.05
Co	19%-No Limit	2.3-14 (0.53-18%)	28	8	<0.02
Ir	22-29	0.21-0.27 (0.37-0.48)	<0.05	2	0.05
Nb	2.4-3.5	0.055-0.08 (0.055-0.08)	3	0.5	<0.02
Os	560-3100	5.2-29 (9.3-52)	<0.05	<0.05	<0.02
Pd	110-1700	0.17-2.5 (0.23-3.5)	<0.05	<0.05	<0.05
Dy	4.6-140	0.095-2.0 (0.11-2.8)	<0.05	<0.05	<0.05
Er	28-285	0.73-6.5 (0.82-7.3)	<0.05	<0.05	<0.05
Eu	1.3-1.4%	0.016-0.0054 (2.4-1.3)	<0.05	<0.02	0.01
Ho	0.7-1.2	0.017-0.028 (0.019-0.032)	<0.05	<0.05	0.01
Tb	1.9-5	0.0046-0.012 (0.0099-0.026)	<0.02	<0.02	<0.001
Al	660-3900	13-79 (13-79)	140	30	0.5
Cu	73%-No Limit	160-No Limit (20%-No Limit)	10	10	<5

[a] Cooling time for waste disposal and hands-on materials recycling 100 y after 20 MW y/m^2 exposure.

[b] The low number of the two is for first wall alone; the high number is for the blanket average.

[c] Concentration limits given in parentheses are for cooling time of 300 y.

As pointed out, the IEA Mod F82H had the highest nickel and cobalt content of the reduced-activation steels. These elements go together; that is, most of the cobalt probably comes from the nickel. Even electrolytic nickel (described as 99.95% Ni+Co), which is also known as "pure nickel," contains 0.3-0.5% cobalt. The data in Table 3 indicate a correlation between the cobalt and nickel in the steels. Nickel (0.5%) is added to the HT9, and this steel also has the highest cobalt (0.04%) content. Of interest is the low level of cobalt in the JLF-1 and the relatively high level in the IEA Mod F82H and 9Cr-2WVTa.

Since no nickel was added to any of these steels, tracing the origin of the nickel should indicate part of the solution to reducing cobalt in future heats, should that be necessary.
These results provide a "starting point" for discussing the present status of reduced-activation ferritic/martensitic steels and the steps required to reach the goal of a steel that meets the criteria for shallow land burial and/or recycling. In Table 3, the Waste Disposal Limit (WDL) and Materials Recycle Limit (MRL) are calculated using FENDL/A-2.0 [5,6] for the elements that need to be restricted for a fusion system after four years of operation at 5 MW/m^2, an integrated wall loading of 20 MW y/m^2. In the range of values given for the WDL and MRL, the low number is for the first wall alone, and the high number is for the blanket average. Values are for a cooling time of 100 y, except for the MRL values in parentheses, which are for a 300 y cooling period. The WDL and MRL values are the c_{imax} of Eq. (1) used to calculate WDR and MRR, which are given in Table 3.

The fourth column of Table 3 gives the concentration of restricted impurity elements for the IEA Mod F82H (the highest of the two values in Table 2 was chosen). A WDR value of 2.2-1.5 was calculated with Eq. (1) for the low and high WDL values, indicating that more of the restricted elements need to be removed before the steel will meet reduced-activation criteria for shallow land burial. Calculated WDR and MRR values are given in Table 4.

Table 4. Waste disposal rating (WDR) and materials recycle rating (MRR) for reduced-activation ferritic/martensitic steels[a]

Rating	IEA Mod F82H	Present	Future
WDR (100 y)	2.1-1.2	0.51-0.28	0.09-0.04
MRR (100 y)	120.2-60.6	33.1-16.8	4.6-3.3
MRR (300 y)	82.2-45.5	21.1-10.7	2.9-1.25

[a] WDR<1 and MRR<1 to meet criteria for shallow land burial and recycling, respectively.

In the column labeled "Present," concentrations are given that are the lowest values that have been measured in different steels (e.g., the low values measured for IEA Mod F82H, the Ni and Co in JLF-1, Os in ORNL 9Cr-2WVTa, etc.). These values should be achievable at present with a relatively modest effort by analyzing the techniques used to achieve the low levels in the different steels. The WDR calculated for these values are 0.53-0.32 (Table 4), thus meeting the criteria for shallow land burial.

The final column in Table 3 labeled "Future" gives estimated concentration values that should be possible to achieve in the near future with the proper choice of techniques to produce "pure" melt stock. These estimated values were arrived at by chemically analyzing "high purity" Fe, Cr, W, and V obtained from commercial vendors and other sources. The materials analyzed included a piece of iron purified by "selective prepurification and oxidation zone melting" [10]. This material contained <0.2 ppm Nb, the lowest value of this element in any of the iron analyzed. The lowest value in commercial high purity iron was 1.2 ppm. WDR values for the "Future" concentrations are 0.09-0.04 (Table 4).

Despite the low WDR values for the "Future" reduced-activation steel, the steel would not meet the criteria for recycling because the MRR is 4.6-3.3 after a 100 y cooling period. For a 300 y cooling period, the MRR drops to 2.9-1.25, still above the value required for "hands-on" recycling. This applies to the 20 MW y/m^2 integrated first wall neutron exposure. It could be hands-on recycled after 100 years if the neutron exposure was reduced to 6 MW y/m^2 or after a 300 y cooling period if the exposure was reduced to 16 MW y/m^2.

These results lead to a similar conclusion for the reduced-activation ferritic/martensitic steels to that reached previously for V-Ti-Cr alloys [8]. Namely, it should be possible to produce steels that will meet the present-day criteria for shallow land burial of the nuclear waste, but this will probably not be achieved without some effort and expense. Much more work and probably considerable more expense will be required to reach the levels required for materials recycling based on a "hands-on" dose-rate limit of 25 μSvh^{-1} at a 100 y cooling time. Even a 300 y cooling time would not allow these criteria to be reached easily for a 20 MW y/m^2 neutron exposure. Indeed, it would probably take considerable effort and expense just to determine if those criteria for recycling could ever be met for the compositions in question.

Another problem for recycling an Fe-Cr-W-V-Ta steel appears when the WDL and MRL values are examined for the major alloying elements (Table 5). Although none of these elements will

Table 5. Estimated Concentration of Typical Elements in Reduced-Activation Steel (wt %)[a]

Element	Waste Disposal Limit	Materials Recycle Limit[b]	IEA F82H	Present	Future
C	No Limit	No Limit	0.1	--	--
Si	No Limit	No Limit	0.1	--	--
Mn	No Limit	No Limit	0.2	--	--
P	No Limit	No Limit	0.008	0.002	0.001
S	No Limit	No Limit	0.002	0.001	0.001
Cr	No Limit	No Limit	7.5	--	--
W	41-No Limit	0.11-0.37 (1.8-19)	2	--	--
V	No Limit	No Limit	0.2	--	--
B	No Limit	No Limit	0.002	--	--
N	0.18-0.36	No Limit	0.006	0.006	0.001
Ti	No Limit	0.14-1.4 (9.3-No Limit)	0.001	0.001	0.0005
Ta	No Limit	0.026-1.0 (2.2-7.8)	0.05	0.05	0.05

[a] Cooling time for waste disposal and hands-on materials recycling 100 y after a 20 MW y/m^2 exposure.

[b] Concentration limits given in parentheses are for cooling time of 300 y.

affect the WDL values calculated from the impurity concentrations (Table 4), there will be an effect of tungsten and tantalum on the MRL. Obviously, if a reduced-activation steel is ever to be recycled under the criteria used for the present calculations—those proposed by Murphy and Butterworth [4]—then they would essentially have to be free of tungsten. Tantalum would probably also need to be restricted, depending on the levels of other restricted elements. This means that new steels need to be developed for the recycling option.

Conclusions

Chemical analysis of potential reduced-activation ferritic steels produced by present technology were analyzed to provide an indication of the level of tramp impurity elements that compromise the reduced-activation characteristics of the steel. The results for the steels indicate that progress has been made in reducing the level of detrimental impurities for two large heats of reduced-activation steel. Silver, niobium, and molybdenum proved to be the most important of the restricted elements, and the steels that have been made up to now do not meet the criteria for low-activation for shallow land burial of nuclear waste made up of these steels after an integrated wall loading of 20 MW y/m^2 after a 100 y cooling off period. However, it appears that reduced-activation steels could be produced with these detrimental impurity elements at levels low enough to meet the present criteria for shallow land burial. If instead of shallow land burial, it is desired to recycle the steel, with a "hands-on" dose rate limit of 25 µSvh^{-1} after a 100 y cooling time, then it appears that considerable research and expense will be required to develop processes that will allow the production of steel that will meet these criteria.

There has probably never been a requirement for a structural material to be processed to have specified impurity levels as low as those required to meet the reduced-activation criteria. Even though the materials will not be needed for some time, it would appear that an effort should be mounted to determine the means to achieve the desired purity levels, especially if recycling is to be pursued. Such an effort should enlist support from industrial materials processors to examine techniques used in the past to produce high-purity materials and determine ways that these techniques might be combined with the latest technology for future application. The effort should not be delayed if reduced-activation materials are to be available when fusion power production is ready to begin operation.

REFERENCES

1. R. W. Conn, E. E. Bloom, J. W. Davis, R. E. Gold, R. Little, K. R. Schultz, D. L. Smith, and F. W. Wiffen, Panel Report on Low Activation Materials for Fusion Applications, UCLA Report PPG-728, (University of California at Los Angeles, 1983).
2. G. J. Butterworth, and L. Giancarli, J. Nucl. Mater. 155-157 (1988) 575.
3. G. J. Butterworth, J. Nucl. Mater. 179-181 (1991) 135.
4. D. Murphy and G. J. Butterworth, J. Nucl. Mater. 191-194 (1992) 1444.
5. A. B. Pashcenko, H. Wienke, and D. W. Muir, Proceedings of the International Conference on Nuclear Data for Science and Technology, 1997, Trieste, Italy; E. T. Cheng, A. B. Pashchenko, and J. Kopecky, Fusion Technol. 30 (1996) 1182.
6. J. Kopecky et al., FENDL/A.2, UKAEA Report, 1996.
7. E. T. Cheng, J. Nucl. Mater., 258-263 (1998) 1767.
8. M. L. Grossbeck, R. L. Klueh, E. T. Cheng, J. R. Peterson, M. R. Woolery, and E. E. Bloom, J. Nucl. Mater., Analysis of V-Cr-Ti Alloys in Terms of Activation of Impurities, J. Nucl. Mater., 258-253 (1998) 1778.
9. M. Tamura, Private Communication, February 18, 1999.
10. B. F. Oliver and E. W. Troy, Mémoires Scientifiques Rev. Métallurg., LXV (1968) 39.

CONSTITUTIVE AND FRACTURE TOUGHNESS PROPERTIES OF AN ADVANCED FERRITIC/ MARTENSITIC STEEL

— P. Spätig, G. R. Odette, G. E. Lucas and M. Victoria (University of California, Santa Barbara); M. Victoria (Technologie de la Fusion–Centre de Recherches en Physique des Plasmas, Ecole Polytechnique Fédérale de Lausanne)

OBJECTIVE

The objectives of this work are to characterize both the constitutive and fracture behavior of advanced ferritic-martensitic steels in support of developing physically based models for accurately predicting defect tolerance in flawed fusion structures, based, in large part, on small specimen test methods. This report focuses on developing a compact, multi-term constitutive equation for the IEA heat of martensitic steel, with special emphasis on strain-hardening behavior. New effective fracture toughness-temperature data are also presented, along with an update on the status of the US-Swiss collaborative Master Curve Experiment (MACE).

SUMMARY

A detailed investigation of the strain-hardening rate of the International Energy Agency (IEA) program heat of 8 Cr unirradiated F82H ferritic-martensitic steel has been undertaken in the temperature range [80K-723K]. The overall tensile flow stress is decomposed into an athermal/ thermal yield stress contribution plus a mildly temperature-dependent strain-hardening component. The latter is based on a phenomenological dislocation mechanics model. Compared to simple power law treatments, this formulation provides a more accurate and physically based representation of the flow stress as a function of the key variables of test temperature, strain and stain rate. Fracture toughness measurements from small 0.18T CT specimens are also reported and analyzed using a constraint correction model to estimate a small scale yielding K_{Ic} (T) toughness curve. Finally, the status of the MACE collaboration is briefly summarized. The first irradiation at 250°C to 0.5 dpa has been tentatively completed, and is awaiting confirmation of the preliminary dosimetry. Near term plans for higher doses and other temperatures are described.

PROGRESS AND STATUS

Materials and testing conditions

The alloy investigated in this study was the modified, normalized and tempered martensitic steel F82H. This is the reduced activation steel internationally investigated as part of the IEA coordinated program on ferritic/martensitic steels. The heat-treatment of this steel was:

- 0.5h at 1313K for normalization and 2h at 1013K for tempering

Tensile tests ware performed on round specimens (3mm diameter, 18 mm gauge length). The tests were carried out with a servo-hydraulic MTS machine at constant nominal strain rate of 2×10^{-4} s^{-1}, 2×10^{-3} s^{-1} and 2×10^{-2} s^{-1}. Tests at higher temperature (up to 723K), performed at the Paul Scherrer Institute in Switzerland at constant nominal strain rate of 2.8×10^{-5} s^{-1} and $2.8 \times 10^{-4} s^{-1}$, are also reported and reanalysed in this report.

The fracture toughness tests were performed on 20% side-grooved 0.18T CT specimens using procedures described elsewhere [1].

Tensile testing

Two typical true stress-true strain curves at 293K and 123K are presented on Figure 1. The two curves look quite similar with a strain-hardening rate, defined as $\theta_p = d\sigma/d\varepsilon_p$, decreasing along the entire curve. The "parabolic" type of curve seen on Figure 1 has been found at all temperatures and strain rates. Prior to necking, a roughly similar amount of strain hardening is observed in both cases. However, there are important and subtle differences as well. For example, near the yield stress $\sigma_{0.2}$, defined at 0.2% plastic strain, the transition between the elastic and the plastic domain is very smooth at 293K, while at 123K a pronounced slope change is observed. Other systematic effects of temperature on hardening at higher strains are not negligible and are analyzed below.

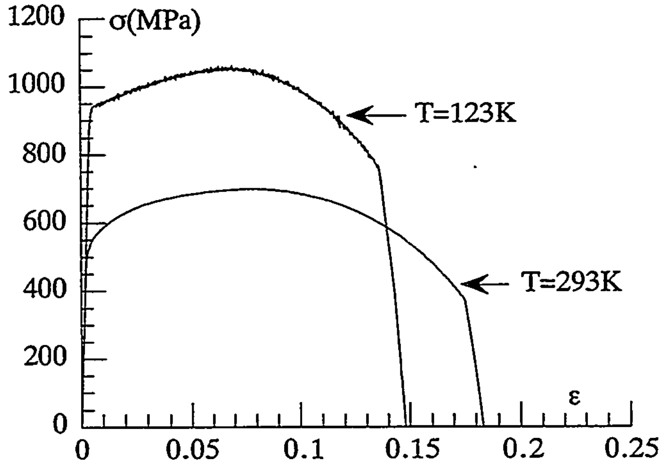

Figure 1: True stress - true strain tensile curve at 293K and 123K.

Understanding of the strain-hardening requires a flow stress decomposition into several contributions. The overall flow stress, which depends on the plastic strain, plastic strain rate and temperature $\sigma = \sigma(\varepsilon_p, \dot{\varepsilon}_p, T)$ can be considered as the sum of the yield stress, σ_y, and the contribution from plastic deformation σ_{pl}, primarily resulting from dislocation-dislocation interactions. It was previously shown [2] that σ_y exhibits a strong temperature and strain rate dependence, as expected for bcc materials. The strain hardening contribution is expected to be much less sensitive to temperature and strain rate. A reasonable general trial decomposition of the flow stress is:

$$\sigma = \sigma_y(\dot{\varepsilon}_p, T) + \sigma_{pl}(\varepsilon_p, \dot{\varepsilon}_p, T) \qquad (1)$$

The σ_y term can itself be decomposed into different athermal and thermal components due to both the lattice friction stress and microstructure resulting from the alloy composition and thermal-mechanical treatment, including contributions from:

- the initial dislocation density
- the distribution of nondeforming particles such as carbides

- the distribution of weaker precipitate phases
- the solid solution hardening
- polycrystalline grain and subgrain boundaries
- the intrinsic friction stress of the lattice (Peierls stress) which is primarily responsible for the strong temperature and strain rate dependence.

The increase of σ_{pl} with strain, i.e. the strain-hardening $\theta_p = d\sigma_{pl}/d\varepsilon_p$, is primarily determined by the evolution of the dislocation microstructure in the material. Both the variation of the total dislocation density with strain and the organization of dislocations into a substructure determine the shape of the deformation curve. A convenient way of presenting the evolutionary behavior of the constitutive behavior of metals, as proposed by Mecking [3], is plotting θ_p, evaluated from the experimental tensile curves between yield and necking, against the corresponding flow stress.

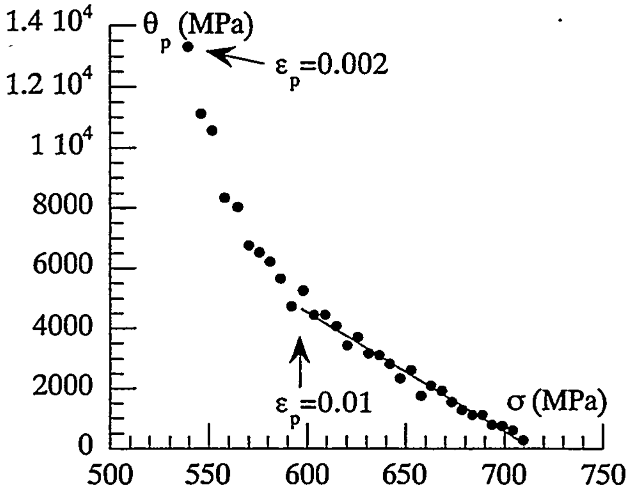

Figure 2: Strain-hardening rate θ_p vs. flow stress at T=273K.

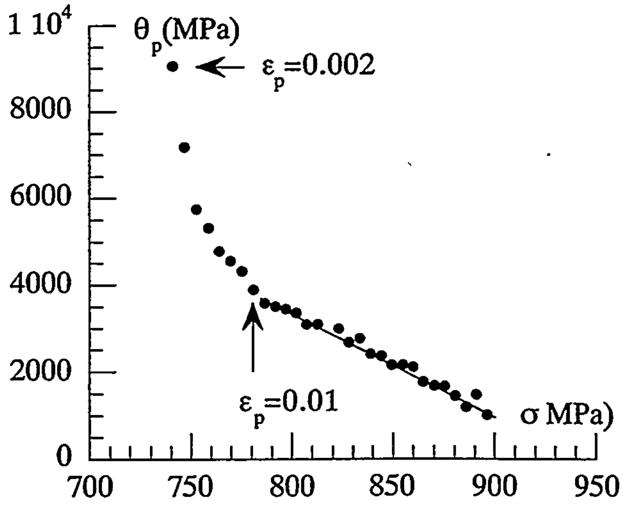

Figure 3: Strain-hardening rate θ_p vs. flow stress at T=173K.

This procedure is not only very useful in establishing appropriate analytical relations for integrated stress-strain laws, $\sigma_{pl}(\varepsilon_p)$, but also in identifying various strain-hardening stages associated with different mechanism regimes. Figures 2 and 3 show θ_p versus the flow stress between ε_p=0.002 and necking at 273K and 173K respectively. In both cases there appears to be a simple linear relation between θ_p and σ_{pl} at high stress. However below a stress, corresponding to $\varepsilon_p \approx 0.01$, θ_p deviates from the simple linear relation, rising increasingly rapidly with decreasing σ_{pl}.

θ_p for plastic strain larger than $\varepsilon_p > 0.01$ can be simply written as:

$$\theta_p = \frac{d\sigma_{pl}}{d\varepsilon_p} = K_1(\dot{\varepsilon}_{p,}T) - K_2(\dot{\varepsilon}_{p,}T)(\sigma - \sigma_{0.01}) \tag{2}$$

where the coefficient K_1 and K_2 are in MPa and dimensionless, respectively. Note an explicit strain rate and temperature dependence on the coefficient K_1 and K_2 have been retained. Integration of Equation 2 with the initial condition $\sigma = \sigma_{0.01}$ at $\varepsilon_p = 0.01$ yields:

$$\sigma_{pl}(\varepsilon_p) = \frac{K_1}{K_2}[1 - \exp[-K_2[\varepsilon_p - 0.01]]] + \sigma_{0.01} \tag{3}$$

However, it is more convenient to write Equation 3 as,

$$\sigma_{pl}(\varepsilon_p) = \sigma_{sat} - \frac{K_1}{K_2}\exp[-K_2[\varepsilon_p - 0.01]] \tag{4}$$

where the saturation stress, σ_{sat}, is equal to $K_1/K_2 + \sigma_{0.01}$. The exponential type of stress-strain relation was originally proposed, accompanied by a mechanistic justification, by Voce [4]. The temperature and strain rate dependence of σ_{pl}, if any, is contained in the K_1, K_2 and σ_{sat} terms. This relation describes the behavior of stress-strain curves tending to a saturation stress, which typically cannot be reached in a tensile test due to necking, nominally at $\theta_p=\sigma$. Note that the classical strain-hardening law for engineering materials of the type $\sigma=K\varepsilon_p^n$, would provide a poor fit to this experimental data, since this representation is not compatible with a linear decrease of θ_p or with a σ_{sat}. Further, n implicitly depends on σ_y and a higher σ_y requires a lower n even if the actual strain hardening behavior were completely athermal. Figure 4 shows the fit to Equation 3 of experimental data at 173K. Similar quality fits at other temperatures were also obtained.

Following the work of Kocks [5] for copper, aluminum and stainless steel, plots of non-dimensional σ_{sat}/μ and $(K_1/K_2)/\mu$ are presented on Figure 5 and Figure 6 respectively as a function of the dimensionless temperature, $100kT/\mu b^3$. Here μ is the shear modulus and b is the Burgers vector. The temperature dependence of μ was deduced from that of the Young's modulus [6]; and b was taken equal to 2.68 Å. The logarithms of both σ_{sat}/μ and $(K_1/K_2)/\mu$ decrease roughly linearly with $100kT/\mu b^3$ between values of about 0.2 to 0.76, corresponding to T=223K and 723K. The temperature dependence of K_2 is given on Figure 7 where it is seen that K_2 increases roughly linearly with normalized temperature between about 0.2 and 0.63, corresponding to 223K and 623K.

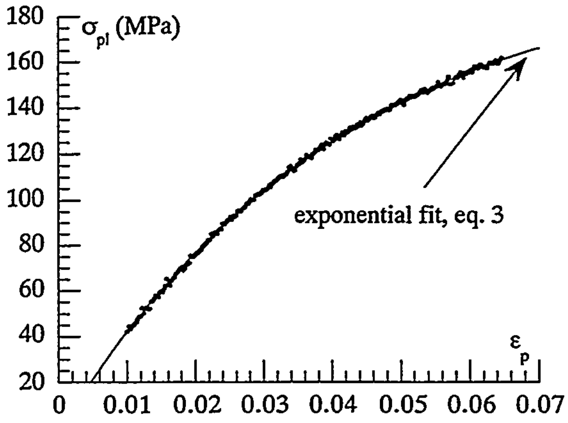

Figure 4: σ_{pl} vs ε_p at 173K with the exponential fit, eq. (4).

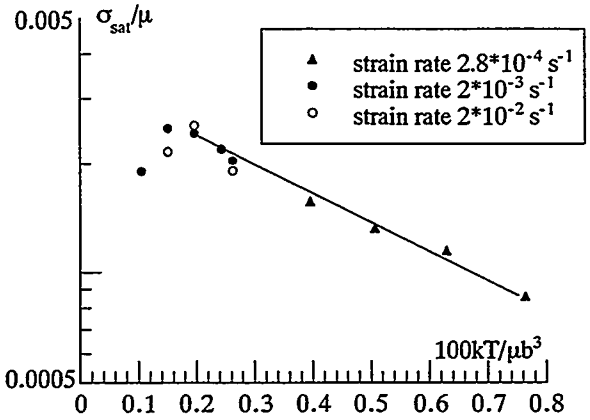

Figure 5: Normalized σ_{sat} against normalized temperature

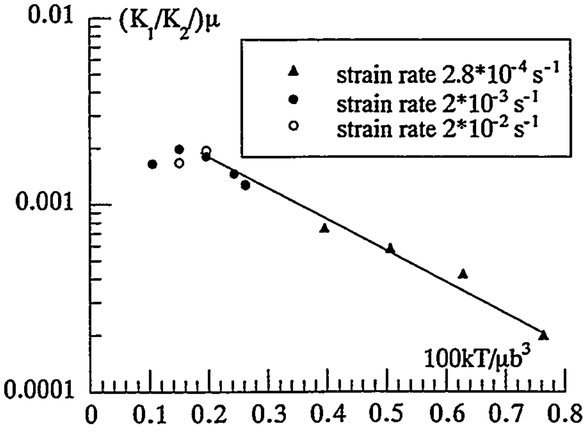

Figure 6: Normalized K_1/K_2 against normalized temperature

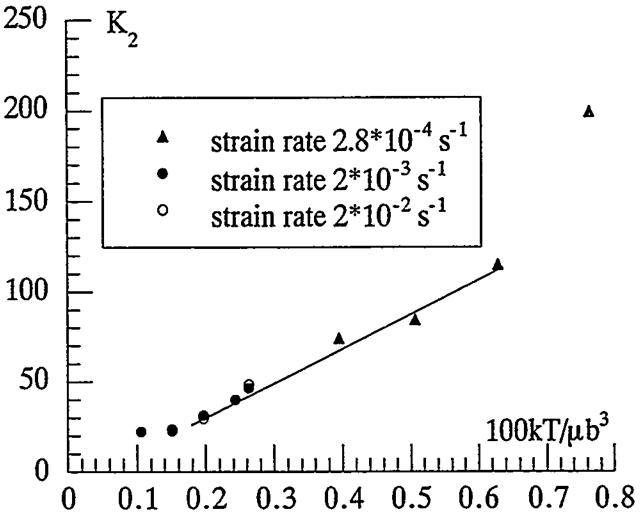

Figure 7: K_2 against normalized temperature

There is no evidence of a strain rate dependence of $(K_1/K_2)/\mu$, σ_{sat}/μ or K_2 for the limited strain rate range in this study. Least square fits to the data from 223K-623K, shown as the solid line in Figures 5, 6 and 7, are:

$$(K_1 / K_2) / \mu = 33.501 * 10^{-4} * (3.232 * 10^{-2})^\wedge x \tag{5a}$$

$$\sigma_{sat} / \mu = 33.174 * 10^{-4} * (1.705 * 10^{-1})^\wedge x \tag{5b}$$

$$K_2 = -4.1087 + 186.86 * x \tag{5c}$$

with $x = 100kT/mb^3$ for $0.2 < x < 0.63$ and $m=E/2(1+n)$ where n is the Poisson's ratio and $E=6900*(32.3-6.16*10^{-3}T-4.34*10^{-6}T^2)$ for E in MPa and T in °K.

Figure 8 plots the absolute magnitude of the saturation stress versus temperature along with $s_{0.2}$ at the strain rate of $2x10^{-3}$ s^{-1}. The total flow stress is simply the sum of these two individually aggregated contributions. However, $s_{0.2}$ depends strongly on the strain rate as well as temperature. The temperature T for a strain rate $\dot{\varepsilon}$ different than a reference strain rate $\dot{\varepsilon}_r$ at T' for the same $s_{0.2}$ is given by the relation:

$$T = T[1 + C\ln(\dot{\varepsilon}_r / \dot{\varepsilon})] \tag{6}$$

Figure 9 shows yield stress, $\sigma_{0.2}/\mu$ versus a strain-rate compensated temperature, T', for a reference strain rate of $2x10^{-4}$ s^{-1}. The solid line is for C =0.0417, which is somewhat larger than found previously [6]. In this case C was derived for the temperature dependent regime I below about 220°K, $\sigma_{0.2}/\mu$ corresponds to an athermal plus activated flow process. In regime I the controlling mechanism is of Peierls type, where $\dot{\varepsilon}_p = \dot{\varepsilon}_0 \exp(-\Delta G / kT)$, and where $\Delta G \approx kT/C$ [2].

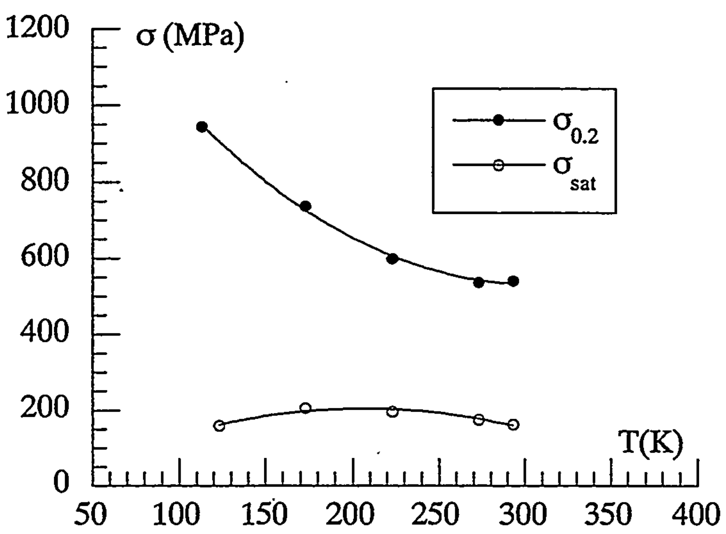

Figure 8: $\sigma_{0.2}$ and σ_{sat} against T for $\dot{\varepsilon}_p = 2x10^{-3}$ s^{-1}

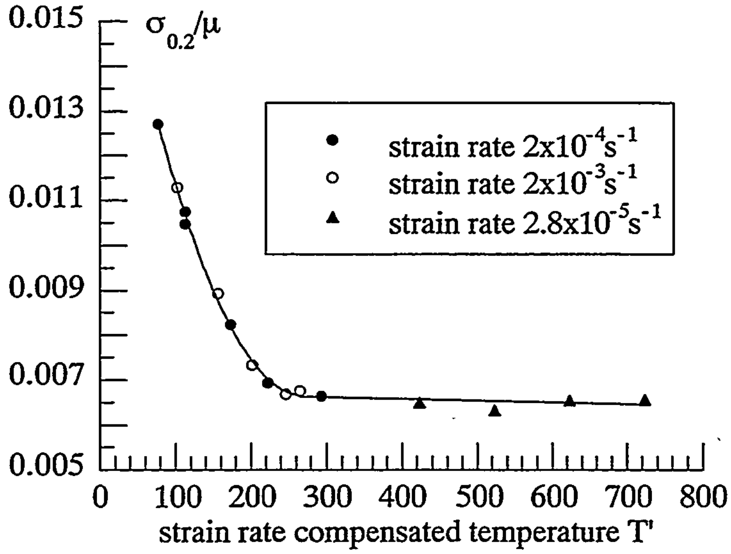

Figure 9: Strain rate compensated temperature dependence of the normalized yield stress

In the temperature regime II from about 220K to 300K the yield stress is more weakly thermally activated and approximately athermal in regime III above 300K. In the latter temperature regime, the plastic flow is considered to be controlled by polycrystalline grain and lath packet sizes, long range stresses, discrete dislocation obstacles and interactions between the moving and the forest dislocations like in the FCC materials. The overall temperature dependence of $\sigma_{0.2}$ is given by:

$$\sigma_{0.2} / \mu = 67.49 * 10^{-4} - 3.90 * 10^{-7} * T' \qquad 270K<T'<723K \quad (7a)$$

$$\sigma_{0.2} / \mu = 18.51 * 10^{-3} - 87.61 * 10^{-6} * T' + 16.17 * 10^{-8} * T'^2 \qquad T'<270K \quad (7b)$$

An example of application of equations 5 to 7 is shown on Figure 10 where the measured flow stress of several tensile tests is plotted against the calculated flow stress. The flow stresses have been calculated between the yield stress $\sigma_{0.2}$ and the stress at necking at different strain levels for tests at temperatures ranging from 223K to 623K and for strain rates between $2\text{x}10^{-4}\text{s}^{-1}$ and $2.8\text{x}10^{-5}\text{s}^{-1}$. Each symbol corresponds to a test at a given temperature and strain rate. A very good agreement between the calculated stresses and the experimental data is found and the model predicts the data within an error margin of less than 4%.

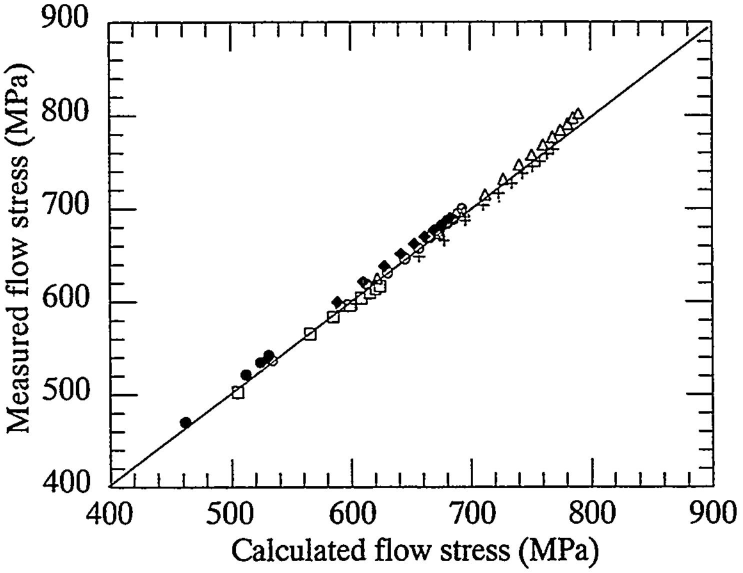

Figure 10: Measured flow stress vs. calculated flow stress for different temperatures and strain rates.

The reversibility of the flow stress has been tested with Cottrell-Stokes experiments [7]. This type of experiment is performed in two steps. First, one specimen is deformed up to a given strain at a fixed temperature T_1 and unloaded. Then, the test temperature is changed to T_2 and the deformation is continued. Usually T_2 is chosen lower than T_1 in order to avoid irreversible annealing processes. The flow stress required to deform plastically the specimen at T_2 can be compared to that obtained on a specimen tested only at T_2. This technique allows one to quantify the influence of temperature on the development of the microstructure and to assess the reversibility of the flow stress for a given strain-hardened state. An example of a Cottrell-Stokes experiment is shown in Figure 11 for which a specimen of the IEA steel has been deformed up to about 0.02 plastic strain and than deformed at a lower temperature. The second deformation curve at T_2 is compared to that of a single reference specimen tested only at T_2. The pre-deformation up to 0.02 plastic strain at T_1 does not influence the flow stress and/or the strain-hardening for deformation at T_2. Similar experiments performed between the temperatures T_1-T_2 equal to 293K-223K and 223K-123K showed no influence of pre-deformation. Thus, while the strain-hardening rate has been found slightly temperature sensitive, the flow stress appears to depend only on the existing deformation. This observation provides additional support to the conclusion that the temperature dependence of the strain-hardening is weak.

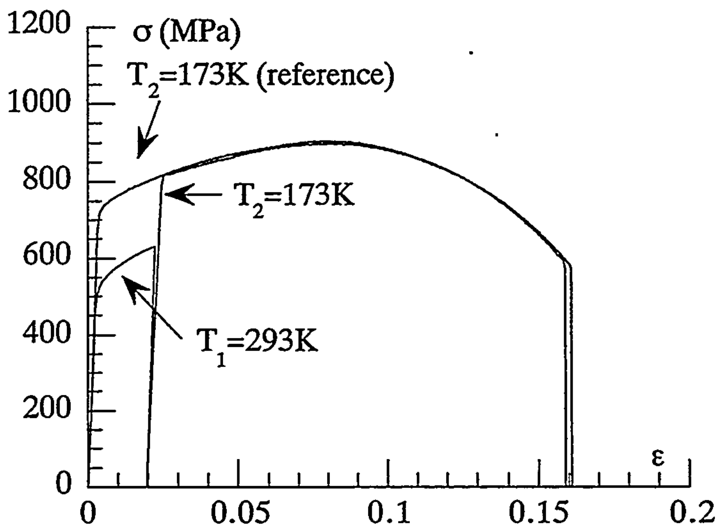

Figure 11: Cottrell-Stokes experiment between T_1=293K and T_2=173K, IEA steel

The strain-hardening law presented above is semi-empirical and the physical meaning of the parameters, K_1 and K_2, is not obvious, especially for a physical system as complex as a ferritic/martensitic steel. The most notable feature of the results is that this BCC alloy shows a strain hardening behavior that is FCC like in character, even at low temperatures. In low dislocation density BCC single crystals dislocation, strain hardening and dislocation interaction mechanisms are dominated by the formation and collapse of junctions at the intersection of bowed edge segments of otherwise straight screw dislocations. In this regime, junction collapse is controlled by the rate of jog nucleation on the straight screw segments [8]. This suggests that strain hardening should be strongly dependent on both temperature and strain rate. However, such mechanisms are only dominant if the overall dislocation density is sufficiently low, and if edge segments are not effectively stored. This is clearly not the case in complex structural alloys, such as F82H, where nascent dislocation densities exceed $10^{14}/m^2$ [9] and complex pinning point and boundary structures result in complex mixed screw and edge substructures.

Kocks [5] rationalized Voce curves for FCC metals and alloys by developing a phenomenological model of strain-hardening, based on the storage and dynamic annihilation of dislocations and derived a linear relation between the strain-hardening and the flow stress similar to Equation 2. In Kocks' model, K_1 is the term related to the storage rate of dislocations, depending on their mean free path while K_2 characterizes the dynamic dislocation annihilation. It has been experimentally shown that dislocation annihilation takes place even at low temperatures in both FCC and BCC metals [10]. The annihilation of the screw segments can occur by cross-slip owing to the strong elastic interaction [11] between them and the annihilation of non-screw segments can take place either by climb (only important at high temperature) or by spontaneous annihilation when the attractive elastic force between two dislocations on different glide planes exceeds the force required for dislocation climb [12,13]. Note, in the Kocks model, the key structure parameter is is the total dislocation density; the detailed distribution of dislocations and their evolution with strain are not treated. Given the complex structure of these steels more detailed models than that of Kocks should be evaluated. In particular, the evolution of the dislocation structure within the laths, the PAG and lath boundaries are likely to play important roles.

More advanced models have been developed to account for the evolution and reorganization of the dislocation structures up to large strain, e.g. [14-17]. For example, the recent cell structure-based (CSB) model of Fang and Dahl [16] yields a relation for the evolution of the dislocation density similar to that of Kocks by taking into account the reorganization of dislocations. They showed that Kocks' model is a simplification of their CSB model. In the context of their model, the physical significance of K_1 has to be related to the mean free path of the dislocation in the cell interior and in the trapping rate of mobile dislocations in the walls, while that of K_2 lumps together all the annihilation effects. The development of the microstructure as a function of strain, the influence of the size distribution of the carbides and the PAG size resulting from the initial heat treatment are a few examples of parameters whose influence on the flow stress and strain hardening needs to be investigated further.

Fracture toughness testing

As a part of an extensive study of the effect of specimen geometry and specimen size on fracture toughness, a series of fracture toughness tests were carried out on fatigue pre-cracked 0.18T compact tension (CT) specimens with a/W=0.5 and a specimen thickness (B) to width (W) ratio of B/W = 0.5. These are the same type of CT specimens which are also currently being irradiated in the Budapest Research Reactor as part of the MACE study. Thus the effective toughness, K_e, results reported here constitute a baseline for the unirradiated material. The typical brittle to ductile transition curve obtained in the lower shelf region is presented on Figure 12, where the typical and inherent large scatter is observed. All specimens failed by quasi-cleavage, in some cases after a large amount of plastic deformation and crack blunting, resulting in the so-called "loss of constraint". Constraint loss is primarily associated with plasticity encompassing a large fraction of the uncracked ligament of length, b. The degree of such in plane constraint loss can be generally characterized by a non-dimensional constraint parameter M as

$$M = b\sigma_y E / K_e^2$$

where E' is the plane strain elastic modulus. For this specimen geometry, values of M greater than about 75 are sufficient to ensure relatively high constraint. Thus in this case the maximum valid toughness that can be measured where $K_e \approx K_{Jc}$ is about 90 MPa√m. Below this value, contraint loss initially occurs gradually, with K_e increasing roughly as $M^{-1/4}$ [18]. At temperatures higher than 180K, a clear lateral contraction of the specimens near the crack tip was observed suggesting additional out-of-plane constraint loss. In this regime both in-plane (controlled by b) and out of plane (controlled by B and side grooving) constraint rapidly diminishes approaching plane stress conditions.

The effective fracture toughness data of the 0.18T CT specimens can be compared to previous results on precracked 20% sidegrooved 0.2T three point bend bars (3PB) [19], with a/W ≈ 0.5 and B/W = 1, shown as the open symbols in Figure 12. Clearly the effective toughness measured by the 3PB specimens is much lower than that found in the recent CT tests.

Figure 13 shows both sets of data corrected to small scale yielding (ssy) values based on three dimensional FEM calculations of Nevalaien and Dodds [20]. The correction is determined by calculating the large scale to small scale yielding ratio of the J/J_{ssy}, required to produce the same area within a specified non-dimensional principal stress (σ_p) contour normalized by the yield stress, $R = \sigma_p/\sigma_y$. The magnitude of the correction for a given M factor depends on the particular specimen geometry, alloy constitutive law and R. The small scale yielding estimates are given by $K_{Ic} \approx K_e/(J/J_{ssy})^{0.5}$. In this case R was taken as 3 and the strain-hardening exponent was assumed to be 0.1. The ssy values are similar, although the CT data still fall somewhat above those for the 3PB specimens.

While providing a reasonably consistent estimate of K_{Ic} from both specimen sets, the results do not fully explain the separation of the uncorrected data. There are several possible explanations including some combination of:

- Weakest link-type statistical effects associated with the crack front length which is roughly 2.8 larger for the 3PB compared to the CT specimens.
- The maintenance of greater lateral constraint for the 3PB specimens with W/B = 1.
- Details of the side grooving.
- Material inhomogeniety.

Unfortunately it is not possible to determine which, or which combination, of these effects may be responsible. Further testing and analysis is planned to clarify this issue.

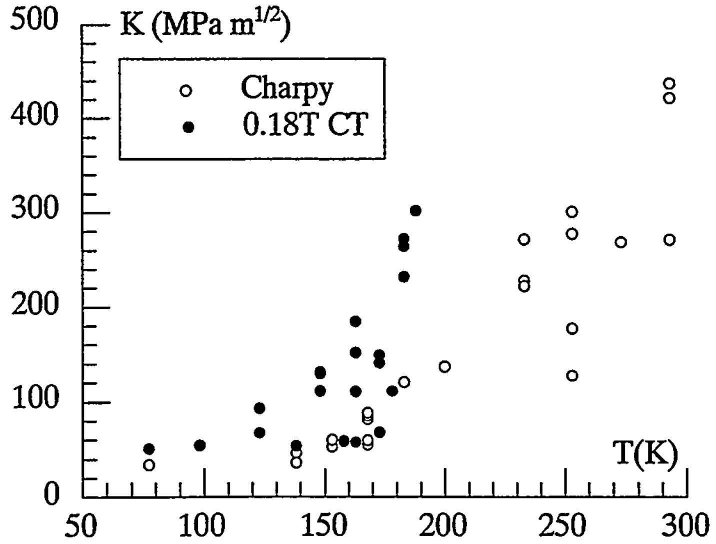

Figure 12: Fracture toughness measured with 0.18T CT and 3PB specimens

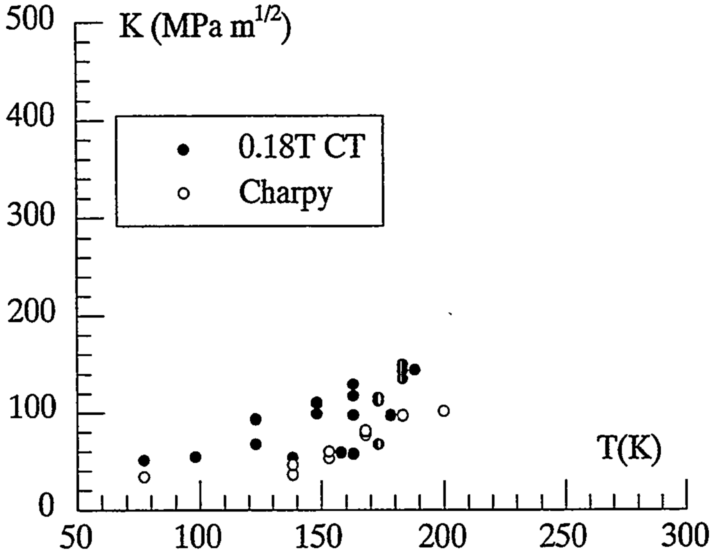

Figure 13: Constraint corrected fracture toughness measured with 0.18T CT and 3PB specimens

MACE status

The first irradiation of the IEA steel specimens started in April 1999 at the Budapest Research Reactor KFKI AEKI. The test matrix is described elswhere [21]. The initial irradiation was carried out at 250°C for 768 hours which is estimated to yield the target dose of 0.5 dpa. Dosimetry capsules are being analyzed to confirm the preliminary estimates and, if necessary the capsule will be re-inserted for a time needed to reach the target exposure. Following irradiation the capsule will be shipped to the PSI for testing in their hot cells. Two additional sets of specimens are now being prepared at UCSB for irradiation at 250°C to 1 dpa and at 350°C to 0.5 dpa.

REFERENCES

[1] P. Spätig, E. Donahue, G. R. Odette, G. E. Lucas, J. Nucl Mat., ICFRM9 Proceedings, in preparation.

[2] P. Spätig, G. R. Odette, G. E. Lucas, J. Nucl Mat. (1999) accepted.

[3] H. Mecking, "Work Hardening in Tension and Fatigue", Ed. A. W. Thompson, p. 67 Am. Inst. Min. Engrs, N.Y. (1977).

[4] E. Voce, J. Inst. Metals, 74 (1968) 537.

[5] U. F. Kocks, ASME J. Eng. Mater. Technol., 98 (1976) 72.

[6] K. Edsinger, PhD Thesis, University of California, Santa Barbara, 1995, p.115

[7] A. H. Cottrell, F. R. S. and R. J. Stokes, Proc. R. Soc. A 233, (1955) 17.

[8] M. Tang, B. Devincre, L. P. Kubin to appear in Model. Simul. Mater. Sci. Eng.

[9] R. Schäublin, P. Spätig, M. Victoria, J. Nucl. Mater. 258-263 (1998) 1178.

[10] U. Essmann, H. Mughrabi, Phil. Mag. A, 40 No 6 (1979) 731.

[11] U. Essmann, Acta Metall., 12 (1964) 1468.

[12] J. Friedel, "Dislocations", Ed. Pergamon Press, London, (1964).

[13] U. Essmann, M. Rapp, Acta Metall. 21 (1973) 1305.

[14] X. F. Fang, W. Dahl, Mater. Sci. Engng. A203 (1995) 14.

[15] X. F. Fang, C. O. Gusek, W. Dahl, Mater. Sci. Engng. A203 (1995) 26.

[16] X. F. Fang, W. Dahl, Mater. Sci. Engng. A203 (1995) 36.

[17] Y. Estrin, L. S. Tóth, A. Molinari, Y. Bréchet, Acta Met. 46 No 15 (1998) 5509.

[18] H. J. Rathnun, G. R. Odette, G. E. Lucas, M. Y. He, J. W. Sheckerd, Proceedings of ASME Pressure Vessels and Piping Conference, Boston 1999, to appear.

[19] G. R. Odette, K. Edsinger, G. E. Lucas, E. Donahue, Small Specimen Test Techniques, ASTM STP 1329, American Society for Testing and Materials (1998) p. 298

[20] M. Nevalainen, R. H. Dodds, Inter. J. Fracture, 74 (1995) 131.

[21] Odette, G.R., Lucas, G.E., Spatig, P., DOE/ER-0313/25, Department of Energy (1999) 119-124

MICROSTRUCTURE OF ISOTOPICALLY-TAILORED MARTENSITIC STEEL HT9 IRRADIATED AT 400°C TO 7 DPA IN HFIR - N. Hashimoto, J.P. Robertson (Oak Ridge National Laboratory), and K. Shiba (Japan Atomic Energy Research Institute)

OBJECTIVE

The objective of this work is to generate TEM data for isotopically-tailored martensitic steel HT9 irradiated in the temperature range for swelling.

SUMMARY

The microstructures of reduced-activation martensitic steel, HT9-std. (12Cr-1MoVW) and HT9 doped with ^{58}Ni and ^{60}Ni, irradiated at 400°C to 7 dpa in the High Flux Isotope Reactor (HFIR), were investigated by transmission electron microscopy. No cavities were observed in any alloys. Irradiation-induced a_0<100> and $(a_0/2)$<111> type dislocation loops were observed in all alloys; the number density and the mean diameter of a_0<100> type loops were higher and larger than that of $(a_0/2)$<111> type loops. Also, there was a tendency for the number density of loops in the HT9 doped with ^{60}Ni to be lower than those in the other alloys. Irradiation-induced precipitates were observed in all alloys, which were identified as $M_6C(\eta)$ type carbide, α' phase and M_2X phase. The $M_6C(\eta)$ type carbides and α' phase were formed along dislocation loops, suggesting that dislocation loops are sites of Cr segregation during irradiation and that Cr segregation plays an important role in the precipitation behavior in martensitic steels.

PROGRESS AND STATUS

1. Introduction

Ferritic/martensitic steels are attractive candidate structural first wall materials for fusion energy systems [1]. The high-energy neutrons produced by the D-T fusion reaction induce displacement damage and generate gas atoms in the materials from (n,p) and (n,α) reactions. Simultaneous production of helium atoms from (n,α) reactions is considered to strongly influence the nucleation processes of cavities. To clarify the effect of helium atoms on the microstructural development and mechanical property change in martensitic steels under fast neutron irradiation, HT9 (12Cr-1MoVW) and HT9 doped with ^{58}Ni and ^{60}Ni were irradiated with neutrons in the High Flux Isotope Reactor (HFIR). Irradiation of ^{58}Ni-doped alloys in a mixed spectrum reactor like the HFIR results in the following transmutation reaction with the thermal neutrons: $^{58}\mathrm{Ni}(n,\gamma)^{59}\mathrm{Ni}(n,\alpha)^{56}\mathrm{Fe}$. The concept of isotopic tailoring to separate the individual effects of Ni and helium on microstructural development was described earlier [2-4]. The specimens examined here are part of an experiment conceived 10 years ago by researchers at ORNL, UCSB and PNNL and irradiated under the US/JAERI collaborative irradiation program. Another part of this experiment utilizing ^{60}Ni and ^{59}Ni doping was described earlier by D.S. Gelles [5].

2. Experimental Procedure

HT9, and HT9 doped with ^{58}Ni and ^{60}Ni were included in this experiment; the compositions and heat treatment are given in Table 1. Standard 3-mm diameter transmission electron microscopy (TEM) disks were punched from 0.25-mm thick sheet stock. Irradiation was carried out at 400°C in the capsules of HFIR-MFE-JP-20 in the High Flux Isotope Reactor (HFIR) to a neutron fluence of ~ 5.16×10^{25} n/cm^2 (E> 0.1 MeV), resulting in a displacement dose of ~ 7.4 dpa. The details of the design, construction, and installation of JP-20 have been reported [6-9]. The irradiation conditions and the calculated helium concentrations in the steels are given in Table 2.

Table 1. Chemical compositions of the specimens (wt%) (Balance Fe) and heat treatment.

Steel	Cr	^{n}Ni	^{58}Ni	^{60}Ni	Si	C	N	Mn	W	V	Nb	Mo
HT9-std.	12.0	0.5	-	-	0.18	0.20	0.02	0.5	0.5	0.3	0.01	1.0
HT9-1.4wt%^{58}Ni	12.0	-	1.4	-	0.18	0.20	0.02	0.5	0.5	0.3	0.01	1.0
HT9-0.5wt%^{60}Ni	12.0	-	-	0.5	0.18	0.20	0.02	0.5	0.5	0.3	0.01	1.0
HT9-1.4wt%^{60}Ni	12.0	-	-	1.4	0.18	0.20	0.02	0.5	0.5	0.3	0.01	1.0

Heat treatment: 1050°C/1 h/ AC + 780°C/2.5 h/ AC

Table 2. Irradiation conditions and helium concentration.

	dpa	appm He	He/dpa
HT9-std.	7.4	10	1.3
HT9-1.4wt%^{58}Ni	7.4	40	5.2
HT9-0.5wt%^{60}Ni	7.4	-	-
HT9-1.4wt%^{60}Ni	7.4	-	-

TEM specimens were thinned using an automatic Tenupol electropolishing unit located in a shielded glove box. TEM disks were examined using a JEM-2000FX (LaB_6) transmission electron microscope equipped with a special objective lens polepiece that lowers the magnetic field at the ferro-magnetic specimen. The foil thicknesses were measured by thickness fringes in order to evaluate quantitative defect density values.

3. Results and discussion

3.1 Dislocations and dislocation loops

During irradiation of Fe-Cr binary alloys, dislocation evolution in an initially almost dislocation-free condition proceeds by the formation of interstitial type dislocation loops with an a_0<100> and/or (a_0/2)<111> Burgers vector [10,11]. Figure 1 shows the dislocation segments and loops in the HT9 alloys after irradiation at 400°C to 7.4 dpa using the diffraction conditions: **g**=110, (**g**,4**g**). Table 3 summarizes the quantitative results of dislocation loops. In all of the alloys, there is a tendency for the number density of irradiation-induced a_0<100> and (a_0/2)<111> type dislocation loops in HT9-std. and HT9 doped with ^{58}Ni to be higher than those in the HT9 doped with ^{60}Ni. This suggests that the existence of helium generated by the (n,α) reaction with the thermal neutrons assists the nucleation of dislocation loops in these alloys. On the other hand, the number density and the mean diameter of a_0<100> type loops in all alloys are higher and larger than that of (a_0/2)<111> type loops, respectively. According to a previous paper which investigated a relationship between the type of dislocation loop and the content of interstitial impurities [12], there is a tendency for a_0<100> type loop to form in alloys which have high concentrations carbon and nitrogen, which is true for the alloys used in this study.

Table 3. The summary of dislocation loops in alloys after irradiation at 400°C to 7.4 dpa in HFIR.

Steel	a_0<100> type loops		(a_0/2)<111> type loops	
	Number density (m^{-3})	Mean diameter (nm)	Number density (m^{-3})	Mean diameter (nm)
HT9-std.	1×10^{22}	14	3×10^{21}	10
HT9-1.4wt%^{58}Ni	1×10^{22}	16	5×10^{21}	8
HT9-0.5wt%^{60}Ni	9×10^{21}	10	4×10^{21}	9
HT9-1.4wt%^{60}Ni	5×10^{21}	16	2×10^{21}	10

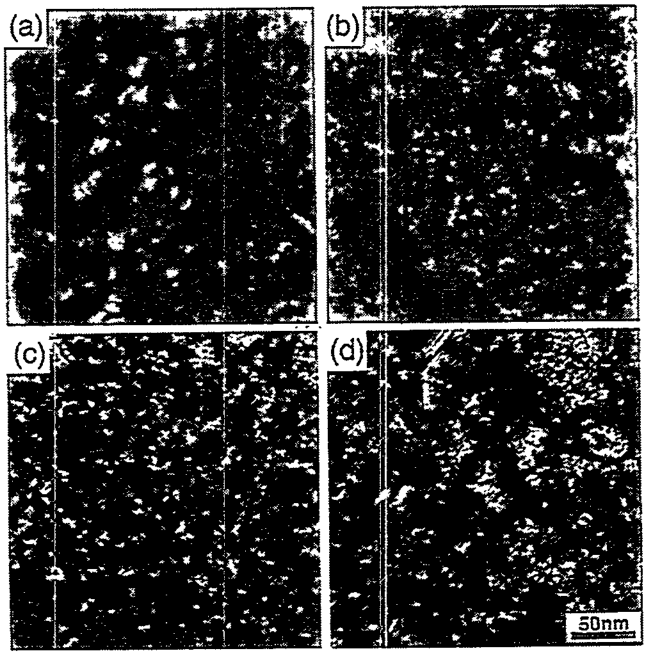

Figure 1 Dislocation segments and loops in (a) HT9-std., (b) HT9-1.4wt%^{58}Ni, (c) HT9-0.5wt%^{60}Ni and (d) HT9-1.4wt%^{60}Ni after irradiation at 400°C to 7.4 dpa using the diffraction conditions: g=110, (g,4g).

3.2 Cavities

Cavities were not observed in any of the alloys irradiated at 400°C to 7.4 dpa in HFIR. This suggests that the irradiation dose in this study was not sufficient to generate visible cavities in these steels.

3.3 Precipitates

Before irradiation, the alloys used in this study include $M_{23}C_6$ precipitates on grain boundaries with the number density and the mean diameter of about $6x10^{19}$ m^{-3} and 75 nm, respectively. The irradiation produced precipitates in the matrix and/or along dislocation loops in all alloys. The spacing of moiré fringes was used to identifiy two of the irradiation-produced precipitates, which were identified as $M_6C(\eta)$-type carbides and M_2X phase. Figures 2 and 3 show the irradiation-induced $M_6C(\eta)$-type carbides in the alloys and M_2X phase in the HT9-1.4wt%^{60}Ni alloy after irradiation at 400°C to 7.4 dpa, respectively. Precipitation of a Cr-rich $M_6C(\eta)$ has been observed in a number of 8-12Cr steels that contain > 0.3wt% Ni during FBR (Fast Breeder Reactor) and HFIR irradiation at about 400°C [13-16]. The M_2X phase was observed in 9Cr-1MoVNb-2Ni and 12Cr-1MoVW steels irradiated in HFIR at 500°C and in 9Cr-1MoVNb steel irradiated in FFTF (Fast Flux Test Facility) at 407°C [13]. XEDS compositional analysis has shown that this phase is composed of mainly Cr and N [13,14]. In addition, another type of precipitate was found along dislocation loops without moiré fringes, which was tentatively identified as α'-phase, which is a Cr-rich body-centered cubic (bcc) ferrite phase. A high density (> $x10^{22}$ m^{-3}) of α' was reported to occer in HT9 steel irradiated in the FFTF at 420°C [17]. In the present study, the M_2X phase was observed only in HT9-1.4wt%^{60}Ni alloy, while the $M_6C(\eta)$ carbides and α'-phase were found along dislocation loops in all alloys, as shown in Figure 2. The number density of $M_6C(\eta)$ carbides and α'-phase in HT9-1.4wt%^{60}Ni alloy were lower than that in the other alloys. As mentioned in section 3.1, the HT9-1.4wt%^{60}Ni alloy showed a lower number density of dislocation loops than that in the other alloys. This results suggests that dislocation loops act as sites of Cr segregation during irradiation and play important roles in the precipitation behavior in martensitic steels. Table 4 summarizes the quantitative results of precipitates.

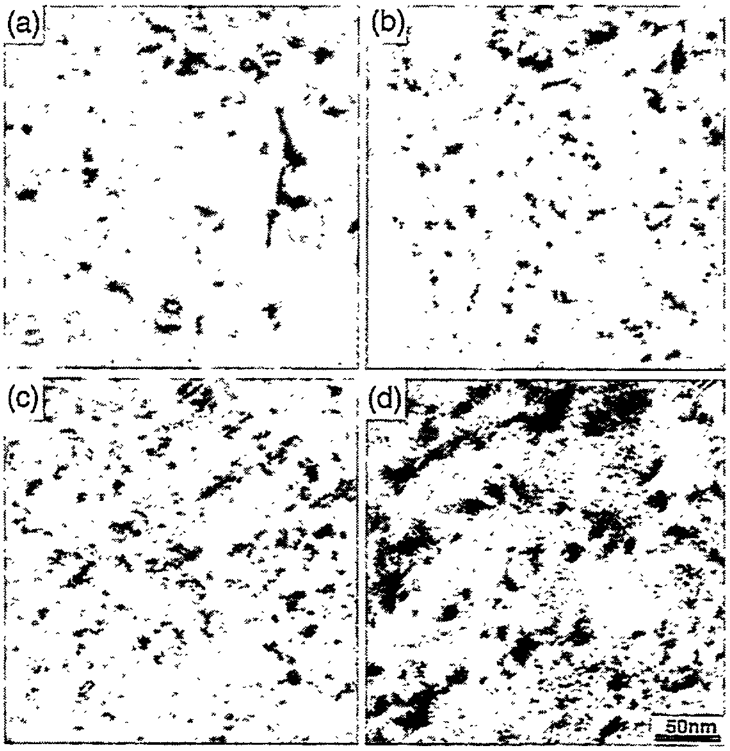

Figure 2 Irradiation-induced precipitates in (a) HT9-std., (b) HT9-1.4wt%^{58}Ni, (c) HT9-0.5wt%^{60}Ni and (d) HT9-1.4wt%^{60}Ni after irradiation at 400°C to 7.4 dpa

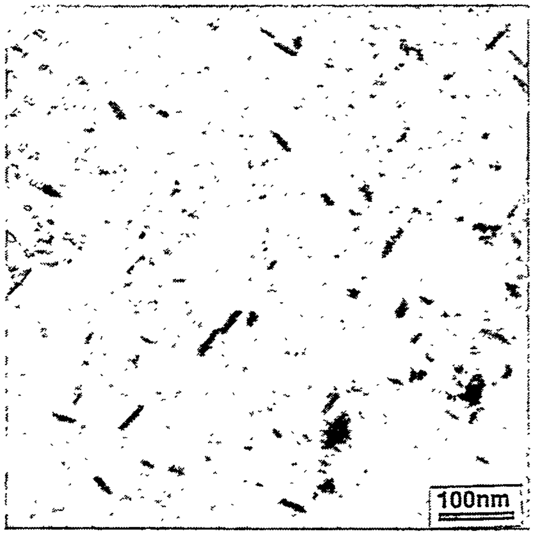

Figure 3 Irradiation-induced M_2X phase in the HT9-1.4wt%^{60}Ni alloy after irradiation at 400°C to 7.4 dpa.

Table 4. Summary of precipitates in the alloys after irradiation at 400°C to 7.4 dpa.

Steel	$M_{23}C_6$		$M_6C(\eta)$		α'		M_2X	
	Mean Size (nm)	Number Density (m^{-3})	Mean Size (nm)	Number Density (m^{-3})	Mean Size (nm)	Number Density (m^{-3})	Mean Size (nm)	Number Density (m^{-3})
HT9-std.	75	6×10^{19}	6	2×10^{21}	4	4×10^{21}	-	-
HT9-1.4wt%^{58}Ni	75	6×10^{19}	7	2×10^{21}	4	3×10^{21}	-	-
HT9-0.5wt%^{60}Ni	75	6×10^{19}	6	2×10^{21}	4	3×10^{21}	-	-
HT9-1.4wt%^{60}Ni	75	6×10^{19}	10	1×10^{21}	5	2×10^{21}	30	1×10^{21}

FUTURE WORK

The investigation of isotopically-tailored martensitic steels irradiated at 400°C to about 18 dpa in HFIR will be carried out to clarify the effect of helium atoms and Ni on the formation of cavities and the microstructural development.

ACKNOWLEDGMENTS

The authors are grateful to Drs. R.L. Klueh, S.J. Zinkle and A.F. Rowcliffe for their helpful discussions. They also would like to thank L.T. Gibson and A.T. Fisher for preparation of specimens for microstructural examination, and J.J. Duff and members of hot laboratory in Oak Ridge National Laboratory for technical support. This research was supported in part by an appointment to the Oak Ridge National Laboratory Postdoctoral Research Associates Program administered jointly by the Oak Ridge Institute for Science and Education and Oak Ridge National Laboratory, and sponsored by the Office of Fusion Energy Sciences, U.S. Department of Energy, under contact DE-AC05-96 OR22464 with Lockheed Martin Energy Research Corp., and the Japan Atomic Energy Research Institute.

REFERENCES

1) R.L. Klueh, K. Ehrlich, and F Abe, J. Nucl. Mater. **191-194** (1992) 116.
2) R.L.Simon, DAFS Quarterly Progress Report, DOE/ER0046/12, p. 37, 1983
3) L.K. Mansur et al, J. Nucl. Mater. **139** (1986) 228
4) G.R. Odette, J. Nucl. Mater. **141-143** (1986) 1011
5) D.S. Gelles, Fusion Materials Semiannual Progress Report for Period Ending June 30 1996, DOE/ER-0313/20, 1996, p. 199
6) J.E. Pawel and R.L. Senn, "Status of U.S./Japan Collaborative Program Phase2 HFIR Target Capsules", Fusion Reactor Materials Semiannual Report for Period Ending March 31, 1995, DOE/ER-0313/12, 1992, p. 15.
7) J.E. Pawel, A.W. Longest, R.L. Senn, K. Shiba, D.W. Heatherly, and R.G. Sitterson, "Status of U.S./Japan Collaborative Program Phase2 HFIR Target and RB* Capsules", Fusion Reactor Materials Semiannual Report for Period Ending September 30, 1993, DOE/ER-0313/15, 1992, p. 3.
8) J.E. Pawel, K. E. Lenox and I. Ioka, "Status of U.S./Japan Collaborative Program Phase2 HFIR Target and RB* Capsules", Fusion Reactor Materials Semiannual Report for Period Ending March 31, 1995, DOE/ER-0313/18, 1995, p. 3.
9) L.R. Greenwood and C.A. Baldwin, "Neutron Dosimetry and Damage Calculations for The HFIR-JP-20 Irradiation", Fusion Reactor Materials Semiannual Report for Period Ending December 31, 1997, DOE/ER-0313/23, 1997, p. 305.
10) N. Yoshida, et al., J. Nucl. Mater., **155-157** (1988), 1232.
11) D.S. Gelles, Annual Progress Report for Fusion Year, (1991), 348.
12) E. Wakai et al., Proceeding of Ultra High Purity Base metals, UHPM-94, 488.

13) E.A. Little and L.P. Stoter, Effects of Radiation on Materials: 11th Conf., ASTM STP-782 (American Society for Testing and Materials, Philadelphia, 1982) p. 207.
14) P.J. Maziasz, R.L. Klueh and J.M. Vitek, J. Nucl. Mater. **141-143** (1986) 929.
15) P.J. Maziasz and R.L. Klueh, Effects of Radiation on Materials: 14th Conf., ASTM STP-1046 (American Society for Testing and Materials, Philadelphia, 1989) p. 35.
16) P.J. Maziasz, J. Nucl. Mater. **169** (1989) 95-115.
17) J.J. Kai and R.L. Klueh, J. Nucl. Mater. **230** (1996) 116-123

TENSILE PROPERTIES OF LOW ACTIVATION FERRITIC STEELS FOLLOWING IRRADIATION IN ORR - M. L. Hamilton, and D. S. Gelles (Pacific Northwest National Laboratory)

OBJECTIVE

The objective of this effort is to determine irradiation hardening response in low activation ferritic steels following irradiation at temperatures below 400°C in order to better understanding behavior in this alloy class at low irradiation temperatures.

SUMMARY

Post-irradiation tensile test results are reported for a series of low activation steels containing Mn following irradiation in the Oak Ridge Reactor at 60, 200, 330 and 400°C to 10 dpa. Alloy compositions included 2Cr, 9Cr and 12Cr steels with V to 1.5% and W to 1.0%.

Strength increases were higher in all alloys for irradiation conditions below 400°C, with peak hardening occurring following irradiation at 200°C, corresponding to a minimum of 4% total elongation. The 9Cr alloy class exhibited the smallest increases in hardening. Test results are provided and compared with behavior following irradiation in FFTF.

PROGRESS AND STATUS

Introduction

Post-irradiation tensile test response has been reported for a series of alloys containing manganese following irradiation in FFTF at 420 and 585°C to 15 and 45 dpa.[1] That work investigated the response of a series of alloys including 2% Cr alloys with V additions, and 9% and 12% Cr alloys containing Mn with V and W additions. It was found that irradiation at 420°C to 15 dpa produced significant hardening in the 2Cr alloys whereas the other alloys where unaffected, and irradiation at 585°C produced softening for all alloys. Further irradiation to 45 dpa resulted either in little change or in softening. Similar specimens irradiated in ORR at 60, 200, 330 and 400°C to 10 dpa were recently retrieved; the tensile data obtained from these specimens are documented in this report.

Experimental Procedure

Compositions and identification codes for specimens irradiated in the ORR-MFE 6J and 7J tests are provided in Table 1. Specimens were of SS-3 flat tensile geometry, with nominal gauge dimensions of 0.3" x 0.030" x 0.060" (7.62 mm x 0.76 mm x 1.5 mm). Tests were performed at both room temperature and the nominal irradiation temperatures. The initial strain rate was 4 x 10^{-4} /sec. The 6J test accumulated a midplane fluence of 2.4 x 10^{22} n/cm^2 (total) or 8.8 x 10^{21} n/cm^2 (E>0.1 MeV) and the 7J test accumulated a fluence of 2.7x 10^{22} n/cm^2 (total) or 9.5 x 10^{21} n/cm^2 (E>0.1 MeV).[2,3] This corresponds to damage levels of 6.6 - 6.8 and 7.1 - 7.3 dpa respectively, variations corresponding to lower or higher chromium levels. Predicted helium levels are 2.1 to 2.3 for both tests, with variations due to higher or lower chromium levels, respectively.

Table 1. Compositions and identification codes for specimens irradiated in the ORR-MFE 6J and 7J tests.[1]

ID code	Heat # or alloy name	Composition (w/o)								
		Cr	V	W	Ta	Mo	C	Mn	Nb	Ni
TE	V02262	2.25	0.5				0.1			
TZ	UC-19	2.25	1.5			0.2	0.1	0.3		
TH	V02263	2.25	1.0				0.1			
	2.25Cr1Mo	2.25	0.03			1.0	0.1	0.5		
TR	V02268	9	0.3	1.0			0.1	2.5		
TM	V02264	9	0.5				0.1			
TP	V02266	9	0.5				0.1	2.0		
TN	V02265	9	1.3				0.2	1.0		
	9Cr1Mo	8.75	0.2			0.9	0.1	0.5	0.08	
TT	V02702	12	0.2	0.8			0.1	6.5		
TU	V02269	12	0.3	1.0			0.1	6.5		
TW	V02754	12	0.3	1.0	0.2		0.1	6.5		
TL	V02267	12	1.0				0.1	6.5		
TF	V02700	12	1.0				0.1	6.5		
TX	V02755	12	1.0	0.2	0.2		0.1	8.0		
	HT9	12	0.3	0.5		1.0	0.2	0.6		0.5

Results

The tensile results are given in Table 2 and plotted in Figures 1 - 8. Significant hardening and loss of ductility were observed at room temperature in all three alloy classes for irradiation at 330°C and below. Similar trends were observed in tests conducted at the irradiation temperature, although the results are less well-defined because of the paucity of data on unirradiated material.

Discussion

Tensile data obtained on FFTF-irradiated specimens were comparable to the data obtained for specimens irradiated in ORR under similar conditions. These results were obtained for all materials where such a comparison was possible, for specimens irradiated at about 400°C to 10 dpa and tested at room temperature. Such a comparison was not possible for all of the alloys. Yield and ultimate strengths, and uniform and total elongations, were essentially the same as the comparable data provided in reference 1 for two of the 2Cr alloys (TE [V02262] and TZ[UC-19]), four of the 9Cr alloys (TN[V02265], TR[V02268], TP[V02266] and TM[V02264]), and a single 12Cr alloy (TU[V02269]).[1] The 9Cr alloys exhibit the most stable properties, and significant hardening can occur following irradiation at low temperatures. The ORR database indicates that property degradation is worst following irradiation at 200°C, but irradiation at 60°C produces similar behavior for the 12Cr alloys. However, it can be anticipated that irradiation to higher dose at 60°C can be expected to degrade properties further,[4] and therefore it appears worthwhile to continue this work by testing identical specimens from ORR that were further irradiated in HFIR.

Table 2. Tensile results on low activation steel specimens following irradiation in ORR.

ID	Dose (dpa)	Thick-ness (mils)	Width (mils)	Irr Temp (C)	Test Temp (C)	YS (MPa)	UTS (MPa)	UE (%)	TE (%)	Comments*
TE22	0	28.74	51.65	0	22	791	886	4.6	13	
TE23	0	29.49	53.33	0	22	769	870	3.4	11.5	Rusty
TE17	10	29.24	53.49	200	22	1315	1345	0.6	4	RP, some rust
TE11	10	29.97	49.99	330	22	1367	1412	0.8	5.8	RP, small P
TE13	10	29.26	51.80	400	22	1198	1230	0.8	6.9	RP?, rusty
TF11	10	28.47	53.66	330	22	954	997	1.4	8.1	Rusty
TF15	10	28.52	52.30	400	22	828	912	3.8	10.4	
TF12	10	27.66	53.81	330	330	787	832	1.2	6	Semi RP, rusty
TF16	10	28.49	55.67	400	400	665	728	1.6	6.7	Rusty
TH09	0	29.02	59.87	0	22	328	532	14.4	28.7	Large bow
TH10	0	29.29	59.16	0	22	345	538	11.9	24.2	Slight bow
TL25	0	29.32	58.70	0	22	761	911	3.2	11.1	P
TL16	10	29.26	57.29	60	22	1073	1114	0.7	5.4	RP, some rust
TL19	10	29.07	56.54	200	22	1203	1255	1	6.8	RP, some rust
TL11	10	29.52	59.47	330	22	970	1004	3	10.8	P
TL13	10	29.34	59.79	400	22	719	846	7.1	15.3	Small P, rusty
TL17	10	29.99	59.61	60	60	1012	1053	0.8	6.5	RP, some rust
TL20	10	28.87	59.47	200	200	1072	1141	1	6.1	RP, some rust
TM25	0	28.89	55.67	0	22	565	646	4.3	15.4	P
TM19	10.4	28.99	61.31	200	22	918	920	0.2	9	RP, some rust
TM11	10.4	29.37	61.88	330	22	879	883	0.3	9.6	RP
TM13	10.4	29.22	62.53	400	22	584	640	3.5	15.4	Rusty
TM26	0	28.89	55.40	0	200	512	566	1.9	12.4	RP
TM22	10	28.79	55.09	200	200	845	851	0.2	9.2	RP, rusty
TN09	0	29.54	60.49	0	22	538	665	7.2	18.7	P
TN10	0	29.02	60.31	0	22	559	688	6.8	17.4	P
TN19	10.2	28.96	59.16	200	22	998	1005	0.4	7.8	RP, rusty
TN11	10.2	29.41	59.11	330	22	917	933	0.6	8.9	RP, rusty
TN13	10.2	29.76	62.22	400	22	504	618	7.4	20.1	P, rusty

ID	Dose (dpa)	Thick-ness (mils)	Width (mils)	Irr Temp (C)	Test Temp (C)	YS (MPa)	UTS (MPa)	UE (%)	TE (%)	Comments*
TP16	10	28.21	62.62	60	22	899	901	0.3	5.5	RP, rusty
TP19	10	29.44	63.03	200	22	1021	1030	0.4	7.5	RP, rusty
TP11	10	29.37	63.00	330	22	960	971	0.5	8.1	RP, some rust
TP13	10	29.29	62.88	400	22	565	643	5.1	17.8	P, rusty
TP17	10	29.39	62.88	60	60	770	773	0.3	5.1	RP, rusty, odd test
TP25	0	31.60	57.88	0	200	500	580	3.8	15.8	Small P
TP20	10	29.31	58.46	200	200	862	902	0.6	9.3	RP, rusty
TR10	9.8	28.82	59.84	200	22	1012	1030	0.5	8.7	RP
TR11	9.8	29.57	52.13	330	22	885	893	0.4	8.4	RP, some rust
TR15	9.8	29.76	54.98	400	22	576	673	6.2	16.6	P
TR22	10	29.07	58.03	200	200	909	918	0.4	9.2	RP
TR12	10	29.29	54.78	330	330	731	736	0.3	8.3	RP, rusty
TR08	0	29.79	59.94	0	400	443	518	2.6	12.8	Small P
TR16	10	29.52	53.91	400	400	468	520	2.1	11	RP, some rust
TT11	10	29.02	57.09	330	22	1016	1073	2.7	10.8	P, some rust
TT15	10	28.76	59.41	400	22	833	938	4.1	10.8	Rusty
TT12	10	28.56	58.14	330	330	828	890	1.3	6.3	Some rust
TT16	10	28.91	59.20	400	400	760	817	1.5	7.7	RP, some rust
TU07	10	28.47	60.22	60	22	1132	1174	0.7	7	RP, rusty
TU10	10	28.96	60.29	200	22	1189	1263	0.8	6.7	RP, some rust
TU11	10	30.02	59.57	330	22	1009	1066	1.4	7.8	Small P, rusty
TU15	10	29.77	59.15	400	22	755	888	5	10.2	Some rust
TU19	10	30.02	60.01	60	60	1010	1067	0.7	7	RP, rusty
TU22	10	28.91	53.84	200	200	1123	1204	1.1	4.2	Small P, some rust
TU12	10	30.09	55.35	330	330	846	912	1.7	6.5	Small P?, rusty
TU16	10	30.22	60.96	400	400	597	678	3	9.6	Small P, some rust
TW11	10	29.62	61.19	60	22	1100	1161	0.8	7.6	RP, rusty
TW14	10	29.05	61.12	200	22	1265	1304	0.8	7.3	RP, some rust
TW13	10	29.07	60.32	60	60	1099	1158	0.8	9.6	RP, rusty
TW15	10	28.79	60.54	200	200	1105	1170	1	6.5	RP, some rust

ID	Dose (dpa)	Thick-ness (mils)	Width (mils)	Irr Temp (C)	Test Temp (C)	YS (MPa)	UTS (MPa)	UE (%)	TE (%)	Comments*
TX12	10	31.30	58.78	60	22	1108	1138	0.5	4.9	RP, some rust
TX14	10	28.72	61.62	60	22	1235	1280	0.6	8.1	RP, rusty
TX15	10	29.15	58.20	200	22	1311	1377	0.9	7.7	RP, some rust
TX13	10	29.39	60.39	60	60	1139	1218	0.8	5.9	RP, rusty
TZ22	10	28.92	56.70	200	22	826	826	0	0	Failed without yielding; yield given as maximum/failure strength
TZ11	10	29.49	56.62	340	22	1014	1014	0	0	Failed without yielding; yield given as maximum/failure strength
TZ15	10	25.39	57.02	400	22	661	700	1.4	8.6	RP, rusty
TZ10	0	28.69	61.07	0	330	240	370	9.2	17.4	P
TZ12	10	26.36	56.29	330	330	872	875	0.4	5.1	RP
TZ25	0	28.27	56.79	0	400	334	437	4.5	13.6	
TZ16	10	28.67	56.87	400	400	598	612	0.4	6.3	RP

*The comment RP indicates that the specimen reached a peak load quite rapidly, with little work hardening. The comment P indicates that the load trace exhibited a load plateau at maximum load.

It has been noted that the alloy series being studied in this effort contains manganese additions for austenite stabilization, and that manganese additions are now understood to cause chi phase formation during irradiation in the vicinity of 400°C,[5] leading to embrittlement as evidenced by an increase in the DBTT.[6] It was therefore expected that the hardening observed in the 9 and 12Cr alloys at 330°C and below would also be due to precipitation of chi phase. Further evaluation of the results in Table 2 (see Figure 9), however, shows that no direct correlation exists between irradiation hardening and Mn content and the hardening observed at 330°C and below must be due to something other than chi phase formation. It must also be concluded that the correlation of DBTT with Mn content is due to the effect of chi phase on toughness per se rather than hardening.

CONCLUSIONS

ORR and FFTF irradiation under comparable conditions (400°C, to ~10 dpa) appear to produce similar changes in tensile behavior for a series of low activation alloys containing Mn additions. Significant hardening and loss of ductility resulted from irradiation at temperatures ranging from 60 to 330°C. The hardening cannot be attributed directly to Mn additions, indicating that chi phase does not cause the hardening. The cause of the observed hardening is not yet understood.

FUTURE WORK

Companion TEM specimens will be shear punch tested and examined by TEM using 1 mm specimen preparation techniques. Effort is then expected to shift to acquisition and testing of the ORR specimens further irradiated in HFIR.

REFERENCES

1. D. S. Gelles and M. L. Hamilton, J. Nucl. Mater., V 148, (1987) 272, or DOE/ER-0045/16 (1986) 131.

2. L. R. Greenwood, DOE/ER-0313/6 (1989) 23.

3. L. R. Greenwood, DOE/ER-0313/8 (1990) 34.

4. W. L. Hu and D. S. Gelles, Influence of Radiation on Material Properties: 13th International Symposium, ASTM STP-956 (1987) 83.

5. D. S. Gelles and W. L. Hu DOE/ER-0313/1 (1986) 251.

6 M. L. Hamilton, L. E. Schubert and D. S. Gelles, Effects of Radiation on Materials: 18th International Symposium, ASTM STP 1325 (1999) 931.

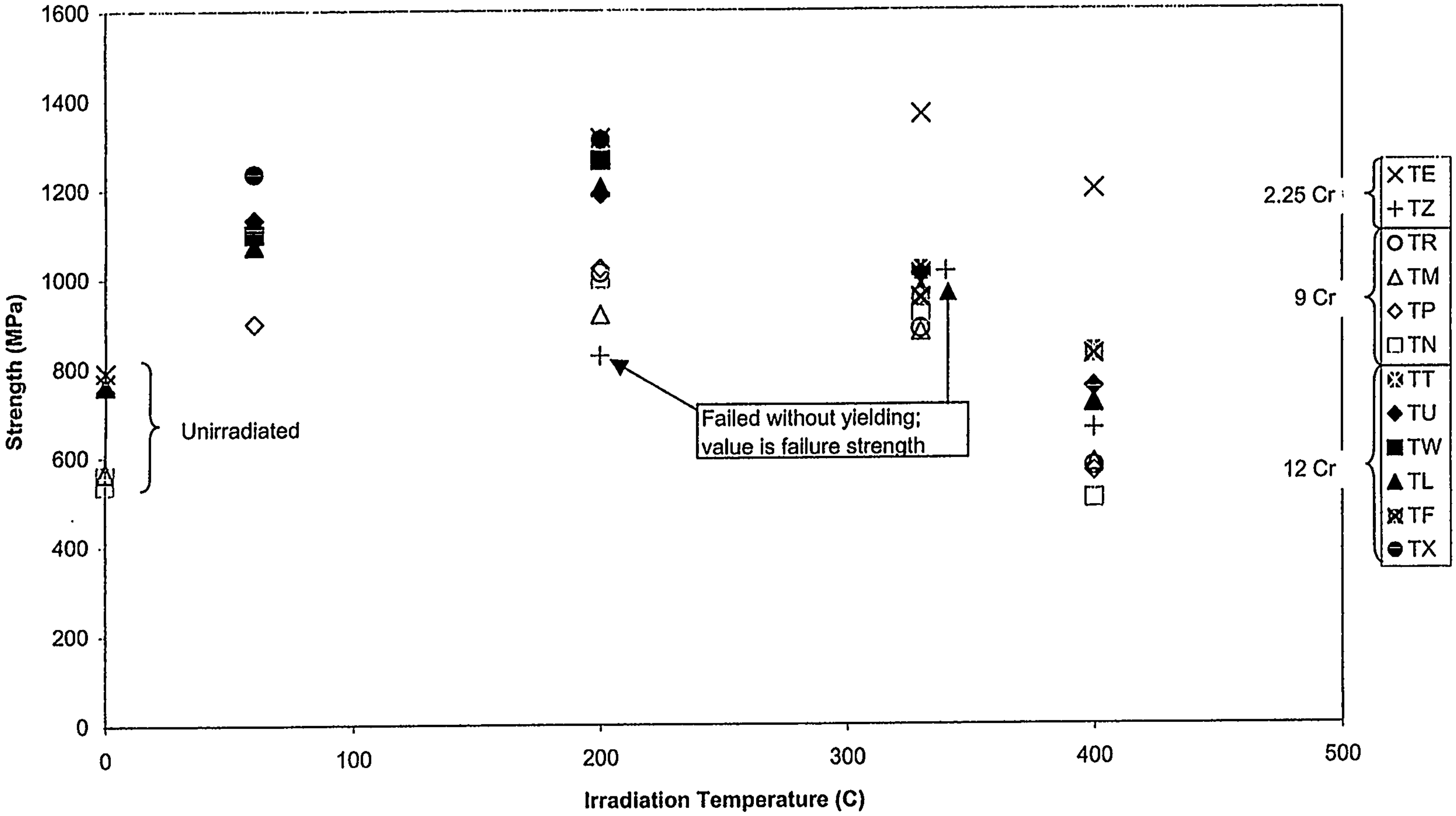

1. Yield strength of low activation alloys at room temperature after irradiation in ORR.

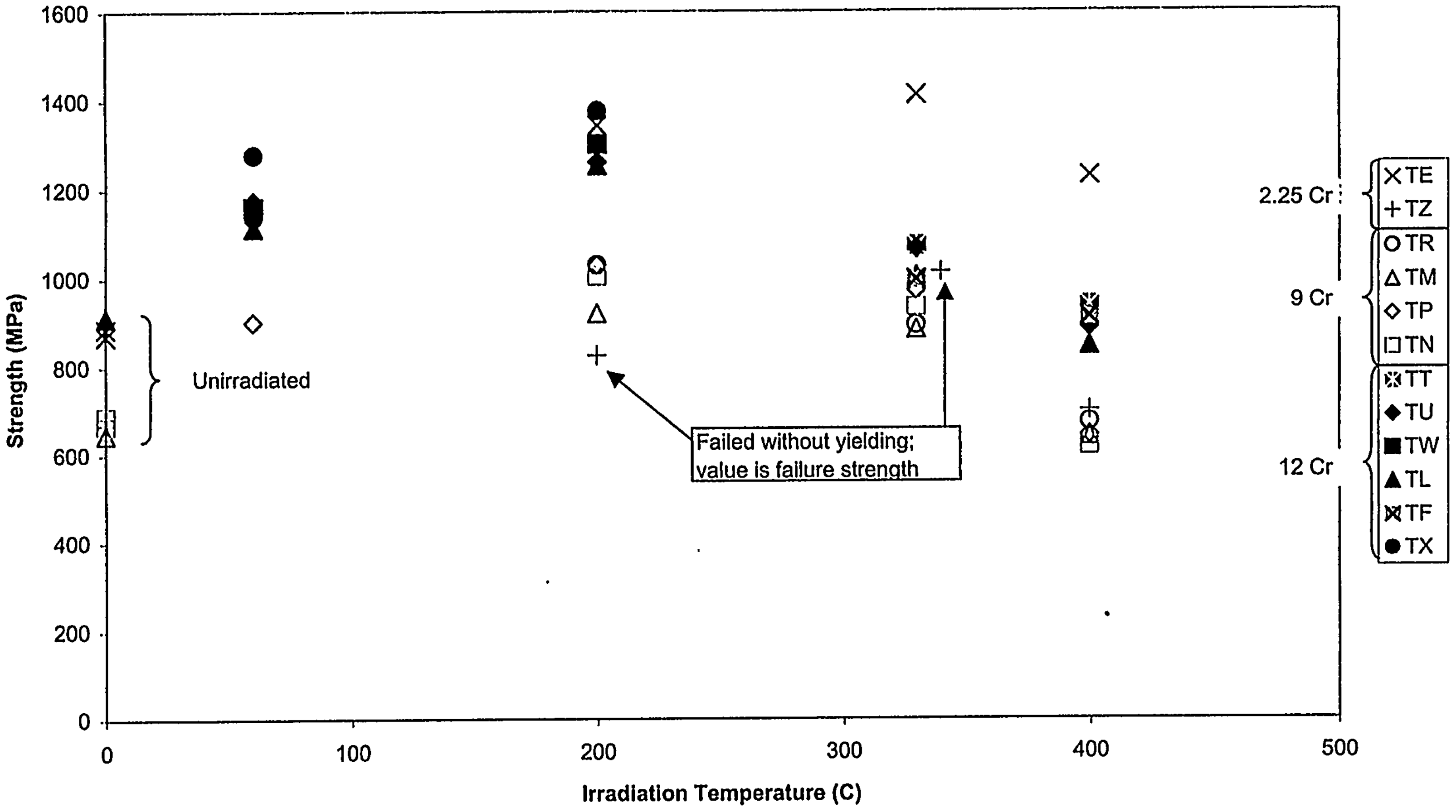

2. Maximum strength of low activation alloys at room temperature after irradiation in ORR.

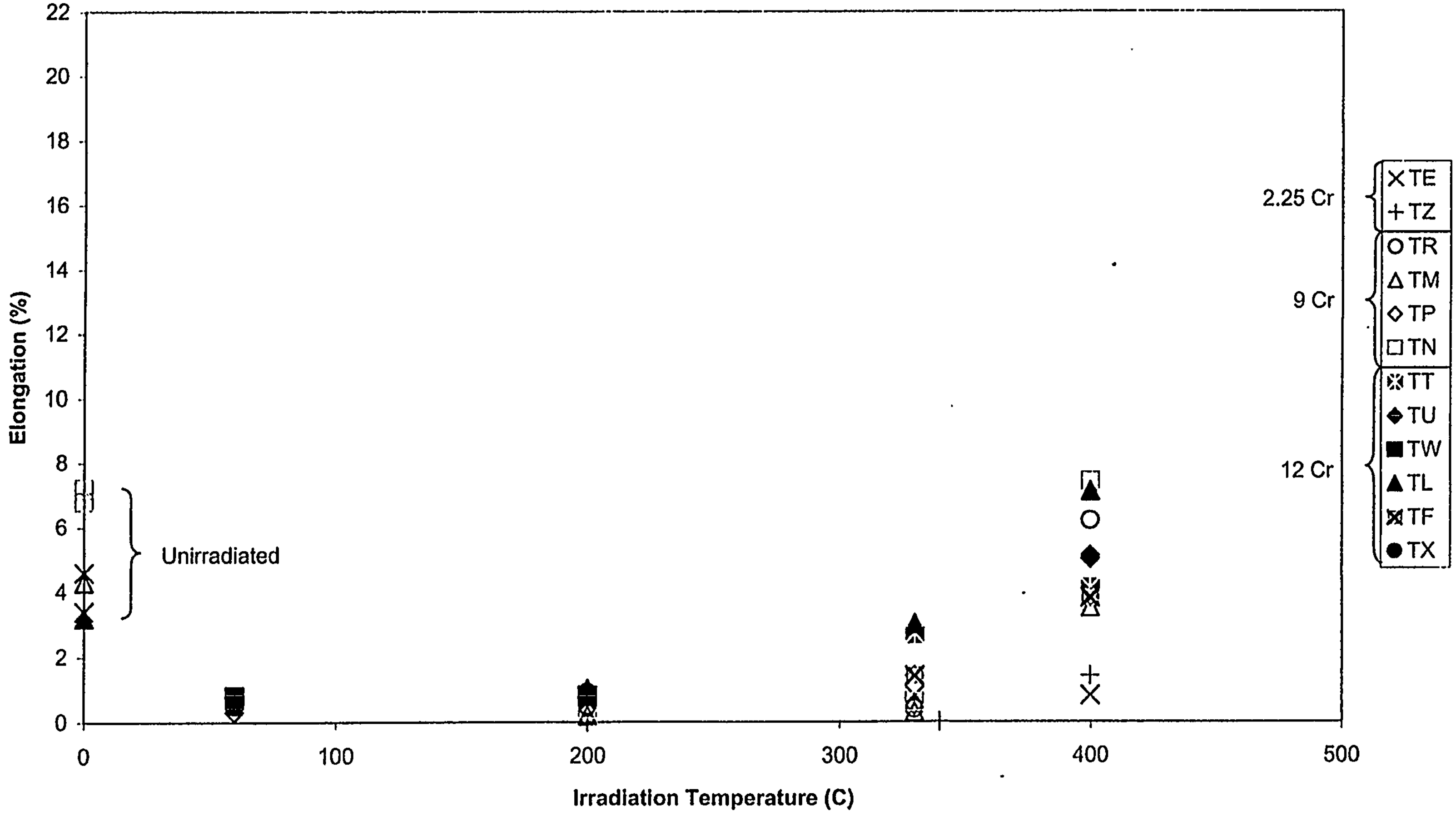

3. Uniform elongation of low activation alloys at room temperature after irradiation in ORR.

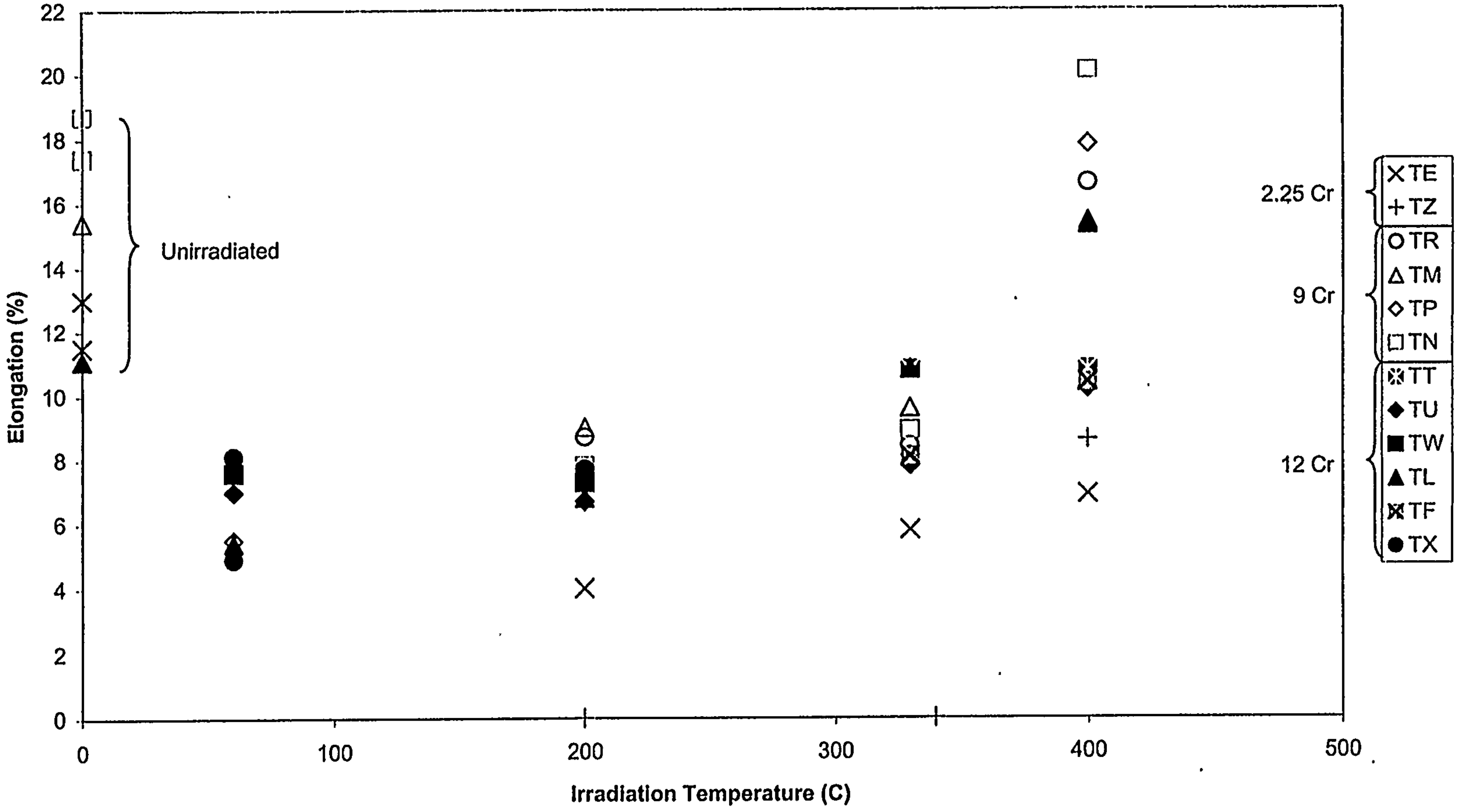

4. Total elongation of low activation alloys at room temperature after irradiation in ORR.

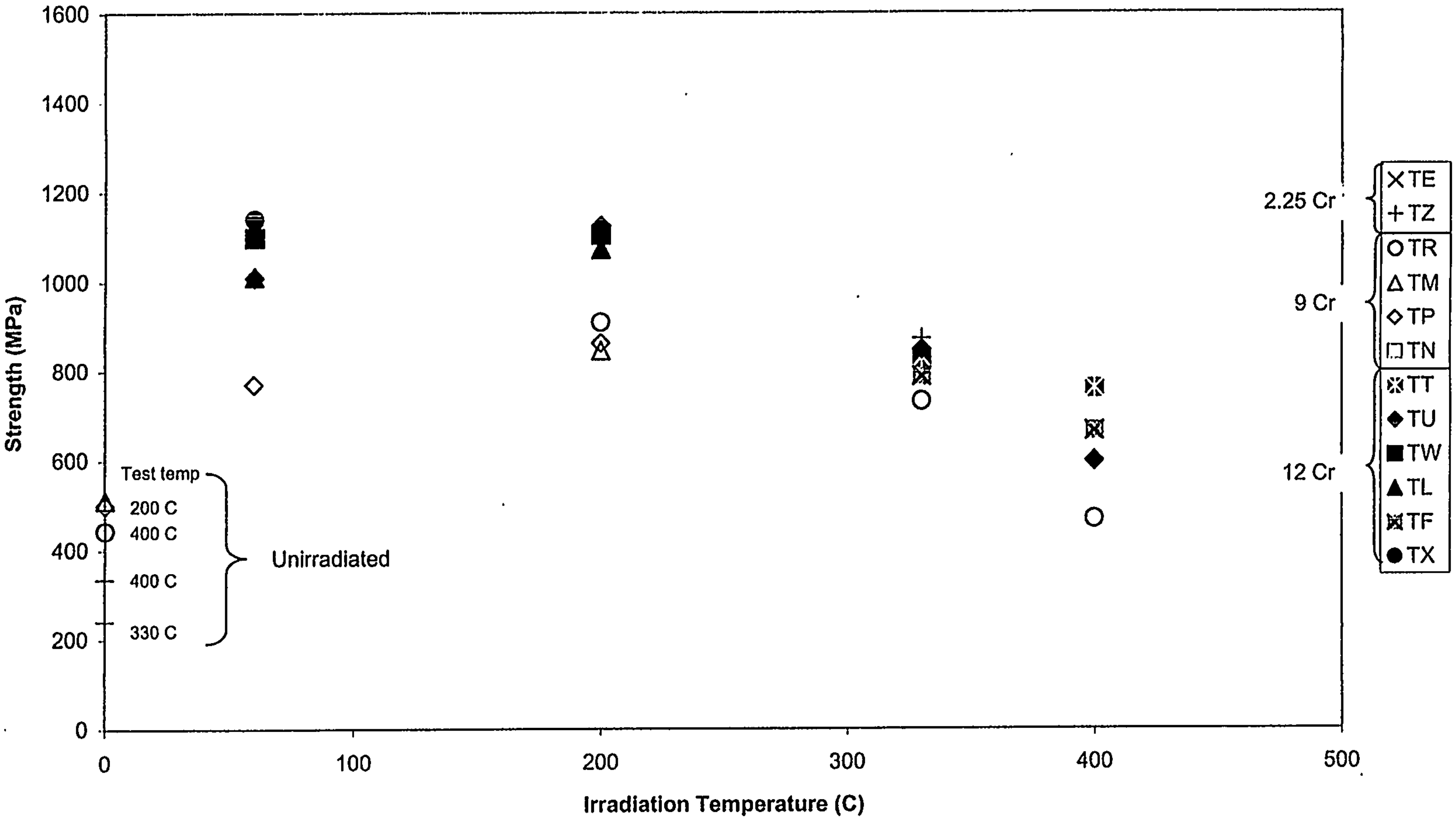

5. Yield strength of low activation alloys at the irradiation temperature after irradiation in ORR.

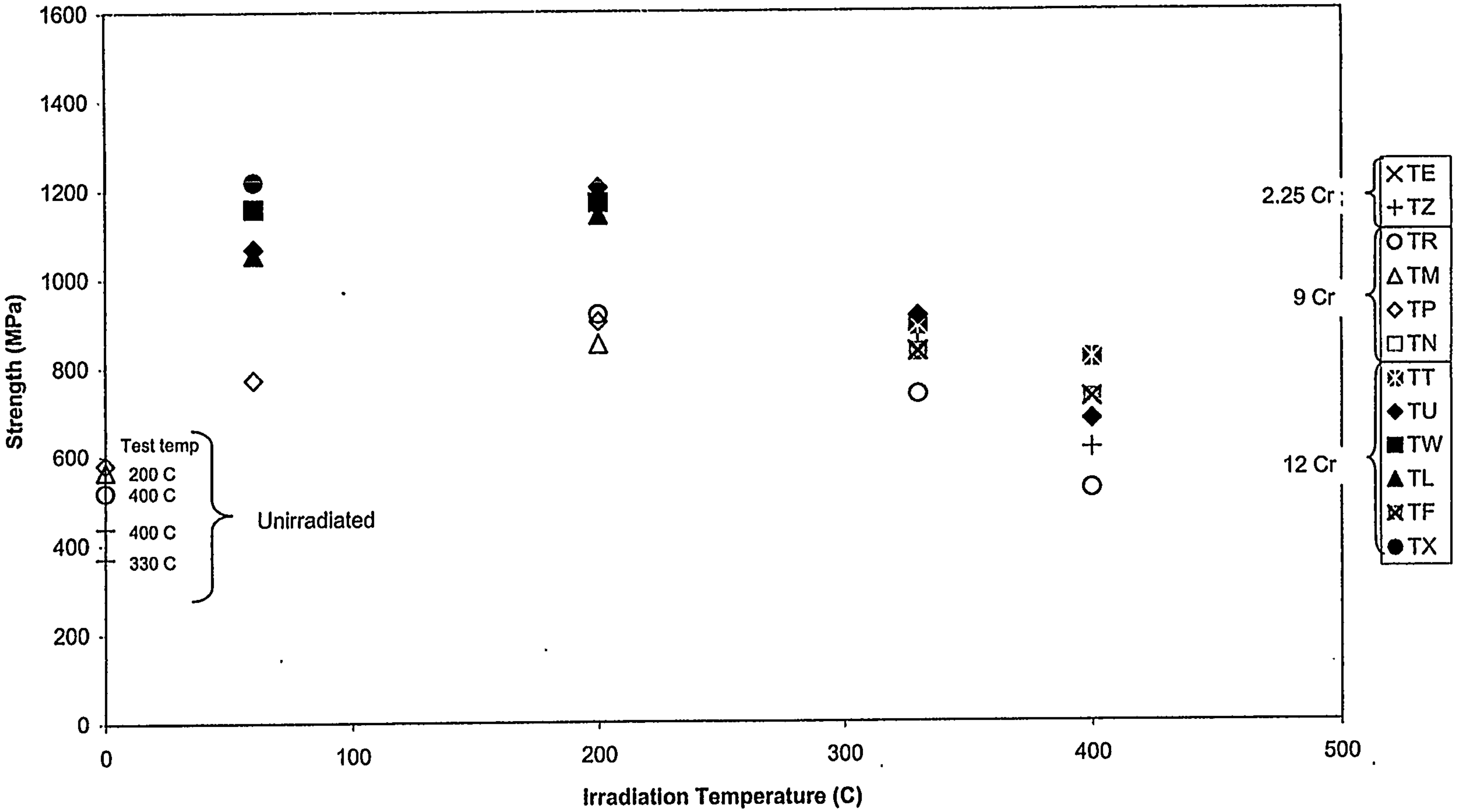

6. Maximum strength of low activation alloys at the irradiation temperature after irradiation in ORR.

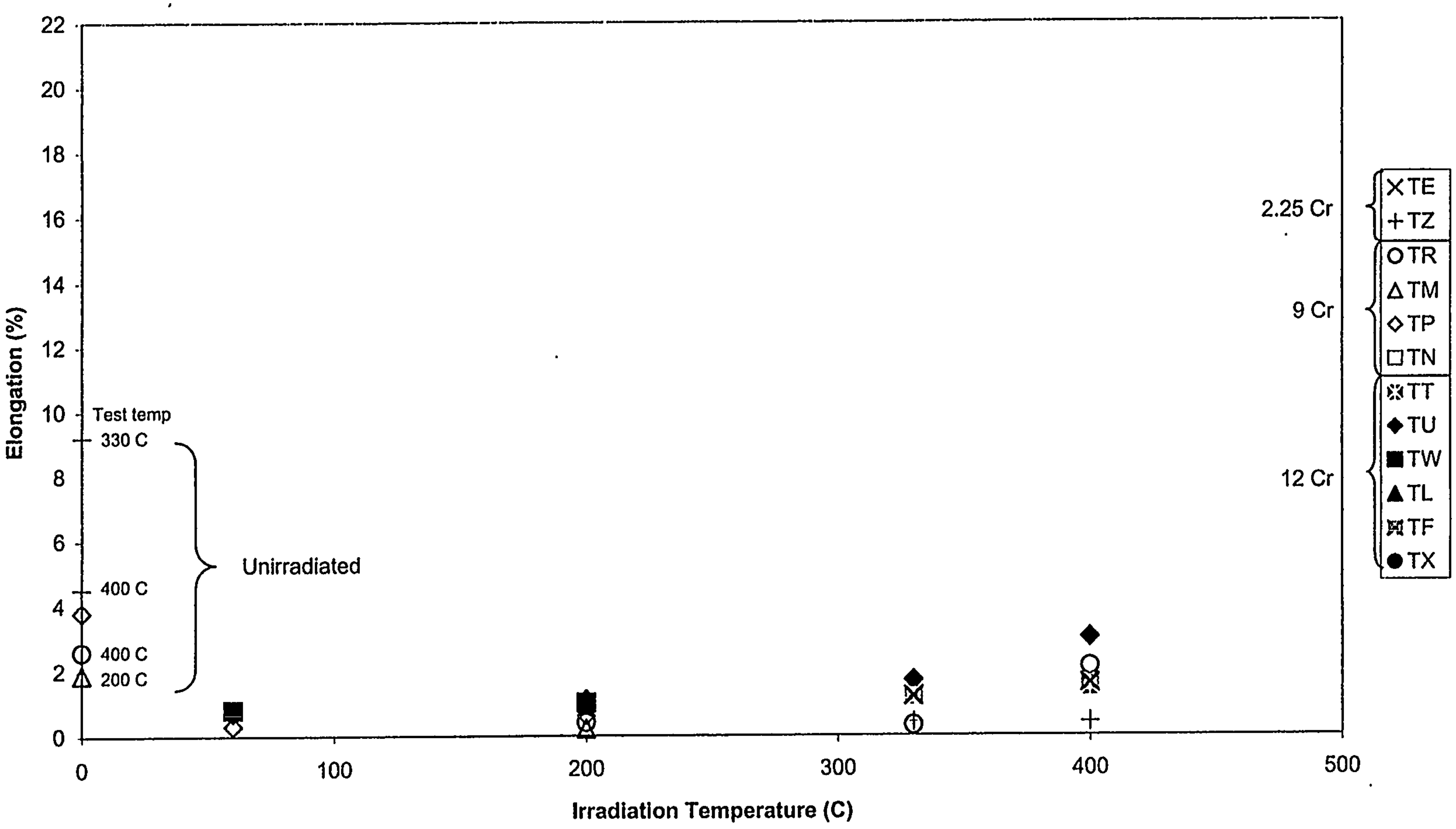

7. Uniform elongation of low activation alloys at the irradiation temperature after irradiation in ORR.

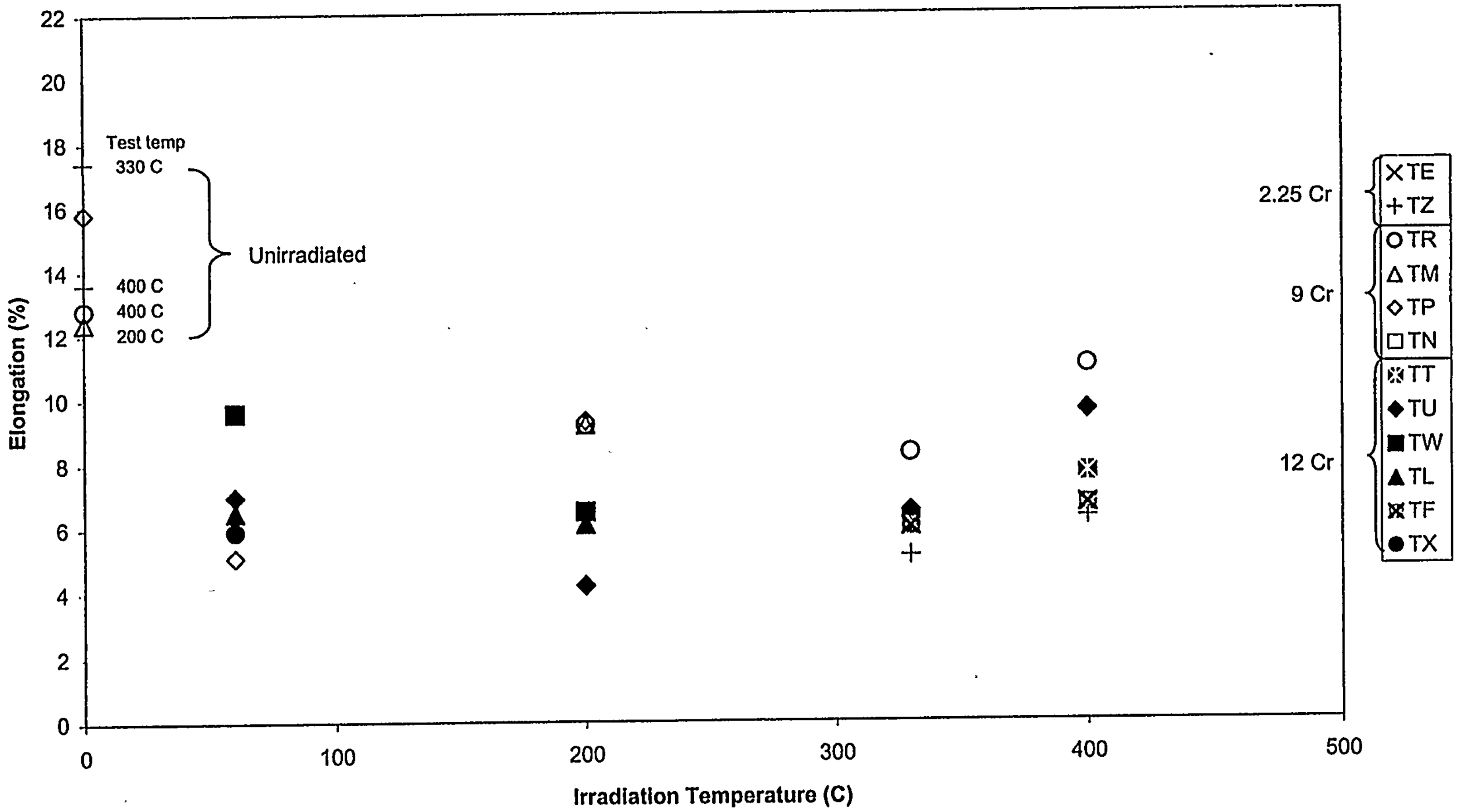

8. Total elongation of low activation alloys at the irradiation temperature after irradiation in ORR.

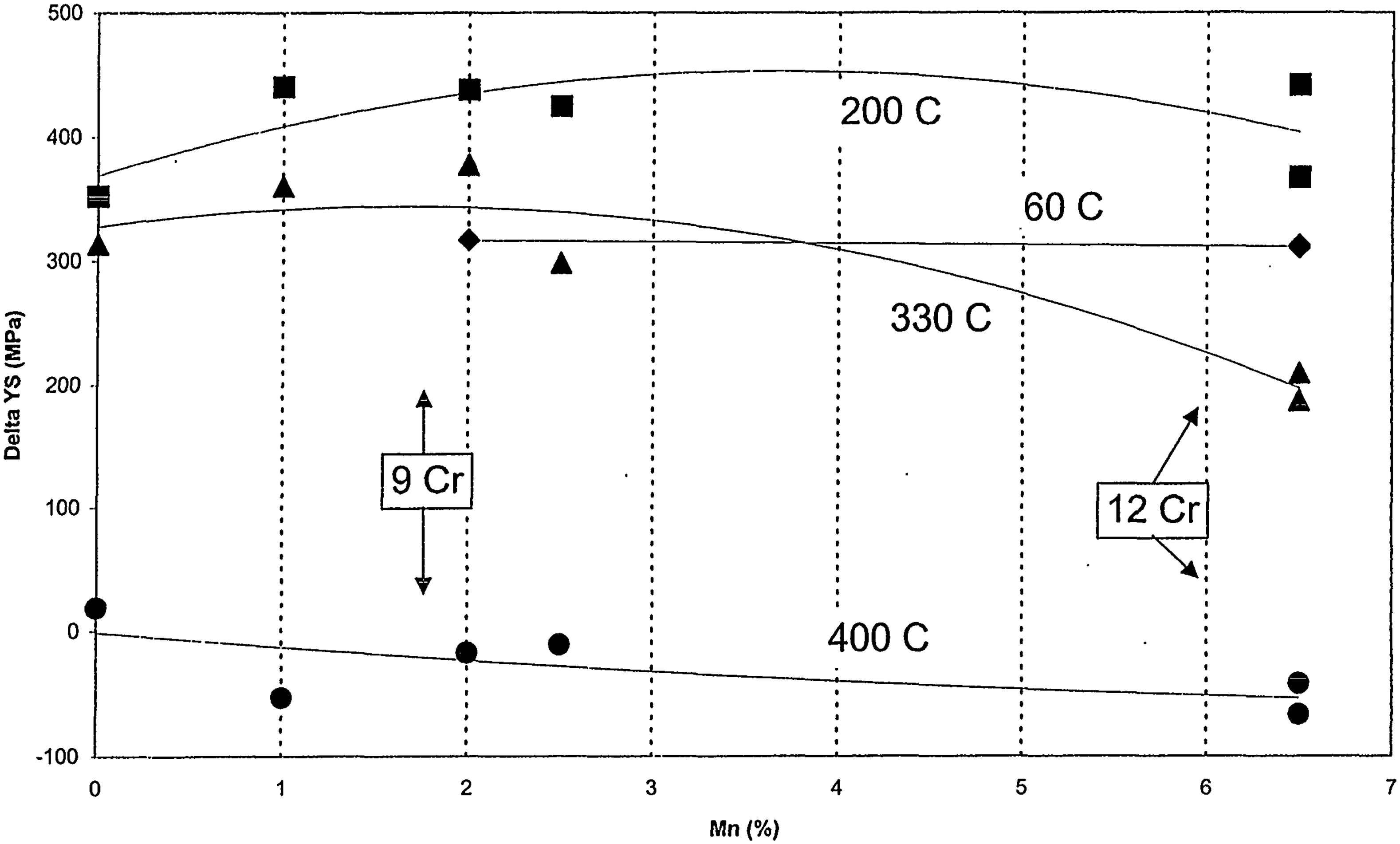

9. Effect of Mn on hardening observed in low activation alloys at room temperature after irradiation in ORR.

EFFECT OF HEAT TREATMENT AND IRRADIATION TEMPERATURE ON IMPACT PROPERTIES OF Cr-W-V FERRITIC STEELS—R. L. Klueh (Oak Ridge National Laboratory) and D. J. Alexander (Los Alamos National Laboratory)

Extended Abstract*

In the development of reduced-activation steels at ORNL, eight experimental steels have been studied. The steels are basically Fe-XCr-2W-0.25V-0.1C (compositions in wt. %) with 2.25% Cr (designated 2¼Cr-2WV) 5% Cr (5Cr-2WV), 9% Cr (9Cr-2WV), and 12% Cr (12Cr-2WV). Also, compositions with 2.25% Cr and 0% W (2¼CrV), 1% W (2¼Cr-1WV), and 0% V (2¼Cr-2W) were studied along with the 9Cr-2WV steel to which 0.07% Ta was added (9Cr-2WVTa).

To determine the effect of heat treatment (cooling rate from the austenitization temperature), specimens were taken from normalized-and-tempered 15.9-mm plate and 3.3-mm bar. Charpy impact properties were determined on the eight reduced-activation Cr-W ferritic steels in the normalized-and-tempered condition and after irradiation in FFTF to ≈14 dpa at 393°C.

In the normalized-and-tempered condition, the microstructure of the 2¼Cr steels in the 15.9-mm plate (slow cool) were bainite with various amounts of polygonal ferrite, and they were 100% bainite when heat treated as 3.3-mm bar. The 5Cr steel and the two 9Cr steels were 100% martensite and the 12Cr steel was martensite with ≈25% δ-ferrite after heat treatment in either geometry.

The change in microstructure caused by heat treatment of the 2¼Cr steels from duplex microstructures of bainite plus ferrite to 100% bainite resulted in improvement in the Charpy impact properties before irradiation. After irradiation, however, there was little difference in the properties for the two different heat treatments. As expected, cooling rate had little effect on the high-chromium (9 and 12% Cr) steels before or after irradiation. However, the Charpy properties for the 5Cr-2WV steel before and after irradiation were improved by the faster cooling rate. The reason for this change is unclear, but it may be due to the different precipitates present in the 5Cr steel as compared to the other martensitic steels (M_7C_3 is the primary precipitate present in the 5Cr-2WV steel, and $M_{23}C_6$ is the primary precipitate in the other martensitic steels).

Results from the present irradiation experiment at 393°C were compared with previous experiments for irradiation at a lower temperature (365°C) but at similar dpa levels. The DBTT values of all but the 5Cr-2WV and 9Cr-2WVTa steels were lower after irradiation at 393°C than after irradiation at 365°C, which is the expected behavior. The contrary behavior of the 5Cr steel was tentatively attributed to the M_7C_3 carbides that form in this composition that are not present in the 9Cr and 12Cr steels. The inverse temperature effect in the 9Cr-2WVTa steel was suggested to be due to the loss of tantalum from solution during irradiation at the higher temperature. Tantalum in solution may give the 9Cr-2WVTa steel its advantage over the other steels by increasing the cleavage fracture stress or changing the flow stress-temperature relationship, and this advantage is decreased by the precipitation of tantalum from solution during irradiation. However, a thorough analytical TEM examination of these steels is required to confirm the suggested mechanism.

* Extended abstract of paper published in the *Journal of Nuclear Materials*, Vol. 265, p. 262-272, March 1999.

4.0 COPPER ALLOYS AND HIGH HEAT FLUX MATERIALS

POST-IRRADIATION ANNEALING RESPONSE OF PURE COPPER IRRADIATED AT 100°C - D.J. Edwards (Pacific Northwest National Laboratory)*, B.N. Singh, P. Toft and M. Eldrup (Risø National Laboratory)

(To be presented at the 9th International Conference on Fusion Reactor Materials)

EXTENDED ABSTRACT

Pure copper and its alloys have long been evaluated for use in fusion reactor designs because of the need for a heat sink material with sufficient thermal conductivity to handle the high heat loads in the plasma facing components. Recent investigations have demonstrated that copper and copper alloys suffer from the irradiation-induced loss of ductility and plastic instability when irradiated at temperatures below the recovery stage V [1-5]. This behaviour has also been observed in fcc, bcc and hcp metals and alloys (see Ref. 6 for a recent review on this topic). The source of the radiation hardening is derived from the radiation-produced damage processes that yield a high density of small defect clusters that are both sessile and glissile depending on their size and nature (vacancy or interstitial). The presence of these defect clusters produced during irradiation can cause substantial changes in the mechanical and physical behaviour of the material, including the loss of uniform ductility and work hardening, large increases in yield strength, formation of a yield drop, and overall loss of conductivity. The changes in the deformation behavior of the material are particularly worrisome given that the formation of the yield drop often signifies the onset of plastic instability (dislocation channelling or microtwinning) during deformation. Several issues remain unclear, in particular the actual mechanism responsible for the yield drop, why a given material will experience work softening or work hardening depending on the dose, and how these changes in deformation mode will affect the cracking susceptibility.

One issue that bears further study is the possibility of being able to anneal the radiation damage out of the irradiated material, for example, during the periodic bakeout of the vessel chamber needed to improve the vacuum. This is a complicated issue since the microstructure evolves over time, and the annealing may in fact produce different results depending on when the anneal is done, that is, at doses of 10^{-2} dpa versus 0.5 dpa. Further complicating the issue is how multiple cycles of annealing and irradiation may affect the microstructural evolution over the lifetime of the component. As a first step toward investigating the effect of annealing on irradiated copper, tensile samples of pure copper (annealed at 550°C for 2h in vacuum, 10^{-6} torr) were irradiated in the DR-3 reactor at Risø National Laboratory at 100°C to different dose levels in the range 0.01 to 0.3 dpa (NRT). All specimens were irradiated with a displacement damage rate of $\sim 5 \times 10^{-8}$ dpa (NRT)/s. A subset of the irradiated specimens were given a post-irradiation annealing treatment under vacuum ($<10^{-5}$ torr). Microstructural examinations have been completed for both the as-irradiated and the post-irradiation annealed samples, and results of the preliminary tensile tests (strain rate of 1.2×10^{-3} s^{-1}, 100°C in vacuum, $<10^{-4}$ torr) are available also. Electrical resistivity measurements have already been reported separately [7].

The microstructure contains a high density of small stacking fault tetrahedra (SFT's) and line dislocations that were present before irradiation. The size distributions of the SFT's in the as-irradiated samples are shown in Figure 1 as a function of dose. A slight broadening of the

---

* Pacific Northwest National Laboratory (PNNL) is operated for the U.S. Department of Energy by Battelle Memorial Institute under contract DE-AC06-76RLO-1830.

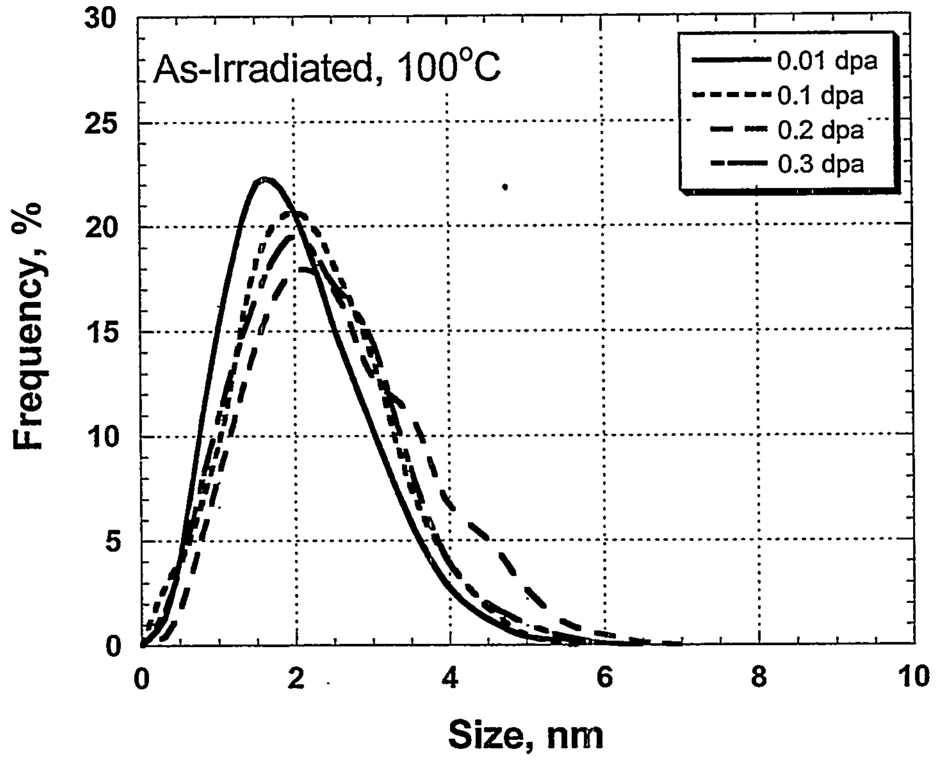

Figure 1. The size distributions for the as-irradiated pure copper are shown, and reveal that irradiation from 10^{-2} to 0.3 dpa produces only slight differences in cluster sizes. The average size of ~2.5 nm is similar for all four conditions.

overall distribution occurs as the dose increases, with the average size staying at bout ~2.5 nm. The effect of post-irradiation annealing on the size distribution of the SFT's is presented in Figure 2, showing that annealing causes a noticeable shift toward larger sizes as well as an overall broadening of the size distribution. However, for the samples irradiated at 0.3 dpa and then annealed, the average size is actually smaller than that of the samples irradiated to 0.1 and 0.3 and then annealed. The dose dependence of the cluster densities shown in Figure 3 for the as-irradiated and post-irradiation annealed samples also demonstrate the effect that annealing has on the microstructure. The cluster densities after annealing are lower than that measured in the as-irradiated samples, and this is particularly true for the 10^{-2} dpa samples where the difference is almost a factor of 5. The annealed 0.3 dpa sample, however, is within a factor of 2, basically within the experimental scatter. Note that the cluster density for the annealed 0.3 dpa sample is almost the same as that of the as-irradiated 10^{-2} dpa sample, but with a larger average size.

The tensile properties are given in Table 1, and show that the as-irradiated samples exhibit a large increase in yield strength even at 10^{-2} dpa. The uniform and total elongation decrease

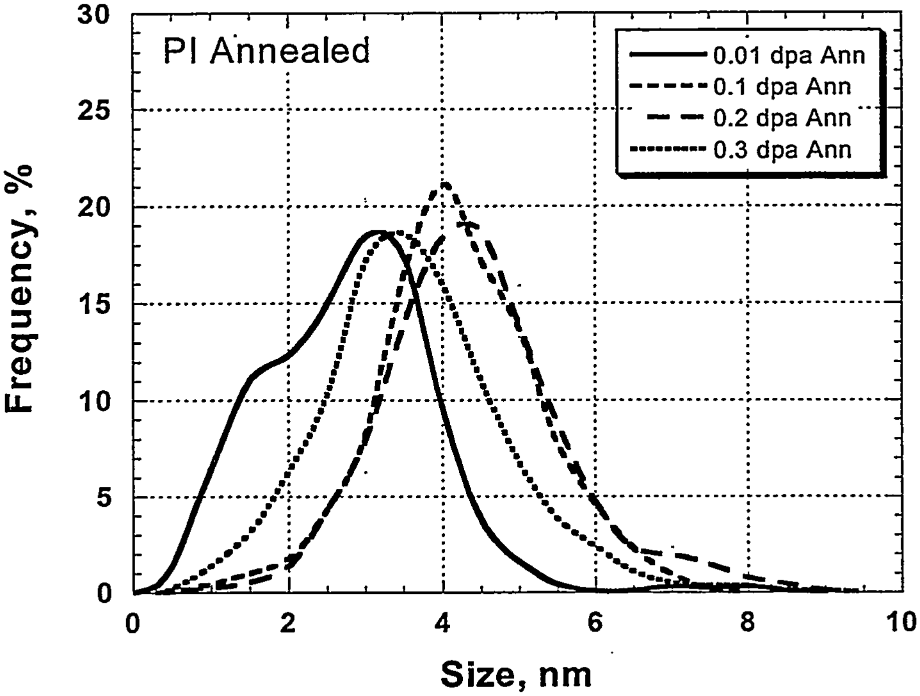

Figure 2. Post-irradiation annealing increases the overall size of the clusters and broadens the size distributions compared to the same dose in the as-irradiated condition. The annealed 0.3 dpa condition has a smaller average size than 0.1 dpa and 0.2 conditions, but the reasons for this are not presently known.

substantially in the as-irradiated samples, and in fact disappear entirely after irradiation to 0.1 dpa and above. A sharp yield point begins to appear even at 10^{-2} dpa, and evolves into an upper and lower yield point at the higher doses. Work hardening after irradiation is negligible after 0.1 dpa and above, and essentially the upper yield strength and ultimate strength are the same due to the poor work hardening ability. Annealing has a profound effect on the mechanical properties, and restores the work hardening ability and uniform elongation of the material at all doses. However, the yield strength remains considerably higher and the ductility lower than that measured for the unirradiated specimens, which agrees with the fact that the microstructure still retains a high cluster density. It is important to note that no yield point is present in the annealed 0.3 dpa sample even though the cluster density is the same as the as-irradiated 10^{-2} dpa sample and the average size is larger. Microstructural examination of the deformed samples from the as-irradiated samples show that dislocation channelling occurs in all conditions, but the degree of dislocation channelling is higher the greater the yield strength and more prominent the yield drop. While dislocation channels are still observed in the annealed and deformed samples, significant dislocation motion in those

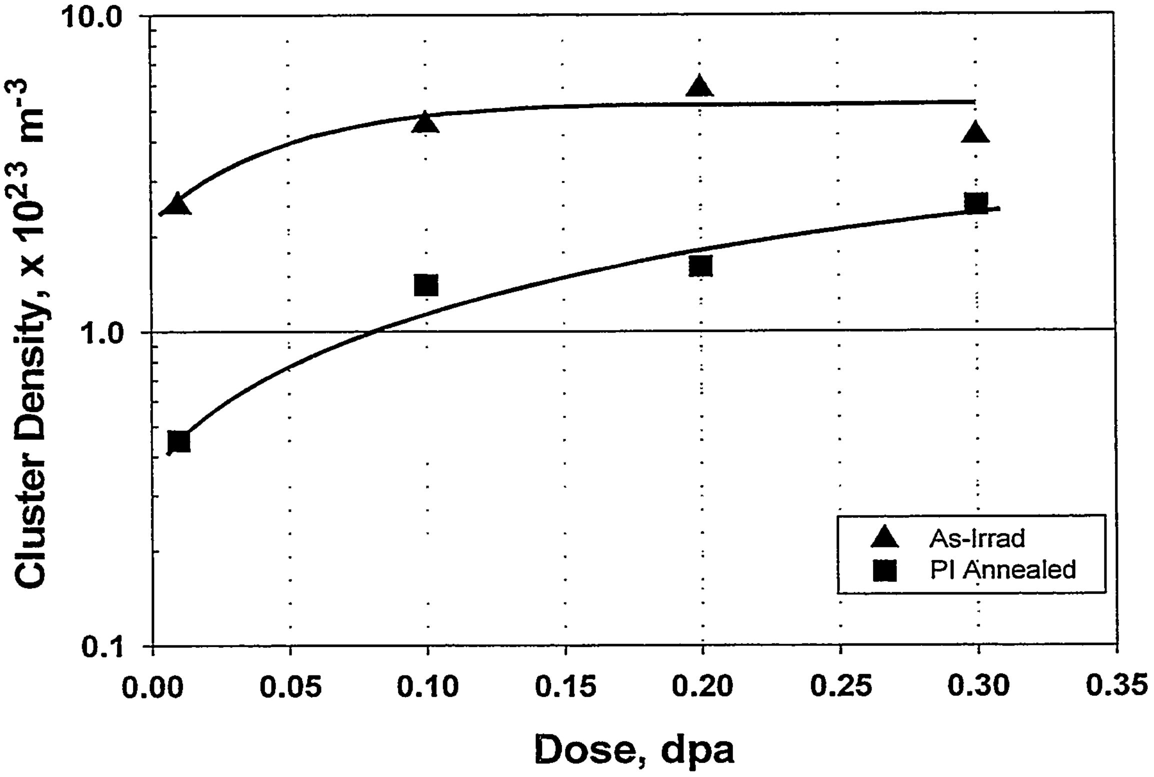

Figure 3. The density of the clusters saturates at about 0.1 dpa in the as-irradiated condition in agreement with results presented in the literature at similar irradiation temperatures. The density in the post-irradiation annealed condition is significantly lower at 10^{-2} dpa compared to its as-irradiated counterpart, but the density begins to approach that of the as-irradiated samples as the dose increases. The high density of clusters and smaller size distribution at 0.3 dpa suggests that the annealing kinetics can change as the microstructure evolves.

Table 1. Tensile properties of OFHC-copper and different copper alloys in the unirradiated, as-irradiated and post-radiation heat treated conditions

Dose [dpa]	Post irr. heat treat. [°C]	σ_y^u [MPa]	$\sigma_{0.2}$ [MPa]	σ_{max} [MPa]	ε_u^p [%]	ε_t [%]
Unirr	-	-	30	190	56	63
0.01	-	-	155	195	24	26
0.1	-	245	-	245	-	23
0.2	-	250	-	250	-	20
0.3	-	265	-	265	-	22
0.01	300°C for 50 h	-	68	170	39	43
0.1	300°C for 50 h	-	135	208	25	28
0.2	300°C for 50 h	-	145	215	24	26
0.3	300°C for 50 h	-	150	220	23	26

areas in-between the few channels is observed that explains why the material exhibits a more normal work hardening behavior.

The formation of the upper and lower yield point is thought to be due to the dislocations being decorated in a manner analogous to that of the solute atoms that form the Cottrell atmosphere in pure Fe [8]. Singh, Foreman, and Trinkaus [6] proposed a new mechanism called Cascade-Induced Source Hardening (CISH) where the grown-in dislocations are decorated by small dislocation loops or clusters formed during irradiation. The possibility also exists that impurities are segregated to the dislocations, a factor which may be more prominent in the case of alloys. The CISH mechanism seems to be supported by the annealing results. Although the density of clusters remains high and the size of the clusters is larger after annealing, normal work hardening occurs during the tensile test without any evidence of a yield drop. This implies that annealing effectively removes or decreases the degree of dislocation decoration and unlocks the grown-in dislocation sources. The clusters in the matrix still contribute to the overall strength of the material since dislocations moving through the matrix must interact with the sessile loops, but these interactions are thought to be rather weak in comparison to the dislocation decoration. Further analysis of the deformed microstructures and overall behavior is needed, and the results will be evaluated in light of the CISH model and the traditional "dispersed barrier" model to explore the radiation-induced increase in yield strength.

ACKNOWLEDGEMENTS

The present work was partly funded by the European Fusion Technology Programme. The authors wish to thank B. F. Olsen, N.J. Pederson and J.L. Lindbo. DJ Edwards would like to thank Risø National Laboratory for the support and assistance during his visit. His work was also partly supported by the U.S. Department of Energy under contract DE-AC06-76RLO 1830 with the Battelle Memorial Institute at the Pacific Northwest National Laboratory.

REFERENCES

1. B.N. Singh, D.J. Edwards and P. Toft, J. Nucl. Mater. 238 (1996) 244.
2. B.N. Singh, D.J. Edwards, A. Horsewell and P. Toft, Dose Dependence of Microstructural Evolution and Mechanical Properties of Neutron Irradiated Copper and Copper Alloys, Risø-R-839 (EN) ,Risø National Laboratory, Roskilde, Denmark, September (1995).
3. S.A. Fabritsiev, A.S. Pokrovsky, S.J. Zinkle, D.J. Edwards, J. Nucl. Mater. 233-237 (1996) 513.
4. A.F. Rowcliffe, S.J. Zinkle, J.F. Stubbins, D.J. Edwards, and D.J. Alexander, J. Nucl. Mater. 258-263 (1998) 183.
5. D.J. Edwards, B.N. Singh, P. Toft, and M. Eldrup, J. Nucl. Mater. 258-263 (1998) 978.
6. B.N. Singh, A.J.E. Foreman and H. Trinkaus, J. Nucl. Mater. 249 (1997) 103.
7. M. Eldrup and B.N. Singh, J. Nucl. Mater. 258-263 (1998) 1022.
8. A.H. Cottrell, Theoretical Structural Metallurgy, (Edwards Arnold, London, 1955) p. 228.

MICROSTRUCTURES OF Ti-Al INTERMETALLIC COMPOUNDS IRRADIATED AT 673 K IN HFIR

- Y. Miwa, T. Sawai (Japan Atomic Energy Research Institute), D. T. Hoelzer (Oak Ridge National Laboratory) and A. Hishinuma (JAERI)

OBJECTIVE

The objective of this work is to present recent TEM data of Ti-Al intermetallic compounds neutron irradiated at 673 K in High Flux Isotope Reactor.

SUMMARY

Four kinds of Ti-Al intermetallic compounds were irradiated at 673 K to the fluence of 5.16×10^{25} n/m^2 (E>1MeV) in HFIR. One consists of α_2-Ti$_3$Al single phase, and the others consist of α_2-Ti$_3$Al and γ-TiAl duplex phases. After irradiation, transmission electron microscopy was carried out. In both α_2-Ti$_3$Al and γ-TiAl phases of the specimens, loop-shaped and dot-like clusters were observed. However the nucleation behavior of cavities in α_2-Ti$_3$Al and γ-TiAl phases has been influenced by chemical compositions and fabrication processes.

PROGRESS AND STATUS

Introduction

Ti-Al intermetallic compounds offer advantages of large strength-to-weight ratio and high strength and good oxidation resistance at elevated temperature. In Ti-Al intermetallic compounds, α_2-Ti$_3$Al with the hexagonal ordered D0$_{19}$ structure and γ-TiAl with the tetragonal ordered L1$_0$ structure are promising candidates for nuclear apprication. Both Ti and Al are elements with low neutron-induced radioactivity and small cross sections of neutron absorption, compared with conventional austenitic stainless steels. In spite of the generation of a long-lived γ-emitter ^{26}Al from ^{27}Al(n,2n)^{26}Al reaction by 14 MeV neutron, the fast decay of radioactivity of Al to safe maintenance level within 2 weeks after reactor shutdown is attractive [1]. Therefore Ti-Al intermetallic compounds are attractive candidates for application in future fusion nuclear systems, as well as in fission nuclear systems.

Several papers have been published on the effect of electron irradiation [2], He$^+$ irradiation [3, 4, 5, 6] and neutron irradiation [7, 8] on Ti-Al intermetallic compounds. The ordered intermetallic compounds showed a superior resistance to void swelling under electron irradiation at 873 K [2], and ductilization after neutron irradiation at 873 K to 1×10^{24} n/m^2 (E>1 MeV) [7]. On the other hand, they showed a poor resistance of He bubble nucleation in γ-TiAl after He$^+$ irradiation to 2.9 dpa at room temperature [6] and a significant ductility loss with neutron irradiation to the fluence level of 1.6×10^{26} n/m^2 at 376-873 K [8]. Little is known on the effects of irradiation, especially neutron-irradiation, on Ti-Al intermetallic compounds.

In this report, the microstructural observation of 4 kinds of Ti-Al intermetallic compounds irradiated at 673 K to the fast neutron fluence of 5.16×10^{25} n/m^2 (E>1MeV) are presented.

Experimental procedure

The materials used were 4 kinds of Ti-Al intermetallic compounds, and were produced by powder metallurgical processing. The powders for 3 kinds (K1, K2, K3) of intermetallic compounds were prepared by the mechanical alloying, and another powder for K4 was prepared by the plasma rotating electrode process (PREP). The nominal chemical compositions and notations are listed in Table 1. The conditions of powder metallurgical processes are also listed in Table 1. The nominal microstructures were an α_2-Ti_3Al single phase for K1, an α_2-Ti_3Al + γ-TiAl duplex phase for K2, a γ-TiAl single phase for K3, and an α_2-Ti_3Al + γ-TiAl duplex phase for K4, respectively. Hereafter, α_2 and γ denote α_2-Ti_3Al and γ-TiAl, respectively.

The powders used for K1, K2 and K3 had an average particle diameter of about 30 μm. The main impurities in those powders were Fe (50 ppm), C (70 ppm), H (120 ppm) and O (3200 ppm) in Ti, and Fe (1600 ppm) and Si (600 ppm) in Al, respectively. These powders were mixed in order to obtain the nominal compositions listed in Table 1. These mixed powders were then mechanically alloyed in an Ar gas atmosphere for 720 ks using a stainless ball mill. The mechanically alloyed powders were isostatically hot pressed in a pure titanium capsule in vacuum under 176.8 MPa at 1373 K for 10.8 ks to obtain high density compacts. In order to obtain higher strength and ductility, these compacts were annealed in vacuum at 1473 K for 36 ks.

The powder used for K4 was prepared from cast mother alloys by PREP, and had an average particle diameter of about 250 μm. A cylindrical compact, about 60 mm in diameter and about 100 mm in height, was made by hot isostatic pressing (HIP) under 176.8 MPa at 1323 K for 10.8 ks in a pure titanium capsule. This was followed by isothermal hot forging up to a reduction of 78% in height with a strain rate of 3.8×10^{-4} s^{-1} at 1223 K in vacuum.

TEM disks, 3 mm in diameter and 0.25 mm in thickness, were prepared by wire cutting. These TEM disks were irradiated at about 673 K in a HFIR target position in the capsule of HFIR-MFE-JP20/position 9. The resulting thermal and fast neutron fluences, taking into account the specimen position in the reactor were 1.83×10^{26} n/m^2 (E<0.5 eV) and 5.16×10^{25} n/m^2 (E>1MeV), respectively [9]. The He production in Al was 6.42 appm [9]. The He production in Ti calculated by using the Japanese evaluated nuclear data library, JENDEL-3.2, was about 3.7 appm.

After irradiation, the disks were electrically thinned by a twin jet technique in a solution of 12.5 vol.% sulfuric acid and 87.5 vol.% methyl alcohol at 263 K with a constant current of about 150 mA and a varying voltage of 10~12 V. The TEM observation was carried out using a JEM 2000-FX microscope. The unirradiated disks were also observed using a Phillips CM12 equipped with an energy dispersive X-ray (EDX) analyzing system, VP9900.

Table 1 Nominal chemical compositions (atomic %) and heat treatment conditions

	Ti	Al	O	N	H	Powder	HIP	heat treatment
K1	65.78	31.49	1.49	0.17	1.08	MA	1373 K/10.8 ks/176.8 MPa	annealing/1473 K/ 36 ks
K2	52.53	45.90	1.26	0.12	0.19	MA	1373 K/10.8 ks/176.8 MPa	annealing/1473 K/ 36 ks
K3	49.30	48.11	2.31	0.19	0.09	MA	1373 K/10.8 ks/176.8 MPa	annealing/1473 K/ 36 ks
K4	52.41	46.87	0.63	0.06	0.03	PREP	1323 K/10.8 ks/176.8 MPa	hot forging/ 1223 K

MA: Mechanical alloying, PREP: Plasma rotating electrode processing

Results and discussion

Unirradiated Ti-Al intermetallic compounds

Figure 1 shows low-magnification microstructures of the unirradiated Ti-Al intermetallic compounds. In mechanically alloyed compounds (K1, K2 and K3), the grain size of K1 (fig. 1(a)) was the largest, and that of K3 (fig. 1(c)) was the smallest. The grain size of K4 (fig. 1(d)) which was made by PREP was larger than that of K1. The ASTM grain size numbers measured by lineal analysis were listed in table 2. The distribution of phases observed in the microstructures of fig. 1 is illustrated schematically in figure 2.

Table 2 ASTM grain size number before and after irradiation.

	before irradiation	After irradiation
K1	16.8	16.9
K2	17.5	17.8
K3	19.1	18.7
K4	16.1	No observation

K1 consisted of a duplex structure of matrix and island grains, as seen in figs. 1(a) and 2(a). The matrix was α_2 phase. The islands existed in matrix grains and along grain boundaries. In the islands, the concentration of Ti was higher than that in the matrix, and a higher number density of planar defects was observed. From diffraction pattern analyses, the island grains seemed to be also α_2 phase. The volume fractions of matrix and island grains were ~93% and ~7%, respectively (table 3). The diametral size distribution of matrix and island grains is shown in fig. 3(a). The grain size of the islands was smaller than the matrix and was generally smaller than 1.0 μm. However a large island grain about 2 μm in diameter was observed. The maximum diameter of matrix grains was about 4 μm. The average diameter of matrix and island grains were ~1.64 μm and ~0.53 μm (table 4), respectively. No impurities were detected in both the matrix and islands by EDX analysis. Dislocation lines were not observed in the matrix and islands, but twin boundaries were observed in both. Pores were observed in grains and especially on grain boundaries (fig. 4(a)). The pores on grain boundaries seemed to be larger than those in grains. The pores had a variety of shapes, so the shorter diameter was measured in each pore. The diametral size distribution of pores is shown in fig. 5(a). The size distribution had a peak at about 8 nm, and the maximum diameter was about 70 nm. The pores in islands were smaller than those in matrix, and average diameter in islands and matrix were 9.7 nm and 14.4 nm, respectively (table 5). The number density of pores in K1 was about $6x10^{19}/m^3$ (table 6), and that in island seemed to be higher than that in matrix. In these pores, Ar was detected by EDX analysis.

K3 was designed to be a single phase, γ-TiAl, intermetallic compound. However K3 consisted of three phases of Al_2O_3, α_2 and γ. The volume fractions among Al_2O_3, α_2 and γ were 3~4%, ~10% and ~87%, respectively (table 3). In the other intermetallic compounds, there were no alumina grains. The diameter of most alumina grains ranged from 0.3 to 0.9 μm, but larger grains ranging to 2.8 μm in diameter also existed. The average diameter of alumina grains was ~0.63 μm. Impurities such as P, Ti, Cr, Fe, Ni and Ar were detected in alumina by EDX analysis. As seen in figs. 1(b) and

2(b), relatively larger γ grains and smaller α_2 grains were observed. Figure 3(b) shows the diametral size distribution of γ and α_2 grains. The average diameter of α_2 and γ grains were 0.46 μm and 0.83 μm, respectively (table 4). The diameter of α_2 grains was not larger than 1.0 μm, and that of γ grains was over 2 μm. From EDX analyses, impurities such as Fe, Cr and Ni were detected in γ phase, but not in α_2 phase. It appeared that these impurities came from the stainless balls during mechanical alloying processes. From the comparison of the presence of impurities between γ and α_2 phase in K1 and K2, it seemed to be more difficult to dissolve the impurities in α_2 phase than in γ phase. Twin boundaries were observed in γ grains, but only a few twin boundaries were observed in α_2 grains. There were pores in γ grains and especially on grain boundaries (fig. 4(b)). Pores were not typically observed in the α_2 grains. The diametral size distribution of the pores is shown in fig. 5(b). The size distribution has a peak at ~10 nm, and the maximum diameter was ~70 nm. The average diameter of the pores was ~13.0 nm (table 5). The distribution of pores which existed on γ-γ boundaries was similar to that in K1 which had only α_2-α_2 boundaries. The number density of pores in K3 was about 9×10^{19} /m^3 (table 6). In these pores, Ar was detected by EDX analysis.

K2 was designed to have a duplex microstructure consisting of the α_2 and γ phases in order to obtain better ductility. The analysis of K2 showed that it consisted of two phases. The volume fraction of α_2 and γ phases measured by areal analysis were ~22% and ~78%, respectively (table 3). A combination of relatively larger γ-TiAl grains and smaller α_2-Ti$_3$Al grains was observed, as seen in figs. 1(c) and 2(c). These microstructural characteristics were similar to that in K3 (figs. 1(b) and 2(b)). But the grain size in K2 is slightly larger than that in K3. The diametral size distribution of α_2 and γ grains is shown in fig. 3(c). The average diameter of α_2 grains in K2 was ~0.65 μm, and was larger than that in K3. The average diameter of γ grains in K2 was ~0.98 μm, and was similar to that in K3. The maximum diameter of γ grains in K2 was similar to that in K3, and was about 2 μm. Impurities such as Fe, Cr and Ni were detected in both α_2 and γ phases by EDX analysis. Though no impurities were detected in α_2 phase of K3 and also of K1, impurities were detected in α_2 phase of K2. The amount of impurities in α_2 phase of K2 is less than that in γ phase. Twin boundaries were observed in both α_2 and γ grains. Twin boundaries existed in α_2 grains of K2, but few twin boundaries existed in those of K3. Pores were observed in grains and especially on grain boundaries, as seen in fig. 4(c). The pores were not observed in α_2 grains, which was a similar result to K3. Therefore it is more difficult for pores to occur in α_2 phase than in γ phase. Figure 5(c) shows the diametral size distribution of pores in K2. The diametral size distribution has two peaks at ~4 nm and 10~12 nm, and the maximum was about 60 nm. The larger peak and maximum diameter in K2 were about the same as those in K3, and also about the same as those in K1. The average diameter and number density of pores in K2 were ~13.4 nm and ~6×10^{19} /m^3, respectively (table 5 and 6).

K4 consisted of a duplex microstructure of the α_2 and γ phases, as seen in figs. 1(d) and 2(d). The volume fraction of the α_2 and γ phases measured by areal analysis were ~11% and ~89%, respectively (table 3). Some α_2 grains were isolated within γ grains. These isolated α_2 grains sometimes crossed γ-TiAl grains, or arranged in parallel rows. The diametral size distribution of α_2 and γ grains is shown in fig. 3(d). The grain size of α_2 and γ grains in K4 was much larger than in both K2 and K3, which had similar duplex microstructures. The average diameter of α_2 and γ grains were ~1.07 μm and ~2.40 μm, respectively (table 4). No impurities were detected in the α and γ phases by EDX analyses. Dislocation lines and twin boundaries were observed in both α_2 and γ phases, as seen in fig. 4(d). The dislocation density in γ was 8~9×10^{13} /m^2. No pores were observed in K4, which might have resulted from a fabrication process that used hot forging instead of mechanical alloying.

Table 3 The volume fraction of phases in Ti-Al intermetallic compounds (%)

	γ-TiAl	α_2-Ti_3Al	Al_2O_3
K1	———	100 (Matrix: ~93, Island ~7)	———
K2	~78	~22	———
K3	~87	~10	3~4
K4	~89	~11	———

Table 4 Average grain size of phases in Ti-Al intermetallic compounds (diameter, μm)

	γ-TiAl	α_2-Ti_3Al
K1	———	matrix : 1.64, island : 0.53
K2	0.98	0.65
K3	0.83	0.46
K4	2.40	1.07

Table 5 Average diameter of pores in Ti-Al intermetallic compounds (nm)

	γ-TiAl	α_2-Ti_3Al
K1	———	matrix : 14.4, island : 9.7
K2	13.4	
K3	13.0	
K4	No	

Table 6 The number densities of pores in Ti-Al intermetallic compounds (m^{-3})

K1	~ $6x10^{19}$
K2	~ $6x10^{19}$
K3	~ $9x10^{19}$
K4	No

Irradiated Ti-Al intermetallic compounds

After irradiation, the TEM specimens were stored for about 5 years to decay the radioactive isotope. The dose rates of TEM specimens were ~9.8 mR/h at 1 cm in K1, ~53 mR/h at 1 cm in K2, ~150 mR/h at 2.54 cm in K3 and ~3.7 mR/h at 1 cm in K4, respectively. As seen in the nominal chemical compositions in table 1, the amount of impurities such as Fe, Cr and Ni were not measured, but these impurities were detected by EDX analysis. By assuming that the ionizing radiations mainly come from these impurities, the amount of these impurities in K1 was the lowest among mechanically alloyed specimens of K1, k2 and K3. The amounts of these impurities in K2 and K3 were about five times and over fifteen times higher than in K1, respectively. This estimation about the amounts of these impurities corresponded roughly to the results of EDX analysis.

The ASTM grain size number of the Ti-Al intermetallic compounds after irradiation were similar to those before irradiation. Those numbers are listed in table 2.

Figures 6(a) and (b) show cavities observed in both the matrix and island grains of the irradiated K1, respectively. The faceted cavities occurred in both matrix and islands after irradiation. The cavities in the matrix occurred preferentially around pores within the range of about 75 nm from the surface of the pores (fig. 6(a)). Some small cavities also occurred far from pores. The distribution of cavities in the matrix was not uniform. In the island grains where a high density of planar defects was observed before irradiation, the cavities were smaller than in matrix (fig. 6(b)). The number density of cavities in the islands was much higher than that in matrix. In the island, the cavities seemed to be arranged in rows, and few cavities were on the planar defects. On the grain boundaries between the matrix and island grains or between matrix grains, few cavities were observed. The diametral size distributions of cavities in the matrix and island grains are shown in figs. 6(c) and (d), respectively. The size of cavities in both matrix and island grains was much smaller than that of pores. The average diameter of cavities in the matrix and island grains was ~5.6 nm and ~3.4 nm, respectively (table 7). The maximum diameter in the matrix was ~10 nm, and was similar to that in the islands. The number densities of cavities in the matrix and island grains were ~4x10^{20} /m^3 and 2x10^{22} /m^3, respectively (table 8). Loop-shaped and dot-like defects were observed in both matrix and island grains, as seen in figs. 7(a) and (b). In the matrix, dislocation loops about 20 nm in diameter were observed. Some of these dislocation loops seemed to be tangled. In islands, smaller dislocation loops about 5 nm in diameter were observed. It seemed that the dislocation loops in the matrix were larger than those in the islands, and that the number density of dislocation loops in the islands was higher than that in the matrix. In both the matrix and island grains, these dislocation loops occurred near the grain boundaries and near cavities or pores. In the island grains, the planar defects which existed before irradiation remained after irradiation.

In irradiated K3, small cavities occurred only in the γ phase. Figures 8(a) and (b) show that the faceted cavities occurred uniformly in γ grains. As seen in fig. 8(a), there were cavity free zones around γ-γ grain boundaries, and the width of the cavity free zones was about 100 nm. However, there was a γ-γ grain boundary where many cavities occurred. There were no cavities around pores in γ grains, which was different from the cavity nucleation behavior in α_2 phase of K1. In the α_2 grains of K3, no cavities were observed after irradiation, though many cavities occurred in α_2 grains of K1. The diametral size distribution of cavities in γ phase is shown in fig. 8(c). This size distribution looked like a bi-modal distribution, and has two peaks at ~2 nm and ~10 nm. This distribution did not include the pores located on grain boundaries. The larger peak in the diametral size distribution of cavities was similar to the peak for pores. The maximum diameter was ~ 20 nm, which was larger than that in K1. The average diameter and number density of cavities in γ phase were ~9.4 nm and ~2x10^{21} /m^3, respectively (table 7 and 8). Loop shaped clusters and dot-like defects formed in both γ and α_2 phases after irradiation. Figures 9(a) and (b) show the dislocation loops in γ and α_2 grains, respectively. The dislocation loops in γ grains were smaller than those in α_2 grains, and the diameter was about 5 nm. The loop diameter in α_2 grains was about 15 nm. In the γ grains, the number density of dislocation loops near grain boundaries seemed to be lower than that in grain interiors. However the loop density near twin boundaries in the grain was not different from that in grain interiors, and defects existed on the twin boundaries. The dislocation loops also existed near both cavities and pores.

Figures 10(a) and (b) show the cavities that were observed in both the α_2 and γ phases in irradiated K2. As seen in fig. 10(a), small cavities appeared in some γ grains, but not in all the γ grains. There were no cavities around pores in γ grains, which was similar to K3. There were no cavities on γ-γ grain boundaries, but there were some cavities on twin boundaries in γ grains. On the other hand, a higher density of small cavities occurred in α_2 grains (fig. 10(b)). These cavities were faceted. The cavities appeared around pores in the range of about 75 nm from surface of pore, which was similar to the cavity nucleation behavior in K1. The cavities also formed on α_2-γ grain boundaries (fig. 10(a)). The diametral size distributions of cavities in γ and α_2 grains are shown in figs. 10(c) and (d), respectively. The size distribution of cavities including pores in γ phase shows a bi-modal distribution (fig. 10(c)). From a comparison of the diametral size distributions of pores or cavities in γ phase before (fig. 5(c)) and after irradiation (fig. 10(c)), it appeared that the fraction of cavities that were 4~6 nm in diameter increased and the peak for larger cavities group shifted from 10~12 nm before irradiation to ~20 nm after irradiation. This suggested that irradiation might cause nucleation of small cavities and growth of the pores. As seen in fig. 10(d), the diametral size distribution of cavities in α_2 phase was similar to that in α_2 phase (matrix) of K1. The average diameter of cavities in α_2 and γ grains were ~5.7 nm and ~17.5 nm, respectively (table 7). The number densities of cavities in α_2 and γ grains were ~$1\text{x}10^{21}$ /m^3 and ~$4\text{x}10^{19}$ /m^3, respectively (table 8).There were loop-shaped and dot-like defects in both α_2 and γ phases after irradiation. Figures 11(a) and (b) show the dislocation loops in γ and α_2 grains, respectively. The diameter of dislocation loops in γ grains was similar to or slightly larger than that in α_2 grains. These dislocation loops were about 10 nm in diameter. The number density of dislocation loops in α_2 grains seemed to be higher than that in γ grains. These defects existed near grain boundaries and cavities.

In irradiated K4, TEM specimen did not electropolish uniformly which resulted in limited thin regions of the foil. As a result, only two γ grains were observed. In these γ grains, small cavities occurred after irradiation, as seen in fig. 12(a). These faceted cavities formed along the dislocation lines which existed before irradiation. There were some cavities on twin boundaries in the γ grain, but no cavities on grain boundaries. Figure 12(b) shows the diametral size distribution of cavities in γ grains. A bi-modal distribution was observed. The critical diameter of smaller cavities was ~2 nm. The average diameter and number density of cavities in γ grains were ~5.6 nm and ~$8\text{x}10^{20}$ /m^3, respectively (table 7 and 8). Large stacking fault dislocation loops that were about 50 nm in diameter formed in γ grains. Figure 13(a) and (b) show the dislocation loops the γ grain. These dislocation loops were much larger than those in γ grains of K2 or K3. These loops formed near the dislocation lines that existed before irradiation, and also formed preferentially near grain boundaries. The distribution was not uniform. The number density of dislocation loops was much lower than that in γ-TiAl grains of K2 or K3.

Table 7 Average diameter of cavities in phases (nm)

	γ-TiAl	α_2-Ti$_3$Al
K1	———	matrix : 5.9, island : 3.4
K2	17.5	5.7
K3	9.4	No
K4	5.6	xxxxxxxx

xxxxxxxx : TEM observations were not carried out

Table 8 Number densities of cavities in phases (m^{-3})

	γ-TiAl	α_2-Ti$_3$Al
K1	———	matrix : $\sim 4\times10^{20}$, island : 2×10^{22}
K2	4×10^{19}	1×10^{21}
K3	2×10^{21}	No
K4	$\sim 8\times10^{20}$	xxxxxxxxx

xxxxxxxx : TEM observations were not carried out

Cavity nucleation in α_2-Ti$_3$Al and γ-TiAl phase

Cavities formed in both α_2 and γ phases during neutron irradiation at 673 K, though there were some exceptions in K2 and K3. This irradiation temperature corresponded to 0.27 T_m (T_m: melting point) for γ and 0.34 T_m for α_2, respectively. The size distributions of cavities looked like bi-modal distributions. The relatively larger cavities were faceted. This suggests that the larger cavities might be voids. It is well-known that voids form during irradiation in the temperature range from 0.3 to 0.55 T_m in metals. It was expected, therefore, that the Ti-Al ordered intermetallic compounds also experienced void swelling in this temperature range.

In the α_2 phase of K1, K2 and K3, cavities formed in K1 (both the matrix and islands) and in K2, but not in K3. In K1 and K2, the cavities formed preferentially around pores. These pores existed prior to irradiation, and contained Ar gas. The range where cavities existed from the surface of pores was about 75 nm. It is suggested that Ar is recoiled from the pore by the elastic collision with neutrons, which makes an atomic displacement, and assists the nucleation of gas bubble. The maximun recoil energy of Ar with 1 MeV neutron by the elastic scattering was about 96 keV. The range of these energetic Ar ions in α_2 phase was calculated using TRIM 85 with the displacement energy of 25 eV for both Ti and Al, and was about 73 nm. This calculated range corresponded well to the measured range of cavities from the pores surface. Therefore the cavities around pores might be Ar gas bubble, and Ar gas might assist the nucleation of cavities. In K3, however, cavities were not observed both in α_2 grains and around pores. The Ar gas was also detected in pores of K3. This means that the presence of Ar gas and other gas might be the key factor for the formation of cavities in the α_2 phase. In addition to Ar gas, helium was also generated from nuclear reactions of Al and Ti. The calculated He concentration in α_2-Ti$_3$Al was about 4.4 appm. However although helium was produced in K3, cavities were not observed. Therefore this amount of helium might not have an influence on the cavity nucleation, or might be less effective than Ar. Oxygen is also present in these compounds. K3 contained twice the amount of oxygen compared to K1 or K2. However alumina was observed only in K3, and the volume fraction of alumina was about 3%. From the estimation of the amount of oxygen in alumina, almost all oxygen sis assosiated with alumina. Therefore K1 and K2 dissolved the oxygen, but K3 dissolved much less oxygen. This suggested that the oxygen had an influence on the cavity nucleation in the α_2 phase. Other impurities such as Fe, Cr and Ni were detected only in K2 but not in K1 and K3, which did not correspond to the nucleation behavior of cavities among them.

In the γ phase, the cavities were observed in every specimen, except for K1. However there were differences in the nucleation behavior of cavities among K2, K3 and K4. In K2, the number density of cavities was much lower than in K3 and K4. In K3, the number density of cavities was the largest, and cavities formed uniformly in γ grains. In K4, cavities occurred along dislocation lines which existed before irradiation. The size distribution of cavities in K3 and K4 showed bi-modal distributions. In all the γ grains investigated, there were no cavities near pores. Therefore the Ar gas in pores was not effective to form cavities in γ phase, which was different from the effect of Ar in α_2 phase. The calculated concentration of He gas which was generated from nuclear reaction of Ti and Al was about 5 appm. This amount is similar among K2, K3 and K4. Such an amount of He gas had little influence on the nucleation behavior of cavities in γ phase. Oxygen was also contained in these materials. Though the content of oxygen was highest in K3, almost all the oxygen was tied up with alumina, as discussed above. The amount of free oxygen in K3 seemed to be very low. The amount of oxygen in K2 was higher than in K4. The number density of cavities was the largest in K3, and the smallest in K2. Therefore the tendency of oxygen gas affecting the cavity nucleation in γ phase was opposite in α_2 phase. Nakata et. al. reported a similar effect of gas atoms on cavity nucleation behavior in He^+ ion irradiation experiment [3, 4]. In front of the calculated projected range of He ions, where the He concentration was very low, the number density of cavities in γ phase was larger than that in α_2 phase [3]. In the calculated projected range of He ion, where the He concentration was high, the number density of cavities in α_2 phase was larger than that in γ phase [4]. Therefore the effect of gas atoms on the cavity nucleation behavior might be different between γ and α_2 phases. Other impurities such as Fe, Cr and Ni were detected in K2 and K3 but not in K4. This did not correspond to the cavity nucleation behavior among them.

Reference

[1] T. Noda, F. Abe, H. Araki and M. Okada, J. Nucl. Mater. 155-157 (1988) 581-584.

[2] A. Hishinuma, K. Nakata, K. Fukai, K. Ameyama and M. Tokizane, J. Nucl. Mater. 199 (1993) 167-171.

[3] K. Nakata, K. Fukai, A. Hishinuma, K. Ameyama and M. Tokizane, J. Nucl. Mater. 202 (1993) 39-46.

[4] K. Nakata, K. Fukai, A. Hishinuma and K. Ameyama, J. Nucl. Mater. 240 (1997) 221-228.

[5] O. Okada, K. Nakata, K. Fukai, A. Hishinuma and K. Ameyama, J. Nucl. Mater. 258-263 (1998) 1750-1755.

[6] M. Song, K. Furuya, T. Tanabe and T. Noda, J. Nucl. Mater. 271&272 (1999) 200-204.

[7] A. Hishinuma, J. Nucl. Mater. 239 (1996) 267-272.

[8] A. Kohyama. T. Yamada, M. Ogawa, H. Matsui and M. Narui, Proc. of 2nd Japan/China Sym. on Materials for Advanced Energy Systems and Fission and Fusion Engineering (The University of

Tokyo, Japan, 1994) p.472.
[9] L. R. Greenwood and C. A. Baldwin, Fusion Reactor Materials Semiannual Progress Report, DOE/ER-313/23, p.305 (1997)

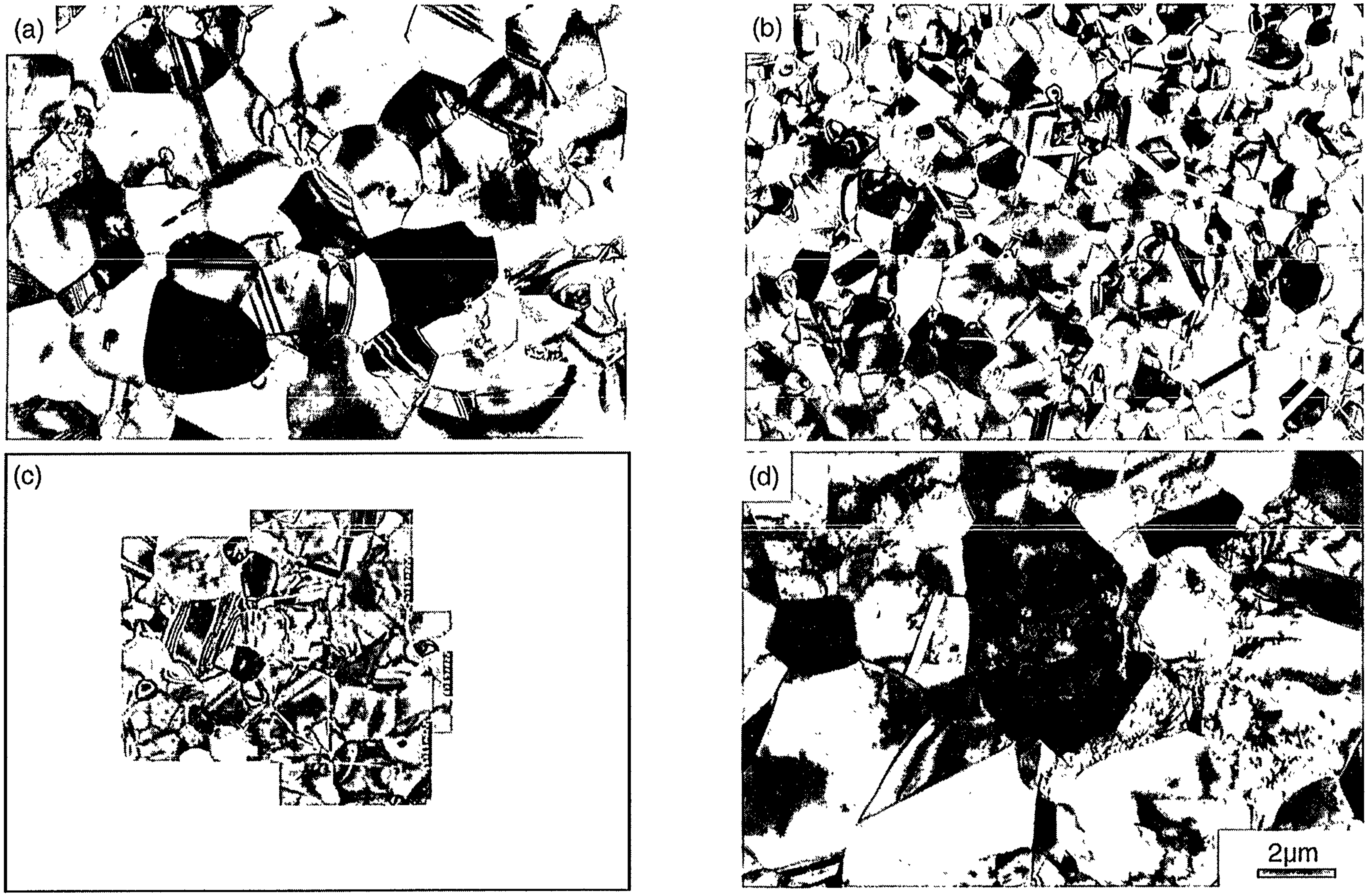

Figure 1 Low magnified TEM images of unirradiated Ti-Al intermetalic compounds.

(a) K1: α_2-Ti_3Al, (b) K3: γ-TiAl/α_2-Ti_3Al/Al_2O_3, (c) K2: γ-TiAl/α_2-Ti_3Al, (d) K4: γ-TiAl/α_2-Ti_3Al. K1, K2 and K3 were made by the mechanical alloying, and K4 was made by the plasma rotating electrode process.

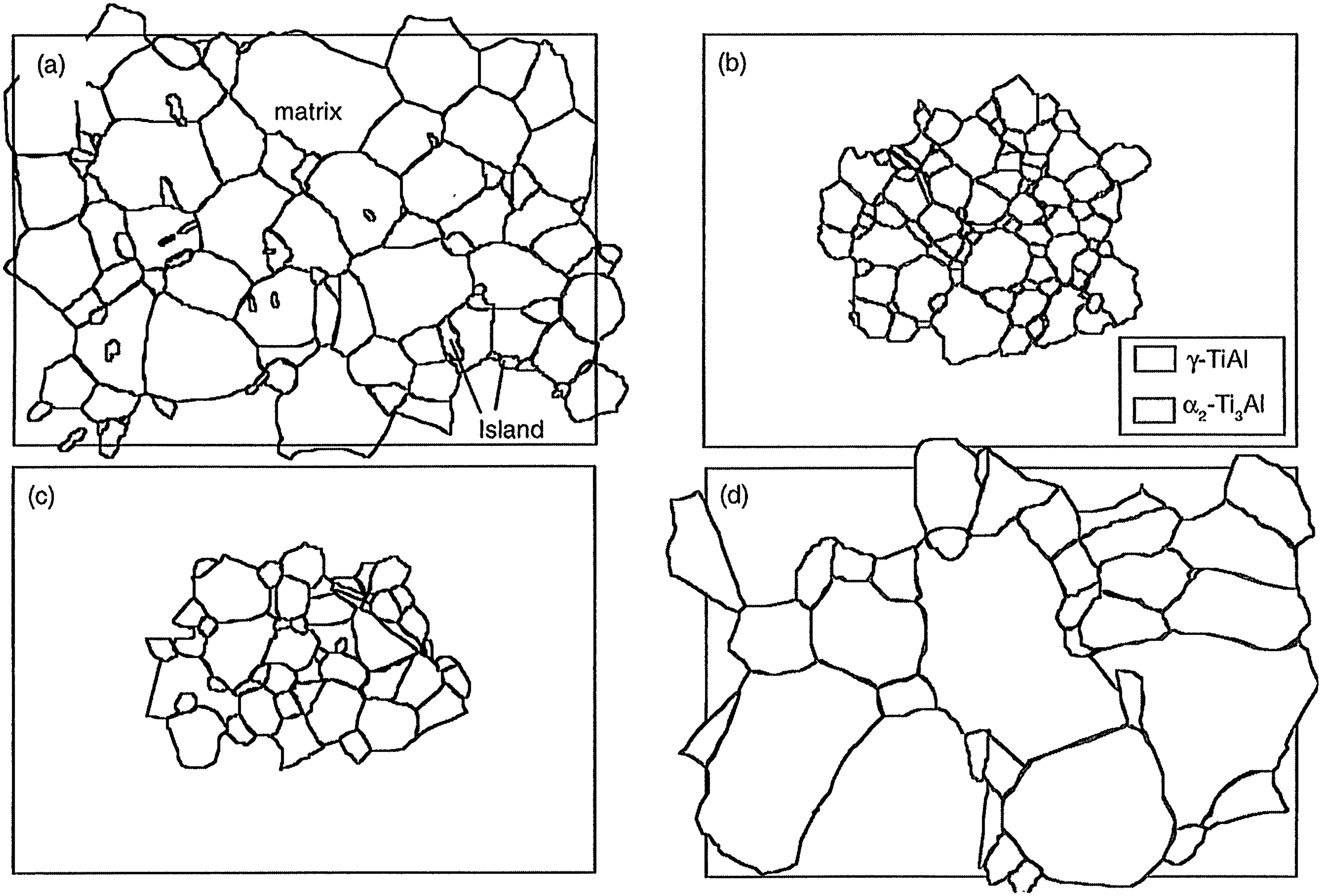

Figure 2 Schimatical illustrations of phase distribution of microstructures observed in figure 1.
(a) Duplex structure of matrix and island grains of α_2-Ti_3Al in K1; (b), (c) and (d) Distributions of γ-TiAl and α_2-Ti_3Al grains in K3 , K2 and K4, respectively.

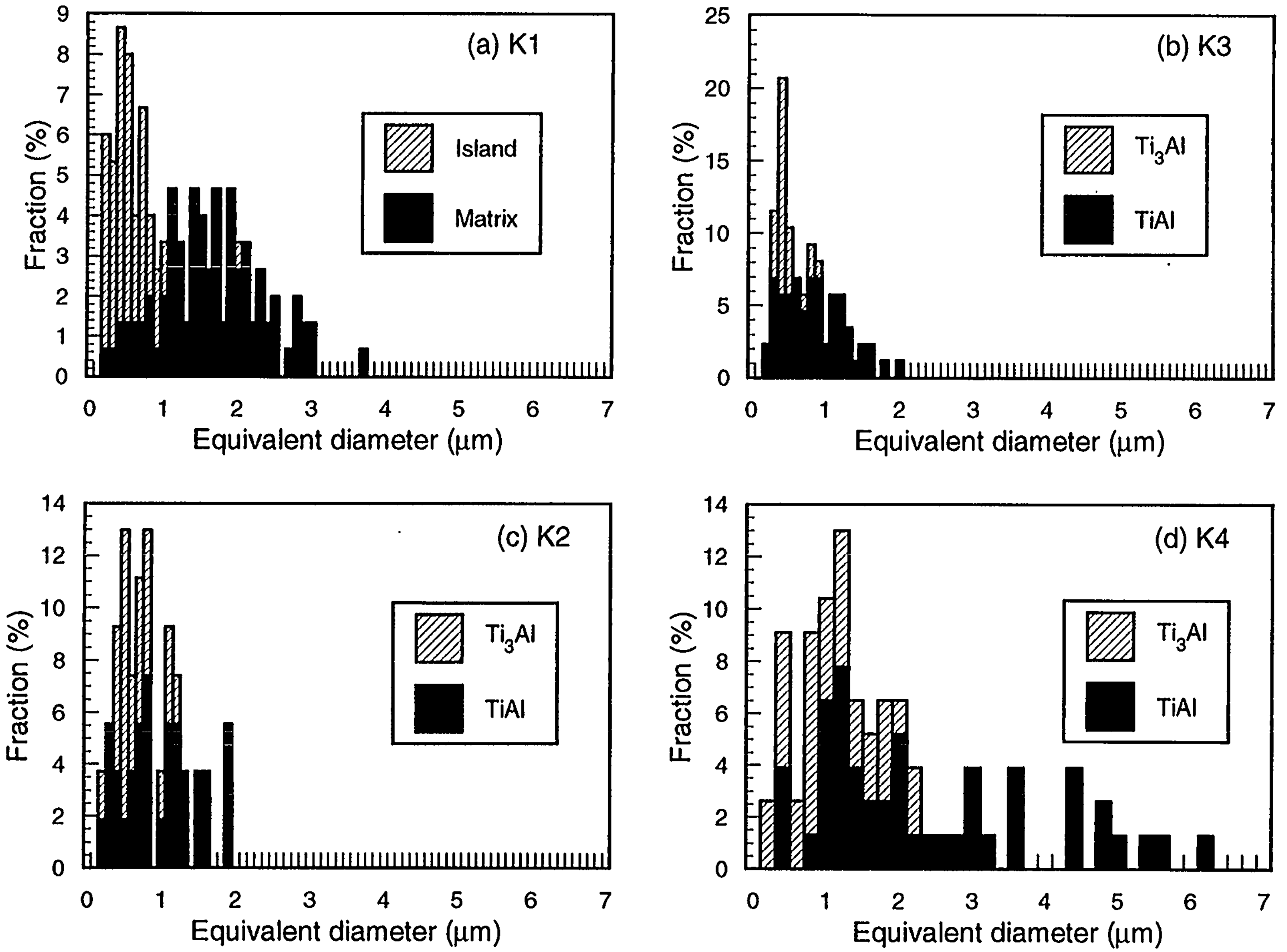

Figure 3 diametral size distributions of grains in unirradiated (a) K1, (b) K3, (c) K2 and (d) K4.

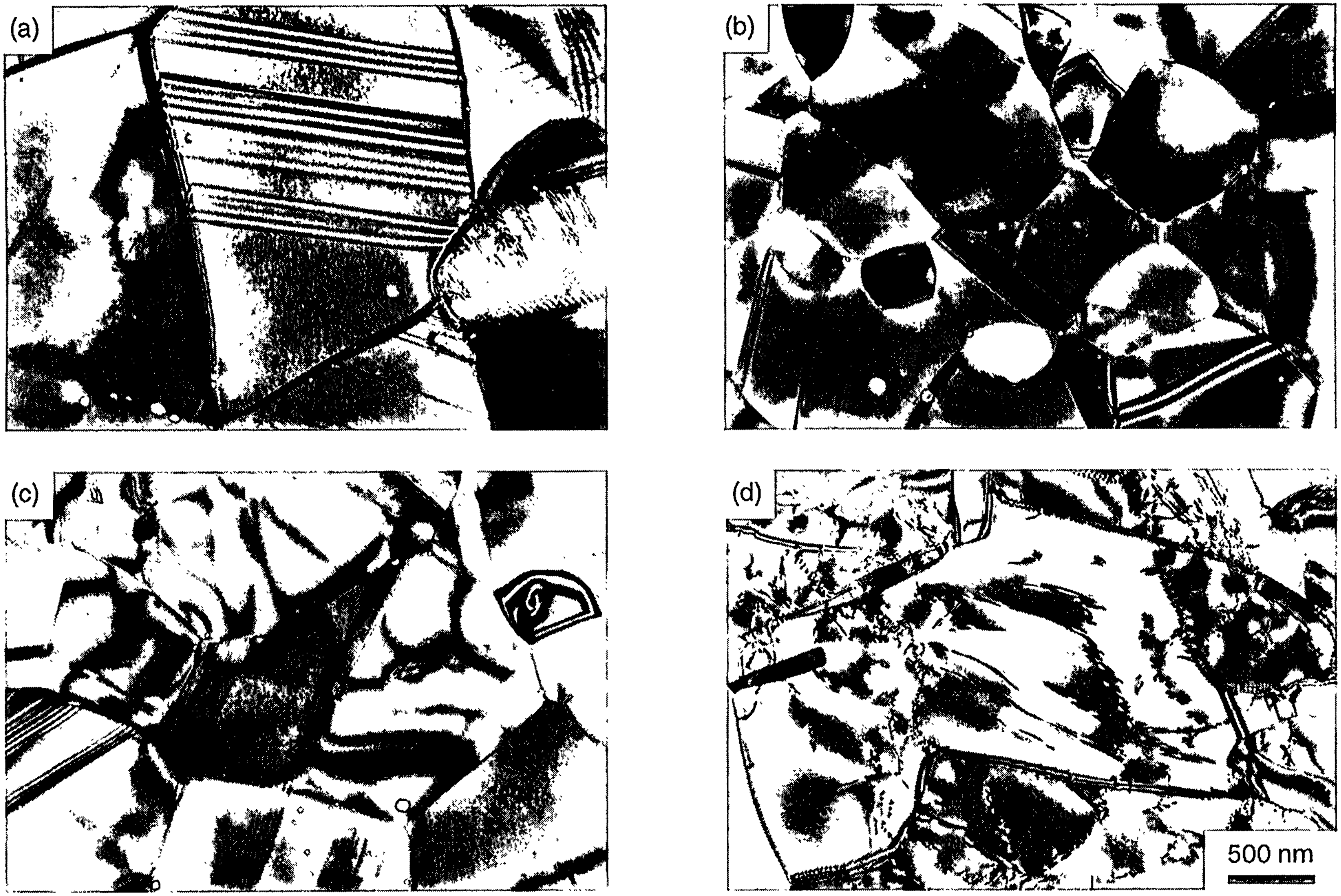

Figure 4 Microstructures of unirradiated (a) K1, (b) K3, (c) K2 and (d) K4. In mechanically alloyed K1, K3 and K2, pores were observed especially on grain boundaries.

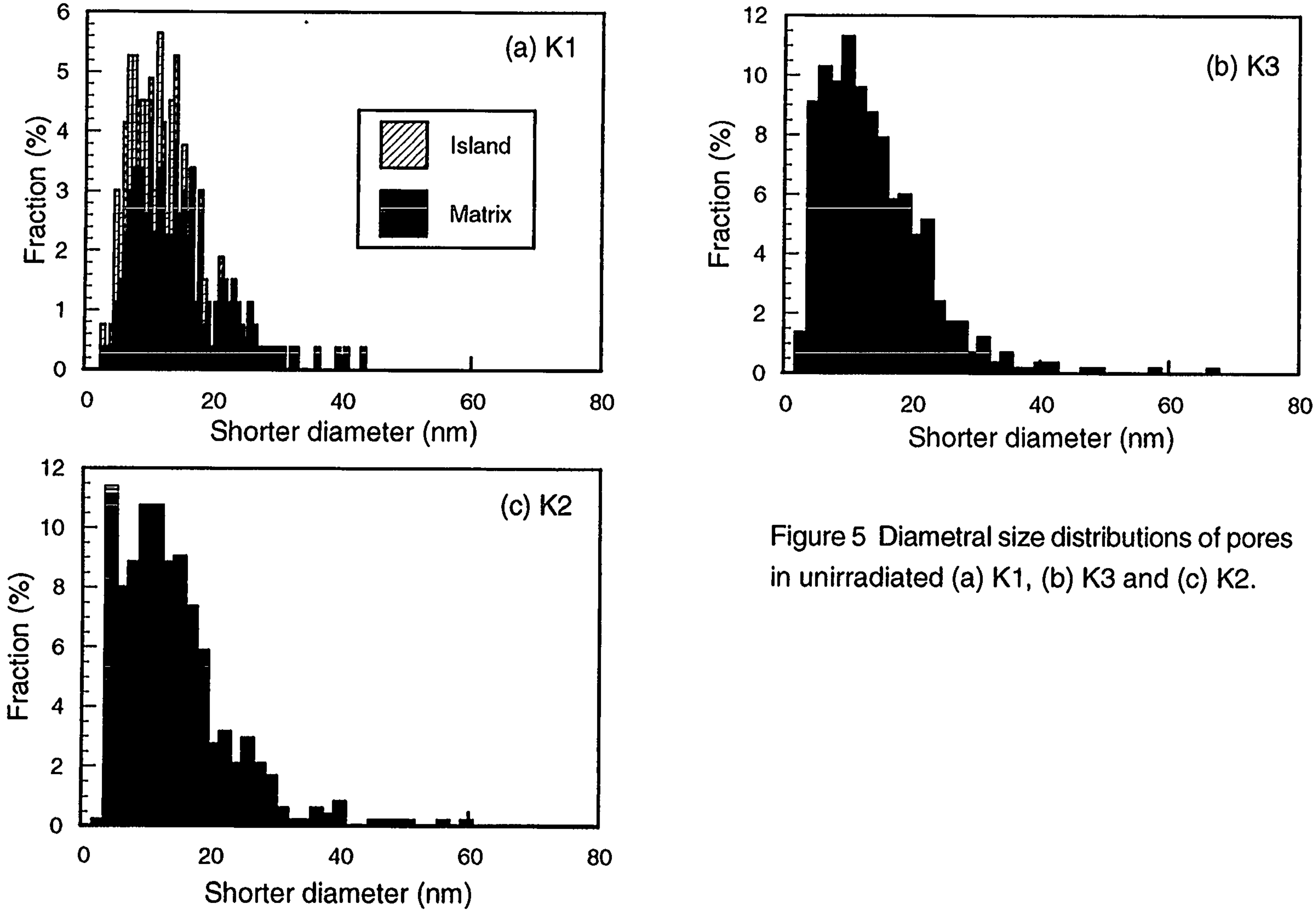

Figure 5 Diametral size distributions of pores in unirradiated (a) K1, (b) K3 and (c) K2.

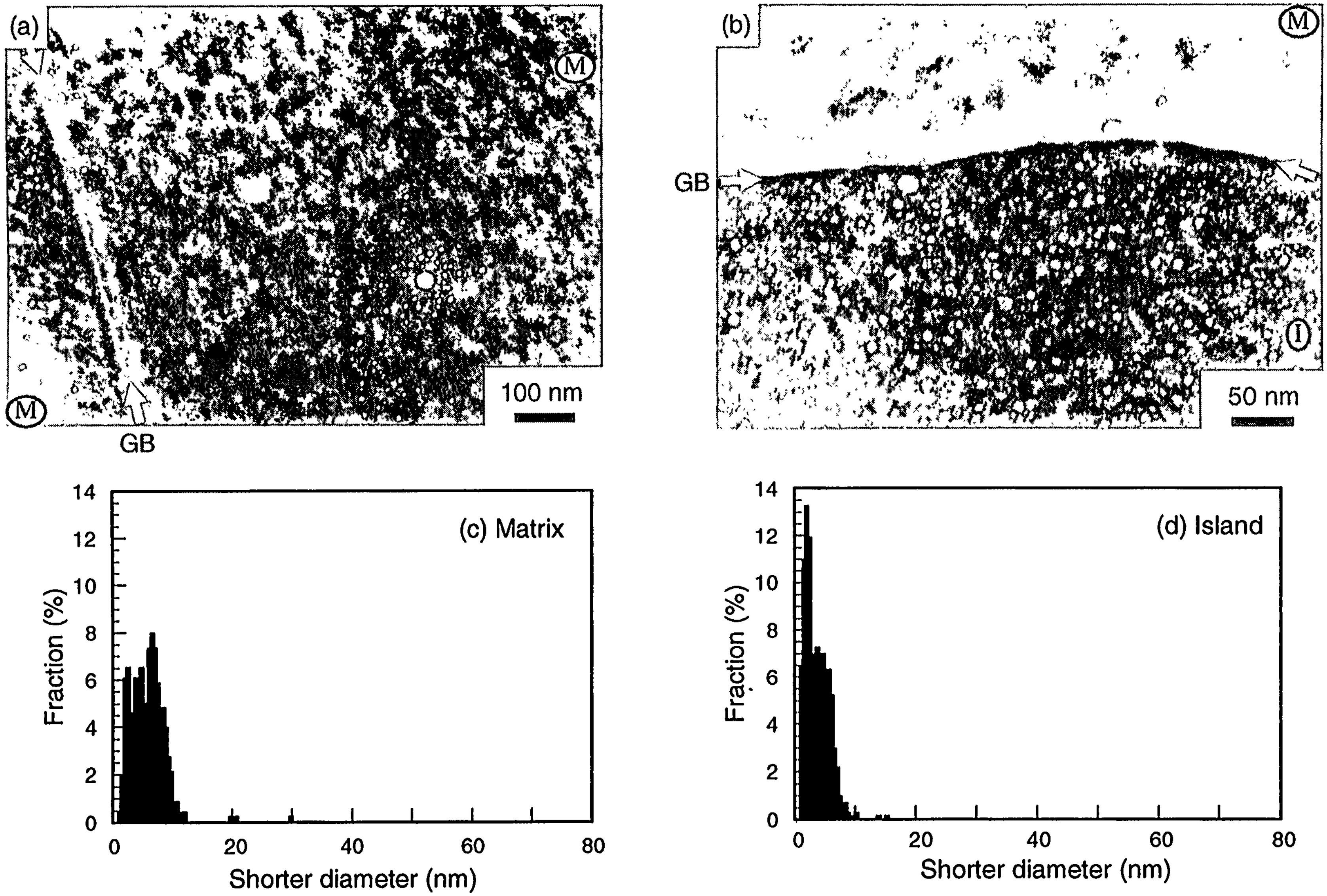

Figure 6 Cavities and diametral size distributions in matrix ((a), (c)) and island ((b), (d)) of irradiated K1.

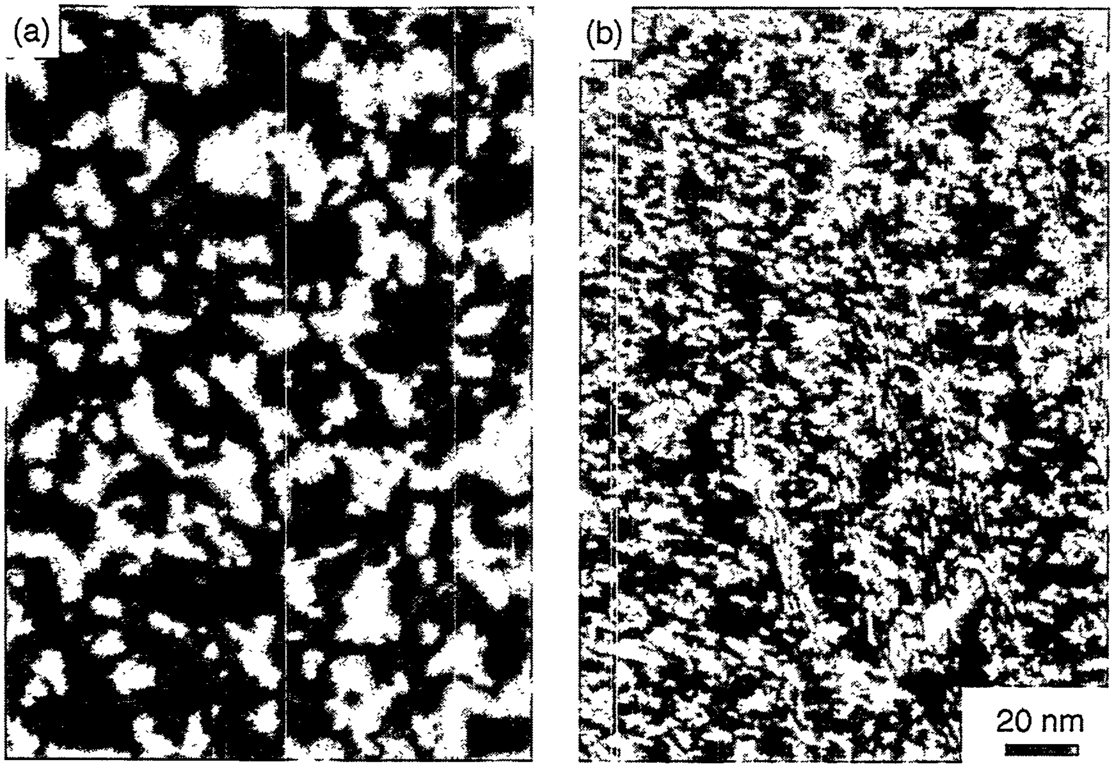

Figure 7 Weak-beam dark-field images in (a) matrix and (b) island of irradiated K1.

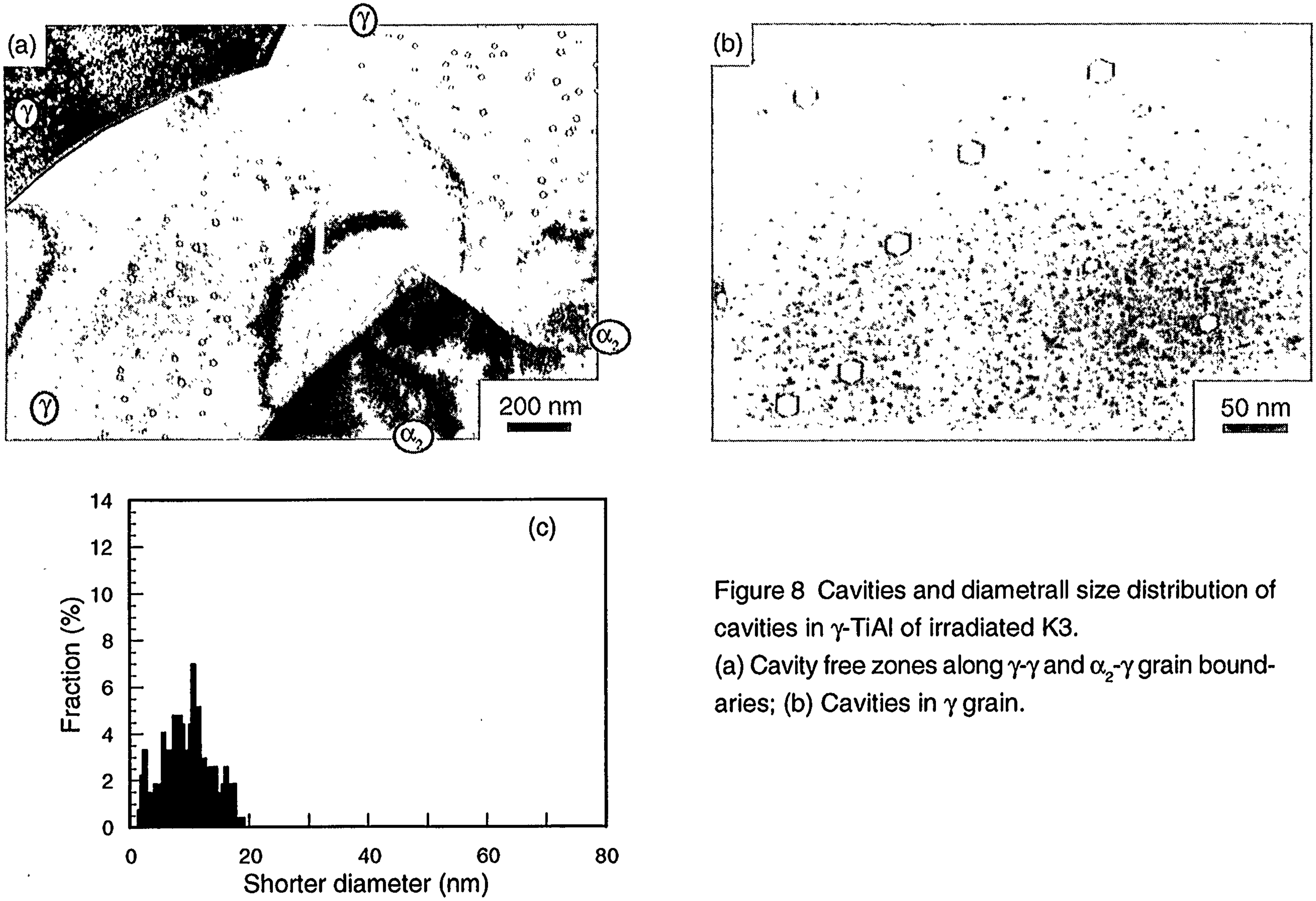

Figure 8 Cavities and diametrall size distribution of cavities in γ-TiAl of irradiated K3.
(a) Cavity free zones along γ-γ and α_2-γ grain boundaries; (b) Cavities in γ grain.

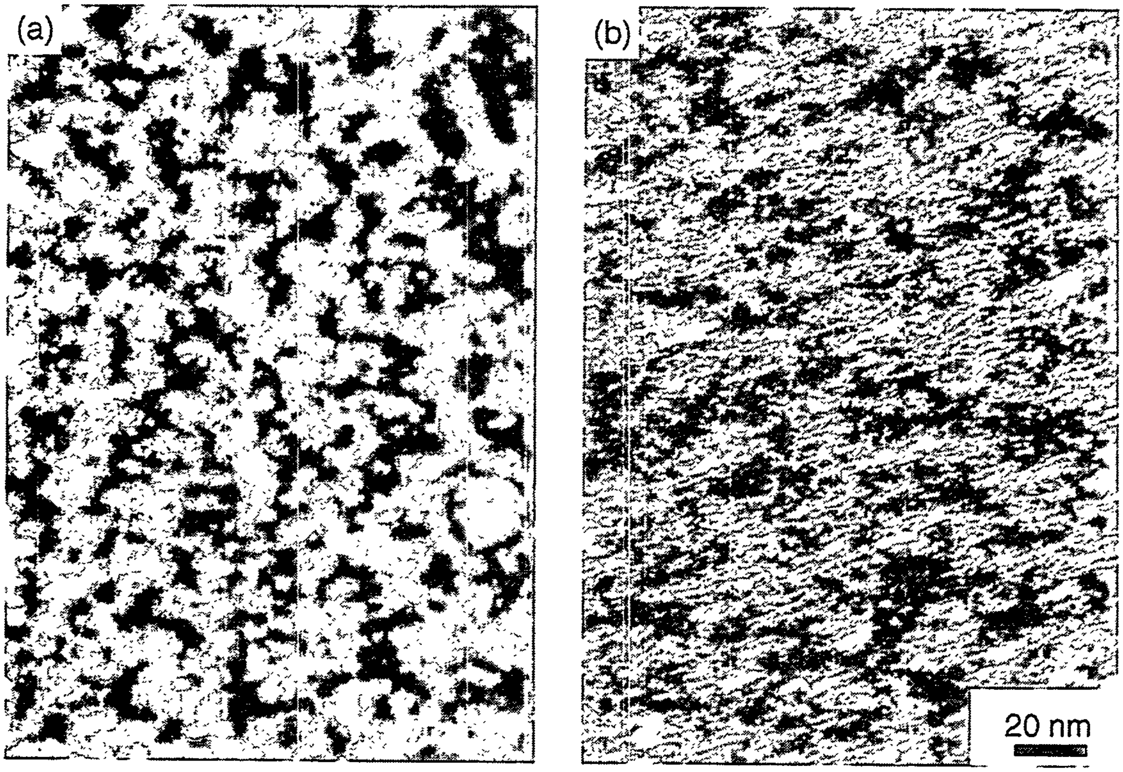

Figure 9 Weak-beam dark-field images in (a) γ-TiAl and (b) α_2-Ti_3Al of irradiated K3.

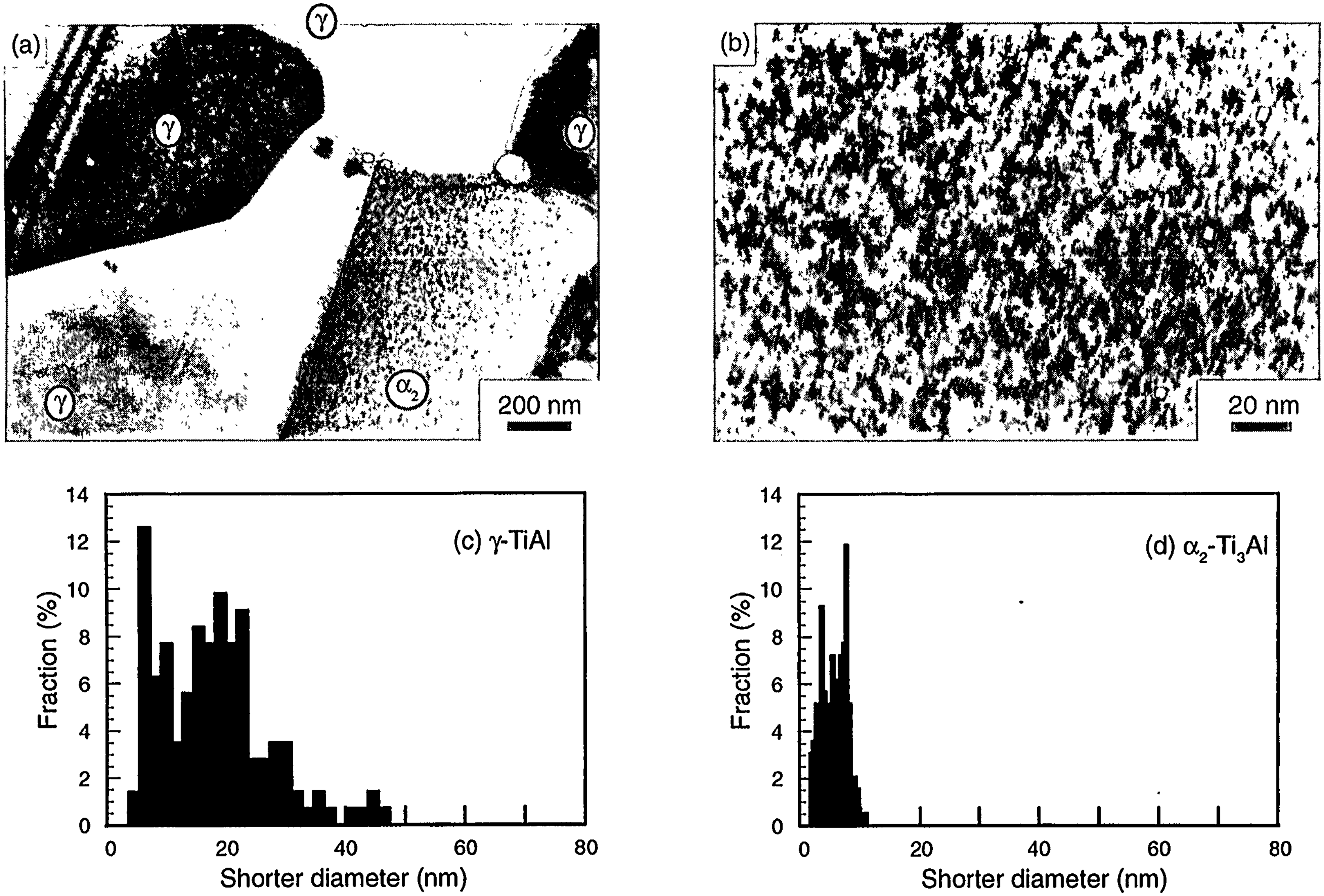

Figure 10 Cavities and diametral size distributions in γ-TiAl ((a), (c)) and α_2-Ti_3Al ((b), (d)) of irradiated K2.

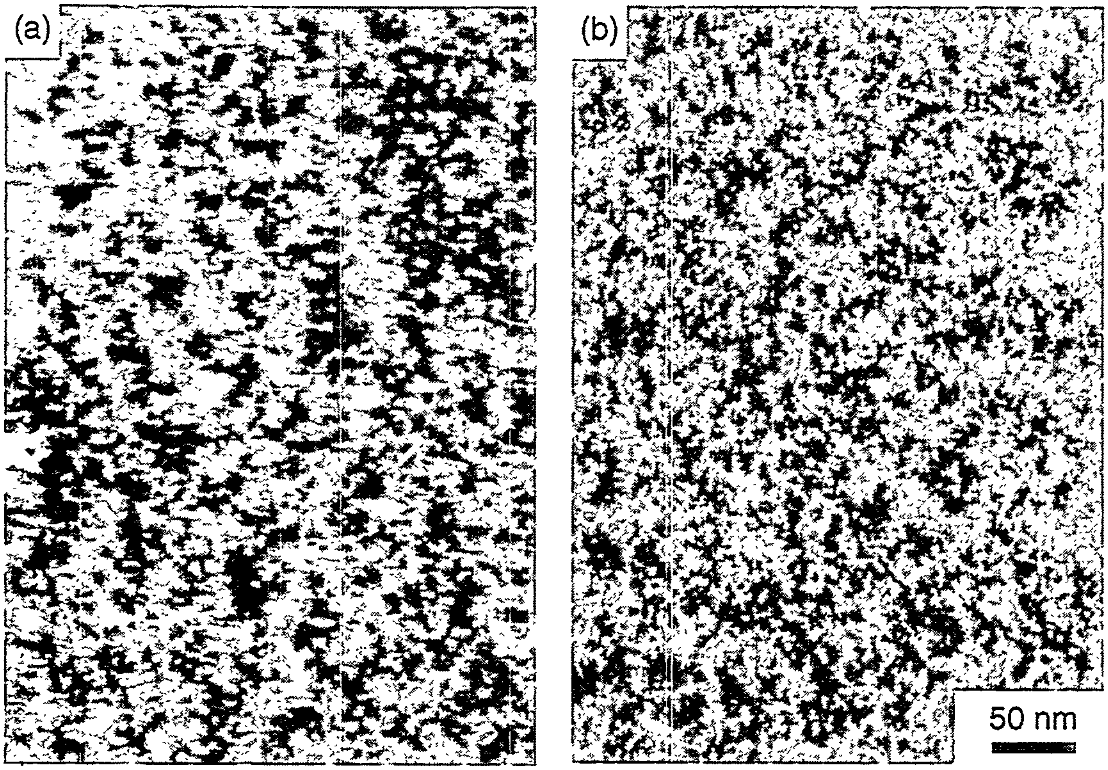

Figure 11 Weak-beam dark-field images in (a) γ-TiAl and (b) α_2-Ti_3Al of irradiated K2.

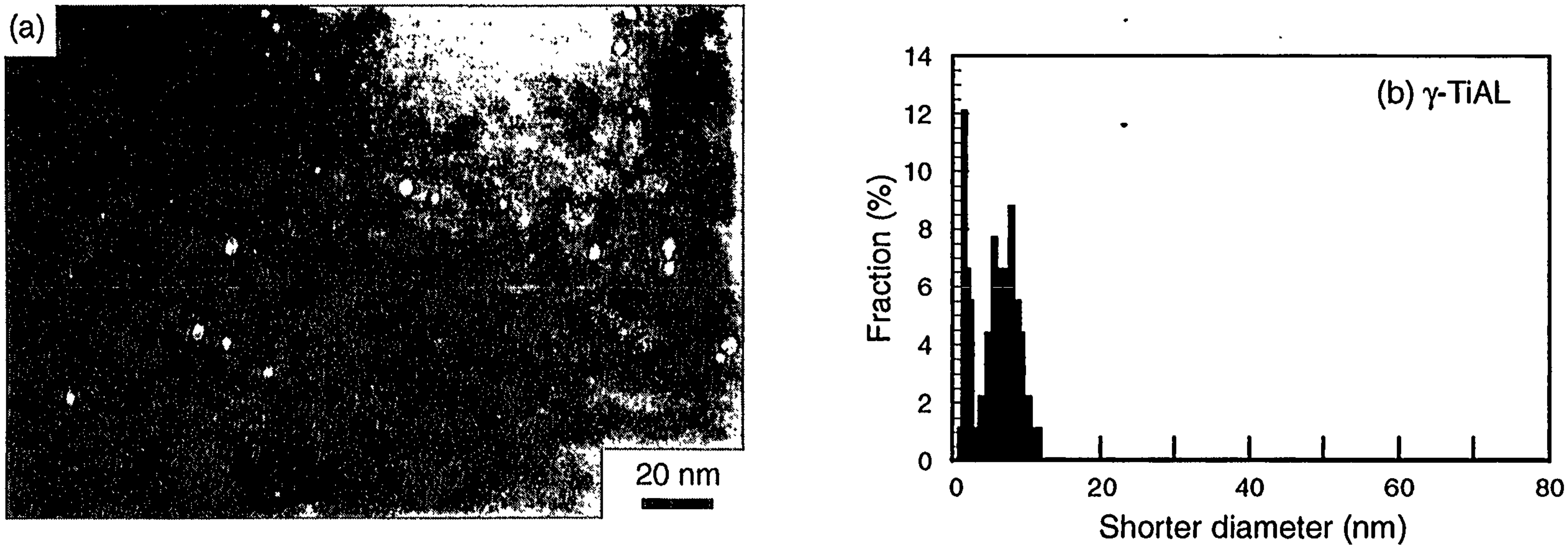

Figure 12 Cavities and diametral size distribution in γ-TiAl of irradiated K4.

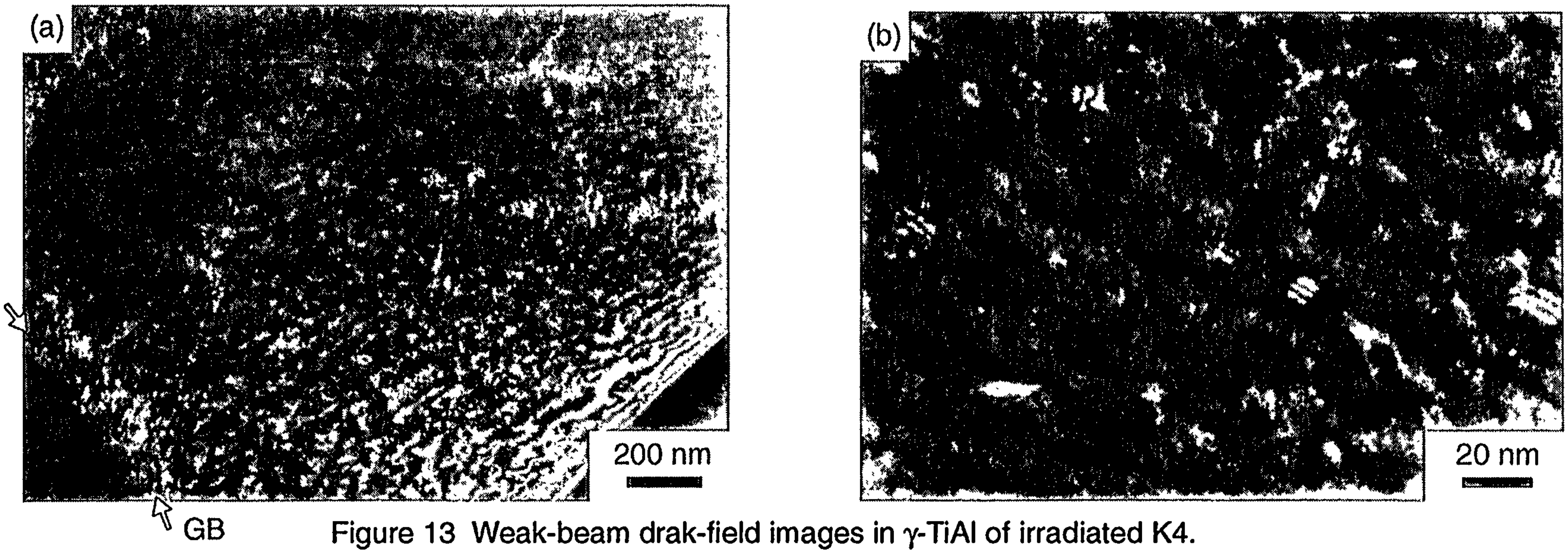

Figure 13 Weak-beam drak-field images in γ-TiAl of irradiated K4.

5.0 AUSTENITIC STAINLESS STEELS

No contributions.

6.0 INSULATING CERAMICS AND OPTICAL MATERIALS

No contributions.

7.0 SOLID BREEDING MATERIALS

No contributions.

8.0 RADIATION EFFECTS, MECHANISTIC STUDIES, AND EXPERIMENTAL METHODS

AN INTEGRATED THEORY, MODELING, EXPERIMENTAL, AND DATABASE PROGRAM FOR THE DEVELOPMENT OF ADVANCED FUSION MATERIALS —

R. E. Stoller (Oak Ridge National Laboratory), G. R. Odette (University of California-Santa Barbara), and H. L. Heinisch (Pacific Northwest National Laboratory)

SUMMARY

A *Whitepaper on an Integrated Theory, Modeling, Experimental, and Database Program* has been prepared as part of the overall AMP planning process. A review of the current program status has lead to the following primary recommendations: (a) an ambitious integrated modeling program should be initiated and closely linked to the entire AMP program, (b) program planning should consider the items identified by the workshop participants described in Appendix A and those listed in Table 4.1, (c) the program should encourage inter-institutional collaborations, i. e. between national laboratories and universities as well as between national laboratories, (d) regular program exchanges and reviews should be an integral part of the program, (e) both new and ongoing research should demonstrate relevance to the issues described in this document and the overall AMP White paper.

OBJECTIVE

The objective of this report is to describe the program's response to the FESAC panel recommendation for increased attention to modeling and the relationship between the modeling and experimental components of the program. It has been prepared as part of the larger AMP planning process. The overall AMP White Paper identifies the technological challenges to establishing the feasibility of utilizing the four groups of structural materials currently under consideration for applications in fusion environments. These feasibility issues provided the anchor-point for the development of the integrated modeling and experimental program discussed below.

PROGRESS AND STATUS

1. INTRODUCTION AND OBJECTIVES OF PLANNING ACTIVITY

This white paper attempts to describe an improved framework for establishing an integrated theory, modeling, experimental, and data base program for developing advanced fusion materials. This document is not intended to be a complete review of the current program with examples, data, models and references. Rather, the intent is to provide guidance on fundamental issues related to fusion materials development and to describe the concept of integrated modeling. The overall objective is to infuse the program with new ideas and people, to leverage broad advances in science and engineering and, most importantly, to accelerate the development of materials systems that will help make the promise of fusion energy into a 21st century reality.

The Advanced Materials Program (AMP) is funded through the U.S. DOE Office of Fusion Energy Sciences. This program is currently being restructured to reflect an increased focus on the underlying science required to develop materials for use in a fusion power system. As part of this process, the AMP was recently reviewed by an expert panel appointed by the Fusion Energy Sciences Advisory Committee (FESAC). In its report, the FESAC Materials Review Panel recommended that the AMP should adopt the following as its primary goal: "To provide the materials science knowledge base that will enable the utilization of fusion energy. The near-term emphasis will be on feasibility issues for in-vessel components for deuterium-tritium systems."

The panel recognized that combined advances in materials science understanding and modern computing capabilities can be used to extend the AMP's ability to develop meaningful physically-based, semi-empirical models that can guide and help interpret 'costly and difficult to obtain' experimental information. The panel recommended that these models should be developed and applied to the key feasibility issues associated with each class of material, and that crosscutting phenomena common to multiple materials are particularly good candidates for their application.

The greater emphasis on modeling should primarily be seen in the context of increased integration of theory, experiment, and database development as part of the long-term effort to build a knowledge base. It is essential that an expanded computational materials effort should:

a) focus on the key issues in fusion materials,
b) be closely integrated with the experimental program, which should include experiments designed for model validation and obtaining parameters requited by the models,
c) be as collaborative as possible and be leveraged by other activities,
d) produce tangible useful results (e.g. more reliable predictions of properties), and finally
e) provide the scientific basis for improved design and methods of structural integrity assessment.

In a related recommendation, the panel encouraged the AMP to utilize a system of roadmaps as a means of defining feasibility issues, and of identifying the skills and resources required to address them. In response to this recommendation, the AMP has recently developed a draft White Paper and a roadmap that discusses its current strategic pathway to fusion materials development. The AMP White Paper identifies the long-term goal of the AMP as the development of structural materials that will permit fusion to be developed as a safe, environmentally acceptable, and economically competitive energy source. This goal is to be accomplished through a science based program of theory, experiment, and modeling that:

a) provides an understanding of the behavior of candidate material systems in the fusion environment and identifies limiting properties and approaches to improve performance,
b) undertakes the development of alloys and ceramics with superior properties for service in the fusion environment through the control of composition and microstructure, and
c) provides the materials technology required for production, fabrication, and power system design.

This *Whitepaper on an Integrated Theory, Modeling, Experimental, and Database Program* (hereafter referred to as the *integrated modeling program*) has been prepared as part of the overall AMP planning process. In particular, it is the program's response to the FESAC panel recommendation for increased attention to modeling and the relationship between the modeling and experimental components of the program. The overall AMP White Paper identifies the technological challenges to establishing the feasibility of utilizing the four groups of structural materials currently under consideration for applications in fusion environments. These feasibility issues provided the anchor-point for the development of the integrated modeling and experimental program discussed below.

As part of the process of developing this document, the authors circulated a draft version of this document to the larger materials science community to solicit comments. That draft version also provided the basis for discussion at an open workshop that was held to obtain further input from the community. A summary of the workshop is provided in Appendix A. This final version of the whitepaper attempts to incorporate the comments that have been received. Although the conclusions and recommendations represent primarily the views of the authors, they have been assisted by an ad hoc peer-planning group of other AMP-funded scientists: G. E. Lucas (UCSB), K. Natesan (ANL), S. J. Zinkle (ORNL), A. F. Rowcliffe (ORNL), and R. J. Kurtz (PNNL). Contact information for the authors is given in Appendix B.

2. INTEGRATION OF MODELING AND EXPERIMENTAL ACTIVITIES IN ADVANCED MATERIALS PROGRAM

The overall strategy is a commitment to developing physically-based models that can be used to address the materials feasibility issues in the AMP White Paper, e.g. to make predictions of key mechanical properties starting in the as-fabricated state and evolving as a function of prolonged service in a fusion environment. Including consideration of the pre-service properties forms a strong and interactive link to material design and the influence of the entire thermal-mechanical history experienced by a material in a component, from initial processing though fabrication of integrated structures. It also serves as a basis to develop the requisite fundamental microstructure- property and basic property-engineering property models.

In-service effects will be mediated by a combination of factors including temperature, stress, the chemical environment and the neutron flux, fluence and spectrum. It is well known that there are synergistic interactions among this multitude of variables; and that complexity is further amplified by the overall temporal history of the service environment. Thus as a reasonable and necessary expedient, this effort will start with relatively simple models for selected properties, with ongoing development leading to more robust and comprehensive models as the knowledge base is improved. Finally, the integrated modeling program should also establish links with researchers involved in the development of advanced design and structural integrity assessment methods. For example, a better understanding of the micromechanics of the ductile-to-brittle transition can be obtained by linking our understanding of both atomic scale processes and embrittlement phenomena to an engineering code-based structural integrity assessment such as the master curve method.

Generally, the underlying physical basis of these models developed under OFES funding will be microstructural, including the mechanisms that lead to the production, transport and fate of defects and key constituent species as a function of the material and irradiation-service variables. The microstructure must be linked to basic structure-sensitive properties, like the yield stress, and such basic properties must in turn be linked to other engineering properties, like fracture toughness. Microstructural information and mechanical property data developed within the experimental component of the AMP, as well as relevant data generated by other programs such as Basic Energy Sciences (BES), the Nuclear Regulatory Commission (NRC), and the wider materials community, will provide the basic information needed for model development and verification. This implies developing and applying:

- integrated multiscale models of microstructural evolution and material properties mechanistic models describing key phenomena
- an appropriate mix of mechanical property testing and microstructural characterization tools
- experiments to investigate specific mechanisms (e.g., to explore helium transport, fate and consequences)
- verification of model predictions using the results of integral database experiments
- physically-based, engineering correlation models from evolving databases

A key product commitment is the development of mechanical performance maps (similar to Ashby maps) by systematizing and condensing the information in the knowledge base. This will also help to provide an interface between materials research and engineering design studies.

Clearly the long-term tasks outlined above are an enormous challenge and cannot be fully, or even primarily, funded by OFES. Thus, a critical part of this effort will be establishing links to the expanding general knowledge base regarding the microstructures, properties, and performance of materials to fusion specific applications. A high priority should also be given to developing and enhancing interactions between OFES-funded research and other research efforts in the larger materials science community. Support for new research efforts should require effective awareness and expertise in the larger field of materials science, while at the same time demonstrating a useful fusion focus. The efficient use of resources also requires that the research groups funded by OFES collaborate effectively. This will ensure that information flows freely and will eliminate unnecessary duplication of effort. Thus, an additional commitment is to improve the framework for collaboration between those institutions and individuals that are funded by the program. This involves cooperation and the development of partnerships between the national laboratories as well as between the laboratories and university programs.

3. FUNDAMENTAL MATERIALS ISSUES IN THE FUSION REACTOR ENVIRONMENT

As noted above, an effective integrated modeling effort cannot focus solely on effects of the radiation environment. Not only do many other factors in the service-environment itself affect material performance and lifetimes (e.g., fatigue loading, environmentally assisted cracking,...), but a myriad of other issues such as materials processing, fabrication and joining, developing functional coatings, fracture and structural mechanics need to be considered. However, it is also clear that the microstructural changes induced by the radiation environment and, hence, corresponding changes in the constitutive and fracture properties are an overarching consideration. Further, because of limitations in available irradiation facilities, assessing long- term high-fluence radiation effects in a fusion environment represents perhaps the most difficult challenge. Given this circumstance and the practical limitations of preparing this brief background paper, radiation effects, and the unique aspects of the fusion environment, will be the primary focus of the following discussion.

3.1 Radiation Effects Issues

3.1.1 DT fusion radiation environment

The basic irradiation environment in the high neutron flux regions of a fusion system is in many ways similar to that experienced by the in-core components in a high flux fission reactor. Thus many of the phenomena noted above can, and indeed have been, studied in fission reactors. Unfortunately, however, there are significant differences between the neutron spectra in fission and fusion systems that must be considered. It is expected that early fusion systems will generate energy by the fusion of deuterium and tritium (DT). The primary differences between the radiation damage source term in the two environments are related to the fact that the DT fusion neutrons are all born at 14.1 MeV, while the fission source exhibits a spectrum with a peak near 2 MeV. The neutron spectra in both cases cover a wide range of energy as a consequence of scattering reactions. However, the presence of higher energy fusion neutrons has two major impacts: a) higher energy primary atomic recoils; and b) high nuclear transmutation production since many such reactions have energy thresholds well above 2 MeV. In particular, the rate of helium and hydrogen generation by (n,a) and (n,p) reactions is on the order of 10 to 100 times higher in the DT fusion case.

Since fission reactor experiments are a major source of radiation effects data, much of the previous experimental and modeling work in the fusion materials program has been aimed at determining the impact of the higher energy DT neutrons. The impact of higher energy atomic recoil cascades has been most successfully examined by molecular dynamics (MD) simulations of displacement cascades. Considerable evidence based on simulations now supports the view that the net effect of spectral differences between fission and fusion may be rather small. This conclusion is also supported by various experimental evaluations that suggest dpa is often a good correlation parameter to account for spectral effects arising from differences in primary displacement damage production. However, the MD results provide information on the radiation damage source term only for times up to ~100 picoseconds. Understanding the correlated local evolution of the nascent cascade damage over times as long as gigaseconds, and the consequences of this process to long-time and long-range defect transport and fate is a key unresolved issue. Further, subtle differences between cascade damage in fusion versus fission environments may be amplified at these longer times. The resolution of these issues requires the use of techniques such Monte Carlo (MC) simulations to examine the evolution of the cascade residue for times long enough to permit diffusion of and reactions between the point defects.

Finally, it should be mentioned that there is no single "fusion irradiation environment." The neutron flux level and the energy spectrum change significantly as the distance from the plasma increases due to neutron scattering and absorption. The flux and spectrum are also influenced by the different neutronic characteristics of the various coolants (water, helium, or lithium) and structural materials (iron-based, vanadium-based, SiC) that may be employed. These flux and spectrum changes are particularly important for assessing the anticipated effects of transmutation products. Thus, the irradiation environment for any one location in a given fusion reactor design must be evaluated in detail to determine how different the conditions are from those available in a fission reactor environment or other available irradiation test facilities.

3.1.2 Modeling radiation damage

The high energy neutron bombardment leads to elastic collisions with atoms which are in turn ejected from their crystal lattice positions (atomic displacements), and the production of transmutant products by nuclear capture reactions. Insoluble helium and reactive hydrogen gases are major transmutation products. Typical end-of-life fluences for fusion structural materials will lead to 200 displacements per atom (dpa), 2000 appm of helium, 20,000 appm hydrogen and percent-level production of solid transmutants. These "primary damage" products act in tandem with thermally and stress-driven processes to produce profound changes in the pre-existing microstructure (e.g., dislocations, precipitates, lath boundaries, ...). In addition, radiation damage leads to the formation of new microstructural features such as dislocation loops, voids, bubbles, regions of chemical segregation, and radiation-induced or enhanced precipitate phases that are often new and non-equilibrium in character.

The processes controlling microstructural evolution are mediated by a complex combination of atomistic level dynamics, defect physics, non-equilibrium thermodynamics, and transport kinetics. Relevant length scales range from atomistic to continuum, and time scales from femto to gigaseconds. The microstructural changes often lead to severe degradation of a wide range of important mechanical properties, as well as significant dimensional instabilities. Radiation- induced changes in physical properties are generally not a concern for metals, but changes in properties such as thermal and electrical conductivity will be important for ceramic components as discussed in section 3.3.

The ultimate aim of radiation materials science is to understand the production, transport, fate and consequences of all defect and material elemental species. This requires an integration of sophisticated theory, models, mechanistic experiments and comprehensive engineering databases. Understanding of key microstructural processes is the underlying requirement for developing practical methods to accurately assess the in-service performance under irradiation, and to develop more radiation stable materials. For example, superior performance can be achieved by enhancing the recombination of displaced atoms and vacant lattice sites, and by controlling the distribution of helium. Such understanding requires combining atomistic (e.g., electronic, MD and MC) and mesoscopic models (e.g., rate theory) with high-resolution microanalytical characterization measurements and specially designed single variable experiments. Further, modeling the consequences of microstructural evolution on property changes requires developments at the frontiers of the science of deformation, fracture and fatigue.

The production of primary defects and aged cascade features is only one small, albeit critical, part of irradiation induced/enhanced microstructural evolution. Long range transport of defects leads to: a) additional clustering (vacancies, interstitials and gases) and extended defect formation; b) defect annihilation, that may or may not change the character of the corresponding sinks (e.g., increases or decreases in network dislocation density); and c) rearrangement of solutes accelerated by radiation enhanced diffusion or driven by coupling with persistent defect fluxes (e.g., the inverse Kirkendall effect). A key feature of these processes that has received very little attention in most previous radiation damage studies to date is the profound role of alloy chemistry. All the post cascade formation stages of these processes are likely to be affected by details of the interaction of multiple atomic species. For example, it has been shown that even small defect clusters formed in cascades are complexed with various solutes. Thus it is critical that atomic level descriptions of alloy thermodynamics and kinetics be developed and coupled with mean field rate theory models. The former can be accomplished by combining appropriate models of interatomic interactions, like the embedded atom method, with MD, MC and similar simulation tools. Treating long range interactions (e.g., strain fields) is another major challenge that will require the application of new tools like domain decomposition methods.

Rate theory is based on spatially and short time averaged solutions to the production, diffusion, drift, reaction equations that describe conservation of all pertinent species. These typically take the form of large sets of coupled ordinary differential equations, where the pertinent physics is included in the coefficients for the various reaction terms, invoking the assumption of local equilibrium. It should be noted here that there is a natural synergism in such atomistic-continuum couplings. Specifically, while rate theory has been shown to be a powerful tool in understanding effects of irradiation on microstructures, it has three main drawbacks:

a) computational challenges associated with solving large sets of coupled equations;
b) substantial uncertainties in the averaged reaction coefficients; and
c) all the key physics must be input in the model equations and coefficients.

If some of the relevant physics is missing, it will not be revealed in the solutions to the rate theory equations. Some of the barriers to rate theory are dissolving in the face of the expanding capabilities of computers and more sophisticated mathematical methods of computation. Electronic-atomistic methods can now be used to provide much-improved estimates of not only the rate theory coefficients themselves, but also insight into the key physics and phenomena that must be modeled.

Ongoing model development may lead to a healthy competition between the rate-theory-based models and more atomistic approaches, such as MC simulations. Computational advances are extending the reach of MC into larger length and longer time scales, while the rate theory is being enhanced by increasing physical robustness and the computational tractability of solving large scale simulations. Both approaches are likely to be important sources of new insights and their hybrids will provide the basis for developing powerful microstructural evolution models.

3.1.3 Helium effects

Returning to the unique aspects of the fusion environment, a variety of techniques have been applied to examine the role of transmutant helium on microstructural evolution and mechanical property changes. Although some insight has been obtained, key aspects of the behavior and effects of helium remain unresolved. The effects of transmutant helium (and to a lesser extent hydrogen) can be synergistic with displacement damage. Helium stabilizes small vacancy clusters; depending on other factors, this may lead to either more or less void swelling and a potential reduction in creep rupture times and ductility due to enhanced grain boundary cavitation. The effects of helium on creep rupture are an example of a direct connection between microstructure and properties. In this case the combination of applied stress, temperature, helium, matrix hardening, irradiation and thermal creep all combine to influence this key property.

Helium management, generally accomplished by trapping a fine distribution at stable sinks, is a major objective of alloy development efforts, and leads to a belief that the effects of helium may be greater in single-phase alloys, particularly at high temperatures. There is also some puzzling evidence that high helium levels may produce low temperature embrittlement in excess of that associated with hardening. Thus, understanding the generation, transport, fate and consequences of helium transmutation remains a very high priority that cuts across material types. Similar arguments may be pertinent to environmental and transmutant induced hydrogen; however, the high mobility of this element may limit its consequences.

3.2 Performance Related Mechanical Properties in Metallic Alloys

While understanding and modeling microstructural evolution is a necessary condition for developing useful physically based models, it is far from sufficient. It is also necessary to develop models of how the altered microstructure influences the basic constitutive properties and local 'fracture' properties that control material separation by both ductile and brittle processes. This information must in turn be related to continuum measures of engineering mechanical properties, like fracture toughness, and ultimately to structural load and displacement capacities. Even when fully focused on fusion specific issues, this subject is too large to be reviewed here. Rather, selected targets for developing microstructure-property and property-property models are given. Indeed, in several of these cases there has been a great deal of recent progress.

3.2.1 Radiation induced elevations of the yield stress.

At low strains, obstacle hardening due to precipitates, cavities, defect cluster-complexes and dislocations in the form of loops and a dislocation network can be reasonably modeled by combining assessments of the individual strengths of the obstacles with models of how dislocations move though arrays of such features. Key unresolved issues include: a) details of dislocation-obstacle interactions, b) dislocation self-interaction effects, and c) multiple dislocation effects.

3.2.2 Static post-yield constitutive properties and deformation patterns.

Engineering alloys normally strain harden and can be well modeled at a continuum level by relatively simple flow and plasticity laws. However, post yield behavior following irradiation is often characterized by softening and highly localized flow in coarse slip regions and, in extreme cases, in flow channels. The macroscopic consequences of such strain softening and flow localization range from negligible uniform elongation in tensile tests to severe reductions of toughness associated with fracture by shear band decohesion. This problem is very rich, involving the effect of local plasticity on dislocation obstacles, the dynamics of dislocation structure formation, strain induced damage generation and dilatational plasticity, and internal stress and multiaxial stress state redistributions.

3.2.3 Swelling and irradiation creep

It seems unlikely that dimensional instabilities in fusion structures can be avoided due to void swelling and irradiation creep. The basic mechanisms of these phenomena are reasonably well understood. In the simplest view, both arise from biased partitioning of vacancies and interstitials to various sinks. In the case of swelling, excess vacancies flow to growing voids; in the case of creep, excess interstitial fluxes flow to stressed dislocations as a function of their Burgers vector. Swelling and creep are interactive as demonstrated by phenomena such as stress assisted swelling. Although irradiation creep appears to be ubiquitous, some alloys fortunately appear to be swelling resistant. However, a number of major issues remain to be fully resolved, including:

a) the effects of high helium levels and consequential interactions with displacement damage;
b) the mechanisms which give rise to apparent swelling resistance in some bcc alloys and the persistence of this resistance;
c) interactions between swelling and phase instabilities;
d) the role of defect cluster-complexes formed in cascades, and the properties of these complexes; and
e) the effects of stress and stress sate.

Since swelling and creep are directly linked to microstructural evolution, resolution of these issues will require a combination of tools listed above.

3.2.4 Thermal creep, creep rupture and creep crack growth

At temperatures above about 40% of the absolute melting point, thermal creep, creep ductility and rupture times are important. The influence of irradiation on thermal creep rates depends primarily on changes in the microstructural features that act as obstacles to dislocation climb and glide. A more serious issue is the effect of high helium levels on rupture times and ductility because of its influence on fracture mechanisms. Helium promotes the nucleation of high concentrations of grain boundary cavities that become unstable to growth at lower stresses and coalesce at smaller strains than coarser populations of normal creep cavities. The presence of stress concentrations at the tips of growing creep cracks could lead to very short time, low ductility failures. Simple models focusing only on cavity growth are inadequate; the effects of local microstructures and deformation processes in the matrix, near boundaries, and in the boundaries themselves play key roles. Inhomogeneous deformation processes lead to complex internal stress and stress state redistributions. Thus, better understanding will require the application of sophisticated multiphysics models that can deal with combined geometrically and constitutively complex defect flow-deformation processes.

3.2.5 Fast fracture and the ductile-to-brittle transition temperature (DBTT)

There are two types of low toughness fracture processes that are of concern. The first is associated with loss of strain hardening/ductility and flow localization; in the extreme this may lead to very low toughness and shear band decohesion. Progress will require understanding the microstructural conditions that mark this regime, developing basic constitutive laws for materials in this state, and large deformation modeling of local processes leading to material separation. Elevation of the DBTT is caused either by hardening or a reduction in the local tensile stresses required to produce cleavage or intergranular fracture. For example, the latter may occur due to segregation of elements such as phosphorous at grain boundaries, which may be accelerated by radiation-enhanced diffusion. The presence of hydrogen (from various sources) may also lead to this type of embrittlement. Progress will require continued development of combined micromechanical-macromechanical models of brittle fracture based on detailed observations of local fracture processes. These efforts should also seek close and direct ties to advanced structural integrity assessment methods based largely on small specimen testing.

3.2.6 Fatigue, creep fatigue and fatigue crack growth

Given the anticipated extreme thermal-mechanical loading conditions, avoiding fatigue related failures in complex fusion structures represents a tremendous challenge even when the complications of the effects of irradiation are not considered. One part of the challenge is that "fatigue" has numerous manifestations (for example, S-N limits in both low and high cycle ranges, da/dN rates, thermal-mechanical local and global ratcheting, and creep fatigue, just to name a few). Each of these types of fatigue are, in turn, controlled by a large number of intrinsic (material) and extrinsic (loading-geometry) variables. In fact, fatigue failures are very sensitive to details of the structure as well as the underlying material properties. Some, and perhaps most, multiphase alloy systems that have a useful balance of properties tend to experience cyclic softening and high rates of mechanical damage formation. Of course radiation-induced changes in the microstructure, basic constitutive properties (including irradiation creep) and deformation patterns may have a profound effect on the various types of fatigue processes. Given this tremendous complexity and the relative paucity of pertinent data, it is recommended that fatigue not be a high priority target of early-integrated modeling research. However, experiments aimed at generating engineering type data should be carried out with an eye to the ultimate development of microstructure-mechanism based fatigue models.

3.2.7 Environmentally-assisted cracking

The chemical environment often has very large deleterious effects on fracture and fatigue processes, enhancing crack initiation and subcritical growth. However, these effects not only involve multiple physical mechanisms that are complex and poorly understood, but are also often very system specific. Further, while there may be significant effects of the radiation environment, the relevant database for fusion.alloys is very limited. Thus as in the case of fatigue, it is recommended that integrated modeling research on environmentally assisted cracking should not be an early priority for the initial integrated modeling effort.

3.3 Other Significant Materials Issues

The previous discussion has focused on metallic alloys and their microstructural and mechanical stability in a fusion environment. However, there are many other opportunities for an integrated modeling effort dealing with issues such as:

a) ceramic composites and the stability and functionality of their engineered constituents;
b) insulator and barrier coatings;
c) corrosion and system level corrosion product transport;
d) the kinetics and consequences of impurity pick-up;
e) processing, fabrication and joining;
f) detailed component-level integrity-lifetime assessments that involve many phenomena (neutronics, magnetics, thermalhydraulics, stress and inelastic deformation) when the

materials are used in a complex, time-dependent stress state arising from gradients in the damage and thermal and mechanical loads.

3.3.1 Silicon carbide composites

SiC composite materials have been considered an attractive possible fusion structural material for primarily two reasons. The first reason is their potential for use at high temperatures with a concomitant increase in the thermal efficiency of the system. Successful high temperature application will require that the thermal conductivity of the material be high enough to limit stresses induced by thermal gradients. The thermal conductivity of current commercial materials is not sufficiently high due to the presence of impurities, and irradiation will lead to reductions in the thermal conductivity. The second desirable feature of SiC is its neutron activation and decay properties. The relatively low level of induced activity in SiC minimizes the amount of decay heat that must be removed after reactor shutdown. In addition, the induced radioactivity of pure SiC components would quickly decay, leading to possible hands-on maintenance of the structure within several days. However, the level of purity than can be obtained in commercial materials also limits this potential benefit. Even modest levels of metallic impurities significantly raise the level of induced radioactivity.

A short summary of current key issues for SiC composites would include:

a) fiber and coating stability and the consequences to bridging mechanics,
b) hermeticity and sealing coatings
c) swelling and creep (at high helium levels)
d) radiation-induced reductions in thermal conductivity,
e) joining; and
f) the integrity of complex, thermal-mechanically loaded brittle structures.

The role of nuclear transmutation, potentially leading to a high level of SiC burnup in service also warrants further investigation.

It is recommended that near-term modeling is best directed toward developing an understanding of the response of monolithic materials. A coordinated effort of fundamental modeling and experiments is needed to determine parameters such as the atomic displacement threshold on both the Si and C lattices, point defect formation and migration energies, and point defect binding energies for helium and hydrogen.

3.3.2 Ceramic coatings

The blanket system is one of the most important components in a fusion reactor because it has a major impact on both the economics and safety of fusion energy. The primary functions of the blanket in a deuterium/tritium-fueled fusion reactor are to convert the fusion energy into sensible heat and to breed tritium for the fuel cycle. In fusion applications, the structural material of the system must be capable of maintaining structural integrity for long periods while exposed to moderately elevated temperatures, mechanical loads, thermal cycling, and possibly intense irradiation. The material must be compatible with the coolant, which may water, helium, or a liquid metal

A major challenge in the design of liquid-metal-cooled blankets for use in high magnetic field tokamaks is the accommodation of the strong influence of the magnetic field on coolant flow. If the flow direction is perpendicular to the field, a potential difference across the duct is induced in the liquid metal. This can cause a large electrical current flow if the potential difference is short-circuited by the duct walls. An electrical current flowing perpendicular to a magnetic field leads to a mechanical force that causes a magnetohydrodynamic (MHD) pressure drop. It has been shown that even thin conducting walls would lead to a rather high pressure drop under the conditions of a fusion reactor blanket. For example, the pressure drop in a poloidal duct in an inboard blanket segment would reach 8.6 MPa if the conducting liner was 0.1 mm thick. This unacceptably high pressure drop shows the need for electrically insulating coatings in contact with the flowing liquid metal. It has been shown that a perfectly insulating coating on the wall would decrease the pressure drop from 8.6 to 0.22 MPa.

The current focus of insulator coating research is for the self-cooled lithium blanket with a vanadium alloy structure. Primary criteria for selection of candidate coating materials include the following:

- chemical stability/compatibility of the coating with both the vanadium alloy and the lithium of normal or specified practical purity at elevated temperatures
- high electrical resistivity
- potential for coating of complex channel geometries
- potential for *in situ* self-healing of any defects that might occur in the coating under prototypic operating conditions.

Other considerations important to the development of insulating coatings for the fusion applications include:

- a thermal expansion coefficient similar to that of the vanadium alloy structure
- low-activation characteristics
- minimal chemical toxicity
- low cost and adequate resources

In the case of a lithium-vanadium system, considerations of chemical compatibility and electrical resistance appear to limit the options for coating materials to AlN and CaO. It has been demonstrated that these materials can have adequate insulating capacity in thin layers, but it has not been shown that they will exhibit long-term stability in a thermal gradient. Methods of applying such coatings with adequate mechanical integrity and adherence, achieving and retaining electrical insulating capability, and a practical approach to producing a self-healing system are still to be developed.

3.4 Issues related to development or use of alternate materials

It is anticipated that the AMP will continue to focus on selected feasibility issues identified with four primary material systems (see Section 4 below). However, several factors motivate some interest in alternate materials. The first is the possibility that the targeted materials will prove to be unacceptable for their proposed applications. Secondly, future changes in the configuration, mechanical design, or operating parameters of proposed fusion reactors could alter the choice of materials. Finally, materials development efforts in other fields could yield new materials that better meet the needs of the fusion program.

This highlights the importance of maintaining active ties with the wider materials research community in order to leverage developments outside the purview of OFES. It is in the best interest of OFES to keep this larger community informed of the desired properties and service requirements of potential fusion reactor materials and to monitor the progress of research being conducted outside the program. At the same time, researchers within the program should make use of these outside contacts to maintain an awareness of where OFES-funded advances in basic materials science will have a larger application.

3.5 Links to Experiment

As emphasized in the beginning, all integrated modeling efforts must be closely linked to experiments of various sorts. To reiterate, these experiments must include:

1. Focused studies of key phenomena and mechanisms, including those required for model development and validation. An obvious example is special experiments to understand how helium diffuses and is trapped under irradiation.

2. Controlled experiments on carefully conditioned samples, specially designed to reveal the effects of material and irradiation variables, both singly and in synergistic combinations. For example, doping with iron, boron and nickel isotopes, spectral tailoring, and the tritium-trick can be used to systematically vary the He/dpa ratio for irradiations over a range of temperatures and fluences and for various alloy systems.

3. Integral experiments to develop a database for alloy selection and optimization, and ultimately, engineering design.

Since the integrated modeling effort aims to have a microstructural foundation, development and application of high-resolution microanalytical characterization techniques, such as atom probe, electron microscopy and radiation scattering, will be very important. Further, understanding of the consequences of microstructural evolutions to property changes will require development and application of small specimen testing methods.

4. CURRENT PRIMARY STRUCTURAL MATERIALS: CROSSCUTTING PHENOMENA AND MECHANISMS

Research in the fusion materials program is currently focused on three primary alloy classes: advanced ferritic-martensitic steels, vanadium alloys, and silicon carbide composites. In addition, copper alloys have a role in high heat flux components and as a potential structural or magnet material in specialized reactor designs. However, a number of key phenomena crosscut multiple material systems. Thus coordinated research with emphasis on these would have a highly leveraged impact.

Examples of these crosscutting issues are listed in Table 4.1, where an "x" in the table indicates that the phenomenon is relevant for the indicated material. Several of these were also identified as critical feasibility issues in the AMP white paper; these are indicated by a "W" in the table. The metallic alloys share more issues in common among themselves than does SiC with the metals. Furthermore, even in cases where an item has been identified as common between the metals and SiC, e.g. welding and joining, the details may be quite different for SiC. All these areas, and in all likelihood others not included, are good targets for enhanced integrated modeling. The importance of the first four issues, and good prospects for making progress in dealing with them, make these issues our top priorities for initial emphasis in an integrated modeling program. No additional prioritization should be inferred by the order of the remaining issues in the table.

We note that the second item in Table 4.1, flow localization, was not mentioned as a critical feasibility issue in the AMP Whitepaper for any of the material systems. We include it here as a high priority issue because of the growing realization that the phenomenon is more general than previously thought. It appears that flow localization may limit the performance of most structural

Table 4.1 Key Crosscutting Phenomena for Fusion Reactor Materials *

FM	V	Cu	SiC	Phenomena, Issues, Comments
W	W	W	-	hardening and nonhardening embrittlement including underlying microstructural causes and the effects of helium on fast fracture
x	x	x	-	flow localization, consequences and underlying microstructural causes
-	W	-	x	coatings, multilayers, functionally graded materials
W	**W**	-	x	helium effects on high temperature deformation and fracture, and development of improved multiphase alloys for helium control
x	W	x	x	thermal and irradiation creep
x	x	x	**W**	swelling and general microstructural stability
x	W	x	W	welding, joining and processing issues
x	x	x	x	fatigue
x	W	-	-	hydrogen and interstitial impurity effects on deformation and fracture
-	-	-	W	physical properties, e.g. thermal conductivity
-	-	-	W	permeability of gases
x	x	x	x	erosion, chemical compatibility, bulk corrosion, cracking, product transport

* x relevant phenomenon, W phenomenon identified in AMP White Paper

alloys under certain irradiation conditions. Developing an understanding of flow localization, and how to prevent it or mitigate its consequences will be directly relevant to the use of all the current target materials and to any alloy development work that may take place in the AMP.

The role of both equilibrium and nonequilibrium alloy thermodynamics could also be considered a crosscutting phenomenon. This topic was extensively discussed at the open workshop, and has significance to radiation-induced microstructural evolution and mechanical property changes as well as alloy development. The importance of thermodynamics has not been explicitly acknowledged in much of the previous radiation damage modeling work, although it may have been accounted for through the use of "effective" material parameters in these models. Thermodynamics is not listed in Table 4.1 because it is qualitatively different than the listed phenomena, but an increased emphasis on understanding alloy thermodynamics and more detailed theoretical treatments of its impact in fusion reactor materials should be encouraged. We can note that research carried out under the auspices of the Steel Research Group at Northwestern University provides a good example of such work.

5. SUMMARY RECOMMENDATIONS

Based on the previous discussion we offer the following recommendations:

- An ambitious integrated modeling program should be initiated and closely linked to the entire AMP program.
- Program planning should consider the items identified by the workshop participants described in Appendix A and those listed in Table 4.1
- The program should encourage inter-institutional collaborations, i. e. between national laboratories and universities as well as between national laboratories.
- Regular program exchanges and reviews should be an integral part of the program.
- Both new and ongoing research should demonstrate relevance to the issues described in this document and the overall AMP White paper.
- When evaluating program research, several factors should be considered; these include:
    a) scientific quality and innovation of the researchers and their ideas,
    b) demonstrated focus on the key issues in fusion materials,
    c) close integration with other elements of the AMP program and, as noted above, specific collaborations between institutions,
    d) likelihood of tangible useful results including more reliable predictions of properties and/or improved design and methods,
    e) leveraging from other associated research activities, and
    f) an effective awareness of and expertise in the larger fields of materials science and engineering.

Appendix A
Description of Planning Workshop

A.1 Workshop Scope and Agenda

Workshop on Integration of Theoretical and Experimental Research
in the U.S. Fusion Materials Program

December 3-4, 1998

Sheraton Boston Hotel
Independence East Room
Boston, MA

The purpose of this workshop is to obtain input to further develop the AMP whitepaper on the integration of theory/modeling and experiments. The workshop is open to anyone working in a relevant area of research, but the format is intended to focus discussion on the draft version of the roadmap in order to highlight areas where it may be improved. The breakout sessions and contributed talks are expected to identify any shortcomings or omissions in this document. Research presented in the contributed talks should specifically relate to the fusion materials feasibility issues described in the draft roadmap.

Thursday, December 3

1:00 pm Session 1: Introduction and Overview of Issues

- OFES plans and activities - F. W. Wiffen (U.S. DOE)
- Summary of AMP White paper - E. E. Bloom (ORNL)
- Summary of FESAC Panel Report and Planning Process - R. E. Stoller (ORNL)
- Initial questions and comments on planning process and whitepaper
- Invited Examples of Modeling-based Materials Development
    - C. J. Kuehmann, QUESTEK: Computer-aided Materials Design
    - T. Diaz de la Rubia, LLNL: Applications of Multiscale Modeling
    - G. R. Odette, UCSB: Investigation of Embrittlement in RPV Steels

3:30 pm Break

4:00 pm Session 2: Breakout of Working Groups

- Microstructural processes and helium effects, A. F. Rowcliffe (ORNL) and B. D. Wirth (LLNL)
- Deformation and fracture, G. E. Lucas (UCSB) and A. El-Azab (PNNL)
- Coatings and compatibility, K. Natesan (ANL) and G. S. Was (U of MI)

- Ceramics and composites, W. J. Weber (PNNL) and L. L. Snead (ORNL)

Friday, December 4

8:30 am Session 3: Working Group Reports and Discussion

- Working group chairmen reports (as above)
- Moderated discussion

10:15 am Break

10:30 am Session 4: Open Forum (As contributed)

- John Vitek, ORNL, thermodynamic databases, a neural net application

11:30 am Workshop wrap-up, closing remarks: Workshop organizers

A.2 Workshop Discussion and Breakout Sessions

Invited presentations at the workshop provided examples of model-based materials development, applications of multiscale modeling in the semiconductor industry, and the interactive role of theory and experiment in successfully dealing with an applied materials problem. These examples illustrated the recent progress in our ability to use modeling and computer simulations to develop materials and to solve "real world" problems. A substantial portion of the workshop was devoted to four breakout sessions that will be summarized below. Themes that were emphasized throughout the meeting included the increasingly general observation of flow localization in irradiated structural materials, the potential usefulness of a greater role for computational thermodynamics, and a materials engineering approach to designing radiation-resistant materials. Overall, the discussion in both the breakout and general sessions was generally supportive of the approach described in the draft white paper, i.e. that an increased level of modeling work may lead to substantial progress when it is well integrated with a focused experimental activity.

A.2.1 Microstructural processes and helium effects

Discussion in this session focused primarily of four topics, primary damage production and damage accumulation, helium management, computational thermodynamics, and alloy development. With respect to damage production and accumulation, it was recommended that alloy effects should be addressed. This will require the development of interatomic potentials for concentrated alloys (e.g. Fe-xCr, V-xTi), and ways to implement the effects of alloy thermodynamics in the parameters used in kinetic models employing both the rate theory and Monte Carlo techniques. The effect of displacement cascades on the stability of oxide particles is an unresolved issue for the ODS ferritic alloys, and for precipitate phases in general. Atomistic modeling tools should be employed at the appropriate level and be used to provide information to higher level models. Further modeling of helium interactions in the lattice (migration, trapping and sinks and interfaces) must be closely tied with experiments to aid understanding and model development.

The current successful use of thermodynamic models to treat multiphase steels was extensively discussed. Work should be initiated to develop a similar level of sophistication for the alloys of direct interest to the AMP. In particular, the effects of persistent point defect and solute fluxes must be incorporated into the thermodynamic models in order to predict phase stability under irradiation. The approach of engineering materials to produce radiation-resistant microstructures was suggested for any alloy development work that goes on in the program. For example, modeling and focussed experiments could be used to identify and understand effective sinks for helium, and such information could be applied in the development of microstructures that will mitigate the effects of helium by trapping. Other materials problems that may yield to microstructure-design-based solutions include developing grain boundary structures that are creep resistant and the ability of a material to maintain its strain hardening capability under irradiation.

The development of innovative materials to expand the current limits on maximum damage level and operating temperatures was discussed in the context of recent advances in the computational design of materials. In other fields, systems approaches have been successfully used to integrate processing, structure, properties, and performance relationships into the design of multilevel- structured materials. Similar approaches could provide far-reaching benefits to the fusion program.

A.2.2 Deformation and fracture

Several aspects of material flow and fracture behavior were discussed, the outstanding issues in each area were described, and modeling-based approaches to develop an understanding of these phenomena were proposed. Obtaining a sufficient degree of knowledge about the predominant microstructure is a significant (although primarily experimental) issue for improving our understanding of most aspects of a materials mechanical response. Outstanding issues with respect to the yield strength, or yield strength change, of materials include a better definition of the barrier strengths of various defect structures and the development of improved superposition laws for realistic microstructures that contain multiple barrier types. These can be investigated by an appropriate combination of atomistic and mesoscale models of dislocation dynamics and dislocation-barrier interactions with key experiments on both irradiated and surrogate materials. Knowledge and understanding of post-yield constitutive behavior is also important, and the loss of work hardening and the onset of flow localization head the list of important post-yield phenomena. A similar set of theoretical tools may be used to investigate how dislocation obstacles are destroyed, leading to the formation of clear channels for deformation. The critical conditions for the onset of channeling should be determined to help guide efforts to design microstructures that will resist this phenomenon.

Although thermal creep may not be an issue for many fusion applications, irradiation creep and creep-swelling interactions will be important for most materials in the high flux regions near the first wall. Improved kinetic models are needed to describe and simulate the effect of stress on radiation-induced microstructural evolution. A combination of modeling studies and experiments should be used to develop material performance maps (Ashby maps) for the materials and irradiation conditions of interest to the AMP.

Issues related to fracture behavior include the need to obtain an improved understanding of the micromechanics of fracture (including cleavage, quasi-cleavage, ductile fracture, and intergranular fracture) and the relationship between micromechanics and the failure assessment of irradiated structures that contain flaws. The micromechanics of fracture can be investigated with a combination of phenomenological and finite element models with input from techniques such as fracture surface reconstruction. These same tools can be used to quantify local crack tip critical fracture conditions such as the critical stress and length scale parameters that control cleavage behavior. Similar to the topic of post-yield behavior mentioned above, it is important that accurate constitutive relationships be developed and used. Since two of the AMP-target materials exhibit a ductile-to-brittle transition, the mechanisms causing an increase in the DBTT must be elucidated. Since a DBTT shift can arise by either matrix hardening, a reduction of the critical fracture stress, or by intergranular fracture, determining the predominant mechanism(s) is essential for efforts to mitigate embrittlement.

A.2.3 Coatings and compatibility

Although the focus of fusion reactor research in this area has been on lithium-based coolants, it has built on the foundation of earlier work in the sodium-cooled fast breeder reactor program. The concerns for compatibility between a liquid metal coolant and the structural materials are similar, but the fusion reactor environment adds the requirement for an electrical insulating coating on the structure to prevent unacceptable pressure drops due to magnetohydrodynamic (MHD) forces. For the candidate system that employs lithium coolant and vanadium as the blanket structural material, there are several issues that need to be considered with respect to the compatibility of the coating involve. These include:

a) the thermodynamic stability of the coating when contacted with the liquid lithium,

b) the extent of dissolution of the coating in the liquid lithium, which is dictated by the solubility of coating constituents in liquid lithium under the temperature and temperature gradient that exist in the system,

c) the degree of interaction between the coating constituents and other reactive elements in the liquid lithium, and

d) compatibility relationships between the coating and the structural material.

For example, reactions with elements such as oxygen, carbon, nitrogen, and hydrogen may lead to changes in coating chemistry, thereby altering its insulating characteristics. Dissolution of structural material constituents can also be an issue if parts of the system are not coated or if the coating is damaged.

Nonmetallic elements such as O, C, N, and H are known to migrate in structural-material/liquid-metal systems as a result of differences in chemical activity. Since coating reliability is of concern, the program requires approaches to address several issues such as the thermodynamic stability, physical and chemical characteristics of the coating; the viability of different coating methods; and the insulating characteristics of the coatings before and after exposure to controlled purity lithium.

A previous review of electrical resistivity data for several oxides, nitrides, and mixed oxides showed that oxides such as CaO, MgO, SiO_2, Al_2O_3, $MgAl_2O_4$ and nitrides such as AlN and Si_3N_4 exhibit resistivities of $>10^5$ ohm·m at temperatures below about 600°C. The system requirement is for the product of the electrical resistivity and the thickness of the insulator coating to exceed a nominal value of 0.01 ohm·m^2 under operating conditions. This translates to a minimum resistivity value of 10^4 ohm·m for a coating thickness of 1 μm, or 10^3 ohm·m for a coating thickness of 10 μm. Based on the resistivity values of materials listed above, a coating layer of ≤ 1 μm in thickness of any of these materials would be adequate from the insulating standpoint, provided the resistivity is not reduced during operation, i.e., by irradiation or other operational parameters.

The electrical resistivity of two of the prime candidate coatings CaO and AlN has been assessed for application in a lithium environment. The effort examined the development of CaO coatings by thermal/chemical vapor deposition and *in situ* in lithium. Similarly, detailed investigations of AlN's fabrication and metallurgical microstructure, and preliminary studies of its compatibility with liquid lithium were conducted. The electrical characteristics of AlN material obtained from several sources were examined. Methods of applying thin coatings of CaO and AlN with adequate mechanical integrity and adherence, achieving and retaining electrical insulating capability, and a practical approach to producing a self-healing system are still to be developed

Theoretical modeling of the thermodynamics and kinetics of the chemical interactions between the coating and a lithium environment can aid in the in-situ formation of insulating coatings in lithium and can guide the experimental program to aid in the interpretation of experimental results. Much of the original analyses conducted to identify potential candidate coating materials were based on thermodynamic calculations to assess the stability of the coating materials and the chemistry requirements for both the liquid lithium and the vanadium alloy systems. More detailed calculations are necessary to assess not only the thermodynamic aspects of the coating processes, but also the kinetics of reactions such as transport rates of oxygen, calcium, aluminum, and nitrogen, etc.

Calculations of oxide or nitride growth rates can be used to estimate the ranges of temperature and time required for coatings of desired thickness to form. Calculations of the thermodynamic stability of various phases, e.g. CaO, CaV_xO_y, Ca-Mg-O, AlN, Al-O-N, $LiAlO_2$, that can potentially be formed need to be correlated with experimental observations and measured compositions of the liquid lithium and vanadium alloys. The dependence of electrical resistivity on composition in functionally gradient materials needs to be determined. Both modeling and experimental work are required to investigate the in situ formation and repair of ceramic coatings. Current models address primarily mechanical degradation such as cracking and spallation; the impact of mechanical degradation on the electrical properties of the coatings needs to be addressed. Finally, it is imperative that the coatings be evaluated in the presence of an irradiation environment from the standpoint of their chemical stability, mechanical integrity, and electrical resistivity.

A.2.4 Ceramics and composites

There is only limited experience applying ceramic matrix composites as structural materials, and there is considerable international effort currently being invested in this general area. Therefore, it was recommended that the fusion program adopt the strategy of focusing on those areas that are specific to the fusion environment. For instance, engineering design codes and micromechanical (constitutive) modeling are two examples of topics that will be critically important for the use of SiC composites in fusion applications. However, these are being aggressively pursued in other programs and therefore are not focus areas of the fusion materials program.

Areas of research which are of unique interest to the application of SiC composites to the fusion program are typically those dealing with the effects of radiation on monolithic or composite structures. A significant example is the potential degradation of thermal conductivity as a result of radiation exposure. While there has been some study of the effects of radiation on monolithic materials there is still considerable work remaining experimentally and theoretically. Some examples of areas which warrant study are: radiation damage production, transport and trapping of transmutation gases (e.g. H and He), basic defect properties such as activation energies for formation and migration, effects of various defect types on phonon scattering, and effects of swelling on mechanical properties. The goal of these studies would be to provide the knowledge base necessary to predict the performance of the composite material which is critically dependent on the evolution and interaction of its three components: fiber, matrix and interphase.

It is hoped that the process of developing an understanding of radiation effects and their potential impact on the constitutive properties will proceed in parallel with micromechanical model development outside of the fusion community. As this work matures, integration of these models should permit the evolution of thermophysical properties in SiC composites under irradiation to be predicted.

A.3 Workshop Participants and Affiliations

Participants: 42 participants on Thursday (28 Friday), 16 with current ties to U.S. DOE Office of Fusion Energy Sciences, 6 international

Affiliations: 7 from U.S. universities
25 from U.S. national laboratories
1 from U.S. commercial
3 from U.S. DOE Offices
3 from foreign universities
3 from foreign national laboratories or institutes

Appendix B
Author Contact Information

Roger E. Stoller (Chair)
phone: 423-576-7886
Oak Ridge National Laboratory
fax: 423-574-0641
Bldg. 5500
email: rkn@ornl.gov
P. O. Box 2008
Oak Ridge, TN 37831-6376

Howard L. Heinisch
phone: 509-376-3278
Pacific Northwest National Laboratory
fax: 509-376-0418
MS P8-15
email: hl_heinisch@pnl.gov
P. O. Box 999
Richland, WA 99351

G. Robert Odette
phone: 805-893-3525
Department of Mechanical and
fax: 805-893-8651
Environmental Engineering
email: odette@engineering.ucsb.edu
University of California
Santa Barbara, CA 93106

A KINETIC MONTE CARLO STUDY OF MIXED 1-D/3-D DEFECT MIGRATION - H.L. Heinisch (Pacific Northwest National Laboratory)*, B.N. Singh (Risø National Laboratory, Denmark), S.I. Golubov (Institute of Physics and Power Engineering, Russia)

(Summary of a paper presented at the International Union of Materials Research Societies Fifth International Conference on Advanced Materials, Beijing, China, June 13-18, 1999. The paper will appear in the Journal of Computer-Aided Materials Design)

EXTENDED ABSTRACT

Kinetic Monte Carlo (kMC) techniques are being used to study a key element of microstructure evolution under irradiation: diffusion of defects by migration that has characteristics of both one-dimensional (1-D) and three-dimensional (3-D) random walks.

It has been shown in virtually all MD simulations of displacement cascades in metals that self-interstitial atoms (SIA) readily form clusters that are, or can become, glissile dislocation loops. In MD simulations of collision cascades in pure metals it has been observed that clusters of coupled crowdions can form directly during the production of cascades [1]. Such clusters are crystallographically equivalent to small, perfect interstitial dislocation loops that are glissile. Like single crowdions, the crowdion clusters can move one-dimensionally by thermal activation, having extremely small migration energies [2]. In general, cascade-producing damage events in metals introduce localized damage regions containing a mix of SIA and vacancy defects that include (depending on the material and the temperature) immobile clusters, mobile defects moving by three-dimensional random walks and mobile defects moving by one-dimensional random walks. Analytical theories describing the evolution of the defect population and the microstructure under irradiation must be able to address the disposition of all these types of defects. It has also been observed in recent MD simulations of glissile SIA cluster motion that the 1-D gliding clusters can change the direction of their 1-D motion by thermal activation [3,4] or by interaction with another defect [5]. The result is that a gliding SIA cluster effectively moves in three dimensions by a series of segments of 1-D random walks along different directions, we call this "mixed 1-D/3-D" migration.

The production bias model of void swelling (PBM) is an analytical theory that has been developed to explicitly address the issues arising from cascade damage, including the formation and transport of glissile SIA clusters [6]. In the current PBM model defect reaction kinetics of both 1-D and 3-D migration can be accommodated using different functional forms for the dependence of 1-D and 3-D reaction kinetics on the size and number densities of the microstructural features. However, a functional form for the reaction kinetics of mixed 1-D/3-D migration is not known.

To gain insight into the reaction kinetics for mixed 1-D/3-D migration, kMC simulations of simple idealized problems can be performed and analyzed to determine the functional relationships of relevant variables to the degree of mixed 1-D/3-D migration. For example, the probability of absorption into a concentration of stationary absorbers of spherical capture radius R varies as 1/R for pure 3-D migration and as $1/R^2$ for pure 1-D migration [7]. It is of interest to examine the dependence on the absorber radius for mixed 1-D/3-D migration.

---

* Pacific Northwest National Laboratory is operated for the U.S. Department of Energy by Battelle Memorial Institute under contract DE-AC06-76RLO 1830.

In the kMC model, the locations of defects are monitored as they hop on a face-centered cubic lattice. The defects can execute 1-D, 3-D or mixed 1-D/3-D random walks of various 1-D segment lengths simply by choosing a value for the variable NJDC, the number of jumps between direction changes, for 1-D migrating defects. The basic concepts of the kMC method for studying defect kinetics under mixed 1-D/3-D migration are described further in earlier publications [8,9]. In these idealized studies all defects have the same properties and there is no recombination or clustering. The migrating defects interact with stationary spherical absorbers of uniform absorption radius R. The absorbers are unsaturable and do not change size upon absorbing a migrating defect.

Simulations were done by placing a mobile defect at a random initial position near the center of a random array of absorbers of radius R in a computational cell of fixed volume and following it until it was either absorbed by a spherical absorber or escaped from the cell (or equivalently, was absorbed by the boundary of the cell). Simulations were done with 1000 defects for each set of conditions, i.e., each data point on the following figures represents the average results for 1000 defects.

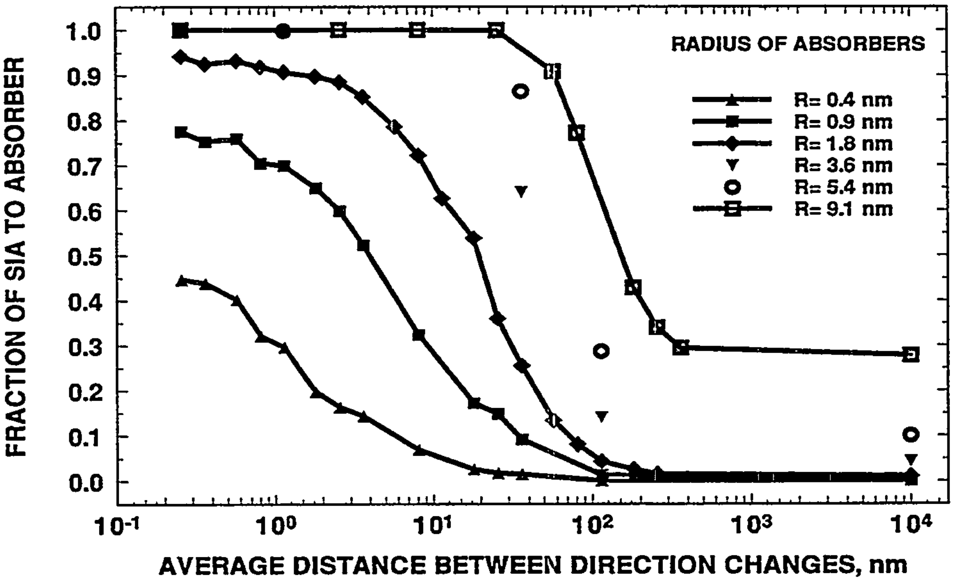

Figure 1. The fractions of mobile defects absorbed by a periodic array of absorbers of radius R as a function of the average distance traveled between direction changes, L, in nm for various values of R.

Figure 1 shows the fraction of defects absorbed in absorbers as a function of the average distance traveled between direction changes L = a $(NJDC/2)^{1/2}$, where a is the FCC lattice parameter. Data are plotted for various values of absorber radius, R, illustrating how the fraction absorbed varies with both R and L. The curves clearly illustrate the difference in reaction kinetics of defects that are transported by 1-D, 3-D and mixed 1-D/3-D migration.

Figure 2 shows the mean free path (the average distance traveled by a defect before being absorbed) as a function of the absorber radius. Data are plotted for different constant values of NJDC. These log-log plots are essentially straight lines of different slope, depending on the value of NJDC. For pure 3-D migration (NJDC=1) the mean free path should vary as 1/R, while for pure 1-D migration it should vary as $1/R^2$. In general, we might expect that for mixed 1-D/3-D migration the mean free path should vary as $1/R^M$, where M depends on the value of NJDC.

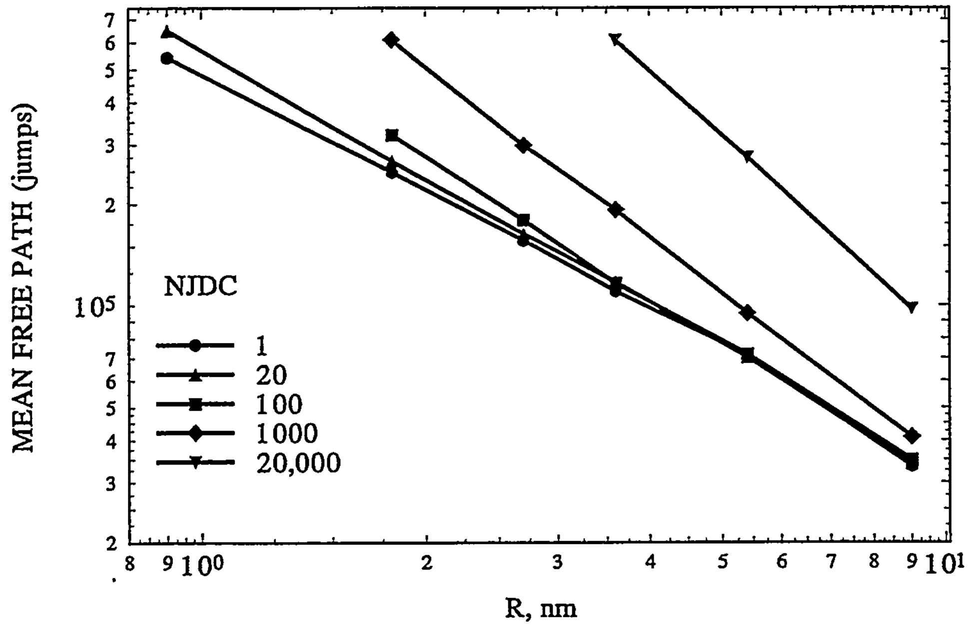

Figure 2. The mean free path (average distance traveled by a defect to an absorber) in units of defect jumps on a FCC Cu lattice as a function of the absorber radius R in nm for various values of the number of jumps between direction changes NJDC for mixed 1-D/3-D migration.

In Figure 3 a plot of the negative slope M of the lines in Figure 2 as a function of L reveals that M varies from M=1.1 for NJDC=1 (pure 3-D migration) to M=2 for NJDC=20,000 (near pure 1-D migration). Thus, the dependence of mean free path on absorber radius varies approximately from 1/R to $1/R^2$ as expected, as the dimensionality of the migration changes from pure 3-D to mixed 1-D/3-D to pure 1-D.

The values of M in Fig. 3 for pure 1-D and pure 3-D migration are somewhat higher than the ideal values because of the finite size of the computational cell and the fixed length of time used in the kMC simulations. In essence, the entire distribution of diffusion paths is not being sufficiently sampled by the simulation. Thus, it is premature to determine the functional dependence of M on L from data such as presented in Fig. 3. However, these results illustrate the power of kMC simulations to explore phenomena and display relationships between variables that would be very difficult or impossible to obtain through analytical methods or results of experiments. Establishing such functional relationships is important because, as an irradiation proceeds, the scale of the microstructure changes, so the reaction kinetics for defects under mixed 1-D/3-D migration change continuously as the size and concentration of reaction partners changes. Also, the value of L that determines the nature of the mixed 1-D/3-D reaction kinetics may well depend on the changing microstructure as well as on the temperature.

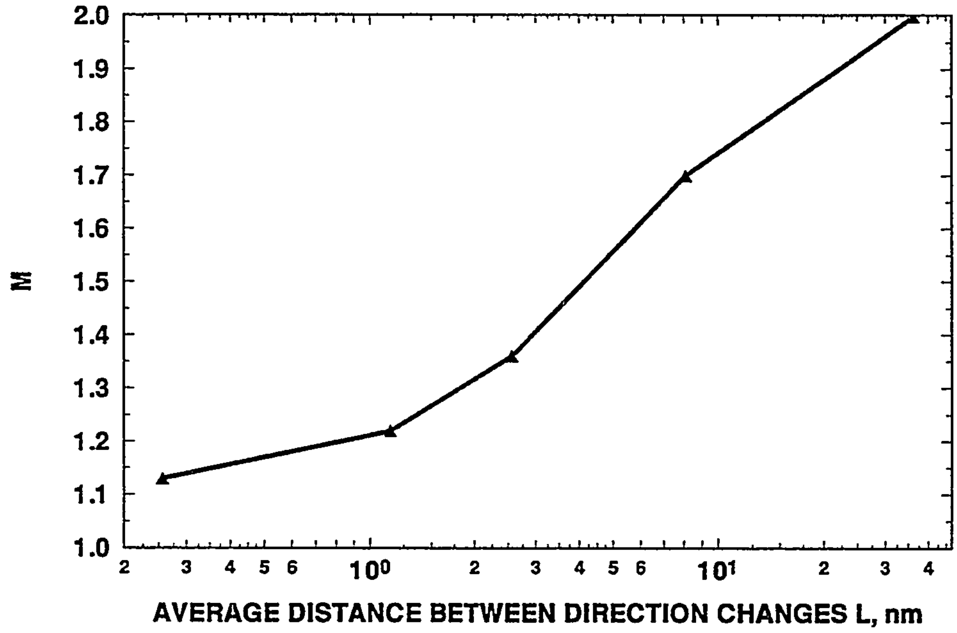

Figure 3. Values of the exponent M, where the mean free path of defects to absorbers varies as $1/R^M$, as a function of L, the average distance between direction changers for mixed 1-D/3-D migration.

Future work will include revising the kMC simulation technique for extraction of complete mean free path information, followed by subsequent analysis of the functional relationships involved in the reaction kinetics of mixed 1-D/3-D migration and the scale of microstructural features, e.g. the size and concentration of absorbers.

ACKNOWLEDGEMENTS

This work was partly supported by the European Fusion Technology Programme and partly supported by the U.S. Department of Energy under contract DE-AC06-76RLO 1830.

REFERENCES

1. Yu. N. Osetsky, V. Priego, A. Serra, B.N. Singh and S.I. Golubov, Philos. Mag. A, in press.
2. Yu. N. Osetsky, V. Priego, A. Serra, B.N. Singh and S.I. Golubov, submitted to Phil. Mag. A.
3. N. Soneda and T. Diaz de la Rubia, Philos. Mag., in press.
4. G. Gao, D.J. Bacon and Yu. N. Osetsky, submitted to J. Nucl. Mater.
5. Yu. N. Osetsky, V. Priego and A. Serra, submitted to J. Nucl. Mater.
6. S.I. Golubov, B.N. Singh and H. Trinkaus, submitted to J. Nucl. Mater.
7. U. G¬sele and W, Frank, phys. stat. sol. (b) 61 (1974) 163.
8. H.L. Heinisch, B.N. Singh and S.I. Golubov, J. Nucl. Mater. in press.
9. H.L. Heinisch, B.N. Singh and S.I. Golubov, Fusion Materials Semiannual Progress Report for period ending Dec. 31, 1998, DOE/ER-0313/125 (1999) 271.

9.0 DOSIMETRY, DAMAGE PARAMETERS, AND ACTIVATION CALCULATIONS

RADIATION DAMAGE CALCULATIONS FOR THE FUBR AND BEATRIX IRRADIATIONS OF LITHIUM COMPOUNDS IN EBR-II AND FFTF - L. R. Greenwood (Pacific Northwest National Laboratory)*

OBJECTIVE

To calculate displacement damage for lithium compounds irradiated in the EBR-II and FFTF reactors.

SUMMARY

The Fusion Breeder Reactor (FUBR) and Breeder Exchange Matrix (BEATRIX) experiments were cooperative efforts by members of the International Energy Agency to investigate the irradiation behavior of solid breeder materials for tritium production to support future fusion reactors. Lithium ceramic materials including Li_2O, $LiAlO_2$, Li_4SiO_4, and Li_2ZrO_3 with varying ^{6}Li enrichments from 0 to 95% were irradiated in a series of experiments in the Experimental Breeder Reactor (EBR II) and in the Fast Flux Test Facility (FFTF) over a period of about 10 years from 1982 to 1992. These experiments were characterized in terms of the nominal fast neutron fluences and measured ^{6}Li burnup factors, as determined by either mass spectrometry or helium measurements. Displacement per atom (dpa) values have been calculated for each type of material and irradiation. Values up to 11% ^{6}Li-burnup and 130 dpa are predicted for the longest irradiations. Using these new calculations, previously measured radiation damage effects in these lithium compounds can be compared or correlated with other irradiation data on the basis of the dpa factor as well as ^{6}Li-burnup.

PROGRESS AND STATUS

The recoiling alpha and triton from the $^6Li(n,\alpha)^3H$ reaction create a cascade of secondary recoil atoms from their interactions with atoms in the compound material. Fast neutron interactions with atoms in the compounds can also cause primary recoil atoms that also lead to a cascade of secondary recoil atoms. Both of these processes lead to radiation damage characterized by the total number of displacements per atom (dpa). Although dpa is not in itself a measurable effect, it has proven useful as an exposure parameter for correlating material effects for different materials and radiation environments. The purpose of this report is to document the calculation of dpa for the Li breeder compounds in the FUBR and BEATRIX series of irradiations.

It should be noted, however, that other effects besides dpa will also be important for characterizing the irradiation performance of these materials, especially transmutation which leads to the creation of Li vacancies and the buildup of transmutant product interstitials. The absolute value of the calculated dpa is somewhat irrelevant due to the very high rate of atomic recombination in most materials. As an example, the longest exposures in this study lead to the prediction of about 11% burnup of ^{6}Li and 130 dpa. However, if 99% of the displaced atoms recombine, then burnup (transmutation) effects may be a factor of ten more important than stable product dpa in the evolution of material property changes. Irradiation experiments performed on these lithium ceramics do not indicate any significant property

---

*Pacific Northwest National Laboratory (PNNL) is operated by the U.S. Department of Energy by Battelle Memorial Institute under contract DE-AC06-76RLO-1830.

changes at these burnup or dpa levels that would seriously degrade the usefulness of these materials for tritium breeding in fusion reactor applications. Ultimately, it is the measured performance of lithium ceramic breeder materials as a function of irradiation exposure that determines their applicability in fusion reactor designs. Comparisons with dpa levels in structural materials such as stainless steel may thus be irrelevant.

The lithium containing ceramic materials were prepared by members of an International Energy Agency collaborative program, as documented in several publications.[1,2,3,4,5,6,7,8,9,10,11,12] In EBR-II, ceramic pellets were irradiated in canisters placed in several pins located in row 7 at different radial and axial locations. The irradiations in the FFTF MOTA were designed to measure tritium release. The lithium was enriched in ^{6}Li in varying amounts from 0 to 95%.

All of the irradiation histories are summarized in Table 1. Details of the EBR-II irradiations were provided by D. G. Porter (Argonne National Laboratory – West, 1999.) Details of the FFTF-MOTA irradiations are documented in references 9 -12. Neutron dosimetry measurements have been published for the EBR-II reactor[13,14] and for the FFTF irradiations.[15,16]

Table 1. Summary of the FUBR and BEATRIX Irradiation Histories

Experiment	**Subassembly**	**Subcapsules**	**Runs**	**MWd**	**EFPD**
	EBR-II				**@62.5 MW**
FUBR-1A	X370	1,2,3,4	119-120	6041	96.7
	X370A	5,6,7,8	123-126	11101	177.6
	In both runs	9,10,11	119-126	17142	274.3
FUBR-1B	X415	B1,B3,B6,B7	135A-141C[a]	21344	341.5
BEATRIX-I	X415A	B8,B9,B10,B11	144A-151	37455	599.3
	In both runs	B2,B4,B5	135A-151	58799	940.8
FUBR-1B	X416	S1,S2	135A-141C[a]	21104	337.7
BEATRIX-I	X416A	S4,S5	144A-151	37455	599.3
	In both runs	S3	135A-151	58559	936.9
	FFTF				**@291 MW**
BEATRIX-II	MOTA-2A	1B,1C,1D,1E, 5E,8B	11	87213	299.7
BEATRIX-II	MOTA-2B	1B,2C,5F,8B	12	59160	203.3

[a] X415 was removed for runs 137E and 138B; X416 was removed for 137E, 138B, and 138C.

Radiation Damage Calculations

The ^{6}Li(n,α)^{3}H reaction releases 4.782 MeV of energy (Q value) resulting in energetic tritium (2.733 MeV) and alpha (2.050 MeV) particle recoils. These high-energy recoils lose energy and are stopped within a short distance in the lithium compounds. A small fraction of the time, the recoiling particles hit a nucleus of one of the atoms in the compound leading to either an elastic scattering event or a nuclear reaction. These nuclear events cause secondary atoms to be displaced from their lattice sites. If we use the Lindhard model of energy loss and a modified Kinchin-Pease model for secondary displacements, then we can calculate the total number of displaced atoms for each $^6Li(n,\alpha)^3H$ reaction. This leads to a fixed relationship between burnup of ^6Li atoms and dpa (for this reaction only). Each compound will have a different ratio of burnup to dpa due to the differences in lithium content and energy loss characteristics. In the modified Kinchin-Pease model, constant displacement energy is assigned to each atom in a given compound. Unfortunately, these values are not readily available for these compounds. Efforts are underway to use a better model for these compounds; however, these results are not currently available. If we assign values of 10 eV for Li, 30 eV for O, 27 eV for Al, 25 eV for Si, and 40 eV both for Ti and Zr, then the calculated conversion of ^6Li burnup to dpa is given in Table 2, assuming 100% enrichment of ^6Li. For a measured level of ^6Li burnup and enrichment, the dpa can be calculated by multiplying the values in Table 2 times these two factors. For example, if we start with 56% enriched Li_2O and the ^6Li burnup is measured to be 8%, then the dpa due to this reaction will be 117 x 0.56 x 0.08 = 5.2. Once the ^6Li is fully burned out, this process will stop and no further dpa can be generated from this reaction. It should be noted that the conversion factors in Table 2 are technically only correct at low neutron energies since at higher energies the energy of the incident neutron will raise the recoil energies slightly. However, since this reaction mainly occurs with neutrons well below 1 MeV, this correction for the neutron spectra of interest is negligible. Due to the burnup of ^6Li as well as the variations in the ^6Li enrichment, dpa cross sections for these compounds depend on both of these factors and change with irradiation as the ^6Li burns up. Both of these effects were taken into account in these calculations. Due to the high cross section of ^6Li at lower neutron energies, neutron self-shielding can also be an important time-dependent effect. Simple approximations to the neutron self-shielding effects for the materials and neutron spectra used in these experiments indicate that the corrections would typically be on the order of 5%. Due to the complicated geometries of these experimental assemblies and the relatively small order of these corrections, neutron self-shielding corrections were not included. The calculated ^6Li burnup values presented below agree favorably with measurements made for these materials, as documented in various references in this report.

Table 2. Conversion of ^6Li Burnup to dpa
(Multiply times ^6Li enrichment)

Material	Dpa / % ^6Li Burnup
Li_2O	117.0
$LiAlO_2$	33.7
Li_2ZrO_3	44.9
Li_4SiO_4	67.8

Of course, all other possible nuclear reactions will also cause dpa. The SPECOMP[17] computer code was used to calculate these more conventional dpa cross sections as a function of neutron energy for each type of lithium compound. These dpa cross sections were then added to the SPECTER[18] computer code for integration over the neutron flux spectra in each series of irradiations. The calculated dpa values for each series of irradiations are discussed below. Specific comments describe each experiment. In all of these irradiations, the reactor power and hence dpa rates are essentially constant (<10% variation over the run cycles) except during reactor downtimes. For all of the irradiations, the Li compounds were encapsulated in 316 stainless steel containers. The dpa values for the 316 SS cladding are also presented below along with the total neutron fluences. The composition of 316 SS was taken as Ni(0.13), Cr(0.18), Mn(0.019), Mo(0.026), and Fe(balance).

FUBR-1A Irradiation in EBR-II

Eleven pins were fabricated for irradiation designated PIN-1 through PIN-11. Solid pellets were irradiated at four different elevations in each pin. Canisters were placed symmetrically about the reactor centerline at 1.2 to 7.9 cm and at 15.2 to 21.6 cm for irradiations of 96.7, 177.6, and 274.3 EFPD at a nominal power of 62.5 MW. The dpa calculations for the highest exposure in these positions and exposure parameters are given in Table 3. The dpa values in the table are average values for the assemblies and radial variations are <10%. Axial flux variations are also relatively small (<10%) near core midplane.

Table 3. dpa Calculations for FUBR-1A – Capsules 9, 10, 11 – 274.3 EFPD

Fluence (x10^{22} n/cm^2)		3.94	4.11	3.79
Dpa, 316 SS		15.9	16.8	15.2
^{6}Li Burnup,% :		3.38%	3.46%	3.14%
Height,cm:		-20	0	+20
Material	^{6}Li Enrichment,%	dpa	dpa	dpa
Li_2O	56	35.4	37.3	34.0
$LiAlO_2$	95	37.1	39.1	35.6
Li_2ZrO_3	95	37.6	39.5	36.0
Li_4SiO_4	95	34.6	36.4	33.1

FUBR-1B/BEATRIX-I Irradiations in EBR-II

Two different types of pins were fabricated for these irradiations. B7A pins labeled B1 through B11 contained canisters with Li ceramic pellets at three different elevations, -15.5 to –21.6 cm, -7.6 to –13.2 cm, and +16.8 to +22.4 cm. S pins labeled S1, S2, and S3 contained canisters with Li ceramic pellets at two elevations symmetrically around midplane at 1.3 to 7.9 cm. The B7A pins were irradiated for 341.5, 599.3, and 940.8 EFPD at 62.5 MW. Table 4 lists the dpa values at the maximum exposure. Calculations for capsules S1-S3 differed slightly due to small differences in the irradiation exposures of 337.7, 599.3, and 946.9 EFPD. Variations in dpa are not very large for all of the different positions. The dpa values in the table are average values for the assemblies and radial variations are <10%. Axial flux variations are also relatively small (<10%) near core midplane.

Table 4. dpa Calculations for FUBR-1B/BEATRIX-I – Capsules 2, 4, 5 – 940.8 EFPD

Fluence (x10^{22} n/cm^2)		13.5	14.1	13.0
Dpa, 316 SS		54.5	57.6	52.2
^{6}Li Burnup,% :		11.11%	11.36%	10.38%
Height,cm:		-20	0	+20
Material	^{6}Li Enrichment,%	dpa	dpa	dpa
Li_2O	56	121.0	127.3	116.1
Li_2O	7.5	114.6	120.8	110.0
Li_2O	0.07	113.7	119.9	109.1
$LiAlO_2$	95	127.1	134.0	122.0
Li_2ZrO_3	95	128.6	135.2	123.2
Li_4SiO_4	95	118.1	124.5	113.2

BEATRIX-II Irradiations in FFTF

The BEATRIX-II experiments were conducted in the MOTA-2A and MOTA-2B irradiations in FFTF. These experiments were primarily designed to evaluate the rate of recovery of tritium during irradiation. The experimental assemblies consisted of solid pellets or tubes (rings) of lithium ceramics with flowing gas in the center or sphere beds. In MOTA-2A, the Li_2O ring canister was in position 1E and solid pellets and single crystals were in positions 1B, 1C, 1D, and 1E. In MOTA-2B, the Li_2O ring canister was located in position 1B and a Li_2ZrO_3 sphere bed was located in position 2C. $LiAlO_2$, Li_2ZrO_3 and Li_4SiO_4 disc samples were also irradiated in both experiments. The dpa calculations listed in Tables 5 and 6 are quoted for positions where the neutron flux spectra were determined from neutron dosimetry measurements. Radial flux gradients are relatively small (<10%). Axial flux gradients are relatively small near midplane where the main testing was done, but become quite steep at the top of the core 8B position. However, the dpa values are so low at these out-of-core positions that the materials damage effects are probably negligible.

Table 5. dpa Calculations for BEATRIX-II – MOTA-2A – 299.7 EFPD

Fluence ($x10^{22}$ n/cm^2)		8.89	7.44	0.24
Dpa, 316 SS		24.9	21.8	0.25
^{6}Li Burnup,% :		9.96%	7.60%	1.68%
Reactor Position:		1-B,C,D,E	5E	8B
Height,cm:		-42.7	+37.7	+122.4
Material	^{6}Li Enrichment,%	dpa	dpa	dpa
Li_2O	61	68.1	56.6	1.93
Li_2O	0.07	60.8	51.2	0.72
$LiAlO_2$	95	68.3	57.5	1.27
Li_2ZrO_3	95	63.9	53.7	1.39
Li_4SiO_4	95	70.4	58.8	1.81

Table 6. dpa Calculations for BEATRIX-II – MOTA-2B – 203.3 EFPD

Fluence ($x10^{22}$ n/cm^2)		5.63	7.91	4.77	0.20
Dpa, 316 SS		14.2	21.1	12.9	0.23
^{6}Li Burnup,% :		6.68%	7.92%	5.29%	1.27%
Reactor Position:		1B	2C	5F	8B
Height,cm:		-41.2	-27.3	+44.3	+121.3
Material	^{6}Li Enrichment,%	dpa	dpa	dpa	dpa
Li_2O	95	41.5	59.9	36.9	2.07
Li_2ZrO_3	85	35.5	52.4	32.3	1.08
Li_2ZrO_3	0.2	32.9	49.4	30.3	0.59
Li_4SiO_4	0.2	35.3	53.1	32.4	0.64

CONCLUSIONS

The calculations clearly show that most of the dpa damage in these materials arises from fast neutron reactions such as elastic and inelastic scattering rather than from the $^6Li(n,\alpha)t$ reaction. This effect can be seen most clearly in the tables that include materials that were both enriched and depleted. For example, in Table 4 at midplane the dpa for Li_2O with 56% enrichment is 127.3 compared to 119.9 for depleted Li_2O. This means that with 56% enrichment, only 6% of the dpa is coming from the $^6Li(n,\alpha)t$ reaction. Using the dpa to burnup conversion factors in Table 2, it is easy to estimate the contribution to the dpa from the ^{6}Li(n,α)t reaction for any entry in the dpa tables. The dpa values in this report were calculated using the conventional dpa model. Newer calculations are in progress using improved models. When these cross sections become available, it would be straightforward to recalculate the dpa factors for these experiments. However, the current dpa values are compatible with the conventional dpa calculations that are widely used and quoted in the literature. For example, the dpa values for the 316 SS cladding is also given for each of the irradiations. Transmutation effects due both to the ^{6}Li(n,α)t reaction as well as other nuclear reactions may be very important in influencing the degradation of materials since these effects produce a permanent change in the irradiated material. In the comparison of these fast neutron experiments on lithium ceramics to similar experiments in thermal or mixed-spectrum reactors, it is likely that the fast neutron dpa rates are much lower in the mixed-spectrum reactors. Fusion reactors will also exhibit differences from fast reactors in the neutron spectra due to both the 14 MeV neutrons and increased lower-energy neutron flux due to Be blankets and other moderating materials. A more comprehensive technical report of this work is being prepared.[19]

ACKNOWLEDGMENTS

G. W. Hollenberg (Pacific Northwest National Laboratory) and C. E. Johnson (Argonne National Laboratory - East) provided guidance and technical assistance with assembling the information concerning these experiments. D. G. Porter (Argonne National Laboratory – West) was very helpful in providing information regarding the irradiation history of these experiments in the EBR II reactor.

REFERENCES

1. R. C. Knight and G. W. Hollenberg, HEDL-TC-2147, Fabrication Data Package for HEDL FUBR Solid Breeder Irradiation Experiment in EBR-II, February 1982.
2. G. W. Hollenberg, Journal of Nucl. Mater. 122&123, 896-900 (1984).
3. G. W. Hollenberg and D. L. Baldwin, Journal of Nucl. Mater. 133&134, 242-245 (1985).
4. D. L. Baldwin and G. W. Hollenberg, Journal of Nucl. Mater. 141-143, 305-310 (1986).
5. G. W. Hollenberg and R. C. Knight, HEDL-TC-2682, Revised Data Package for FUBR-1B Solid Breeder Experiment in EBR-II – First Insertion, April 1985.
6. L. S. Williams and G. W. Hollenberg, HEDL-TC-2704, Fabrication Data Package for FUBR-1B Solid Breeder Experiment in EBR-II, June 1985 and Addendum A-Second Insertion, March 1987.
7. G. W. Hollenberg, R. C. Knight, P. J. Densley, L. A. Pember, C. E. Johnson, R. B. Poeppel, and Y. Ya G. W. Hollenberg, C. Alvani, B. Rasneur, H. Elbel, H. Wedemeyer, D. E. Walker, T. Takahashi, K. Noda, and H. Akiyama, Journal of Nucl. Mater. 155-157, 563-567 (1988).
8. O. D. Slagle, G. W. Hollenberg, and D. L. Baldwin, Tritium Release and Physical

Stablility of Solid Breeder Materials, Fusion Reactor Materials Semiannual Progress Report, DOE/ER-0313,8, pp. 281-285, August 1990.

9. M. L. Hamilton and R. M. Ermi, Preparation and Irradiation of the Fusion MOTA-2A, Fusion Reactor Materials Semiannual Progress Report, DOE/ER-0313/8, pp. 3-16, August 1990.

10. G. W. Hollenberg, H. Watanabe, I. J. Hastings, and S. E. Berk, Journal of Nucl. Mater. 191-194, 23-29 (1992).

11. R. A. Verrall, O. D. Slagle, G. W. Hollenberg, T. Kurasawa, and J. D. Sullivan, Journal of Nucl. Mater. 212-215, 902-907 (1994).

12. M. L. Hamilton, R. M. Ermi, and A. M. Ermi, Preparation and Irradiation of Fusion MOTA 2B, Fusion Reactor Materials Semiannual Progress Report, DOE/ER-0313/12, pp. 3-14, July 1992.

13. L. R. Greenwood, Fission Reactor Dosimetry – EBR-II X287, Damage Analysis and Fundamental Studies Quarterly Progress Report, DOE/ER-0046/7, pp. 8-16, November 1981.

14. F. C. Franklin, E. R. Ebersole, and R. R. Heinrich, Analysis of EBRII Low-Power Dosimetry Run 78C, ANL-77-76, 1977.

15. L. R. Greenwood and L. S. Kellogg, Neutron Dosimetry for the MOTA-2A Experiment in FFTF, Fusion Reactor Materials Semiannual Progress Report, DOE/ER-0313/12, pp. 49-52, July 1992.

16. L.R. Greenwood and L. S. Kellogg, Neutron Dosimetry for the MOTA-2B Experiment in FFTF, Fusion Reactor Materials Semiannual Progress Report, DOE/ER-0313/16,pp. 21-27, September 1994.

17. L. R. Greenwood, ASTM STP 1001, 598-602 (1989).

18. L. R. Greenwood and R. K. Smither, ANL/FPP/TM-197, Argonne National Laboratory (1985).

19. L. R. Greenwood, PNNL-12200 (1999).

NEUTRON DOSIMETRY AND DAMAGE CALCULATIONS FOR THE TRIST ER-1 EXPERIMENT IN HFIR - L. R. Greenwood (Pacific Northwest National Laboratory)* and C. A. Baldwin (Oak Ridge National Laboratory)

OBJECTIVE

To provide dosimetry and damage analysis for fusion materials irradiation experiments.

SUMMARY

Neutron fluence measurements and radiation damage calculations are reported for the TRIST ER-1 experiment, which was conducted in the removable beryllium position in the High Flux Isotope Reactor (HFIR) at Oak Ridge National Laboratory (ORNL). The maximum neutron fluence at midplane varied from 1.38 to 1.57x 10^{22} n/cm^2 resulting in about 2.4 to 2.8 dpa in Al_2O_3.

PROGRESS AND STATUS

The ER-1 experiment was irradiated in the Temperature-Regulated In-Situ Test (TRIST) facility in the Removable Beryllium (RB*, without thermal neutron shielding) position of the HFIR during cycles 344 through 346. The irradiation started March 8, 1996, and ended June 28, 1996, for a net exposure of 75.78 effective full power days at 85 MW. The goal of the experiment was to determine radiation induced electrical degradation (RIED) in Al_2O_3 ceramic insulators. A complete description of the specimen matrix and irradiation assembly has been published previously.[1,2,3]

Neutron dosimetry capsules were inserted in between the specimen holders, as shown in reference 1 and illustrated in figure 1. The dosimetry capsules consisted of small, welded aluminum tubes measuring about 1.5 mm in diameter and 6.4 mm in length. Each tube contained small monitor wires of Cu, Fe, Ni, Ti, Nb, 80.2% Mn-Cu alloy, and 0.112% Co-Al alloy. Five dosimetry capsules were positioned in grooves 180° apart on each side of the experimental assembly, which measured about 3.2 cm in diameter. Dosimeters were also placed at two additional radial locations (90° to the other positions) at midplane to determine the radial flux gradients. The experimental assembly had 12 equally spaced grooves around the outside circumference. Dosimetry capsules were located at five different elevations between grooves 1 and 2 and between grooves 7 and 8, as shown in figure 1. Dosimetry capsules were placed at midplane between grooves 4 and 5 and between grooves 10 and 11. In an effort to minimize radial flux gradient effects, the experimental assembly was rotated 180° two times (after each cycle). After irradiation, each capsule was opened in a hot cell at ORNL and each individual monitor wire was gamma counted to determine the residual activation. Due to the delay between the end of irradiation and the opening of the capsules for analysis, the shorter-lived isotopes could not be detected. The activation results were then forwarded to PNNL for analysis.

The measured activities were converted to activation rates as listed in Table 1 by correcting for nuclear burnup, gamma self-absorption, decay during and after irradiation, isotopic abundance,

---

[*] Pacific Northwest National Laboratory (PNNL) is operated by the U.S. Department of Energy by Battelle Memorial Institute under contract DE-AC06-76RLO-1830.

and atomic weight. Burnup corrections are based on an iterative procedure for the thermal/epithermal monitor reactions. The resultant estimates of the thermal/epithermal neutron fluences were then used to calculate burnup corrections for the threshold, fast neutron monitor reactions. Burnup corrections averaged 5-10%. The activation rates listed in Table 1 are normalized to full reactor power of 85 MW and have a net absolute uncertainty of about 5%.

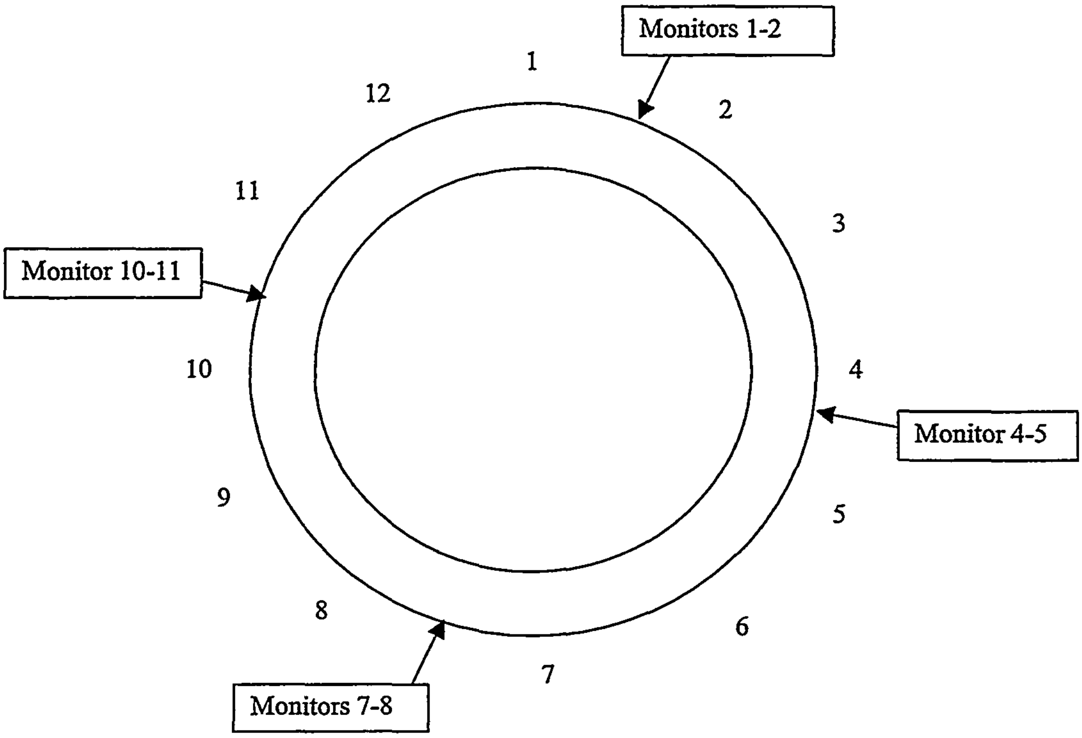

Figure 1. Top view of the neutron flux monitor locations for the TRIST ER-1 experiment. The numbers refer to axial grooves around the circumference of the assembly, which was rotated each cycle.

The activation rates in Table 1 were fit to a polynomial function of form $f(x) = f(0) [1 + a x^2]$, where x is the vertical height from reactor centerline in cm, separately for the measured activation rates in grooves 7/8 and 1/2. . All of the data are reasonably well fit by the average polynomial (coefficient $a = -1.08 \times 10^{-3}$). Figure 2 shows the activity data for the $^{54}Fe(n,p)^{54}Mn$ reaction for the axial locations between grooves 1-2 (solid line) and between grooves 7-8 (dotted line), which were 180° apart. As can be seen, the activities differ by about 18% between these two positions. The flux monitors located at 90° to these grooves, also shown on the figure, fall between these two positions. The flux in between grooves 4-5 is about midway between grooves 7-8 and 1-2 whereas the flux in between grooves 10-11 is nearly identical (2% higher) to grooves 1-2. This radial flux pattern repeats for all of the measured activities except that the thermal neutron gradients appear to be much lower (5-10%).

Table 1. Activation Rates (at/at-s) – TRIST ER-1

Monitor-Grooves	Ht,cm	^{54}Fe(n,p) ^{54}Mn (E-11)	^{46}Ti(n,p) ^{46}Sc (E-12)	^{63}Cu(n,α) ^{60}Co (E-13)	^{55}Mn(n,2n) ^{54}Mn (E-14)	^{59}Co(n,γ) ^{60}Co (E-8)	^{93}Nb(n,γ) ^{94}Nb (E-9)
J12 1-2	21.34	0.652	0.86	0.39	1.91	1.15	0.50
J13 7-8	21.34	0.773	1.04	0.47	2.20	1.07	0.48
J16 1-2	9.17	1.22	1.64	0.74	3.45	2.50	1.03
J17 7-8	9.17	1.43	1.96	0.86	4.11	2.52	1.06
J19 7-8	0.00	1.72	2.26	1.00	4.61	3.18	1.31
J20 1-2	0.00	1.44	1.90	0.86	3.88	2.69	1.26
J25 4-5	0.00	1.55	2.13	0.92	4.39	3.37	1.28
J27 10-11	0.00	1.45		0.89			
J24 1-2	-12.17	1.20	1.57	0.71	3.29	2.54	1.02
J21 7-8	-12.17	1.39	1.90	0.84	4.01	2.53	1.05
J26 1-2	-21.34	0.744	1.00	0.45	2.18	1.69	0.68
J23 7-8	-21.34	0.900	1.19	0.54	2.63	1.71	0.65

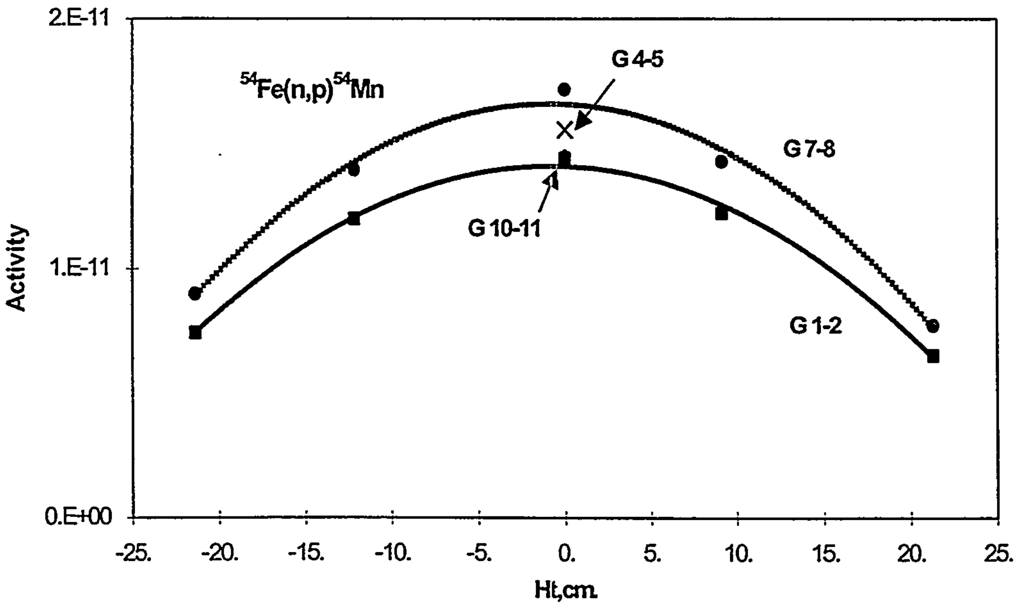

Figure 2. Measured activation rates vs. reactor elevation for the ^{54}Fe(n,p)^{54}Mn reaction. Data from grooves 7-8 are shown by the circles and dotted line; grooves 1-2 are shown by squares and the solid line; the X is for grooves 4-5 and a triangle is for grooves 10-11.

Midplane activation rates were then used in the STAY'SL[4] computer code to adjust the neutron flux spectrum determined in previous spectral measurements in the RB* position in HFIR.[5] STAY'SL performs a generalized least-squares adjustment of all measured and calculated values including the measured activities, calculated spectra, and neutron cross sections. Neutron cross sections and their uncertainties were generally taken from the ENDF/B-V[6] evaluation. The resultant neutron fluence values are listed in Table 2. The activation rates and the derived neutron spectra and fluences are in excellent agreement with previous measurements in the HFIR RB* position.[5]

Neutron damage calculations were performed using the SPECTER computer code[7] at the midplane position of HFIR. Midplane dpa and helium (appm) values are also listed in Table 2. The fluence and damage values at other experimental positions can be calculated by the gradient equation given above. The dpa values for Al2O3 were calculated using the SPECOMP computer code[8] using threshold energies of 25 eV for Al and 65 eV for O.

Table 2. Midplane Fluence and Damage Values for TRIST ER-1

Neutron Fluence,x10^{21} n/cm^2			Element	dpa		He,appm	
Grooves:	7-8	1-2		7-8	1-2	7-8	1-2
Total	15.71	13.83	C	2.6	2.2	2.4	2.0
Thermal (<.5 eV)	6.92	5.80	Al	4.1	3.6	0.9	0.8
0.5 eV - 0.1 MeV	5.33	5.03	V	2.8	2.5	0.03	0.03
> 0.1 MeV	3.46	3.00	Cr	2.4	2.1	0.2	0.2
> 1 MeV	1.34	1.14	Fe	2.1	1.8	0.4	0.4
			Ni Fast	2.4	2.1	6.5	5.5
			59-Ni	0.8	0.6	454.3	331.9
			Total Ni	3.2	2.7	460.8	337.4
			Cu	2.8	2.4	0.4	0.3
			316SS*	2.3	2.0	60.2	44.2
			Al_2O_3	2.8	2.4	7.7	6.5

*316SS = Fe(0.645), Ni(0.13), Cr(0.18), Mn(0.019), Mo(0.026) wt%

REFERENCES

1. W. S. Eatherly, D. W. Heatherly, M. T. Hurst, A. L. Qualls, D. G. Raby, R. G. Sitterson, L. L. Snead, K. R. Thoms, R. L. Wallace, D. P. White, S. J. Zinkle, E. H. Farnum, K. Scarborough, K. Shiiyama, T. Sagawa, M. Narui, and T. Shikama, Fusion Reactor Materials Semiannual Progress Report, DOE/ER-0313/19, pp. 241-248 (1995).

2. A. L. Qualls, W. S. Eatherly, D. W. Heatherly, M. T. Hurst, D. G. Raby, R. G. Sitterson, L. L. Snead, K. R. Thoms, R. L. Wallace, and S. J. Zinkle, Fusion Reactor Materials Semiannual Progress Report, DOE/ER-0313/20, pp. 267-271 (1996).

3. S. J. Zinkle, D. P. White, L. L. Snead, W. S. Eatherly, A. L. Qualls, D. W. Heatherly, R. G. Sitterson, R. L. Wallace, D. G. Raby, M. T. Hurst, E. H. Farnum, K. Scarborough, T. Shikama, M. Narui, and K Shiiyama, Fusion Reactor Materials Semiannual Progress Report, DOE/ER-0313/20, pp. 257-266 (1996).

4. F. G. Perey, Least Squares Dosimetry Unfolding: The Program STAY'SL, ORNL/TM-6062 (1977).

5. L. R. Greenwood, Alloy Development for Irradiation Performance Semiannual Progress Report, DOE/ER-045/15, pp. 4-14 (1985).

6. Evaluated Nuclear Data File, Part B, Version V, National Nuclear Data Center, Brookhaven National Laboratory.

7. L. R. Greenwood and R. K. Smither, SPECTER: Neutron Damage Calculations for Materials Irradiations, ANL/FPP-TM-197, January 1985.

8. L. R. Greenwood, ASTM STP 1001, H. Farrar and E. P. Lippincott, Eds., ASTM, Philadelphia, pp. 598-602, 1998.

NEUTRON DOSIMETRY AND DAMAGE CALCULATIONS FOR THE HFIR-CTR-62 and 63 IRRADIATIONS -

L. R. Greenwood (Pacific Northwest National Laboratory)* and C. A. Baldwin (Oak Ridge National Laboratory)

OBJECTIVE

To provide dosimetry and damage analysis for fusion materials irradiation experiments.

SUMMARY

Neutron fluence measurements and radiation damage calculations are reported for the CTR-62 and –63 experiments, which were conducted in the High Flux Isotope Reactor (HFIR) at Oak Ridge National Laboratory (ORNL). The maximum neutron fluence at midplane was 6.9E+22 n/cm^2 resulting in about 14 dpa in type 316 stainless steel.

PROGRESS AND STATUS

The CTR-62 and -63 experiments were irradiated in the target position of the HFIR during cycles 335 through 341, starting April 13, 1995, and ending December 16, 1995, for a net exposure of 180.45 effective full power days at 85 MW. The two irradiation assemblies were nearly identical and they were co-irradiated in HFIR. The goal of the experiment was to irradiate reduced-activation and conventional ferritic steels at temperatures of 300 and 400°C. A complete description of the specimen matrix and irradiation assembly has been published previously.[1]

Neutron dosimetry capsules were inserted in between the specimen holders, as shown in reference 1. The dosimetry capsules consisted of small, welded aluminum tubes measuring about 1.5 mm in diameter and 6.4 mm in length. Each tube contained small monitor wires of Cu, Fe, Ni, Ti, Nb, 80.2% Mn-Cu alloy, and 0.112% Co-Al alloy. Five dosimetry capsules were irradiated with each of the experiments; however, only six of the capsules were analyzed. Each capsule was opened in a hot cell at ORNL and each individual monitor wire was gamma counted to determine the residual activation. Due to the delay between the end of irradiation and the opening of the capsules for analysis, the shorter-lived isotopes could not be detected. The activation results were then forwarded to PNNL for analysis.

The measured activities were converted to activation rates as listed in Table 1 by correcting for nuclear burnup, gamma self-absorption, decay during and after irradiation, isotopic abundance, and atomic weight. Burnup corrections are based on an iterative procedure for the thermal/epithermal monitor reactions. The resultant estimates of the thermal/epithermal neutron fluences were then used to calculate burnup corrections for the threshold, fast neutron monitor reactions. Burnup corrections averaged 20-30% for the thermal/epithermal reactions and 5-30% for the threshold reaction rates. The activation rates listed in Table 1 are normalized to full reactor power of 85 MW and have a net absolute uncertainty of about 5%.

The activation rates in Table 1 were fit to a polynomial function of form $f(x) = f(0) [1 + a x^2]$, where x is the vertical height from reactor centerline in cm. All of the data are reasonably well fit

---

*Pacific Northwest National Laboratory (PNNL) is operated by the U.S. Department of Energy by Battelle Memorial Institute under contract DE-AC06-76RLO-1830.

by the average polynomial (coefficient a = -1.06×10^{-3}). Midplane activation rates were then used in the STAY'SL[2] computer code to adjust the neutron flux spectrum determined in previous spectral measurements in the target position in HFIR.[3] STAY'SL performs a generalized least-squares adjustment of all measured and calculated values including the measured activities, calculated spectra, and neutron cross sections. Neutron cross sections and their uncertainties were generally taken from the ENDF/B-V[4] evaluation. The resultant neutron fluence values are listed in Table 2. The activation rates and the derived neutron spectra and fluences are in excellent agreement with previous measurements in the HFIR target position.[3]

Table 1. Activation Rates (at/at-s) - HFIR CTR-62 and -63

Experiment/ Monitor	Ht,cm	^{54}Fe(n,p)^{54}Mn (E-11)	^{63}Cu(n,α)^{60}Co (E-13)	^{55}Mn(n,2n)^{54}Mn (E-13)	^{59}Co(n,γ)^{60}Co (E-8)	^{93}Nb(n,γ)^{94}Nb (E-9)
62-J1	18.3	3.94	2.45	1.22	5.38	1.74
62-J3	0.0	5.60	3.70	1.81	7.09	2.68
62-J5	-18.3	-	2.32	1.17	4.53	1.68
63-J6	21.3	3.22	1.98	0.97	2.97	1.43
63-J8	6.1	-	3.59	1.76	7.23	2.65
63-J11	-15.2	4.38	2.75	-	-	1.97

Table 2. Midplane Fluence and Damage Values for HFIR CTR-62 and -63

Neutron Fluence,n/cm2		Element	dpa	He,appm
Total	6.91E+22	C	12.1	26.0
Thermal (<.5 eV)	3.15E+22	Al	21.9	9.8
0.5 eV - 0.1 MeV	2.08E+22	V	15.6	0.33
> 0.1 MeV	1.68E+22	Cr	13.7	2.3
> 1 MeV	8.50E+21	Fe	12.1	4.0
		Ni Fast	13.1	53.7
		59-Ni	11.5	6526.5
		Total Ni	24.6	6580.3
		Cu	105	3.6

Neutron damage calculations were performed using the SPECTER computer code[5] at the midplane position of HFIR. Midplane dpa and helium (appm) values are also listed in Table 2. The fluence and damage values at other experimental positions can be calculated by the gradient equation given above. Damage parameters for other elements or compounds have been calculated and are readily available on request.

Helium production in nickel and nickel alloys requires a more complicated non-linear calculation.[6] Helium production in stainless steel is detailed in Table 3.

FUTURE WORK

Additional experiments are in progress in HFIR.

Table 3. dpa and He Values for 316 SS in HFIR CTR-62 and -63
(Includes ^{59}Ni effect)

Height,cm	dpa	He,appm
0	14.0	820
3	13.9	810
6	13.5	779
9	12.9	729
12	12.0	659
15	10.9	570
18	9.5	464

316SS = Fe(0.645), Ni(0.13), Cr(0.18), Mn(0.019), Mo(0.026) wt%

REFERENCES

1. K. E. Lennox, R. L. Klueh, and R. L. Senn, Fusion Reactor Materials Semiannual Progress Report, DOE/ER-0313/18, pp. 7-20 (1995).
2. F. G. Perey, Least Squares Dosimetry Unfolding: The Program STAY'SL, ORNL/TM-6062 (1977).
3. L. R. Greenwood and D. V. Steidl, Dosimetry for the HFIR-CTR 53/54 Experiments, Fusion Reactor Materials Semiannual Progress Report, DOE/ER-0313/8, pp. 40-42 (1990).
4. Evaluated Nuclear Data File, Part B, Version V, National Nuclear Data Center, Brookhaven National Laboratory.
5. L. R. Greenwood and R. K. Smither, SPECTER: Neutron Damage Calculations for Materials Irradiations, ANL/FPP-TM-197, January 1985.
6. L. R. Greenwood, A New Calculation of Thermal Neutron Damage and Helium Production in Nickel, Journal of Nuclear Materials 116, pp. 137-142 (1983).

10.0 MATERIALS ENGINEERING AND DESIGN REQUIREMENTS

No contributions.

11.0 IRRADIATION FACILITIES, TEST MATRICES, AND EXPERIMENTAL METHODS

CONCEPTUAL DEVELOPMENT OF FUSION-2 EXPERIMENT FOR IRRADIATION TESTING OF VANADIUM ALLOYS IN A LITHIUM ENVIRONMENT AT ≈500-750°C IN THE BOR-60 REACTOR[1]

– V. Kazakov, V. Chakin, V. Efimov, V. Petukhov, A. Tuktabiev, P. Gabiev (Research Institute of Atomic Reactors), H. Tsai, T. S. Bray, D. L. Smith (Argonne National Laboratory); and A. Rowcliffe (Oak Ridge National Laboratory)

OBJECTIVE

BOR-60 is a sodium-cooled fast reactor in Russia with a coolant inlet temperature of 300-330°C. Previous irradiation experiments conducted in the BOR-60, EBR-II, HFIR, ATR, and SM reactors indicate that the threshold for low-temperature embrittlement of vanadium-base alloys is ≈400°C. The purpose of the proposed Fusion-2 experiment in BOR-60 is to study the effects of neutron damage in vanadium-base alloys at or just near the high-temperature end, i.e., 500-750°C. The objective of the present task is to develop the conceptual design of the experimental assembly based on the functional requirements of the experiment. Conceptual development focuses on construction of the experimental assembly, methods of temperature control and measurement, thermal performance of the assembly, and feasibility of conducting assembly and disassembly in the Research Institute of Atomic Reactors (RIAR), where BOR-60 is located.

SUMMARY

The requirements of this task are to complete the conceptual designs of irradiation capsules to be exposed to a neutron dose of ≈20 dpa in BOR-60. The specimen matrix will include sheet tensile specimens, compact tension specimens, bend bars, TEM disks, and pressurized creep tubes. To better utilize the test volume and provide additional temperature options, it was decided to modify the experiment from a two-capsule to a three-capsule design. All capsules will be liquid-metal-bonded for temperature uniformity. Goal temperatures for the three capsules will be 450, 600, and 700-750°C, with an emphasis on 600°C. A key objective of the experiment will be to generate irradiation creep data for vanadium-base alloys, especially at the emphasized temperature of 600°C, where thermal creep may not be dominant.

PROGRESS

The design for Fusion-2 would be similar to that shown in Fig. 1, with the exception of the number of axially-arranged capsules, which would be increased from two to three. A three-capsule design would permit better utilization of the high-value, high-flux space at the core midplane and, because each capsule can operate at a different temperature, a more diverse study of temperature effects on irradiation. By adopting three shorter capsules, there would also be less axial power/temperature tilt in each capsule would be reduced.

The materials of construction for the Fusion-2 experiment would be as shown in Table 1. The double-wall capsule (Item 3) would be made of austenitic stainless steel or Inconel for compatibility with the bond sodium at elevated temperature. The subcapsules (Items 4 and 5) containing the test specimens would be made of TZM (an Mo-base alloy) for impurity control and compatibility with the specimen lithium bond. There would be two sizes of subcapsules; those of smaller diameter (Item 5) are sized to accommodate pressurized creep tubes.

Preliminary thermal analysis has been conducted, and the results indicate that a wide range of irradiation temperatures are attainable in the Fusion-2 experiment with this design. For performance assessment of the vanadium-base alloy for fusion applications, we decided that the most important test temperature at this time would be 600°C. Accordingly, the high-flux middle capsule would be allocated for this temperature. Because the lengths of the three capsules need

---

[1] This work has been supported by the U.S. Department of Energy, Office of Fusion Energy Research, under Contract W-31-109-Eng-38.

not be the same, the middle capsule would be slightly elongated to provide a ≥40% total test volume. The top and bottom capsules would be designed for 700-750 and 450°C, respectively, and would have a smaller test volume than that of the middle capsule.

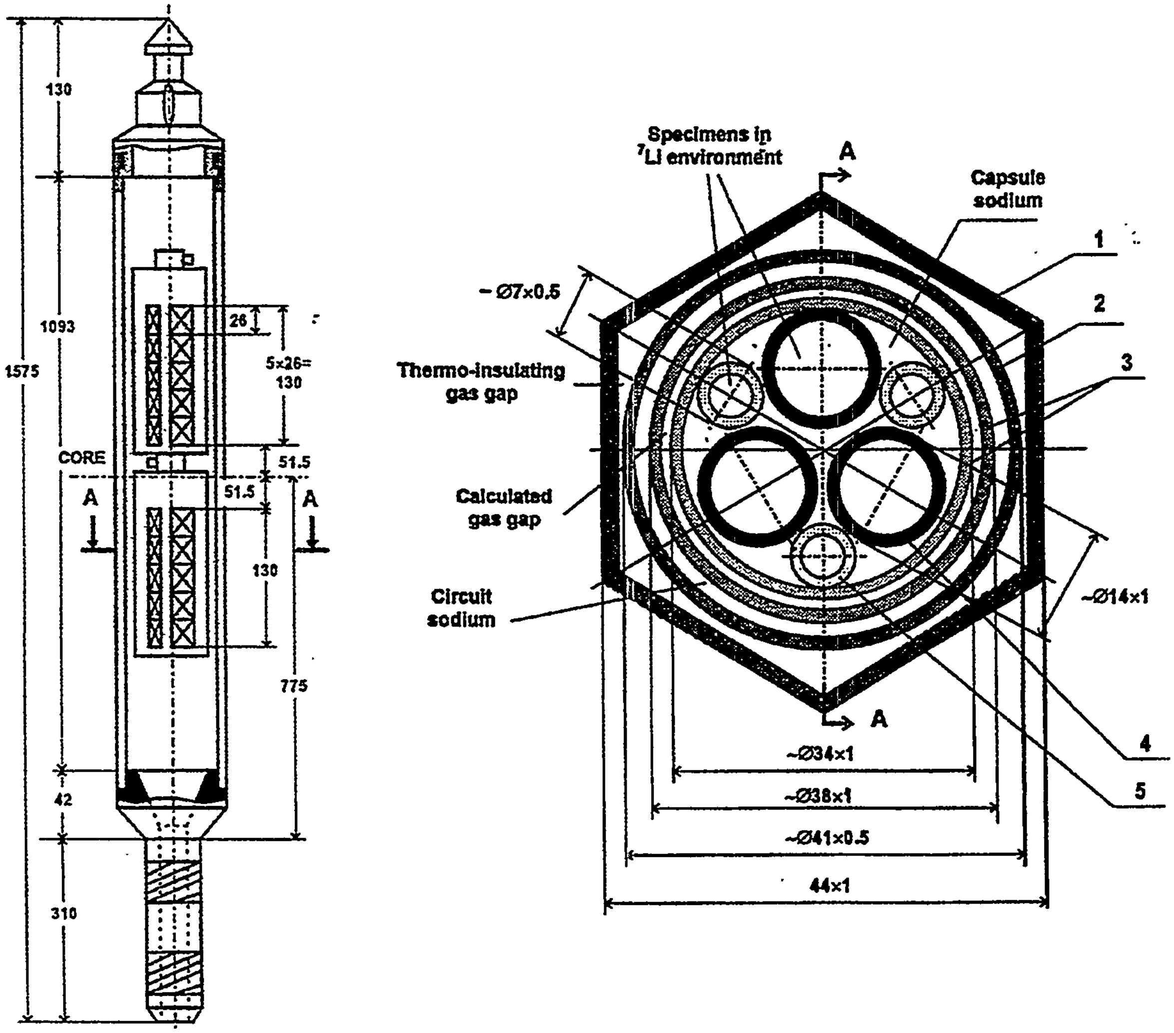

Fig. 1. Fusion-2 test vehicle (left, showing two capsules) and cross section of capsule (right). Note: design is being revised to accommodate three axial capsules.

Table 1. Materials of construction for Fusion-2 test assembly

Item No.	Test Temperature = 450, 550, 600°C	Test Temperature = 700°C	Fill Medium
1	Hex Can	Hex Can	He
2	SS	SS	Na
3	304 SS	Inconel	He (outer) Na(inner)
4	Mo alloy of TZM or VM-1A type	Mo alloy of TZM or VM-1A type	Li-7, specimens
5	Mo alloy of TZM or VM-1A type	Mo alloy of TZM or VM-1A type	Li-7, specimens

Another decision made in this reporting period was to forego the option of conducting a dynamic helium charging experiment (DHCE) in Fusion-2. (In a DHCE, tritium is implanted in the capsule. During irradiation, some of the tritium diffuses into the specimen and decays in-situ into ^{3}He, thereby yielding the concurrent effects of helium generation and neutron damage.) This decision was made to ease the logistic constraint of tritium handling/transport and to provide additional time to better prepare for such an eventual experiment.

To monitor the specimen temperature, a limited number of thermocouples would be incorporated in the top and middle capsules in the Fusion-2 vehicle. Because only one core location (D-23) in BOR-60 permits deployment of thermocouples, the Fusion-2 experiment would be irradiated at this location, at least at the onset of the experiment. If this location is available for the entire irradiation time and the cost is not prohibitive, the Fusion-2 capsule would remain at D-23 for the entire $\approx$1-year irradiation to $\approx$20 dpa. Otherwise, it would be irradiated for a finite period, possibly several weeks, at D-23 to confirm the test temperatures before being relocated to a comparable core location (possibly E-23) to complete the irradiation.

Steady irradiation temperature is important in testing structural materials samples. For pressurized creep specimens, this is particularly, because temperature fluctuation affects not only creep properties but also internal gas pressure. Means to ensure steady irradiation temperatures are being explored.

Future Activities

The Fusion-2 conceptual design effort will be completed in the next reporting period. A full assessment of the experiment based on the optimized design will be conducted.

REFERENCE

1. V. Kazakov et al., "Conceptual Development of Fusion-2 Experiment for Radiation Test of Vanadium Alloys in BOR-60 Reactor at 500-700°C in Lithium Environment," Report on Milestone 1 of Subcontract 28X-SZ738V of 06/08/98 with Lockheed Martin Energy Systems, Inc., USA, 1998.

SCHEDULE AND STATUS OF IRRADIATION EXPERIMENTS – A. F. Rowcliffe (Oak Ridge National Laboratory)

OBJECTIVE

To provide an updated summary of the status of irradiation experiments for the fusion materials program.

SUMMARY

The current status of reactor irradiation experiments is presented in tables summarizing the experimental objectives, conditions, and schedule.

PROGRESS AND STATUS

Currently, there are three experiments in-reactor (RB-10J, RB-14J, and JP-25). Post-irradiation testing is in progress on CTR-62/63 and RB-11J/12J. Experiments TRIST-TC1 and RB-13J have been removed from reactor and are awaiting disassembly.

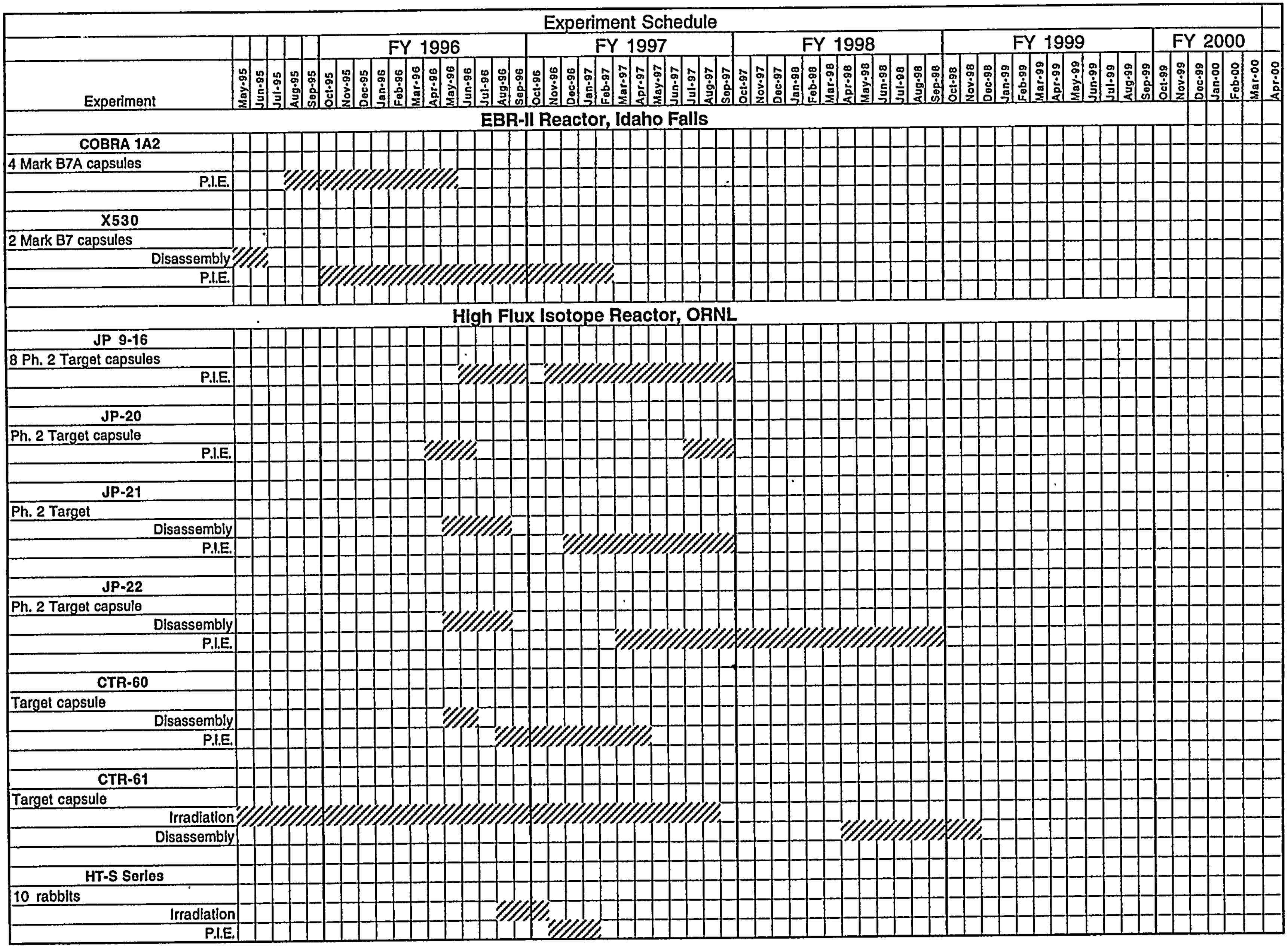
Experiment Schedule
FY 1996
FY 1997
FY 1998
FY 1999
FY 2000
Experiment
May-95
Jun-95
Jul-95
Aug-95
Sep-95
Oct-95
Nov-95
Dec-95
Jan-96
Feb-96
Mar-96
Apr-96
May-96
Jun-96
Jul-96
Aug-96
Sep-96
Oct-96
Nov-96
Dec-96
Jan-97
Feb-97
Mar-97
Apr-97
May-97
Jun-97
Jul-97
Aug-97
Sep-97
Oct-97
Nov-97
Dec-97
Jan-98
Feb-98
Mar-98
Apr-98
May-98
Jun-98
Jul-98
Aug-98
Sep-98
Oct-98
Nov-98
Dec-98
Jan-99
Feb-99
Mar-99
Apr-99
May-99
Jun-99
Jul-99
Aug-99
Sep-99
Oct-99
Nov-99
Dec-99
Jan-00
Feb-00
Mar-00
Apr-00
EBR-II Reactor, Idaho Falls
COBRA 1A2
4 Mark B7A capsules
P.I.E.
X530
2 Mark B7 capsules
Disassembly
P.I.E.
High Flux Isotope Reactor, ORNL
JP 9-16
8 Ph. 2 Target capsules
P.I.E.
JP-20
Ph. 2 Target capsule
P.I.E.
JP-21
Ph. 2 Target
Disassembly
P.I.E.
JP-22
Ph. 2 Target capsule
Disassembly
P.I.E.
CTR-60
Target capsule
Disassembly
P.I.E.
CTR-61
Target capsule
Irradiation
Disassembly
HT-S Series
10 rabbits
Irradiation
P.I.E.

Experiment Schedule

						FY 1996											
Experiment	May-95	Jun-95	Jul-95	Aug-95	Sep-95	Oct-95	Nov-95	Dec-95	Jan-96	Feb-96	Mar-96	Apr-96	May-96	Jun-96	Jul-96	Aug-96	Sep-96
HT-F Series																	
6 rabbits																	
Irradiation								▨	▨	▨	▨					▨	▨
P.I.E.																	
HFIR-TRIST-ER1																	
RB In-situ experiment																	
Irradiation											▨	▨	▨	▨			
Disassembly																	
P.I.E.																	
HFIR-MFE-RB-10J																	
RB Spectrally tailored																	
Design/assembly												▨	▨	▨	▨	▨	▨
Irradiation																	
Disassembly																	
P.I.E.																	
HFIR-MFE-RB-11J, 12J																	
2 RB spectrally tailored																	
Design/assembly						▨	▨	▨	▨	▨	▨	▨	▨	▨	▨	▨	▨
Irradiation																	
Disassembly																	
P.I.E.																	
HFIR-RB-13J																	
RB varying temperature																	
Design/Assembly														▨	▨	▨	▨
Irradiation																	
Disassembly																	
P.I.E.																	
HFIR-RB-14J																	
Unshielded																	
Irradiation																	
Disassembly																	
P.I.E.																	

	FY 1997												FY 1998											
Experiment	Oct-96	Nov-96	Dec-96	Jan-97	Feb-97	Mar-97	Apr-97	May-97	Jun-97	Jul-97	Aug-97	Sep-97	Oct-97	Nov-97	Dec-97	Jan-98	Feb-98	Mar-98	Apr-98	May-98	Jun-98	Jul-98	Aug-98	Sep-98
HT-F Series																								
6 rabbits																								
Irradiation	▨	▨	▨	▨	▨																			
P.I.E.							▨	▨	▨	▨														
HFIR-TRIST-ER1																								
RB In-situ experiment																								
Irradiation																								
Disassembly	▨	▨														▨	▨							
P.I.E.			▨	▨	▨	▨	▨	▨	▨	▨	▨	▨	▨							▨	▨	▨	▨	▨
HFIR-MFE-RB-10J																								
RB Spectrally tailored																								
Design/assembly	▨	▨	▨	▨	▨	▨	▨	▨	▨	▨	▨	▨	▨	▨	▨	▨	▨	▨	▨	▨	▨	▨	▨	
Irradiation																								
Disassembly																								
P.I.E.																								
HFIR-MFE-RB-11J, 12J																								
2 RB spectrally tailored																								
Design/assembly	▨	▨	▨	▨																				
Irradiation					▨	▨	▨	▨	▨	▨	▨	▨	▨	▨	▨	▨	▨	▨	▨	▨	▨	▨		
Disassembly																								
P.I.E.																								
HFIR-RB-13J																								
RB varying temperature																								
Design/Assembly	▨	▨	▨	▨	▨	▨	▨	▨	▨	▨	▨	▨	▨	▨	▨	▨	▨	▨	▨					
Irradiation																						▨	▨	▨
Disassembly																								
P.I.E.																								
HFIR-RB-14J																								
Unshielded																								
Irradiation																								
Disassembly																								
P.I.E.																								

	FY 1999												FY 2000						
Experiment	Oct-98	Nov-98	Dec-98	Jan-99	Feb-99	Mar-99	Apr-99	May-99	Jun-99	Jul-99	Aug-99	Sep-99	Oct-99	Nov-99	Dec-99	Jan-00	Feb-00	Mar-00	Apr-00
HT-F Series																			
6 rabbits																			
Irradiation																			
P.I.E.																			
HFIR-TRIST-ER1																			
RB In-situ experiment																			
Irradiation																			
Disassembly																			
P.I.E.	▨	▨																	
HFIR-MFE-RB-10J																			
RB Spectrally tailored																			
Design/assembly																			
Irradiation	▨	▨	▨	▨	▨	▨	▨	▨	▨	▨	▨	▨	▨	▨	▨	▨	▨	▨	▨
Disassembly																			
P.I.E.																			
HFIR-MFE-RB-11J, 12J																			
2 RB spectrally tailored																			
Design/assembly																			
Irradiation																			
Disassembly		▨	▨	▨	▨	▨													
P.I.E.							▨	▨	▨	▨	▨	▨	▨	▨	▨	▨	▨	▨	▨
HFIR-RB-13J																			
RB varying temperature																			
Design/Assembly																			
Irradiation	▨	▨	▨	▨	▨	▨	▨	▨	▨	▨									
Disassembly																		▨	▨
P.I.E.																			
HFIR-RB-14J																			
Unshielded																			
Irradiation							▨	▨	▨	▨	▨	▨	▨	▨	▨	▨					
Disassembly																		▨	▨
P.I.E.																			

Experiment Schedule

Experiment						FY 1996											
	May-95	Jun-95	Jul-95	Aug-95	Sep-95	Oct-95	Nov-95	Dec-95	Jan-96	Feb-96	Mar-96	Apr-96	May-96	Jun-96	Jul-96	Aug-96	Sep-96
HFIR-TRIST-TC1																	
In-situ																	
Irradiation																	
Disassembly																	
P.I.E.																	
HFIR-CTR-62, 63																	
2 Target capsules																	
Irradiation	▨	▨	▨	▨	▨	▨	▨										
Disassembly													▨	▨	▨	▨	
P.I.E.																	
HFIR-JP-25																	
Target capsule																	
Design/Assembly																	
Irradiation																	
Disassembly																	
P.I.E.																	
High Flux Beam Reactor, Brookhaven																	
HFBR-V1, V2																	
8 rabbits																	
Irradiation	▨	▨	▨	▨													
Disassembly									▨	▨	▨	▨					
P.I.E.													▨	▨	▨	▨	▨
HFBR-V3, V4																	
Irradiation																▨	▨
Disassembly																	
P.I.E.																	
Advanced Test Reactor, Idaho Falls																	
ATR-A1																	
Drop-in																	
Irradiation	▨	▨	▨	▨	▨	▨	▨	▨	▨	▨	▨	▨	▨	▨			
Disassembly																	
P.I.E.																	

Experiment	FY 1997												FY 1998											
	Oct-96	Nov-96	Dec-96	Jan-97	Feb-97	Mar-97	Apr-97	May-97	Jun-97	Jul-97	Aug-97	Sep-97	Oct-97	Nov-97	Dec-97	Jan-98	Feb-98	Mar-98	Apr-98	May-98	Jun-98	Jul-98	Aug-98	Sep-98
HFIR-TRIST-TC1																								
In-situ																								
Irradiation																								
Disassembly																								
P.I.E.																								
HFIR-CTR-62, 63																								
2 Target capsules																								
Irradiation																								
Disassembly																								
P.I.E.																	▨	▨	▨	▨	▨	▨	▨	▨
HFIR-JP-25																								
Target capsule																								
Design/Assembly																	▨	▨	▨	▨	▨	▨	▨	▨
Irradiation																								
Disassembly																								
P.I.E.																								
High Flux Beam Reactor, Brookhaven																								
HFBR-V1, V2																								
8 rabbits																								
Irradiation																								
Disassembly																								
P.I.E.	▨	▨	▨	▨																				
HFBR-V3, V4																								
Irradiation																								
Disassembly	▨	▨	▨	▨																				
P.I.E.					▨	▨	▨	▨	▨															
Advanced Test Reactor, Idaho Falls																								
ATR-A1																								
Drop-in																								
Irradiation																								
Disassembly	▨	▨	▨	▨																				
P.I.E.					▨	▨	▨	▨	▨	▨	▨	▨	▨	▨	▨	▨	▨	▨	▨					

Experiment	FY 1999												FY 2000						
	Oct-98	Nov-98	Dec-98	Jan-99	Feb-99	Mar-99	Apr-99	May-99	Jun-99	Jul-99	Aug-99	Sep-99	Oct-99	Nov-99	Dec-99	Jan-00	Feb-00	Mar-00	Apr-00
HFIR-TRIST-TC1																			
In-situ																			
Irradiation				▨	▨	▨	▨	▨	▨	▨									
Disassembly																			
P.I.E.																			
HFIR-CTR-62, 63																			
2 Target capsules																			
Irradiation																			
Disassembly																			
P.I.E.	▨	▨	▨	▨	▨	▨	▨	▨	▨	▨	▨	▨	▨	▨					
HFIR-JP-25																			
Target capsule																			
Design/Assembly	▨																		
Irradiation					▨	▨	▨	▨	▨	▨	▨	▨	▨	▨	▨	▨	▨	▨	▨
Disassembly																			
P.I.E.																			
High Flux Beam Reactor, Brookhaven																			
HFBR-V1, V2																			
8 rabbits																			
Irradiation																			
Disassembly																			
P.I.E.																			
HFBR-V3, V4																			
Irradiation																			
Disassembly																			
P.I.E.																			
Advanced Test Reactor, Idaho Falls																			
ATR-A1																			
Drop-in																			
Irradiation																			
Disassembly																			
P.I.E.																			

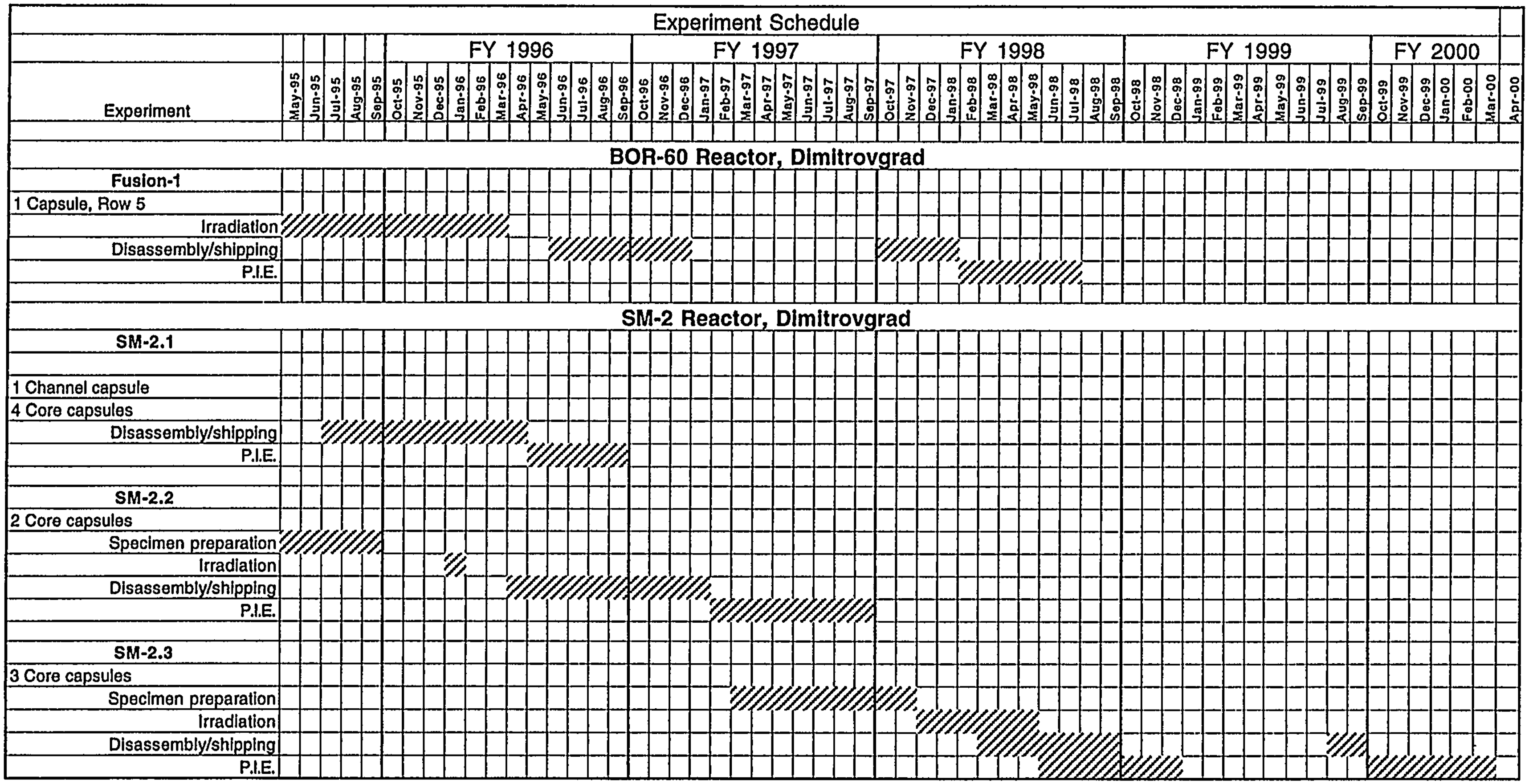
Experiment Schedule
FY 1996
FY 1997
FY 1998
FY 1999
FY 2000
Experiment
May-95
Jun-95
Jul-95
Aug-95
Sep-95
Oct-95
Nov-95
Dec-95
Jan-96
Feb-96
Mar-96
Apr-96
May-96
Jun-96
Jul-96
Aug-96
Sep-96
Oct-96
Nov-96
Dec-96
Jan-97
Feb-97
Mar-97
Apr-97
May-97
Jun-97
Jul-97
Aug-97
Sep-97
Oct-97
Nov-97
Dec-97
Jan-98
Feb-98
Mar-98
Apr-98
May-98
Jun-98
Jul-98
Aug-98
Sep-98
Oct-98
Nov-98
Dec-98
Jan-99
Feb-99
Mar-99
Apr-99
May-99
Jun-99
Jul-99
Aug-99
Sep-99
Oct-99
Nov-99
Dec-99
Jan-00
Feb-00
Mar-00
Apr-00
BOR-60 Reactor, Dimitrovgrad
Fusion-1
1 Capsule, Row 5
Irradiation
Disassembly/shipping
P.I.E.
SM-2 Reactor, Dimitrovgrad
SM-2.1
1 Channel capsule
4 Core capsules
Disassembly/shipping
P.I.E.
SM-2.2
2 Core capsules
Specimen preparation
Irradiation
Disassembly/shipping
P.I.E.
SM-2.3
3 Core capsules
Specimen preparation
Irradiation
Disassembly/shipping
P.I.E.

Summary of Reactor Irradiation Experiments

Experiment	Lead Lab	Collaborators	Responsible Person	Major Objectives	Materials	Temperature ℃	Dose (dpa) or fluence	Irrad. Start	Irrad. Finish	Status
EBR-II, Reactor, ANL, Idaho Falls, ID										
COBRA 1A2	PNL	ORNL, ANL, MONBUSHO	M.L. Hamilton	Tensile and fatigue prop., Charpy impact, fracture toughness, TEM	Austenitic and ferritic steels, Fe-alloys, V, Be, low act. materials, Cu alloys, Ti-Al, SiC, C-C comp.	370, 400, 800	33	Nov-92	Sep-94	
X530	ANL		H. Tsai, H.M. Chung	He-effects, swelling, Charpy impact, fracture toughness, tensile prop.	V alloys	370	5	Aug-94	Sep-94	
High Flux Isotope Reactor, ORNL, Oak Ridge, TN										
HFIR-CTR-60	ORNL		S.J. Zinkle	Flexure bars, TEM, indentation disks	Isotopically tailored ceramics	100-600	2.4E+26 n/m2	Dec-94	Aug-95	
HFIR-CTR-61	ORNL		S.J. Zinkle	Similar to HFIR-CTR-60			7.20E+26	Dec-94	Aug-98	
HFIR-JP-9	ORNL	JAERI	P.J. Maziasz/ J.E. Pawel	He effects by isotopic tailoring, tensile prop., TEM	Austenitic and ferritic steels	300-600	57	Jul-90	Apr-94	
HFIR-JP-12	ORNL	JAERI	P.J. Maziasz/ J.E. Pawel	Similar to HFIR-JP-9			57	Jul-90	Apr-94	
HFIR-JP-15	ORNL	JAERI	P.J. Maziasz/ J.E. Pawel	Similar to HFIR-JP-9			57	Jul-90	Apr-94	
HFIR-JP-20	ORNL	JAERI	J.E. Pawel	Tensile Prop., TEM, He effects by isotopic tailoring	Austenitic and ferritic steels	300-600	8	Dec-93	Jun-94	
HFIR-JP-21	ORNL	JAERI	J.E. Pawel	Similar to HFIR-JP-20			18	Dec-93	Apr-95	
HFIR-JP-22	ORNL	JAERI	J.E. Pawel	Similar to HFIR -JP-20			34	Dec-93	Jan-96	
HFIR-JP-23	PNL	MONBUSHO	D.S. Gelles	TEM	Austenitic and ferritic steels, Cu, Mo, V alloys, TiAl	300-600	8	Dec-93	Jun-94	
HFIR-HT-S1, -S7	ORNL		L.L. Snead	Thermal conductivity	Various Insulators	80-350	0.01-1.0	Jun-95	Aug-95	
HFIR-HT-F Series	ORNL		L. L. Snead	Fiber tensile	SiC	80-800	0.001-1.0	Jan-95	Mar-96	

Summary of Reactor Irradiation Experiments

Experiment	Lead Lab	Collaborators	Responsible Person	Major Objectives	Materials	Temperature ℃	Dose (dpa) or fluence	Irrad. Start	Irrad. Finish	Status
HFIR-TRIST-ER1	ORNL	MONBUSHO/ JAERI	S.J. Zinkle	In-situ electrical conductivity	Al2O3	450	3E+25 n/m2	Apr-96	Jun-96	▨
HFIR-RB-10J	ORNL	JAERI	J.E. Pawel	Tensile, fracture	Vanadium, 316LN-1G, J316	200, 500	5	Oct-98	Oct-99	▦
HFIR-RB-11J	ORNL	MONBUSHO/ JAERI	M. L. Grossbeck	Tensile, fracture, TEM	Low activation ferritics, V alloys, SiC	300	5	Feb-97	May-98	▨
HFIR-RB-12J	ORNL	MONBUSHO/ JAERI	M. L. Grossbeck	Tensile, fracture, TEM	Low activation ferritics, V alloys, SiC	500	5	Feb-97	May-98	▨
HFIR-RB-13J	ORNL	MONBUSHO/ JAERI	S. J. Zinkle	Varying temp. experiment	Ceramics, Fe-Cr-Ni, V alloys, ferritics, copper	200, 350, 500	5	Jul-98	Jul-99	▨
HFIR-RB-14J	ORNL	MONBUSHO	L. L. Snead	Strength, fracture, dim. stability, diffusivity	2nd generation SiC/SiC	300, 500, 800	5	Feb-99	Feb-00	▦
HFIR-TRIST-TC1	ORNL	MONBUSHO/ JAERI	L. L. Snead	In-situ thermal conductivity	SiC/SiC, SiC	150-700	3	Jan-99	Dec-99	▨
HFIR-CTR-62	ORNL	JAERI	R.L. Klueh	Charpy impact and He effects	and conventional ferritic steels	300, 400	13	Apr-95	Dec-95	▨
HFIR-CTR-63	ORNL	JAERI	R.L. Klueh	Charpy impact and tensile, TEM, He effects	and conventional ferritic steels	300, 400	13	Apr-95	Dec-95	▨
HFIR-JP25	ORNL	JAERI	R.L. Klueh	Tensile, fracture, TEM	Low activation ferritics	300, 500	20	Feb-99	Jan-00	▦
High Flux Beam Reactor, Brookhaven National Laboratory										
HFBR-ISEC-3	ORNL		L.L. Snead	In-situ electrical	WESGO Al2O3	450	1.5	Jul-95	Sep-95	▨
HFBR-V1	ORNL		L.L. Snead	Tensile, fracture	V-4Cr-4Ti	75, 150, 225	0.4	May-95	Jun-95	▨
HFBR-V2	ORNL		L.L. Snead	Tensile, fracture	V-4Cr-4Ti	75, 225, 300, 375	0.4	Jul-95	Aug-95	▨
HFBR-V3	ORNL		L.L. Snead	Tensile, fracture	V-4Cr-4Ti	160, 265, 315, 420	0.4	Aug-96	Sep-96	▨
HFBR-V4	ORNL		L.L. Snead	Tensile, fracture	V-4Cr-4Ti	105-505	0.1	Aug-96	Sep-96	▨

Summary of Reactor Irradiation Experiments

Experiment	Lead Lab	Collaborators	Responsible Person	Major Objectives	Materials	Temperature ℃	Dose (dpa) or fluence	Irrad. Start	Irrad. Finish	Status
Advanced Test Reactor, Idaho Falls										
ATR-A1	ANL	MONBUSHO	D.L. Smith	Tensile, fracture toughness, TEM, creep	Vanadium alloys	200, 300	5	Dec-95	May-96	▨
BOR-60 Reactor, RIAR, Dimitrovgrad, Russia										
BOR-60-Fusion-1	ORNL, ANL	RDIPE, RIAR	A.F. Rowcliffe, D.L. Smith	Mechanical and microstructural properties	V alloys	350-380	10	Jul-95	Mar-96	▨
SM-2 Reactor, RIAR, Dimitrovgrad, Russia										
SM-2.1	ORNL, PNL	RIAR	S.J. Zinkle	Tensile, electrical, microstructural, and creep properties	Cu alloys	100, 200, 330	1, 5	Dec-93	Feb-94	▨
SM-2.2	PNL	SRIAR	D.J. Edwards	Mechanical behavior of bonded materials	Cu alloys/SS, Cu/Be	120, 300	0.2	Mar-96	May-96	▨
SM-2.3	PNL	SRIAR	D.J. Edwards	Mechanical behavior of bonded materials	Cu alloys/SS, Cu/Be	150, 300 200	0.4 2.0	Sep-97 Jul-98	Dec-97 Oct-98	▨

▨	Irradiation complete
▦	Irradiation in progress
░	Irradiation planned

Distribution

1. Advanced Micro Devices, Inc., 5204 E. Ben White Blvd., MS-613, PCAL-Analytical TEM Section, Austin TX 78741
J. Gazda

2-14. Argonne National Laboratory, 9700 South Cass Avenue, Argonne, IL 60439
M. C. Billone
T. S. Bray
O. K. Chopra
H. M. Chung
D. R. Diercks
A. B. Hull
C. E. Johnson
J. P. Kopasz
R. F. Mattas
K. Nateson
J. H. Park
D. L. Smith
H. C. Tsai

15-16. Argonne National Laboratory, EBR-II Division, P.O. Box 2528, Idaho Falls, ID 83403-2528
H. P. Planchon
D. L. Porter

17. Auburn University, Department of Mechanical Engineering, 201 Ross Hall, Auburn, AL 36849
B. A. Chin

18-19. Boeing, Mail Code S 106 7220, P.O. Box 516, St. Louis, MO 63166-0516
J. W. Davis
G. W. Wille

20. Carnegie Institute of Technology, Carnegie-Mellon University, Schenley Park, Pittsburgh, PA 15213
W. M. Garrison, Jr.

21. Commissariat à l'Energie Atomique, Direction des Technologies Advancées, M2R1/DECM Cen-Saclay, Gif Sur Yvette, Cedex, France
F. Tavassoli

22. Dow Corning Corporation, 3901 S. Saginaw Rd., MS-500, Midland, MI 48686-0995
R. E. Jones

23-25. General Atomics, P.O. Box 85608, San Diego, CA 92138
W. R. Johnson
K. R. Schultz
C. Wong

26. Georgia Institute of Technology, Fusion Research Center, 0225, Atlanta, GA 30332
W. M. Stacey

27. Grand Canyon University, Department of Natural Science, 3300 W. Camelback Rd., Phoenix, AZ 85017
W. A. Coghlan

28-30. Idaho National Engineering Laboratory, Fusion Safety Program, P.O. Box 1625, Idaho Falls, ID 83415-3523
G. Longhurst
K. McCarthy
D. Petti

31. Knolls Atomic Power Laboratory, P.O. Box 1072, Schenectady, NY 12301
G. Newsome

32-34. Lawrence Livermore National Laboratory, P.O. Box 808, Livermore, CA 94550
T. Diaz de la Rubia
W. G. Wolfer
J. Perkins

35-41. Los Alamos National Laboratory, Los Alamos, NM 87545
J. L. Anderson
R. G. Castro
D. W. Cooke
E. H. Farnum
R. E. Siemon
W. F. Sommer
K. E. Sickafus

42-44. Massachusetts Institute of Technology, Department of Metallurgy and Materials Science, Cambridge, MA 02139
L. W. Hobbs
N. J. Grant
K. C. Russell

45. Massachusette Institute of Technology, Plasma Fusion Center Headquarters, Cambridge, MA 02139
D. B. Montgomery

46. McMaster University, Engineering Physics, Hamilton, Ontario, Canada L8S 4L7
D. P. Jackson

47. MER Corp., 7960 South Kolb Rd., Tucson, AZ 85706
W. Kowbel

48. Merrimack College, Dept. of Physics, 315 Turnpike Street, North Andover, MA 01845
D. P. White

49. M. J. Schiff & Associates, 1291 N. Indian Hill Blvd., Claremont, CA 91711-3897
G.E.C. Bell

50-51. NASA Lewis Research Center, MS-106-5, Cleveland, OH 44135
J. DiCarlo
G. Morscher

52-54. National Institute of Standards and Technology, Boulder, CO 80302
F. R. Fickett
H. I. McHenry
R. P. Reed

55-56. Naval Research Laboratory, Code 6506, Washington, DC 20375
D. L. Griscom
J. A. Sprague

57-98. Oak Ridge National Laboratory, P.O. Box 2008, Oak Ridge, TN 37831
Central Research Library
Document Reference Section
Laboratory Records-OSTI (2)
Laboratory Records-RC
J. Bentley
E. E. Bloom
T. D. Burchell
T. S. Byun
S. D. Connery
J. R. DiStefano
R. H. Goulding
M. L. Grossbeck
N. Hashimoto
J. F. King
E. A. Kenik
R. L. Klueh
E. H. Lee
L. K. Mansur
P. J. Maziasz
S. Milora
Y. Miwa
B. A. Pint
L. Qualls
T. C. Reuther
J. P. Robertson
A. F. Rowcliffe (10)
J. Sheffield
L. L. Snead
R. E. Stoller
K. R. Thoms
N. L. Vaughn
S. J. Zinkle

99-112. Pacific Northwest National Laboratory, P.O. Box 999, Richland, WA 99352
D. J. Edwards
F. A. Garner (5)
D. S. Gelles
L. R. Greenwood
M. L. Hamilton
H. L. Heinisch
G. W. Hollenberg
R. H. Jones
R. J. Kurtz
J. Youngblood

113. Oregon Graduate Institute, Dept. of Materials Science & Engineering, 19600 N.W. Von Neumann Drive, Beaverton, OR 97006
J. M. McCarthy

114-116. Princeton University, Princeton Plasma Physics Laboratory, P.O. Box 451, Princeton, NJ 08540
R. Goldston Long-Poe Ku D. M. Meade

117-118. Rensselaer Polytechnic Institute, Troy, NY 12181
D. Duquette D. Steiner

119-121. Sandia National Laboratories, Fusion Technology Dept., Dept. No 6531, P.O. Box 5800, Albuquerque, NM 87185-5800
M. J. Davis M. Ulrickson R. D. Watson

122-123. Sandia National Laboratories, Livermore Division 8316, Livermore, CA 94550
W. Bauer K. Wilson

124. San Diego State University, Mechanical Engineering Dept., San Diego, CA 92182-0191
L. D. Thompson

125. Texas A&M University, Box 397, Prairie View, TX 77446
D. Baker

126. TSI Research, 225 Stevens Ave., #110, Solana Beach, CA 92075
E. T. Cheng

127. University of California at San Diego, U.S. ITER Project Office, 9500 Gilman Drive, Bldg. 302, La Jolla, CA 92093-0035
C. C. Baker

128. University of California at San Diego, Fusion Energy Research Program, 9500 Gilman Drive, MC0417, La Jolla, CA 92093-0417
M. Tillack

129-130. University of California at Santa Barbara, Dept. of Mechanical and Environmental Engineering, Engineering II, Room 2355, Santa Barbara, CA 93106-5070
G. E. Lucas G. R. Odette

131-133. University of California at Los Angeles, Dept. of Chemical, Nuclear, and Thermal Engineering, Los Angeles, CA 90024
M. A. Abdou N. M. Ghoniem S. Sharafat

134. University of Illinois, Dept. of Nuclear Engineering, Urbana, IL 61801
J. Stubbins

135. University of Michigan, Dept. of Nuclear Engineering, Ann Arbor, MI 48109
T. Kammash

136. University of Missouri, Department of Nuclear Engineering, Rolla, MO 65401
A. Kumar

137-138. University of Tennessee, Dept. of Materials Science and Engineering, 427-B Dougherty Bldg., Knoxville, TN 37996-2200
P. K. Liaw C. J. McHargue

139-140. University of Wisconsin, Nuclear Engineering Dept., 1500 Johnson Drive, Madison, WI 53706
J. B. Blanchard G. L. Kulcinski

141. Helsinki University of Technology, Laboratory of Engineering Materials, Puumiehenkuja 3, SF-02150 Espoo, Finland
H. Hänninen

142-143. Hokkaido University, Center for Advanced Research of Energy Technology, Kita 13, Nishi 8, Kita-ku, Sapporo 060-8628, Japan
Tamaki Shibayama Heischichiro Takahashi

144-146. Hokkaido University, Faculty of Engineering, Kita 13, Nishi 8, Kita-ku, Sapporo 060-8628, Japan
Somei Ohnuki Akira Okada Seiichi Watanabe

147-151. Japan Atomic Energy Research Institute, Tokai Research Establishment, Tokai-mura, Naka-gun, Ibaraki-ken 319-1195, Japan
Akimichi Hishinuma Tatsuo Kondo R. Yamada
S. Jitsukawa Kenji Noda

152-154. Kyoto University, Institute of Advanced Energy, Gokasho, Uji, Kyoto 611-0011, Japan
Yutai Katoh Akihiko Kimura Akira Kohyama

155-156. Kyushu University, Dept. of Nuclear Engineering, Faculty of Engineering, Kyushu University, Hakozaki, Fukuoka 812-8582, Japan
Chiken Kinoshita Kenichi Shiiyama

157-158. Kyushu University, Research Institute for Applied Mechanics, Kasuga, Fukuoka 816-8580, Japan
Hideo Watanabe Naoaki Yoshida

159. Muroran Institute of Technology, Dept. of Metallurgical Engineering, 27-1 Mizumoto-cho, Mororan 050-8585, Hokkaido, Japan
Toshihei Misawa

160. Nagoya University, Dept. of Nuclear Engineering, Furo-Cho, Chikusa-ku, Nagoya 464-8603, Japan
Tetuo Tanabe

161-164. National Institute for Fusion Science, Oroshi, Toki, Gifu 509-5292, Japan
Osamu Motojima Chusei Namba
Takeo Muroga Nobuaki Noda

165-168. National Research Institute for Metals, Tsukuba Branch, Sengen, Tsukuba-shi, Ibaraki-ken, 305-0047, Japan
Fujio Abe Tetsuji Noda
Josei Nagakawa Haruki Shiraishi

169. PNC Oarai, 4002 Narita, Oarai, Ibaraki 311-1393, Japan
S. Ukai

170. Science University of Tokyo, Dept. of Materials Science & Technology, 2641 Yamazaki, Noda-shi, Chiba 278-8510, Japan
Naohiro Igata

171. Teikyo University, 359 Otsuka, Hachioji, Tokyo 192-0395, Japan
Akira Miyahara

172. Tohoku University, Institute for Materials Research, Katahira 2-2-1, Aoba-ku, Sendai 980-8577, Japan
Hideki Matsui

173-174. Tohoku University, Institute for Materials Research, Oarai Branch, Oarai-machi, Ibaraki 311-13, Japan
Hiroaki Kurishita   Tatsuo Shikama

175-177. Tohoku University, Dept. of Quantum Science & Energy Engineering, Aoba, Aramaki, Sendai 980-8579, Japan
Katsunori Abe   Akira Hasegawa   Manabu Satou

178. Tokai University, Dept. of Nuclear Engineering, 1117 Kitakaname, Hiratsuka-shi, Kanagawa-ken 259-1292, Japan
Shiori Ishino

179. University of Tokyo, Dept. of Nuclear Engineering, 3-1, Hongo 7-Chome, Bunkyo-Ku, Tokyo 113-8654, Japan
Naoto Sekimura

181. University of Tokyo, Dept. of Materials Science, 3-1, Hongo 7-Chome, Bunkyo-ku, Tokyo 113-8654, Japan
Yutaka Kohno

181. VTT Manufacturing Technology, P.O. Box 1704, FIN-02044 VTT, Finland
P. Aaltonen

182. Commission of European Communities, Directorate-General for Research Science and Education, Fusion Programme RUE De La Loi 200, B-1049 Brussels, Belgium
F. Cozzani

183. Southwestern Institute of Physics, P.O. Box 432, Chenedu 610041, Sichuan, P.R. China
Zeng Yu Xu

184-185. Institute of Atomic Energy, Academia Sinica, P.O. Box 275-51, Beijing 102413, P.R. China
J. P. Qian   J. Yu

186. Riso National Laboratory, Materials Dept., P.O. Box 49, DK-4000, Roskilde, Denmark
B. N. Singh

187. CEA-CEREM-CEA, Saclay, CE2M/LECMA, Commissariat a l'Energie Atomique, 91191 Gif-Sur-Yvette, Cedex, France
N. Roux

188. Commission for European Communities, Joint Research Centre, I.A.M. Ispra Establishment, 21020 Ispra (Varese), Italy
P. Fenici

189. EURATOM/CIEMAT Fusion Association, Avenida Complutense 22, 28040, Madrid, Spain
E. R. Hodgson

190. Netherlands Energy Research Foundation ECN, Westerduinweg 3, P.O. Box 1, Nl 1755 LE Petten, Netherlands
B. Van der Schaaf

191. Paul Scherrer Institute, CH-5232 Villigen, Wuerenlingen PSI, Switzerland
M. Victoria

192. Harwell Laboratory, B393, Radiation Damage Dept., Oxfordshire, OX11 ORA, United Kingdom
C. A. English

193. Metallurgical and Nuclear Consultant, 9A Cumnor Rise Road, Cumnor Hill, Oxford OX2 9HD, United Kingdom
D. R. Harries

194. Hahn-Mietner-Institut fur Kernforschung Berlin, Postfach 390128, Glienicker Str. 100, D-14109, Germany
H. Wollenberger

195. Institut fur Festkorperforschung Forschungszentrum Jülich, Postfach 1913, D-52425 Jülich, Germany
H. Ullmaier

196-197. ITER Garching Joint Work Site, Max-Planck-Institute für Plasmaphysik, Boltzmannstrasse 2, D-85748 Garching bei München, Germany
V. Barabash G. Kalinin

198-199. ITER Naka Joint Work Site, 801-1 Mukouyama, Naka-machi, Naka-gun, Ibaraki-Ken, 311-01, Japan
M. Huguet (2)

200-202. Kernforschungszentrum Karlsruhe, Postfach 3640, 75 Karlsruhe 1, Germany
M. Dalle-Donne (INR) A. Moeslang
K. Ehrlich (IMF-II)

203. Max-Planck-Institut für Plasmaphysik, Boltzmannstrasse 2, D-85748 Garching bei München, Germany
Patrick Lorenzetto

204. A. A. Baikov Institute of Metallurgy, USSR Academy of Sciences, Leninsky Prospect 49, Moscow, Russia
L. I. Ivanov

205. CRISM "Prometey," Naberezhnava r. Monastyrick 1, 193167, St. Petersburg, Russia
V. V. Rybin

206. D. V. Efremov Institute of Electro-Physical Apparatus, Scientific Technical Center "Sintez,"189631, St. Petersburg, Russia
S. A. Fabritsiev

207. Kharkov Institute of Physics & Technology, Radiation Damage and Materials Dept.,
Akademicheskaya 1, 310108 Kharkov, Ukraine
I. M. Neckludov

208-210. V. I. Lenin Research Institute of Atomic Reactors, 433510 Dimitrovgrad-10,
Ulyanovsk Region, Russia
V. Kazakov A. S. Pokrovsky V. K. Shamardin

211. Korea Advanced Institute of Science and Technology, Department of Nuclear
Engineering, DaeDukDanji, Taejon, 305-701, Korea
I-S. Kim

212. Korean Atomic Energy Research Institute, P.O. Box 105, Yusung, Taejon, 305-600,
Korea
Jun Hwa Hong

213. Seoul National University, Dept. of Nuclear Engineering, 56-1 Shinrim-Dong,
Kwanak-Ku Seoul, 151-742, Korea
K. H. Chung

214. Sung Kyun Kwan University, Dept. of Metallurgical Engineering, 300 Chunchun-dong,
Jangan-gu, Suwon, 440-746, Korea
J. G. Han

215. Department of Energy, DOE Oak Ridge Field Office, P.O. Box 2008,
Oak Ridge, TN 37831-6269
Assistant Manager for Energy Research and Development

216. Department of Energy, DOE Oak Ridge Field Office, P.O. Box 2008,
Oak Ridge, TN 37831-6269
S. D. Frey

217. Department of Energy, Office of Basic Energy Sciences, Washington, D.C. 20585
R. J. Gottschall

218-222. Department of Energy, Office of Fusion Energy, Germantown, MD 20874
S. E. Berk W. Marton F. W. Wiffen
N. A. Davies R. McKnight

223. Department of Energy, Richland Operations Office, P.O. Box 550, MS-K850,
Richland, WA 99352
J. Turner